

UC Berkeley

UC Berkeley Electronic Theses and Dissertations

Title

Dynamics of excess electrons in atomic and molecular clusters

Permalink

<https://escholarship.org/uc/item/0wj1n3xv>

Author

Young, Ryan Michael

Publication Date

2011

Peer reviewed|Thesis/dissertation

Dynamics of excess electrons in atomic and molecular clusters

by

Ryan Michael Young

A dissertation submitted in partial satisfaction of the
requirements for the degree of

Doctor of Philosophy

in

Chemistry

in the

Graduate Division of the

University of California, Berkeley

Committee in charge:

Professor Daniel M. Neumark, Chair

Professor Stephen R. Leone

Professor Robert W. Dibble

Fall 2011

Abstract

Dynamics of excess electrons in atomic and molecular clusters

by

Ryan Michael Young

Doctor of Philosophy in Chemistry

University of California, Berkeley

Professor Daniel M. Neumark, Chair

Femtosecond time-resolved photoelectron imaging (TRPEI) is applied to the study of excess electrons in clusters as well as to microsolvated anion species. This technique can be used to perform explicit time-resolved as well as one-color (single- or multiphoton) studies on gas phase species. The first part of this dissertation details time-resolved studies done on atomic clusters with an excess electron, the excited-state dynamics of solvated molecular anions, and charge-transfer dynamics to solvent clusters. The second part summarizes various one-color photoelectron imaging studies on tetrahydrofuran clusters with an excess electron or doped with an iodide ion in order to probe the solvent structure of these clusters. Finally, a mixed study is presented exploring the effect of warmer cluster conditions on both the binding energies and relaxation times of excess electrons in water clusters.

Time-resolved studies on mercury cluster anions $(\text{Hg})_n^-$ ($7 \leq n \leq 20$) demonstrate the different timescales of electron-phonon and electron-electron scattering in small systems. Low-energy (1.0-1.5 eV) excitation of the excess electron to a higher-lying electronic state decays via a cascade through the conduction band on a 10-40 ps timescale. Conversely, high-energy (4.7 eV) excitation of an electron from the valence band into the conduction band opens a second relaxation pathway: emission of the excess electron via Auger decay. The larger number of charge carriers and the geometrical changes to the cluster following the creation of the valence band hole state increase the relaxation rate, causing relaxation to occur on a 100s of fs timescale. The size dependence of both relaxation timescales becomes much less significant around $n = 13$ near the van der Waals-to-covalent bonding transition seen in other studies of mercury clusters.

The solvated acetonitrile dimer anion, $(\text{CH}_3\text{CN})_n^-$ ($20 \leq n \leq 50$) is also studied using TRPEI. The dimer anion is selectively excited with 790 nm (1.57 eV) pulses and probed with 395 nm (3.14 eV) pulses, detaching both the ground and excited states. The excited clusters are observed to autodetach on a timescale of ~200-300 fs with no size dependence. The excited-state autodetachment shows a direct link for the first time between the two different binding motifs observed in the gas phase with the two isomers observed in solution from their absorption

profiles.

Electron solvation dynamics following charge-transfer-to-solvent excitation from iodide to small methanol clusters, $I^-(CH_3OH)_n$ ($4 \leq n \leq 11$) are also examined with TRPEI. After electron transfer, the excited state spectrum undergoes significant evolution in both its position and shape. Considerations of the geometries of the initial iodide-doped methanol cluster as well as the intermediate bare methanol anion cluster and final neutral clusters suggest the electron is solvated, as at least one methanol molecule rotates to bring its hydroxyl group inward toward the cluster center, maximizing the hydrogen bond network. The observed relaxation timescales for both the vertical detachment energies and the spectral width (5-30 ps) are consistent with this type of motion. An autodetachment feature is also observed at all pump-probe delays, indicating that this is the primary decay pathway for these clusters, which is consistent with the lack of observed stable methanol cluster anions in this size range.

One-color, one photon photoelectron imaging is applied to study tetrahydrofuran cluster anions $(THF)_n^-$ ($1 \leq n \leq 100$) to probe the nature of the solvated electron in that solvent. An anion at the same mass-to-charge ratio as the THF anion is observed, though THF^- is not expected due to its closed shell electronic structure, high HOMO-LUMO gap and dipole moment. Two peaks are observed in the photoelectron spectrum for this species, one of which is attributed to a long-chain $C_4H_8O^-$ anion formed after ring-opening from the secondary electron attachment. The other peak is likely due to a metastable THF transient negative ion arising from fragmentation of the larger clusters. These features persist until $n = 5$. By $n = 6$, the photoelectron spectra change shape, becoming much larger, and maintain that shape through $n = 100$. This transition is accompanied by an abrupt change in the photoelectron angular distribution. These changes are attributed to onset of the solvated electron state in THF clusters. The binding energy for the smallest cluster of this species is 1.96 eV, much higher than that for other solvated electron clusters at onset. Extrapolation to infinite cluster sizes yields a bulk value of 3.10 ± 0.03 eV. The energetics are analyzed in the frameworks of dielectric continuum theory and the proposed cavity structure for bulk THF.

Iodide-doped THF clusters, $I^-(THF)_n$ ($1 \leq n \leq 30$), are also studied using ultraviolet photoelectron imaging in order to understand the nature of their solvation in THF and in attempt to define their structures. A substantial decrease in the stabilization energy is seen by $n = 9$, indicating the coordination number is maximized. However, the iodide ion continues to be significantly stabilized with addition of THF molecules, suggesting that the solvation shell is not completely closed. Larger sizes are stabilized in a manner similar to the bare cluster anions. *Ab initio* calculations suggest the iodide is at least partially embedded in the solvent cluster near the surface, surrounded by a sub-structure of 7-9 solvent molecules.

The effect of warmer clustering conditions on electron binding energies and relaxation times in water clusters is investigated by using neon instead of argon as the carrier gas in the adiabatic expansion. Only isomer I water cluster anions are observed, with their binding energies only slightly perturbed by the change in cluster internal energy. The relaxation dynamics following $p \leftarrow s$ excitation is monitored using time-resolved photoelectron imaging. Internal conversion lifetimes are seen to be shorter for anions formed in neon compared to those formed in argon, though they appear to converge to the same bulk limit.

*This dissertation is dedicated in
memory of my grandparents
who taught me the value of hard work
and to always push myself to do my best.*

Contents

Abstract.....	1
Dedication.....	i
Contents.....	ii
Acknowledgements.....	vi
Chapter 1. Introduction.....	1
1.1 Anion Clusters as Model Systems.....	1
1.2 Femtosecond Time-Resolved Photoelectron Spectroscopy.....	2
1.2.1 Photodetachment.....	2
1.2.2 Photoelectron imaging.....	6
1.3 Summary of systems studied.....	8
1.3.1 Semiconducting mercury cluster anions.....	8
1.3.2 Acetonitrile cluster anions.....	9
1.3.3 Iodide-doped methanol clusters.....	10
1.3.4 Tetrahydrofuran cluster anions.....	12
1.3.5 Iodide-doped tetrahydrofuran clusters.....	13
1.3.6 Water cluster anions.....	14
Chapter 2. Experimental Apparatus.....	17
2.1 Atomic, Molecular and Cluster Ion Source.....	17
2.2 Femtosecond laser system.....	19
2.2.1 Dispersion compensating prisms.....	22
2.2.2 Optical parametric amplifier.....	23
2.2.3 Tunable UV by four-wave mixing.....	25
2.3 Velocity Map Imaging (VMI) electron detection.....	28
2.4 References.....	29

Chapter 3. Charge Carrier Dynamics in Semiconducting Mercury Cluster Anions $(\text{Hg})_n^-$	
$(7 \leq n \leq 20)$	31
3.1 Introduction	31
3.2 Experimental Setup	33
3.3 Dynamics in Mercury Cluster Anions.....	33
3.3.1 <i>Results</i>	33
3.3.2 <i>Discussion</i>	35
3.4 Outlook.....	38
3.5 References	39
Chapter 4. Time-Resolved Dynamics in Acetonitrile Cluster Anions $(\text{CH}_3\text{CN})_n^-$	
$(20 \leq n \leq 50)$	41
4.1 Introduction	41
4.2 Experimental	42
4.3 Results and Analysis	43
4.4 Discussion	46
4.6 Conclusions	51
4.7 References	51
Chapter 5. Dynamics of Electron Solvation in $\text{I}^-(\text{CH}_3\text{OH})_n$ ($4 \leq n \leq 11$).....	53
5.1 Introduction	53
5.2 Experimental	56
5.3 Results	57
5.4 Analysis.....	59
5.5 Discussion	64
5.5.1 <i>Population dynamics</i>	66
5.5.2 <i>VDE's and peak widths</i>	67
5.5.3 <i>Comparison to larger systems</i>	70
5.6 Conclusions	71
5.7 References	72

Chapter 6. Photoelectron Imaging of Tetrahydrofuran Cluster Anions (THF)_n⁻

(1 ≤ n ≤ 100)	74
6.1 Introduction	74
6.2 Experimental	75
6.3 Results and Analysis	76
6.3.1 <i>Mass spectrum</i>	76
6.3.2 <i>Photoelectron spectra</i>	77
6.4 Discussion	80
6.4.1 <i>Large clusters</i>	80
6.4.2 <i>Small anions</i>	82
6.4.3 <i>General remarks</i>	85
6.5 Conclusion.....	87
6.6 References	87
Chapter 7. Iodide Solvation in Tetrahydrofuran Clusters I ⁻ (THF) _n (1 ≤ n ≤ 30).....	90
7.1 Introduction	90
7.2 Experimental	92
7.3 Results and Analysis	92
7.3.1 <i>Mass spectrum</i>	92
7.3.2 <i>Photoelectron spectra</i>	93
7.4 Discussion	95
7.4.1 <i>Photoelectron and mass spectra</i>	95
7.4.2 <i>Comparison to other solvents</i>	98
7.4.3 <i>Computational results</i>	99
7.4.4 <i>Bound excited states</i>	100
7.5 Conclusion.....	102
7.6 References	102

Chapter 8. Thermal Effects on Energetics and Dynamics in Water Cluster Anions

$(\text{H}_2\text{O})_n^-$ ($11 \leq n \leq 75$)	104
8.1 Introduction	104
8.2 Experimental	106
8.3 Results and Analysis	106
8.4 Discussion	109
8.5 Conclusions	114
8.6 References	114
Appendix 1. Revised Triggering Scheme	116
Appendix 2. Isotope effect on free rotation period of methanol	119
A2.1 Inertia tensor calculation	119
A2.2 References	122
Appendix 3. Fitting Mass Spectra.....	123
A3.1 Time-of-Flight Mass Spectrometry	123
A3.2 Fitting Cluster Distributions.....	125
A3.3 References	126
Appendix 4. Image DAQ 2.0.....	127
A4.1 Program Structure.....	127
A4.2. ImageDAQ 2.0 Interface	130
A4.3 Modifying Parameters and Setting Dead Pixels.....	133
A4.4 Error Codes, Known Issues, and Future Improvements.....	134
A4.5 References	136
Appendix 5. Publications from Graduate Work	137

Acknowledgements

It goes without saying that the work presented in this dissertation could not have been accomplished by me alone. If I have had any success in graduate school it is only because I have had the help of many talented, patient and intelligent people.

Most of all, I would like to thank Dan for his patience and insight. I cannot count the times I would ask his thoughts on some ill-formed idea I had on whatever system we were examining and he would lead me to a better way of thinking about the problem. Probably the most important specific thing I have learned here is to always think of the system in terms of the relevant potential energy surfaces. While that might seem an obvious thing to do, it is easy, at least for me, to get lost in the details. It is not always easy to figure out what they look like, but once the surfaces are established, the dynamics become much easier to think about. I am very pleased to have adopted this idea in time to make good use of it. In general, I have learned to never be afraid of breaking the equipment, since that tends to be when you learn the most. I am unable to list all the things I learned from working for Dan, but I can say with utmost confidence that I would not have been as successful here without his guidance. Dan has fostered a very enjoyable atmosphere in his group, and not just between his students. I have enjoyed a rapport with Dan these last few years that has evolved from a passing acknowledgement of my existence to my being able to goad him into a dirty joke contest in the Faculty Club (which ended in a draw). I have never felt uncomfortable finding Dan in either of his offices and seeking his advice, though he was undoubtedly annoyed by the frequency at times. Perhaps this is why he (hopefully jokingly) chose to use me as an electrical ground when checking the diffusion pumps. I have also enjoyed a large amount of freedom in the past few years regarding the experiment and the systems we looked at, which could have been anything just so long as it was interesting. I cannot imagine a more stimulating and enjoyable environment to work in. Joining Dan's group is of the best decisions (and possibly the best) I have made, and I thank him for the opportunity.

Of course, one of the reasons that Dan's group functions as well as it does is the tireless work of Michelle Haskins. She is perhaps the most positive person I have ever known, and certainly one of the most pleasant. She started in the group right before I did, so many of the administrative tasks I had to deal with were new to both of us, which managed to make things seem less daunting. I have enjoyed many long conversations with her in her office, most of which were completely unrelated to whatever small errand brought me there. Usually these conversations were terminated by nothing more than my guilt at taking her away from her work, but she never would have said anything. Beyond making life in the lab simpler by bearing the brunt of the administrative nightmare that is the University, Michelle always brightened my day with friendly conversation and genuine compassion. Perhaps the highest praise I can give her is that the group simply could not function without her, and she will be deeply missed.

Since I joined the group project I have had the pleasure to work with a handful of great people who were not only very talented scientists but also were endlessly patient in teaching me the ropes of time-resolved photoelectron spectroscopy. I want to especially thank Graham Griffin for showing me the day-to-day workings of the lab, everything from aligning the laser to repairing any electronics that randomly decided to malfunction. More than anything, though, from him I learned how to take good data, especially how to recognize when data are no good altogether or the diminishing returns of longer collection times. Graham always seemed to have a good perspective on things and an understand of when sometimes things were just screwed up and the day had to be written off as a loss. Of course he countered this with a strong work ethic

and an attitude of never letting the ions or the machine win. Graham also had a very good idea of balance between work and fun, something I aspired to, but I do not think I ever got the hang of. He always found a way to make working in the lab fun. Aster Kammrath was in her fifth year here when I showed up and even though she was usually busy writing, she still took the time to show me the right way to align the laser on the table or to make cluster anions. She always seemed to be reading a different book in a different language everyday while taking data, which made for some rather interesting conversations. Besides the actual workings of the science, from Aster I learned how sometimes just waiting for the ions to "get better" or "fix themselves" was sometimes the best thing we could do, and that being patient with the system was fundamental to getting good data.

In 2007, we unexpectedly got a postdoc from Germany on our project. Working with Dr. Oli Ehrler proved to be one of the high points of my graduate career. I can safely say that whatever science I didn't learn from Dan I learned from him. Oli was both superbly professional in the lab while extremely fun outside it. I thank Oli for introducing me to the game of squash, and never taking it too seriously, which was great since I was (and still am) terrible at it. More than anyone he seemed to think that I was well-suited to being a scientist (besides the social awkwardness), and he encouraged me to forget my own doubts about myself. His confidence in me really went a long way. I cannot forget (or let him forget) the fun times we had (the group's outing to Blake's, his "German girls!?!?" comment, and helping Luca move amongst them), and I must say that working with Oli was a distinct pleasure and probably the most fun I've had in the lab.

Right after Oli left in 2009 I was joined on the project by Maggie Yandell. Maggie has been a pleasure to work with, and she has proven to be invaluable to bounce ideas off of. Maggie also has this uncanny ability to know when I'm full of crap, which is probably more frequent than I'd like to admit, and it kept us on track. She also brings a much different background to the experiment than what I had, which has proven to be quite useful when we actually do chemistry in the expansion, as was the case with the THF system, and will likely be essential for the biomolecules to be looked at after I leave. Certainly more than me, Maggie is very methodical in whatever she does in the lab, which has prevented me from making more than a couple silly mistakes. Aside from working in the lab, Maggie has taken it upon herself to ensure that the group is being adequately social, something that would not happen if left to our own devices. The group lunches and game nights as well as random outings she has organized have really made life in the lab more enjoyable and have kept me from working myself into the ground. In my last year here, Sarah King also started working on the project and has proven herself to be very driven and interested in the work. It is very evident that the lab is in good hands and Maggie and Sarah will get a lot of very interesting science done.

I also want to thank Markus Niemeyer. Markus was a diploma student from Berlin when he arrived in the fall of 2009 for a six month research visit. It was obvious very quickly that he was a talented and extremely capable student, and a lot of the data collection for the acetonitrile and THF systems presented here was done with his assistance. The common situation in this lab cropped up (predictably) at the end of 2009, as there was not enough for three people to do. It was about that time that we had been kicked off the network and were unable to upload any data to the server. As a project/team, we had had discussions of rebuilding our data acquisition system and writing a new program, but it never got off the ground. Markus not only got the hardware for this up and running, but had a working version of the acquisition program after only two weeks, without any previous LabView experience. Maggie and I cannot praise this

program and Markus enough, especially considering some of the more frustrating aspects of the previous version. I truly hope the experience was as useful and beneficial for him as it was for us.

The group itself has, of course, changed over my tenure here, which is neither good nor bad. I have definitely learned something from each of them, and they are a big part of how I was able to make it through graduate school. I will undoubtedly be leaving people out, so I want to first thank the entire Neumark group for being patient with me and for always being ready to lend a hand when something came up. Specifically, I want to thank Alex Shreeve for his frequent assistance with the pumps in our lab. Most of his advice (there was one exception) was extremely useful and has made any work on our pumps that came up much faster and simpler. Vacuum systems are one of his self-admitted joys in life, so as annoying as it may have been to be frequently helping us out, I think part of him enjoyed it. Undoubtedly, pump repairs would have been much delayed without his help. I have also benefitted from many interesting and insightful scientific conversations with him and Madeline Elkins, regarding both my experiment and their liquid microject project, particularly regarding the femtosecond laser. I should thank them both not only for putting up with me in that regard, but also for forcing me to explain things better, which ultimately helps me to think about things more clearly. And while hopefully they got something out of it, I certainly learned from the experience.

Whenever I needed some assistance in the student machine shop I could always count on Bogdan "B" Negru, who was so obviously passionate about machining and tinkering in the shop. He always had better things to do, but was unfailingly helpful and polite in lending a hand. Christian Hock has similarly been very helpful with machine drawings for various things I needed from the shop, and a pleasure to work with. I also want to thank Tara Yacovitch for showing Maggie and me (multiple times) how to run *ab initio* calculations on the various computers at our disposal. And though he is no longer here, I really do owe a lot to Oleg Kornilov for helping me with some not-so-obvious issues with the KM Labs lasers. He was my go-to guy for questions with the Dragon amplifier and Griffin oscillator, which was really impressive since he said he had never used a laser before he got here. Oleg was one of the most patient and pleasant people I have worked with, too, for which I am extremely lucky.

Much of the work in this dissertation has been aided by people from other research groups. In particular, the level of detail achieved for a lot of the systems studied here was only possible with complementary electronic structure calculations and molecular dynamics simulations by Julian Azar from the Head-Gordon group. Julian has not only been eager to tackle some rather difficult electronic structure problems motivated by our experiments, but has been a pleasure to work with. The quality of his work is amazing and I am constantly pleasantly surprised by the new ways he wants to tackle these problems. More than any one person, Julian has shown me how theory and experiment can complement each other to make an amazingly detailed molecular level picture of the dynamics we are investigating. I must also say that Julian's unique personality has made our collaboration all the more enjoyable; every email I get from him has a different, hilarious signature. I can only hope he has benefited from our collaboration as much as I have, though I doubt my personality is as entertaining.

Beyond the lab, there are a lot of people I want to acknowledge for making my graduate career enjoyable, both in the D-level and above. Lunches with Scott, Amy, Oli and Luca were always fun, even if we only went to the same three places all the time. Amy dropping by the lab at 4 PM with orange teeth was one of the most memorable days I had in Berkeley. Thanksgiving at Aster and Jia's place was similarly memorable, especially with Art and Beth

being there. Random conversations in the hallway with Aaron Harrison and Neil Cole-Filipiak were always fun. In the last year or so here, I've been able to have a bit more fun than before when I spent almost all of my time working. This has, in large part, been due to Gabriel "Gab" (or Gabby, as he loves to be called) Just, and his wife Yvette. They have been exceedingly generous and thoughtful, and are always up for doing something fun, like going into San Francisco with their Scottish friend or hosting a "terrible movie" night at their place. Gab and Yvette also have an amazing sense of humor about themselves, particularly regarding Gab's copious Frenchness and wonderfully deplorable excess of personality. Usually involved in these escapades are Alex and Madeline, who tend to heighten the sarcasm, which for me makes things much more fun. Our weekly trivia nights during my last semester here were often the highlights of my week. It is rare to find people who not only tolerate but embrace my level of sarcasm and can trade barbs without worrying about causing offense, and I will miss them for that. And Matt Damon.

While it can be argued that I did not have as much fun as I could have outside the lab, I definitely had my share thanks to some of the friends I made along the way. I randomly met Joey Hu in the library during some orientation event. That somehow led to us meeting Nick Halpern-Manners and Westin Kurlancheek, and the four of us ended up trudging through classes together (interestingly, and happy fragmented from the rest of our class - it seemed to work well for us). Through Westin we all met Will Gannett who fit well into that horribly sarcastic mix. The five (plus or minus) of us always managed to have a good time, sometimes just having a drink on the roof of Joey's apartment, or trading the random Futurama or Arrested Development quote (much to Nick's chagrin), or oyster shucking at Point Reyes. I still blame Westin for what happened at Henry's - he knows what he did. As long as I live I will never forget Joey asking for those stuffed olives and somehow... acquiring a sandwich. Nick and Will's (and Joey's) random BBQs were one of the few things that could drag me out of the lab, and I thank them for it. I also want to thank Vi Rapp for our many random lunches and excursions, and the birthday and dinner parties she put together. She is definitely one of the people I will miss the most. My thanks to these people for making life outside the lab much more enjoyable.

I would also like to thank the people who got me here in the first place. My first foray into ultrafast spectroscopy and solvent dynamics was through my undergraduate research in Ben Schwartz's group. I want to thank Ben for the opportunity he gave me which put me on my present path. I suppose I was given this chance in large part due to Alex Ayzner. I learned quite a bit from them during my time there. Molly Cavanagh and Art Bragg were both patient teachers and wonderful colleagues, but also good friends. Ultimately it was Art who convinced me to go to Berkeley and to strongly consider Dan's group. Good advice I would say. Those days with Alex, Steph, Molly, Ian, Art and Ross still make me laugh.

Finally, I would like to thank my parents, Robert and Mary Young, who have always supported me throughout my education and promoted the notion that I should never stop learning. They were my first teachers and the people from whom I learned the most. Growing up, I always heard that I needed to do something I enjoyed. There is probably nothing I enjoy more than learning something new and figuring things out, so they naturally supported my decision to go to graduate school and to do postdoctoral research, and I am sure they'll continue to support me wherever that takes me.

So thank you all. I am being completely honest when I say that I could not have done this without all of you, and I am sure I have forgotten some people. Michelle and Dan have both remarked that I managed to "come out of my shell" after my first year, and to this day I cannot

tell if that is a good thing, but in general graduate school has been a very positive experience for me because of all of you.

Chapter 1. Introduction

This dissertation presents work done in the Neumark group on the dynamics and energetics of anionic clusters using time-resolved photoelectron imaging. Chapter 1 outlines the basic concepts and principles behind the experiment, while Chapter 2 details the experimental apparatus and the various changes made during the course of the author's time in the laboratory. The remaining chapters describe in detail the experiments performed on the various system using the time-resolved photoelectron imaging spectrometer: the dynamics of charge carriers in mercury cluster anions (Chapter 3); vibrational autodetachment dynamics in solvated acetonitrile dimer anions (Chapter 4); electron solvation dynamics following charge transfer from iodide in methanol clusters (Chapter 5); electron and ion solvation in tetrahydrofuran clusters (Chapters 6 and 7); effects of warmer cluster conditions on electron binding energies and internal conversion dynamics in water cluster anions (Chapter 8). Details of the apparatus triggering and data acquisition programs are also presented, along with a routine for fitting mass spectra based on adjacent cluster spacing.

1.1 Anion Clusters as Model Systems

Due to their finite (though often still large) number of degrees of freedom, atomic and molecular clusters can serve as model systems for a variety of interactions such as solvation,¹ media for scattering events,²⁻⁴ or even chemical reactions.⁵ Despite the typically low number densities of anion beam experiments, many effective techniques have been developed to probe their structures and dynamics, such as mass spectrometry, infrared photodissociation and photoelectron spectroscopy (PES). In addition, cluster systems are currently tractable with modern quantum chemical methods even for fairly large sizes, and thus a wealth of information on structure and dynamics can be amassed for a given system, allowing for profound understanding of chemical and physical processes at the mesoscopic level.

Cluster science was born to understand the evolution from the molecular to the bulk regimes. At some point in the size evolution of a system, surface/structural and quantum effects must give way to thermodynamically averaged continuum properties. This evolution cannot, of course, be the same for every system, so careful consideration must be made as to how the property of interest changes with cluster size. A fundamental caveat for anion systems must also be made: the anionic system may not directly correlate with the neutral, especially at small cluster sizes.

Often, information from the clusters can be extrapolated toward an infinite size limit, offering an estimate for the analogous value in the bulk. However, not all systems asymptotically approach the bulk, as is, for example often assumed when extrapolating binding energies or internal conversion lifetimes from solvent cluster anions. Some emergent properties occur at relatively small cluster sizes, such as insulator-to-metal (Kubo) transitions.⁶ At the extreme, some small cluster anions may be so unstable that they do not exist long enough to be measured by conventional methods, such as mass spectrometry. Understanding this metastability and at what size the system achieves stability is only in the purview of cluster science.

Anion photoelectron spectroscopy allows for effective measurement of many of these properties with cluster size, as the photoelectron spectrometer can easily be coupled to a mass

spectrometer, and their binding energies are directly probeable with frequencies conveniently generated from table-top laser systems. The method is readily extendable to include high time resolution by employing a femtosecond laser. The underlying principles of photoelectron spectroscopy are outlined in the next section.

1.2 Femtosecond Time-Resolved Photoelectron Spectroscopy

1.2.1 Photodetachment

In anion photoelectron spectroscopy, the initially prepared anionic ground state of the molecular system is probed with single- or multi-photon detachment to a neutral manifold of final states. As a consequence of the Born-Oppenheimer approximation, in a vertical process (no nuclear rearrangement), photon energy in excess of the electron binding energy (eBE) is carried away through electron kinetic energy:

$$eBE = h\nu - eKE \quad (1.1)$$

Electron kinetic energy is measured and the binding energy distribution is reconstructed. The shape and intensity of this distribution is a consequence of the differential cross section for photodetachment. This quantity can be calculated within the perturbative regime using the Fermi Golden Rule:

$$\Gamma_{f \leftarrow i} = \frac{2\pi}{\hbar} \left| \langle f | \hat{H}^{(1)} | i \rangle \right|^2 \rho_f(E) \quad (1.2)$$

where $\Gamma_{f \leftarrow i}$ is the rate of transition between states i and f , $\rho_f(E)$ is the density of final states at energy E , and $\hat{H}^{(1)}$ is the (first order) perturbative Hamiltonian. Several simplifying assumptions can be made to arrive at a closed-form expression for the differential cross section. Most (though not all) of the experiments presented in this thesis employ weak fields such that multiphoton absorption (from the same pulse) can be ignored and higher-order corrections to the electromagnetic interaction Hamiltonian can be neglected. In addition, all of the clusters studied here are very small compared to the wavelengths of light employed such that the electromagnetic vector potential is effectively constant over the spatial extent of the system. Thus the electric dipole approximation is applicable here. Under these assumptions, the differential cross section for photodetachment from an anion in state $|i\rangle$ (electronic and vibrational state: $|i\rangle = |\phi^{(-)}\rangle|\chi^{(-)}\rangle$) to a free electron in a state $|k\rangle$ such that $\langle \vec{r} | k \rangle \propto e^{i(\vec{k}\cdot\vec{r})}$ can be written as:⁷

$$\frac{d\sigma_k(eKE)}{d\Omega} = \frac{m_e \omega V}{2\pi\hbar^2} \left(\frac{2m_e eKE}{\hbar^2} \right)^{1/2} \left| \langle k, f | \hat{\epsilon} \cdot \vec{\mu} | i \rangle \right|^2 \quad (1.3)$$

where $|f\rangle = |\phi^{(0)}\rangle|\chi^{(-)}\rangle$ is the neutral product state at the geometry of the anion (in a vertical

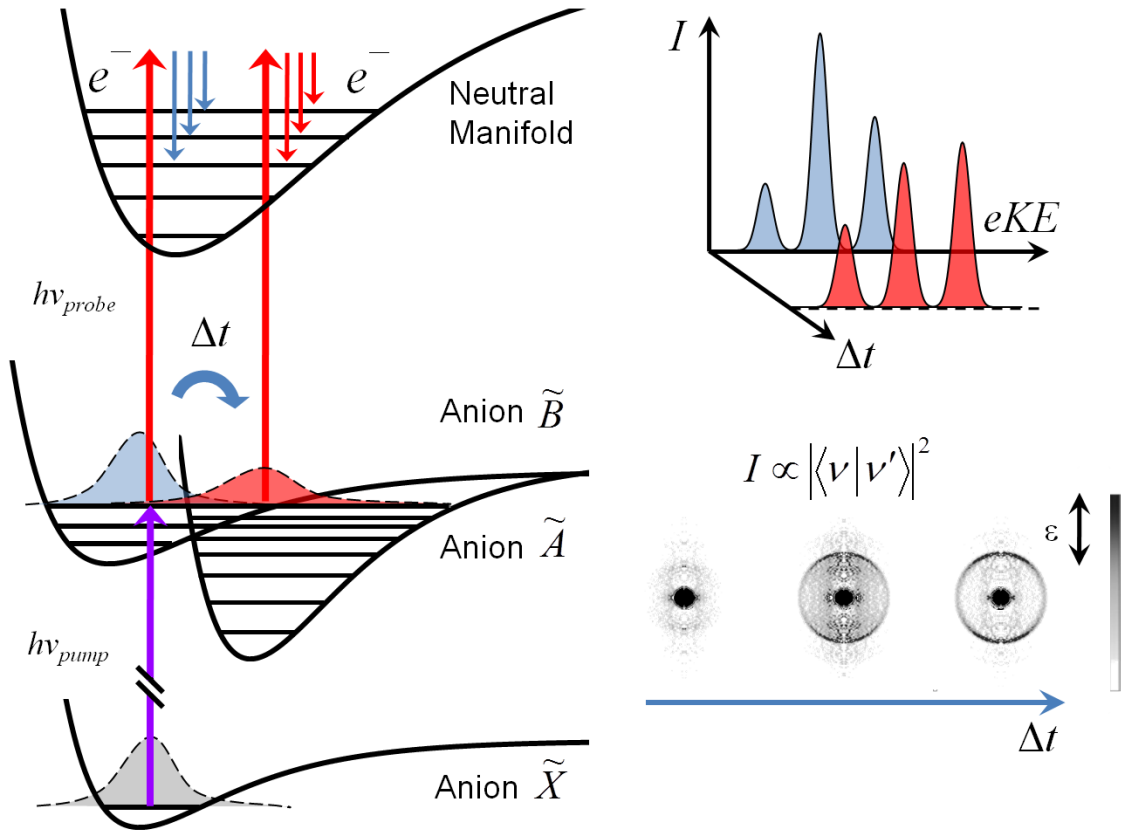


Figure 1.1. Schematic of time-resolved photoelectron spectroscopy and imaging.

process), E is the free electron energy (eKE), V is the volume factor from the free electron wave normalization, (which vanishes in the complete calculation) and m_e and e are the mass and charge of an electron, respectively. Here, $\vec{\mu}$ is the transition dipole operator for a one- or many-electron process and $\hat{\epsilon}$ is the laser polarization. This expression gives valuable insight into the nature of photoemission from molecular systems. Specifically, the transition dipole matrix element requires some degree of spatial overlap between the initial and final wavefunctions (in the real-space representation) in order for the integral to be significant. Thus the cross section is a function of the photon energy used; a localized state will have a higher cross section at higher photon energies, whereas a more delocalized state will experience a drop in the cross section and hence, the measured photoelectron intensity. Note the linear dependence of the cross section with laser frequency; typically the variation in the dipole matrix element is a stronger effect.⁸ This is applied to the study of small anions in Chapter 6.

The shape of the photoelectron spectra is determined by the Franck-Condon overlap of the initial vibrational state of the anion ($|\chi^{(-)}\rangle$) and final vibrational state of the neutral ($|\chi^{(0)}\rangle$):

$$I \propto |\langle \chi^{(0)} | \chi^{(-)} \rangle|^2 \quad (1.4)$$

as implied by Eq. 1.3 when $\hat{\mu}$ is a function only of the electronic coordinates. In this way, photoelectron spectroscopy is sensitive to the energetics of the excess electron, but also the difference in geometries between the anion and neutral solvent structures. Other factors influence the photoelectron spectra, such as the density of final states (both free electrons and neutral cluster states) and the Wigner threshold law.

An alternative but entirely equivalent approach to deriving the photodetachment cross section involves the autocorrelation function of the nuclear wavefunction. For a given energy E the photodetachment cross section can be written as:^{9, 10}

$$\sigma(E) = \frac{4\pi^2 E}{\hbar^2 c} \cdot \frac{1}{2\pi} \int_{-\infty}^{\infty} e^{iEt/\hbar} \langle \chi^{(-)} | \hat{\mu}(0) \hat{\mu}(t) | \chi^{(-)} \rangle dt \quad (1.5)$$

where $\hat{\mu}(t) = e^{i\hat{H}_f t/\hbar} \hat{\mu}(0)$ is the transition dipole moment operator after time-propagation along the upper (neutral) state surface, \hat{H}_f , and $E = E^{(0)} + \hbar\omega$. The action of this time-dependent operator on the lower (anion) state ket is non-trivial, as the anion nuclear state is not an eigenstate of the neutral electronic Hamiltonian. The autocorrelation function is a record of how well the (non-stationary) state overlaps with its initial state at all times, and since it is not an eigenstate, it will mix with every possible vibrational level within that electronic state to some degree. The Fourier transform of this then extracts the frequency (energy) dependence. In this way the photodetachment cross section can be thought of as how the initial state nuclear wavefunction will map onto the final states wavefunctions (given infinite time) as a function of excitation energy.

The photodetachment cross section presented in Eqs. 1.3 & 1.5 can also be approximated from classical mechanics. The following derivation is based on the similar situation for direct photodissociation where the dissociation process occurs without delay. Photodetachment is a vertical process, so the same fundamental framework applies. Assuming a one-dimensional harmonic oscillator (giving rise to a Gaussian classical phase space distribution) with mass m and frequency ω centered at equilibrium bond distance q_0 and a harmonic oscillator for the final (neutral) centered at q_t , the photodetachment cross section can be approximated classically as:

$$\sigma_{PD}(E) \propto \left| \frac{dV}{dq} \right|_{q=q_t}^{-1} e^{-\left(\frac{m\omega}{\hbar}\right) \left[(E-VDE) \left| \frac{dV}{dq} \right|_{q=q_0}^{-1} \right]^2} \quad (1.6)$$

where $V(q)$ is the potential energy, q_t is the classical turning point, E is the applied photon energy and VDE is the vertical detachment energy. This illustrates the "reflection" principle which is illustrated in Figure 1.2. The name originates from the idea that the shape of the absorption/ photodetachment cross section derives from a reflection of the initial state phase space distribution about the final state potential (see figure). From the Eq. 1.6 it can be seen that the width of the photodetachment feature is related to the *steepness* of the final state potential, in this case that of the neutral. This can be generalized to mean the difference in the slopes of the potentials of the two states involved manifests itself in the width of the photodetachment spectrum. The initial phase space distribution will have marked effects on the final spectrum (as

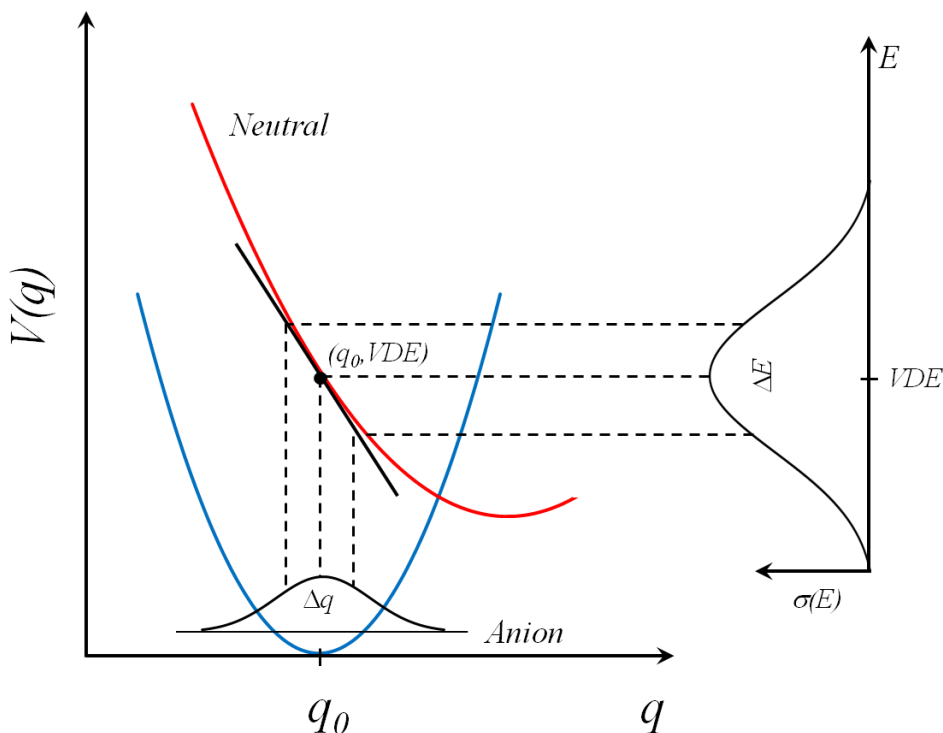


Figure 1.2. The reflection principle as applied to anion photoelectron spectroscopy. The width of the photodetachment cross section is a "reflection" of the original state wavefunction before photodetachment. Adapted from Schinke 1993.¹¹

will spatial variations in the transition dipole moment), and thus the dynamics of the features' shape will give details on the relative shapes of the initial (electronically excited anion) and final (neutral) states. The framework presented here will be used in Chapter 5 to determine the solvation/relaxation pathway for an electron in a methanol cluster.

Pairing a photoelectron spectrometer with a femtosecond laser allows for detailed monitoring of the population dynamics and energetics of a molecular system. In a general time-resolved photoelectron experiment, the initial ground electronic state, typically mostly in the ground vibrational state, is excited with one laser pulse (called the "pump" pulse) to a particular excited state (either electronic or vibrational). The non-stationary excited state then evolves on that potential energy surface until the photodetachment pulse (the "probe" pulse) detaches the electron into the continuum. The delay between the pump and probe pulses can be precisely controlled, allowing the dynamics to be monitored in real time. The pump and probe processes are both vertical, so the nuclear configuration is preserved along each step, with evolution/relaxation occurring after the interaction event. The temporal evolution of the excited state can thus be described by a time-dependent Franck-Condon factor as the wavepacket propagates along the potential energy surface. The initial (anion ground) $|\alpha\rangle = |\phi^{(-)}\rangle|\chi^{(-)}\rangle$ state is excited by the pump electric field $\varepsilon_{pump}(t)$ to a superposition of states on the excited state surface $|n\rangle = |\phi_n^{(-)*}\rangle|\chi_n^{(-)*}\rangle$. After evolution on this surface, the electron is detached by the probe field $\varepsilon_{probe}(t-\Delta t)$ at the prescribed time to the neutral final states $|f\rangle = |\phi^{(0)}\rangle|\chi^{(0)}\rangle|k\rangle$. Here again

the ϕ 's and χ 's represent the electronic and nuclear states, and k is the free electron state. Under second-order perturbation theory and the Franck-Condon approximation, the photoelectron signal S as a function of the wave vector k and the pump-probe delay (Δt) can be computed as:¹²

$$S(k, \Delta t) \propto \left(\frac{1}{i\hbar} \right)^2 \int_{-\infty}^{\infty} dt \int_{-\infty}^{\infty} dt' \left\langle k, \phi^{(0)} \left| \hat{\mu} \cdot \vec{E}_{probe}(t - \Delta t) \right| \phi^{(-)*} \right\rangle \left\langle \phi^{(-)*} \left| \hat{\mu} \cdot \vec{E}_{pump}(t') \right| \phi^{(-)} \right\rangle \times e^{\frac{i}{\hbar}(E_f t' - E_i t)} \left\langle \chi^{(0)} \left| e^{-i\hat{H}_n(t-t')/\hbar} \right| \chi^{(-)} \right\rangle^2 \quad (1.7)$$

where $\hat{H}_n(t)$ is the nuclear Hamiltonian for the intermediate excited state.¹² Analytic pulse shapes for the electric fields can be assumed to simplify calculations. It is readily observable from Eq. 1.7 that the time-dependence of the signal is due to the evolution of the non-stationary state along the excited-state potential energy surface and the Franck-Condon overlap between this state and the neutral surface at any given pump-probe delay. This is shown schematically in Figure 1.1.

1.2.2 Photoelectron imaging

Photoelectron imaging employs velocity-map imaging (VMI)¹³ to accelerate the photoelectrons produced by the laser pulse(s) onto a two-dimensional detector. Spatially inhomogeneous electric fields of the desired strength are applied to cylindrical plates in a repeller/extractor/ground configuration. Due to the symmetry of the apparatus and the fields, all kinetic energy information is carried by the transverse components of the velocity, unlike in TOF or magnetic bottle PES where it is carried longitudinally. The distance traversed by the electrons accelerated from their initial ejection velocities is then recorded by where the electrons strike the detector plane. The slowest electrons strike the detector toward the center, while higher kinetic energy electrons reach a larger radius, thus the image itself is a direct mapping of the electron's linear momentum. Images are amplified using microchannel plates (MCPs) and collected by a charge-coupled device (CCD) camera which averages over detection events to produce an integrated photoelectron image. The fields are aligned in such a way as to focus each ejected electron with the same velocity vector onto the same position on the detector, in essence connecting the laboratory frame to the electron center-of-mass frame. This enables the free electron wave's momentum to be mapped directly. The choice of absolute and relative applied voltages is determined by the desired electron kinetic energy range and the focal length of the detector setup, respectively. The VMI field accelerates the electrons and focuses them onto the detector with near unity collection efficiency. This is one of the primary advantages of charged-particle imaging especially compared to TOF PES. Additionally, the cylindrically symmetric fields only impart momentum to the longitudinal velocity components, not the information-carrying transverse components; this increased longitudinal velocity enhances the detection efficiency for low energy electrons, since the detector plates are normal to the symmetry axis of the VMI field. This improved transmission of slow electrons makes photoelectron imaging desirable compared to magnetic bottle PES. Monitoring of slow electron channels has allowed for significant insight into charge-transfer processes in clusters which directly affect the lifetime

of solvated electrons prepared by ejection from solvated ions. This will be discussed further in Chapter 5.

Electron emission occurs (anisotropically) over a 4π solid angle; this three-dimensional photoelectron distribution is then projected onto a two-dimensional surface resulting in the seeming loss of information. The “lost” information can be recovered because of the apparatus' cylindrical symmetry. The original three-dimensional distribution can be accomplished in a variety of ways. Direct numerical inverse-Abel transformation can be applied, but this is highly sensitive to noise due to the numerical derivative involved in the transformation.¹⁴ Some filtering of the noise can be accomplished by Fourier transformation and using the Fourier-Hankel-Abel cycle.¹⁵ Alternatively, the 2D image can be projected onto a basis set of pre-transformed analytic functions which are then readily “inverted” using matrix methods; this is the “Basis Set EXpansion” or BASEX method.¹⁶ This method is less sensitive to signal noise but still results in a “center-line” image artifact through the origin, parallel to the laser polarization. Versions of this method have been developed using Gaussian or spherical harmonics (pBASEX) as basis sets for improved angular distribution reconstruction.¹⁷ In practice, BASEX is seen to give narrower energy distributions while pBASEX better reconstructs the angular distributions.¹⁸ Near real-time image processing can be accomplished on modern desktop computers using the iterative polar “onion peeling” reconstruction method which deconvolves the image from the outer boundary radially toward the center.^{19,20} However, this leads to problems for the reconstruction of low kinetic energy features, as errors are propagated inward.

Once the three-dimensional distribution is reconstructed, a 2D slice parallel to the detector intersecting the origin of the Newton sphere is taken. This is the photoelectron angular distribution (PAD) containing the angular momentum information of the outgoing electron wave. Due to conservation of momentum this must be connected to the total angular momentum of the original cluster anion, depending on the number of absorbed photons or transferred angular momentum (alignment). Assuming a randomly oriented cluster distribution, the PAD at a given eKE can be fit to:

$$\frac{d\sigma(\theta, eKE)}{d\Omega} = \frac{\sigma_{total}(eKE)}{4\pi} \sum_{i=1}^m \beta_{2i}(eKE) P_{2i}(\cos \theta) \quad (1.8)$$

where, θ is the angle between the emitted electron and the laser polarization, m is the number of photons absorbed in the process, σ_{total} is the total photodetachment cross section, β_{2i} are the anisotropy parameters containing the angular momentum information, and P_{2i} are the even Legendre polynomials.^{21,22} For a single-photon process, β_2 ranges continuously between +2 and -1, representing an outgoing p -wave and an $s+d$ wave, respectively. Isotropic emission results in $\beta_2 = 0$. Higher photon-order photodetachment results in the transfer of additional angular momentum which allows the β parameters to take on other values beyond this range. While angular momentum must be conserved, in practice, however, due to electron-electron scattering in larger clusters or the dynamics of delayed emission this information can often be obscured or lost. Angular integration of the PAD results in the electron speed distribution, which can easily be transformed into the kinetic energy spectrum.

Each electron's momentum vector is directly mapped to the same position on the two-dimensional detector: $\vec{p}_e \propto \vec{r}$ where \vec{p}_e is the electron's momentum vector and \vec{r} is the

(amplified) particle's position on the detector (pixel). Therefore, $E \propto r^2$ and the energy resolution is $\Delta E \propto r\Delta r \sim E^{1/2}$, so higher kinetic energy electrons show broader linewidths for direct photodetachment. Energy resolution can be enhanced by collecting collinearly with the molecular beam axis, reducing the effect of Doppler broadening, which would only affect the velocity components of the photoelectrons parallel to the molecular beam propagation. However, the relative energy resolution for our time-resolved photoelectron imaging spectrometer is $\Delta E/E \sim 5\%$, which is dominated almost entirely by the energy width of the ultrafast laser system, so the collinear collection arrangement is not strictly necessary. In addition, the features and processes studied on this apparatus typically have broad spectral profiles naturally due to the size of the cluster systems we look at. Solvent cluster anions, for example, typically have binding energies of < 4 eV with spectral widths of around 1 eV, making them well suited for study by ultrashort laser pulses.

1.3 Summary of systems studied

1.3.1 Semiconducting mercury cluster anions

The size evolution of mercury clusters $(\text{Hg})_n$ poses an interesting problem in chemical physics. Atomic mercury has a closed $6s^25d^{10}$ shell with a large energy gap to the first excited state (4.6-5.5 eV).²³ Upon aggregation, the discrete states become more densely packed, shifting slightly in energy (due to Pauli Exclusion Principle) becoming quasi-continuous bands capable of supporting a bound excess charge and eventually conducting electrons. The occupied (valence) band and the open (conduction) band both broaden as the size of the cluster increases, leading to a reduction in the HOMO-LUMO energy difference, something akin to a "band gap", BG, for systems with densely packed energy levels. A crystalline system with a well-defined band gap in the electron-volt (eV) range is classified as a semiconductor, as it can conduct an excess electron promoted from the valence band when sufficient energy is applied ($h\nu > \text{BG}$).

Small $(\text{Hg})_n$ clusters are van der Waals-bound systems until about $n \sim 13$ -20 at which point the clusters become covalently bound, sharing their electrons through their (nearly) overlapping energy levels. Of course, bulk mercury is metallic, and so these clusters must undergo a metal-to-insulator transition at some cluster size or range of sizes. A critical feature of metals is the lack of a band gap ($\text{BG} = 0$ at absolute zero); *i.e.* there is no energetic barrier to charge conduction. Thus the size at which this gap approaches zero will signify the transition. If the neutral clusters are semiconductors, then their anions would be analogous to n -doped semiconducting systems, where the excess electron can be utilized to quantify the band gap. Photoelectron spectroscopy of anionic mercury clusters, $(\text{Hg})_n^-$, wherein the excess electron resides at the bottom of the $6p$ conduction band, can be used to track the size evolution of these systems, as they are not only size-selectable, but direct detachment of this electron as well as electrons from the valence band give a direct measurement of the band gap as a function of cluster size. Using this technique, Busani, *et al.* observed band gap closure (*i.e.* the onset of metallic mercury) at $n \sim 400 \pm 30$.²⁴

Subsequent studies by Cheshnovsky's group showed that excitation of electrons from the valence band into the conduction band led to the thermalization of the nascent electron-hole pair prior to Auger emission of the excess electron.^{25, 26} However, the Auger feature did not extend over the entire energy range permissible by the energy levels and the photon energy, implying a

fast dynamical process during the relaxation over this size range. The van der Waals-to-covalent transition represents a fundamental change in the aggregated electronic structure of the cluster. Thus, if the excess electron residing at the bottom of the conduction band is excited to a higher state *within* that band, the dynamics of the electron as it relaxes through the available electronic states will depend on the cluster size. In addition, since there is only one charge carrier following *intraband* excitation, the dynamics will arise only from the density of electronic states and through the electron's interaction with the phonon bath. On the other hand, if an electron is excited from the valence band into the conduction band, there will now be three charge carriers (the original excess electron plus the electron-hole pair, also called a "negative trion") interacting as the electron-hole pair relaxes before the Auger process. These *interband* experiments allow for the electron-electron/electron-hole dynamics to be monitored directly, while the intraband experiments help disentangle the dynamics arising from electron-phonon scattering to develop a more complete picture of relaxation process in excited mercury cluster anions.

Chapter 3 describes a set of complementary experiments on electron relaxation in mercury cluster anions ($7 \leq n \leq 20$) with time-resolved photoelectron imaging. Intraband excitation in the infrared followed by delayed ultraviolet detachment shows the excited electron relaxes through the *p*-band on a ~ 10 s of ps timescale. Lowering the excitation energy to 1.0 eV allows access to smaller clusters but also shows a change in the relaxation timescales for the same sizes studied at 1.5 eV, implying a non-uniform density of electronic states within the conduction band. A second set of experiments exciting at 4.7 eV creates the electron-hole pair and brings the second electron into the conduction band. The Auger feature seen in Busani's experiments is seen to appear here on a ~ 500 fs timescale, an order of magnitude faster than the relaxation seen in the intraband experiments. This indicates a completely different mechanism for charge carrier thermalization, such as electron-electron scattering. Computational results²⁷ suggest the creation of a hole in the valence band leads to a size contraction of the cluster. This could lead to vibrational relaxation of the excited cluster, removing energy from the excited electron-hole pair, effectively thermalizing it.

1.3.2 Acetonitrile cluster anions

Excess electrons in polar media are of fundamental importance to a wide range of processes, such as charge transfer and radiation damage to biologically relevant molecules. In these solvents, the electron is thought to interact physically with its environment, experiencing the average potential arising from the solvent structure and interacting only minimally with other electrons on the solvent molecules. In this sense, it is a solvated species, thought to exist in a cavity within the solvent. Solvent cluster anions pose as gas phase precursors or analogs of these solvated electrons and have been studied extensively by our group in the past.

While water is the most frequently studied solvent, other liquids such as methanol, acetonitrile, and tetrahydrofuran can also support a solvated electron. Acetonitrile (CH_3CN) however, poses a more complicated problem, as it can not only solvate an electron within a cavity (isomer I) much as water does, but it can also *molecularly* bind the excess electron in a metastable dimer anion species (isomer II). Both species have been observed simultaneously in liquid samples, however hole-burning experiments have demonstrated that the two species are independent entities with their own optical properties.²⁸ Acetonitrile cluster anions have also been shown to support two states, though not simultaneously, as only singly-charged clusters

were observed. In addition, neither species was observed until $n \sim 10$, indicating that they are both metastable without a sufficient degree of solvation. The two states have markedly different binding energies, around 1 eV and 2.2 eV for clusters between 10 and 100 acetonitrile molecules. On the basis of photodetachment cross section measurements, the lower binding energy species was assigned to be the cavity state, as its relative cross section decreased with increasing binding energy, while the higher binding energy feature was assigned to the dimer anion for the converse reason. However, no definitive link between the gas phase cluster structures and the liquid species had been demonstrated.

The optical absorption spectrum of liquid acetonitrile following charge injection shows two strong, distinct features. Isomer I, the cavity-bound state, is thought to absorb around 1400 nm on the basis of continuum dielectric models, while isomer II, the dimer anion, is thought to absorb around 550 nm. Using the absorption spectrum as a map, the identities of the cluster species can be correlated to their bulk counterparts based on their optical properties.

The work presented in Chapter 4 bridges the gap between the gas phase isomers and the condensed phase species for the first time. Absorption near the visible 550 nm band of isomer II excites the dimer anion, leading to the emission of a low energy electron via excited-state autodetachment. Analysis of the photoelectron angular distribution shows that isomer II exhibits some degree of s - p mixing, as would be expected from the dimer anion where the excess electron is distributed between the two acetonitriles bridged by a σ -type bond (bond order 0.6).²⁹ The autodetachment lifetimes of the excited dimer anion as a function of cluster size are extracted from the time-resolved photoelectron spectra. This process has a ~ 200 - 270 fs lifetime that is independent of cluster size. Recent theoretical work³⁰ has quantitatively reproduced both the excitation energy of isomer II as well as the autodetachment lifetime for the excited dimer anion.

1.3.3 Iodide-doped methanol clusters

The solvated electron in methanol has presented itself as a fundamental problem in chemical physics as a natural variation of the hydrated electron system. The seemingly simple change from HOH to CH₃OH completely alters the relaxation dynamics after charge transfer from a solvated ion.^{31, 32} Typically in studies of the liquid, the solvated electron is created via excitation of a charge-transfer-to-solvent (CTTS) transition leading to ejection of the electron into the solvent some solvent shells away from the solute. Relaxation/recombination is monitored via either photoproduct, and, owing to the lack of internal degrees of freedom in both the neutral solute and the excess electron (except for electronic, of course), the ensuing dynamics are purely a consequence of solvent motions. Thus a great deal of information about the solvation process can be achieved in these systems. Still, interpretation of these dynamics in the bulk can be difficult due to the large number of solvent degrees of freedom, so it is often useful to look at the cluster analogs of these systems to disentangle the dynamics, molecule by molecule. This however is not without its own complications, due to the influence of structural effects and different possible binding motifs.

In iodide-doped solvent clusters, the CTTS transition is proposed to first bring the electron to a spatially diffuse excited state near the iodide and surrounding solvent molecules. After a brief period (a few hundred femtoseconds), this state localizes onto the solvent moiety. From here, the system behaves like the ground electronic state of a bare solvent cluster anion; the neutral iodine is considered a weak energetic perturbation to the system. As the cluster geometry

may be initially altered due to the presence of the iodide anion, the solvent cluster anion may need to structurally relax to fully solvate the electron and establish its lowest energy structure. These dynamics vary strongly from solvent to solvent^{18, 33, 34} and continue to yield new insight into the electron solvation process.

Much new information has surfaced since the I^- /methanol system was first studied by our group in 2000.³³ Our understanding of bare methanol cluster anions, the purported product states of the electron transfer, was enhanced by photoelectron imaging studies of those anions by Aster Kammrath *et al.* in 2006.³⁵ Methanol clusters can bind an excess electron in two different ways: either weakly with the electron residing on the surface of the cluster (isomer II), or more tightly with the electron possibly penetrating more deeply into the center (isomer I). However, $(CH_3OH)_n^-$ clusters do not appear until $n \sim 71$ for isomer II and $n \sim 130$ for isomer I, suggesting that smaller clusters are metastable. Quantum chemical calculations³⁶ on small methanol cluster anions demonstrated that the anions generally had similar structures to their neutral counterparts, with the hydroxyl groups directed in toward the cluster center to maximize the hydrogen bond network. This leaves the methyl groups pointing outward. The same calculations also showed that the excess electron has favorable interactions with both the methyl and hydroxyl groups, explaining the potential for surface and internally bound anionic structures. Mixed-quantum/classical molecular dynamics simulations on these clusters have also recovered the two states based on these interactions.^{37, 38}

The structures of halide-doped methanol clusters have also been elucidated in recent years. Through infrared dissociation studies^{39, 40} and accompanying *ab initio* calculations, the iodide has been shown to strongly disrupt the hydrogen bond structure around it, typically near the cluster surface. Thus, one or several hydroxyl group(s) point outward while the remaining groups form the solvent network. This initial state evolves into the solvent cluster anion's adiabatic structure following charge transfer to the solvent cluster. The dynamics of this relaxation can be following using time-resolved photoelectron spectroscopy.

Chapter 5 revisits the experiments of Davis, *et al.*³³ on $I^-(CH_3OH)_n$ with time-resolved photoelectron imaging over a larger range of cluster sizes ($4 \leq n \leq 11$). Due to the higher collection efficiency of the imaging technique, a new feature is observed near zero eKE and is assigned to arise from vibrational autodetachment, as speculated in the original study. This confirms the final decay pathway and metastability of the excited cluster. The timescale for this autodetachment feature is determined to be between ~ 1 and 100 ps for the size range studied here (and at this excitation energy), in excellent agreement with (most) of the original lifetimes, despite being fit with a more advanced function designed to capture the entire population decay process. Indeed, the decay dynamics are now seen to be bi-exponential for larger clusters ($n > 5$).

The vertical detachment energies and the spectral widths show nearly the same temporal evolution, both decreasing quickly in the first few hundred fs, and then increasing dramatically over the next 1-2 ps before falling toward a final value over the remaining experimental window (5-30 ps over this size range). The timescales are roughly consistent with the relaxation of the "hot" solvated electron in bulk methanol, suggesting a similar relaxation pathway. These dynamics are interpreted in light of the newly determined structures of the iodide-doped clusters as well as the anionic and neutral solvent clusters. Initially, the iodide resides on the surface of the cluster, disrupting at least one hydrogen bond to create the $I^{\cdots}HO$ link in the equilibrium geometry. Vertical excitation brings the electron off the iodide and onto the cluster moiety prior to solvation. Both neutral and anionic methanol clusters have equilibrium structures that

maximize the number of hydrogen bonds, so a dangling surface OH group will be far from the energetic minimum of the system. Thus the cluster relaxes by rotating the methanol(s) until the hydrogen bond network is reestablished. The difference in structures manifests itself, via the reflection principle, as the changing spectral width as the system relaxes. Meanwhile, the excess energy from the excitation process is being distributed throughout the system leading to the vibrational autodetachment, limiting the experimental window on these dynamics. The variation of the magnitude of VDE changes with cluster size, indicating the dynamics are tied to solvation of the charge as opposed to motion of the iodine. Simplified one-dimensional potential energy surfaces based on this rotation are presented that are consistent with the data.

The mechanism for electron solvation in this work was proposed independently a few months after publication for large methanol cluster following attachment of excess electrons using mixed quantum/classical molecular dynamics simulations.⁴¹ While not exactly the same system as that studied in Chapter 5, the similarity in the relaxation mechanism presented in both studies suggests that the methanol rotation pathway is key in electron solvation for these clusters.

1.3.4 Tetrahydrofuran cluster anions

Tetrahydrofuran (THF, C₄H₈O) is perhaps the most intensely studied aprotic solvent regarding the solvated electron. The solvated electron in THF can be created by multiphoton ionization of the solvent, but also by exciting the CTTS band of iodide or the alkali metal anions (M^-). When an alkali metal, M , is introduced into a solution of THF, a weak equilibrium between the neutral metal and its ions develops: $2M^0 \leftrightarrow M^+ + M^-$. In the late 1970s, Dye, *et al.*⁴² showed that it was possible to synthesize alkali metal anions in THF by complexing the cation with a crown ether or other chelating agent and driving the equilibrium toward the products (Le Châtelier's principle). These alkali metal anions are similar to the halides in several ways, most notably in that they exhibit intense CTTS bands, but in the visible spectrum. This makes them useful tools for creating solvated electrons in THF. In addition, iodide salts are also soluble in THF, allowing for direct comparison of the dynamics following charge transfer.^{43, 44}

The dynamics of the solvated electron in THF are explained mostly in terms of the solvent structure of the neat liquid, which is rather different from that of water, methanol and most solvents. THF is a five-membered, semi-planar, "weakly polar" molecule, in that while it has a dipole moment comparable to that of water, its static dielectric constant is an order of magnitude lower. Its polarity, combined with the shape of the molecule, leads to inefficient, disorganized packing of molecules. Recent molecular dynamics simulations⁴⁵ and neutron scattering experiments⁴⁶ have shown that unlike most solvents, such as water and methanol, neat THF exists in the liquid state with a large number of cavities or voids ~ 2.5 Å across. Moreover, these pockets are partially positively polarized which can act as traps for the injected electrons with little nuclear rearrangement. However, the depth of these traps (the potential of mean force) and hence the binding energy of the electron in the liquid is unknown.

Anionic clusters of THF can shed light on this by tracking the electron binding energy as a function of cluster size. Chapter 6 details the one-photon photoelectron imaging studies on $(\text{THF})_n^-$ ($1 \leq n \leq 100$). The cluster progression begins at the monomer mass, possibly indicating the formation of THF^- , though the THF anion is not thought to be stable (due to THF's high HOMO-LUMO gap) without a major geometric rearrangement. No evidence for such a distortion is seen in the photoelectron spectrum, however. Based on the binding energy and the

photodetachment cross section, the excess electron is proposed to be fairly localized on the molecule itself, and thus not a dipole-bound state. Evidence from previous solvent cluster anion studies of benzene and toluene as well as electron scattering experiments on THF suggest that this is a metastable species resulting from fragmentation of the larger THF cluster anions.

Starting at $n = 6$ ($n = 11$ in fully deuterated THF-d8), the photoelectron spectra change dramatically: the width of the detachment feature approaches 1 eV and the anisotropy parameter drops precipitously, indicating a major change in the binding motif. Based on the asymmetric lineshape and the large width of the feature, this state is assigned to be arising from the solvated electron state. The smallest solvated electron clusters in THF already bind an electron by ~ 2 eV, much higher than the smallest clusters of water and methanol (~ 500 meV). Extrapolation of the binding energy with inverse cluster radius yields an estimate of the bulk photoelectron binding energy of 3.10 eV. This value was later confirmed using photoelectron spectroscopy of a liquid THF jet. Based on the large binding energy of the smallest solvated electron cluster and the small degree of stabilization experienced as it evolves to the bulk, as well as the lack of observation of other binding motifs, we conclude that the excess electron is likely residing in a preformed cavity of positive polarity. This structure would provide for the enhanced binding energy relative to similarly sized water cluster anions.

1.3.5 Iodide-doped tetrahydrofuran clusters

Understanding the ultrafast processes following CTTS excitation from iodide in THF clusters (and hence the bulk) not only requires knowledge of the final state (the solvated electron) but also the initial solvated anion state. This was shown to be key to the interpretation of the $\text{I}^-(\text{CH}_3\text{OH})_n$ system as the structural difference between the different states dictated the relaxation pathway. One-photon photoelectron studies of $\text{I}^-(\text{THF})_n$ clusters can offer some insight to the placement of the iodide either within the cluster or on its surface. Ultraviolet detachment from solvated iodide in 1-30 THF molecules showed a continual stabilization of the anion, with the largest contributions coming from the first 9 solvent molecules. After this size, the stabilization is only in the ~ 10 meV/molecule range and slowly decreasing with cluster size. Close examination also reveals that after $n = 19$, the binding energy vs. the inverse cluster size of the iodide-doped clusters has the same size evolution as the large solvated electron clusters in THF, $(\text{THF})_n^-$, indicating that after this cluster size the ion is stabilized only by the long-range interactions with the solvent molecules and that the cluster geometry is minimally responding to the excess charge. This could be due to the void structure of THF, as the iodide ion is small enough to reside within the largest cavities.

There is also evidence for a bound (or quasi-bound) excited state near 300 nm for the smallest clusters sizes ($n = 4-8$) due to the presence of a weak vibrational autodetachment feature. The autodetachment feature is no longer visible at $n = 8$ even after tuning the excitation energy to remain on resonance with the band as best as possible. This is unusual, as the analogous process in water does not happen until around $n \sim 20$. If the neutral THF clusters also exhibit the same cavity structure as the neat liquid, it is possible that the electron is being ejected from iodide into one of these pockets and readily stabilized, binding the electron deeply enough that the excess energy does not lead to autodetachment.

1.3.6 Water cluster anions

Water cluster anions can be thought of as gas-phase precursors to the hydrated electron,⁴⁷ which has been extensively studied in the bulk.⁴⁸⁻⁵³ Photoelectron spectroscopy of the cluster anions⁵⁴⁻⁵⁸ has shown that the binding energies scale linearly (after a large enough size) with the inverse of the cluster radius, $1/R = n^{-1/3}$, suggesting that the corresponding bulk electron binding energy can be established by extrapolating the cluster results to infinite size. Estimations for this value based on various cluster results place the bulk vertical detachment energy at around 3.3-4.0 eV. Recent development on the photoelectron spectroscopy of liquid jets has measured this value as $\sim 3.3-3.6$ eV,⁵⁹⁻⁶² in good agreement with the cluster extrapolations.

The excited state of these clusters also draws an analogy to the bulk hydrated electron. Time-resolved photoelectron imaging studies in our group have shown⁶³⁻⁶⁵ that exciting the bound electronic state of the water cluster anions results in internal conversion back to the ground state on a 70-300 fs timescale, generally decreasing with cluster size. Extrapolating this timescale with $1/n$ to the infinite size limit yields⁶⁶ an estimation for the bulk internal conversion time of 50-60 fs, in accord with the "non-adiabatic" model proposed from transient absorption experiments.⁴⁹

While it appears the cluster extrapolations provide a legitimate alternate route for estimating some bulk properties, this is not universally accepted, due to the uncertainty in the temperature and thermodynamic phase of the clusters. For example, depending on the source conditions, water clusters can bind the excess electron in multiple different ways.⁵⁵ Conditions typically associated with warmer expansions in argon (lower backing pressures) yield clusters with binding energies previously measured (isomer I), whereas colder conditions (higher backing pressures) give rise to clusters which only weakly bind the electron (isomers II and III). The strongly bound species is thought to be the more internalized state, while the electron in the weakly bound isomer is thought to be surface-bound. This implies that cluster temperature could have a large impact on the binding energies and dynamics, and, thus the validity of the cluster extrapolations.

To investigate the effects of temperature on we have generated water cluster anions under conditions expected to yield vibrationally warm clusters using neon carrier gas instead of argon. Neon has been shown to be less efficient at deactivating vibrational excitations in organic molecules⁶⁷⁻⁶⁹ and metal clusters,⁷⁰ and so it is expected to produce water clusters with warmer internal energy distributions. One-photon photoelectron imaging of cluster anions produced in neon expansions ($11 \leq n \leq 75$) shows only isomer I clusters are formed, even at pressures as high as 250 psig Ne, whereas at only 70 psig Ar only the weakly bound isomers are observed. While substitution of the carrier gas affects which isomer is formed, the vertical detachment energies are not seen to be significantly different than those previously reported for isomer I. Time-resolved photoelectron imaging for clusters ($25 \leq n \leq 40$) born in neon shows that the internal conversion lifetimes are smaller compared to previously measured values, however they appear to converge to the same bulk limit. Moreover, the internal conversion process is still < 100 fs, supporting the non-adiabatic relaxation model. We conclude that the binding energies are not sensitive to the cluster temperature, but the relaxation times are. That the energies and timescales extrapolate to about the same values for these different thermal conditions supports the validity of the cluster extrapolations.

1.4 References

- 1 L. Lehr *et al.*, *Science* **284**, 635 (1999).
- 2 A. E. Bragg *et al.*, *J. Chem. Phys.* **122**, 054314 (2005).
- 3 J. R. R. Verlet *et al.*, *J. Chem. Phys.* **121** (20), 10015 (2004).
- 4 G. B. Griffin *et al.*, *J. Chem. Phys.* **130** (23), 231103 (2009).
- 5 R. Wester *et al.*, *J. Chem. Phys.* **119** (19), 10032 (2003).
- 6 B. von Issendorf, and O. Cheshnovsky, *Annu. Rev. Phys. Chem.* **56**, 549 (2005).
- 7 G. C. Schatz, and M. A. Ratner, *Quantum Mechanics in Chemistry* (Dover Publications, 2002).
- 8 M. Mitsui *et al.*, *Phys. Rev. Lett.* **91** (15), 153002 (2003).
- 9 E. J. Heller, *J. Chem. Phys.* **68** (5), 2066 (1978).
- 10 D. M. Neumark, *Acc. Chem. Res.* **26** (2), 33 (1993).
- 11 R. Schinke, *Photodissociation Dynamics* (Cambridge University Press, New York, NY, 1993), Cambridge Monographs on Atomic, Molecular, and Chemical Physics.
- 12 V. S. Batista *et al.*, *J. Chem. Phys.* **110** (8), 3736 (1999).
- 13 A. T. J. B. Eppink, and D. H. Parker, *Rev. Sci. Instrum.* **68** (9), 3477 (1997).
- 14 B. J. Whitaker, *Imaging in molecular dynamics: technology and applications : a user's guide* (Cambridge University Press, 2003).
- 15 A. Braun, and M. Drabbels, *Rev. Sci. Instrum.* **76** (11), 113103 (2005).
- 16 V. Dribinski *et al.*, *Rev. Sci. Instrum.* **73** (7), 2634 (2002).
- 17 G. A. Garcia, L. Nahon, and I. Powis, *Rev. Sci. Instrum.* **75** (11), 4989 (2004).
- 18 A. Kammrath *et al.*, *J. Phys. Chem. A* **109**, 11475 (2005).
- 19 K. Zhao *et al.*, *Rev. Sci. Instrum.* **73** (8), 3044 (2002).
- 20 G. M. Roberts *et al.*, *Rev. Sci. Instrum.* **80** (5), 053104 (2009).
- 21 J. Cooper, and R. N. Zare, *J. Chem. Phys.* **48**, 942 (1968).
- 22 K. L. Reid, *Annu. Rev. Phys. Chem.* **54**, 397 (2003).
- 23 J. E. Sansonetti, and W. C. Martin, *Journal of Physical and Chemical Reference Data* **34** (4), 1559 (2005).
- 24 R. Busani, M. Folkers, and O. Cheshnovsky, *Phys. Rev. Lett.* **81** (8), 3836 (1998).
- 25 R. Busani, and O. Cheshnovsky, *J. Phys. Chem. C* **111** (48), 17725 (2007).
- 26 R. Busani *et al.*, *Phys. Rev. Lett.* **90** (8), 083401 (2003).
- 27 H. Kitamura, *Eur. Phys. J. D* **43**, 33 (2007).
- 28 C. Xia, J. Peon, and B. Kohler, *J. Chem. Phys.* **117** (19), 8855 (2002).
- 29 T. Takayanagi, *J. Chem. Phys.* **122**, 244307 (2005).
- 30 J. Azar, W. Kurlancheek, and M. Head-Gordon, *Phys. Chem. Chem. Phys.* (2011).
- 31 A. Thaller, R. Laenen, and A. Laubereau, *J. Chem. Phys.* **124** (2006).
- 32 X. Chen, and S. E. Bradforth, *Annu. Rev. Phys. Chem.* **59**, 203 (2007).
- 33 A. V. Davis *et al.*, *J. Electron Spec.* **108**, 203 (2000).
- 34 O. T. Ehrler *et al.*, *J. Phys. Chem. B* **113**, 4031 (2009).
- 35 A. Kammrath *et al.*, *J. Chem. Phys.* **125**, 171102 (2006).
- 36 L. Turi, *J. Chem. Phys.* **110** (21), 10364 (1999).
- 37 L. Mones, P. J. Rossky, and L. Turi, *J. Chem. Phys.* **133** (14), 144510 (2010).
- 38 L. Mones, and L. Turi, *J. Chem. Phys.* **132** (15), 154507 (2010).
- 39 W. H. Robertson *et al.*, *J. Chem. Phys.* **116** (12), 4853 (2002).

40 J. P. Beck, and J. M. Lisy, *J. Phys. Chem. A* **114**, 10011 (2010).
41 L. Mones, P. J. Rossky, and L. Turi, **135** (8), 084501 (2011).
42 J. L. Dye, *The Journal of Physical Chemistry* **84** (10), 1084 (1980).
43 A. E. Bragg, and B. J. Schwartz, *J. Phys. Chem. B* **112**, 483 (2008).
44 A. E. Bragg, and B. J. Schwartz, *J. Phys. Chem. A* **112**, 3530 (2008).
45 M. J. Bedard-Hearn, R. E. Larsen, and B. J. Schwartz, *J. Chem. Phys.* **122**, 134506 (2005).
46 D. T. Bowron, J. L. Finney, and A. K. Soper, *J. Am. Chem. Soc.* **128**, 5119 (2006).
47 D. M. Neumark, *Mol. Phys.* **106** (16-18), 2183 (2008).
48 E. J. Hart, and M. Anbar, *The Hydrated Electron* (Wiley-Interscience, New York, 1970).
49 J. C. Alfano *et al.*, *J. Chem. Phys.* **98** (7), 5996 (1993).
50 B. J. Schwartz, and P. J. Rossky, *Phys. Rev. Lett.* **72** (20), 3282 (1994).
51 C. Silva *et al.*, *Phys. Rev. Lett.* **80**, 1086 (1998).
52 R. E. Larsen, W. J. Glover, and B. J. Schwartz, *Science* **329** (5987), 65 (2010).
53 L. D. Jacobson, and J. M. Herbert, *J. Chem. Phys.* **133** (15), 154506 (2010).
54 J. V. Coe *et al.*, *J. Chem. Phys.* **92** (6), 3980 (1990).
55 J. R. R. Verlet *et al.*, *Science* **307**, 93 (2005).
56 J. V. Coe *et al.*, *J. Chem. Phys.* **125** (1), 014315 (2006).
57 A. Kammrath *et al.*, *J. Chem. Phys.* **125**, 076101 (2006).
58 L. Ma *et al.*, *J. Chem. Phys.* **131** (14), 144303 (2009).
59 A. Lubcke *et al.*, *Phys. Chem. Chem. Phys.* **12** (43), 14629 (2010).
60 Y. Tang *et al.*, *Phys. Chem. Chem. Phys.* **12** (15), 3653 (2010).
61 K. R. Siefermann *et al.*, *Nat Chem* **2** (4), 274 (2010).
62 A. T. Shreve, T. A. Yen, and D. M. Neumark, *Chem. Phys. Lett.* **493** (4-6), 216 (2010).
63 A. E. Bragg *et al.*, *Science* **306**, 669 (2004).
64 A. E. Bragg *et al.*, *J. Am. Chem. Soc.* **127**, 15283 (2005).
65 G. B. Griffin *et al.*, *J. Chem. Phys.* **131**, 194302 (2009).
66 S. F. Fischer, and W. Dietz, *Z. Phys. Chem* **221**, 585 (2007).
67 H. Hippler, J. Troe, and H. J. Wendelken, *J. Chem. Phys.* **78** (11), 6709 (1983).
68 H. Hippler, J. Troe, and H. J. Wendelken, *J. Chem. Phys.* **78** (11), 6718 (1983).
69 H. Hippler, L. Lindemann, and J. Troe, *J. Chem. Phys.* **83** (8), 3906 (1985).
70 J. Westergren, S. Nordholm, and A. Rosén, *Eur. Phys. J. D* **22** (1), 81 (2003).

Chapter 2. Experimental Apparatus

This section describes in brief detail the anion source utilized in the experiments presented in this dissertation. The original photoelectron spectrometer apparatus itself was designed and constructed by Benjamin Jefferys Greenblatt and Martin Zanni; highly detailed descriptions can be found in their dissertations.^{1,2} In 2003 the apparatus was adapted to employ velocity map imaging (VMI) by Roland Wester, Alison Davis and Arthur Bragg whose theses describe those changes.^{3,4} There have been no significant alterations to the apparatus since the conversion to imaging detection except for upgrades in various components, such as the pulsed valve and imaging camera, and, notably, the femtosecond laser. What follows is a brief overview of the experimental setup, shown schematically in Figure 2.1.

2.1 Atomic, Molecular and Cluster Ion Source

Ions are formed by flowing a dilute gaseous mixture (an inert carrier gas seeded with either a gas sample or vapor pressure from a solid or liquid reservoir) through a pulsed valve. All the studies presented here utilized the Even-Lavie (EL) pulsed solenoid valve⁵ as it is well-suited for applications involving femtosecond lasers due to its high repetition rate. The original EL valve had a maximum operating repetition rate of 100 Hz, while a newer model acquired in 2011 has a purported maximum of 1 kHz. In practice, however, repetition rates of > 500 Hz were not observed to be very stable, exhibiting a temporal jitter of ~ 10 ns shot-to-shot. In addition to the higher repetition rate, EL valves are also well suited to high backing pressure and have an internal cartridge reservoir for liquid or solid samples, which is necessary for the mercury cluster anion experiments. Additional reservoirs for liquids are mounted along the gas supply lines which can be heated independently to control vapor pressures and hence the mixture ratio (to a point). The entire unit can be heated to about 250 °C to increase the vapor pressure of the sample and enrich the gas mix.

Once the gas passes through the EL valve, it adiabatically expands into the vacuum chamber, and collision-induced cooling drives cluster formation. This ensemble of clusters is then passed through a ring-shaped electrode (a hot filament cathode around a biased grid pulsed at a delay relative to the valve pulse), which emits electrons and accelerates them to ~ 200 - 500 eV kinetic energy. These electrons undergo ionizing collisions with the carrier gas which produce slower electrons that can be captured by the clusters (secondary electron attachment). Heterogeneous clusters either nucleate around an ionic dopant or can pick it up after forming. Electron attachment to the clusters increases their internal energy distributions which can be reduced via evaporation of one or more constituent atoms/molecules. In this way, an estimate of the cluster temperature can be made, since the timescale of evaporative decay must be longer than the measurement time for a given cluster within the evaporative ensemble.⁶ The application of this model to cluster anion systems will be detailed briefly in Chapter 5 and the thesis of Margaret Yandell.

The ionization process produces an ensemble of anions and cations and is highly inefficient, with ionizing collisions estimated to be around 1 in 10^4 events. The gas pulse is then collimated with a skimmer to reduce the translational temperature distribution and injected into a perpendicularly mounted Wiley-McLaren (three plate) time-of-flight mass spectrometer.⁷ The

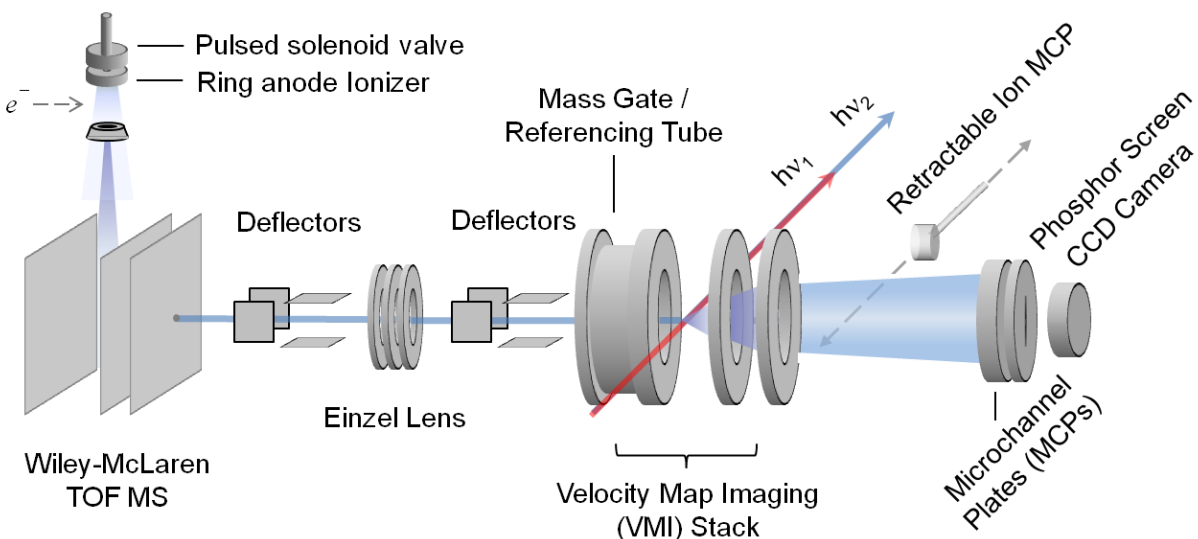


Figure 2.1. Photoelectron imaging apparatus.

voltages applied to the plates are pulsed such that the gas packet enters the spectrometer undisturbed. Then the repeller plate is pulsed to -2 kV while the extractor plate is pulsed to a tuned voltage between ~ -1.4 -1.8 kV depending on the ion of interest. The timing of the voltage pulse relative to the valve pulse is optimized for a given ion. The anions are accelerated and separated by their flight times. After being steered with a first set of ion deflectors they pass through a pinhole to the next differentially pumped region where they are radially focused by an Einzel lens and pass through another pinhole into the second differentially pumped region where they are steered again by a second deflector array. This region also houses a second Einzel lens that is no longer in use. The ions pass through yet another pinhole into the detector region where their times-of-flight (relative to the initial trigger) are measured using a retractable microchannel plate (MCP)/anode detector (see Appendices 1 and 3). The signal on this ion detector is then capacitively coupled out to a digital oscilloscope (Tektronix DPO3034C). Typical arrival times at the ion detector are on the hundreds of microsecond timescales; actual anion lifetimes can be calculated from the time-of-flight measured on the oscilloscope and the timings between the mass spectrometer, valve and ionizer TTL pulse timings for the given ion and day with reference to the trigger tree in Appendix 1.

After passing into the detector region, the ions traverse a metal re-referencing tube which is held at ground until the desired mass enters. When the ions are being initially optimized, this tube is set to ground, allowing the ions to experience field-free flight from the second differentially pumped region on until the ion detector. Once the initial optimization is done, the tube is then pulsed from -4 kV to ground. The voltage pulse is timed to allow the desired mass to enter the tube with its trajectory unaltered ($V=0$), but then drops back to -4 kV after that mass has entered the tube, accelerating it forward and other masses backward, effectively acting as additional mass selection. The voltage pulse on the re-referencing tube can be very short, as short as 180 ns, in order to achieve high mass resolution. However, this width is tunable and can be extended to several microseconds to allow multiple masses through (when single-ion mass resolution is lost, typically around $n > 50$ -100, depending on the material of interest). The back electrode of this tube also acts as the first plate of the velocity map imaging setup. The ions can be optimized again for maximal intensity within the VMI field (once the extraction voltage is

applied). It should be noted that the ion detector is several centimeters from the center of the VMI plates (where laser interaction occurs) and thus the ion beam will have different optimum parameters for ion detection than it will for electron detection via VMI.

2.2 Femtosecond laser system

Ultrafast pulses are generated through an optical technique called "modelocking". Simply, a laser cavity will have a well-defined longitudinal mode structure based on its length, L . The gain medium's emission profile will determine which frequencies are available, and the product of these frequencies with those available from the mode structure will determine which frequencies can actually oscillate in the cavity. If each mode is oscillating with a fixed phase relative to the others, they can constructively interfere to form a short pulse. The more modes oscillating together at a fixed phase, the shorter is the pulse duration. Thus a long cavity and a material with a wide gain profile are desirable for forming short pulses. The exact nature of a mode's phase relative to that of another mode is related to the cavity modes' respective frequencies, leading to brief periods of constructive interference between all the lasing modes, *i.e.* an ultrashort laser pulse.^{8,9}

Modelocking is achieved in the commercial oscillators used for the experiments presented here by Kerr-Lens effect. The Kerr effect (intensity dependent refractive index) preferentially amplifies pulsed emission over continuous-wave (CW) light oscillating in the cavity. A pulse introduced by a disturbance in the optical cavity (e.g. by moving a prism or tapping a mirror) will traverse the gain medium and, due to the Kerr effect, self-focus in the material, leading to higher intensity and thus stronger emission; this happens each time the pulse propagates through the crystal, leading to intense pulse production. Ti:sapphire has a large third-order nonlinear susceptibility ($\chi^{(3)}$) causing it to exhibit a strong Kerr effect (it is said to be strongly "Kerr-active"). Combining this with an asymmetric cavity or a hard aperture will suppress CW emission, yielding an intense pulse train at a repetition rate of $c/2L$.¹⁰

Ti:sapphire is an ideal choice of gain media for ultrashort pulse production. There is a strong absorption around 530 nm, conveniently allowing it to be pumped by an argon ion laser or the second harmonic of a Nd:YAG, Nd:YLF, or (in our case) a Nd:YVO₄ laser. More importantly, the gain profile is exceptionally broad (emitting from ~650-1100 nm), as the energy levels of the Ti³⁺ ions are broadened by coupling to the Al₂O₃ (sapphire) lattice. The large $\chi^{(3)}$ of the sapphire lattice leads to a strong thermal lens effect that can be mitigated by cooling the Ti:sapphire due to its high thermal conductivity. The high thermal conductivity of sapphire at low temperatures allows for high-intensity pumping of the gain medium, leading to strong amplification of the femtosecond pulse. Cryogenic cooling of the gain medium is employed in the amplifier scheme detailed below for the KM Labs Dragon.

While pulses from the oscillator are temporally very short, they are not very intense (~10 nJ/pulse) at the high repetition rate (typically ~100 MHz), and must be amplified for efficient harmonic or parametric generation or spectroscopic application. This is achieved by "chirped-pulse amplification"; both the Clark-MXR and KM Labs systems utilize a form of this process with different implementations of the actual amplification portion. The output of the oscillator is used to seed stimulated emission in a second Ti:sapphire gain medium; however amplifying a femtosecond pulse can lead to optical damage to the crystal and other optics, so it must be stretched in time first and then recompressed after amplification.

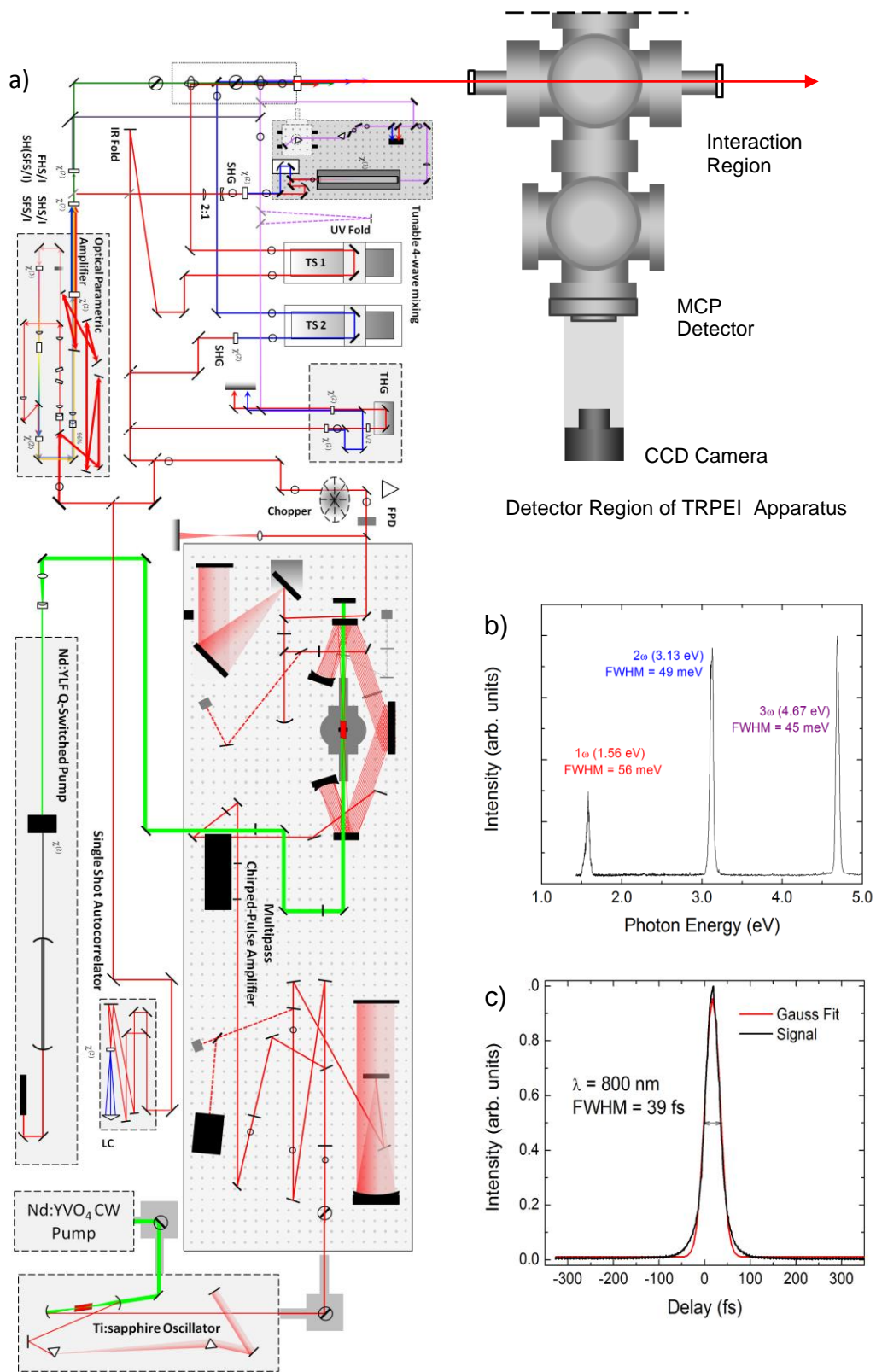


Figure 2.2a. Femtosecond laser table configuration..

Figure 2.2b. Spectra of fundamental, 2nd and 3rd harmonics measured on OceanOptics USB4000 fiber spectrometer.

Figure 2.2c. Autocorrelation of fundamental at amplifier output using Coherent SSA autocorrelator.

The pulse is stretched (chirped) using a diffraction grating pair (in practice, only one grating and a fold mirror are used to minimize costs) to ~ 100 ps before being directed into the amplification medium. However, a megahertz pulse train will distribute the energy of the amplifier pump over a large number of femtosecond pulses. Thus, reducing the pulse repetition rate will lead to stronger amplification of each individual pulse. The repetition rate of the oscillator is strictly controlled by the cavity length and cannot be altered without realignment, so an electro-optical element called a Pockels cell is used. This device is basically a voltage-dependent half waveplate and a polarizer: a pulsed voltage is applied to rotate one femtosecond pulse's polarization to be transmitted by the polarizer while the others are unaffected and are absorbed. Changing the voltage pulse rate allows for a controlled reduction in the femtosecond repetition frequency to the desired kHz range.

The amplifier scheme itself is different in the two systems used for the studies in this thesis. The Clark-MXR CPA-1000 system uses a regenerative amplifier in which a second optical cavity is constructed for the ~ 800 nm Ti:sapphire fundamental which is pumped by a second, nanosecond pulsed laser (~ 5 mJ/pulse of 527 nm or 532 nm light). The Pockels cell acts as a gate allowing a given femtosecond seed pulse into the cavity where it oscillates, stimulating emission and amplifying the seed after a fixed number of round-trips. When amplification is maximized (the losses balance the gain), the pulse is ejected from the cavity by the Pockels cell. This scheme gives pulse energies of a ~ 900 μ J/pulse (at output, after compression) under normal conditions. The KM Labs Dragon amplifier, on the other hand, is based on a multipass design where the isolated pulse from the Pockels cell is injected into a ring of mirrors which steer the seed pulse into the pumped amplifier crystal at an angle. There is no cavity in this design; the first pass of the seed continues to reflect within the ring, making subsequent passes through the crystal, stimulating emission at each pass until the pulse is intercepted by a pickoff mirror and ejected from the ring. The number of passes here is determined geometrically rather than temporally, as in the regenerative system. The 13 passes in this system must be spatially well overlapped in order to produce sufficient gain, a good transverse mode and to avoid "hot spots" - asymmetric regions in the beam profile of high intensity which can cause burning of optical elements, including the crystal. These passes must also be spatially and temporally overlapped in the crystal with the pump pulse for efficient amplification; an infrared camera is crucial for this step. The amplification medium is cryogenically cooled to ~ 50 K to ensure safe pumping by ~ 25 mJ/pulse energy of the 527 nm/532 nm pump laser and to reduce the thermal lensing effects. By doing this, it becomes possible to change the pump laser characteristics (power and repetition rate) in real time without realigning the ring. Amplified pulse energies in this setup can reach above 3 mJ/pulse, though they are typically closer to 2 mJ/pulse during normal operation.

In both systems, the amplified pulse is then directed into a diffraction grating pair oppositely oriented to that of the stretcher. The gratings compress the pulse to nearly the same temporal profile it had before amplification (the dispersion from the Pockels cell, the gain medium and whatever optics the pulse encountered between the stretcher and compressor prevent recovery of the original pulse shape due to higher order dispersion effects). The KM Labs Dragon uses a grating pair, while the Clark-MXR CPA-1000 uses one grating and a fold, similar to the stretcher design in both systems.

The internal layout of the KM Labs Griffin Oscillator and Dragon amplifier and the optical layout of the laser table is shown in Figure 2.2.

2.2.1 Dispersion compensating prisms

An unfortunate but unavoidable consequence of the shorter pulse duration from the KM Dragon femtosecond system is the sensitivity of the pulses to group delay dispersion (GDD) as the pulse propagates through a transparent medium. This arises from the difference in the speed of light through the medium for different frequencies, due to the frequency dependence of the index of refraction. A pulse with central frequency ω_0 accumulates a phase as it travels through a medium according to:⁹

$$\Phi(\omega) = k(\omega)z \approx k(\omega_0)z + k'(\omega_0) \cdot (\omega - \omega_0)z + \frac{1}{2}k''(\omega_0) \cdot (\omega - \omega_0)^2 z + \dots \quad (2.1)$$

where k the wave-vector, $k(\omega) = \omega n(\omega)/c$. The second order term, $k''(\omega)z$ is the GDD. All transparent media will chirp the pulse to some extent (obviously some materials are better than others, depending on the index of refraction); thus by the time the pulses have been manipulated (through harmonic or parametric generation, focusing, beamsplitting, etc.) and steered into the vacuum chamber, the ~ 30 fs pulses are broadened to anywhere between 80 and 150 fs full-width-half-maximum (FWHM). This effect is more severe for shorter pulses: a transform-limited Gaussian pulse with initial temporal width Δt_0 will be broadened as it travels through a medium of thickness z to:⁹

$$\Delta t' = \Delta t_0 \sqrt{1 + \left(\frac{4 \ln 2 k'' z}{\Delta t_0^2} \right)^2} \quad (2.2)$$

Note, however, that the pulses emanating from the amplifier are not transform limited.

The GDD can be calculated for a given point on the table if both the temporal width (Δt) and spectral width ($\Delta \lambda$) are known. This is achieved using an intensity autocorrelator (Coherent SSA) and a fiber spectrometer (Ocean Optics USB4000); both values must be measured at the same position in order to yield meaningful results. Using these parameters, and inverting Eq. 2.2, the accumulated GDD at a given point is:

$$GDD = \frac{1}{4 \ln 2} \sqrt{\left(\frac{K \Delta t}{\Delta \nu} \right)^2 - \left(\frac{K}{\Delta \nu} \right)^4} = \frac{\lambda^2}{4 \ln 2} \sqrt{\left(\frac{K \Delta t}{c \Delta \lambda} \right)^2 - \left(\frac{K \lambda}{c \Delta \lambda} \right)^4} \quad (2.3)$$

using $\Delta \nu = c \Delta \lambda / \lambda^2$ and $K = \Delta \nu \Delta t$, the time-bandwidth product for a transform-limited pulse (0.441 for a Gaussian pulse shape).⁹

The temporal dispersion (Eq. 2.3) of the ultrashort pulses can be corrected using a pair of prisms to introduce a *negative* GDD with minimal attenuation and angular dispersion. For a properly oriented prism pair the GDD can be expressed as:¹¹

$$GDD_{prism} = \frac{2\lambda^3}{\pi c^2} \left\{ \left[\left(\frac{d^2 n}{d\lambda^2} + \left(2n - \frac{1}{n^3} \right) \left(\frac{dn}{d\lambda} \right)^2 \right) l \sin \beta - 2 \left(\frac{dn}{d\lambda} \right)^2 \cos \beta \right] + 2 \left(\frac{d^2 n}{d\lambda^2} \right) D_{1/e^2} \right\} \quad (2.4)$$

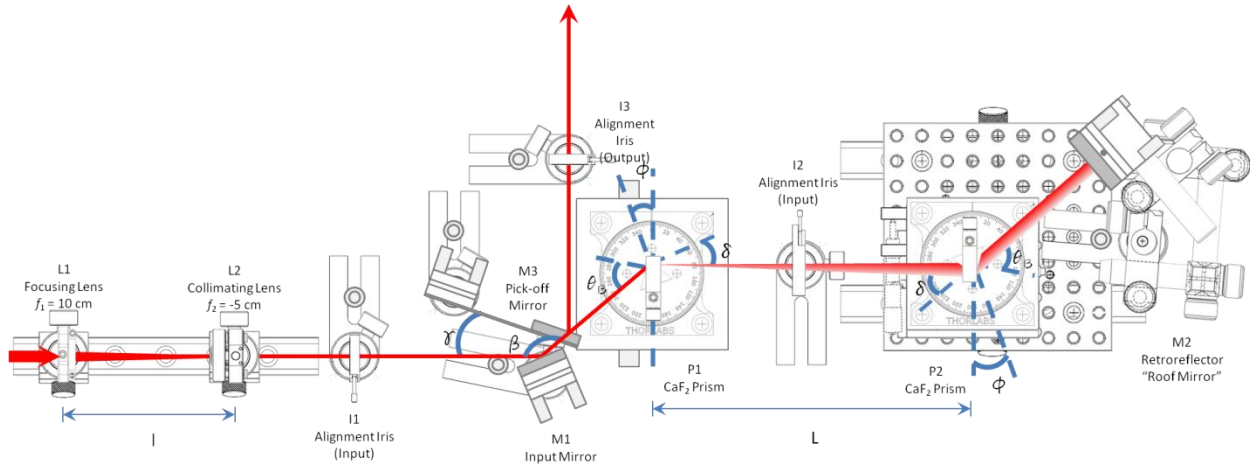


Figure 2.3. Layout for dispersion compensating prism pair.

where λ is the wavelength, c is the speed of light in vacuum, n is the refractive index, l is the prism spacing (apex to apex), β is the angle of the dispersed beam after the first prism, and D_{1/e^2} is the beam diameter at which the laser power is $1/e^2 \sim 14\%$ of the full diameter. This equation can be analytically solved for l , and under the reasonable assumption that β is small can also be vastly simplified, yielding the approximate prism separation based on the measured temporal and spectral bandwidths and the prism material. Note that because the majority of the terms are additive, the ability to induce a negative GDD is due to the slope and, importantly, the *curvature* of the refractive index. The refractive index is well parameterized by the Sellmeier equation; coefficients for a wide range of materials are available in the literature from which the index and its derivatives can be calculated/interpolated. A material is chosen based on these values as well as the net transmission at the desired wavelength. Calcium fluoride (CaF_2) prisms are utilized in the current compressor setup as they transmit well in the ultraviolet (however they suffer from high third-order dispersion); a second compressor has been constructed using BK-7 glass to function in the infrared.

The layout for the dispersion compensator is shown in Figure 2.3. (Note: β in the figure is not the same as in equation 2.4, which corresponds to the width of the dispersed light from the first prism in the figure). Here, the prisms are mounted on rotation stages allowing for easy empirical determination of the angle of minimum deviation (δ), which is wavelength dependent, and the second prism is translatable on two dimensions. Most importantly, the distance between the prisms can be controlled by translating the second prism stage either along an optical rail or a micrometer translation stage. The seeming complicated arrangement of the input steering mirrors is done to allow translation along separation axis to be *parallel* to the breadboard, giving easy tunability for different wavelengths and different amounts of accumulated GDD to be eliminated. The retroreflector is mounted along with the second prism stage to maintain alignment during translation. The prism compressor has been demonstrated to reduce the pulse duration of a 100 fs FWHM pulse by at least 20% with $\sim 60\%$ transmission.

2.2.2 Optical parametric amplifier

Frequency generation via sum- or difference frequency mixing in non-linear crystals

limits one to the harmonics of the laser. However, many electronic resonances (such as the CTTS transition or the $p \leftarrow s$ excitation in solvated electron) are strongly coupled to their solvation environment, and hence the cluster size. Indeed, electronic resonances tend to blue-shift as the cluster size increases as the energy levels are stabilized by the long-range interactions of the solvent, much as how the binding energies increase. This size dependence can bring the desired transition out of resonance with any available harmonic, requiring a tunable laser light source.

The previous laser system employed on this project had a tunable optical parametric amplifier (OPA, Light Conversion TOPAS 4-800) which relied on a superfluorescence seed from a pumped nonlinear crystal before multi-stage amplification. This system worked reliably with the Clark-MXR CPA-1000; however when the femtosecond system was upgraded to the KM Labs Griffin/Dragon system, which delivers ~ 30 fs pulses and ~ 3 times the average power of the Clark, the TOPAS became unstable and the conversion efficiency dropped. While some of this can be accounted for by poor alignment and optical damage to the components, the primary reason for the drop in conversion efficiency was the method of seed generation. As confirmed by technicians from Light Conversion, both the damage threshold and the supercontinuum generation threshold were very close to the optimum pump intensities needed for superfluorescence generation. Due to the shorter pulse widths from the new amplifier, there was always some parasitic continuum light produced with the superfluorescence, and likely some optical damage to the crystal while running at conditions necessary for the experiment, all leading to a reduced conversion efficiency. Changing the lens positions within their acceptable ranges did not eliminate this problem.

Newer generation OPAs have since been developed utilizing a continuum seed for the parametric generation. Here, instead of relying on spontaneous parametric down-conversion to provide the photon to drive the difference frequency mixing process (this is called optical parametric *generation*), a continuum seed is used to provide a range of frequencies which can be mixed with the pump pulse to produce the third pulse. By convention, the higher frequency generated light is called the "signal" and the lower frequency is called the "idler". To be generated in significant amounts the frequencies must satisfy both momentum conservation (phase matching) and energy conservation:

$$\omega_{pump} = \omega_{signal} + \omega_{idler} \quad (2.5)$$

$$\vec{k}_{pump} = \vec{k}_{signal} + \vec{k}_{idler} \quad (2.6)$$

While a new photon at the missing frequency is created, energy conservation requires the creation of another photon of the frequency stimulating the emission; this is optical parametric *amplification*. Angular momentum conservation also requires the polarizations to be opposed and correlated (type II phase matching).

We have recently upgraded our laser system to a newer-generation Light-Conversion TOPAS-C source which is based on continuum generation within a sapphire plate. The layout of the TOPAS-C is shown in Figure 2.4. To generate the seed, a small amount of the fundamental pump is split off and focused into Kerr-active sapphire to generate broadband "white light"

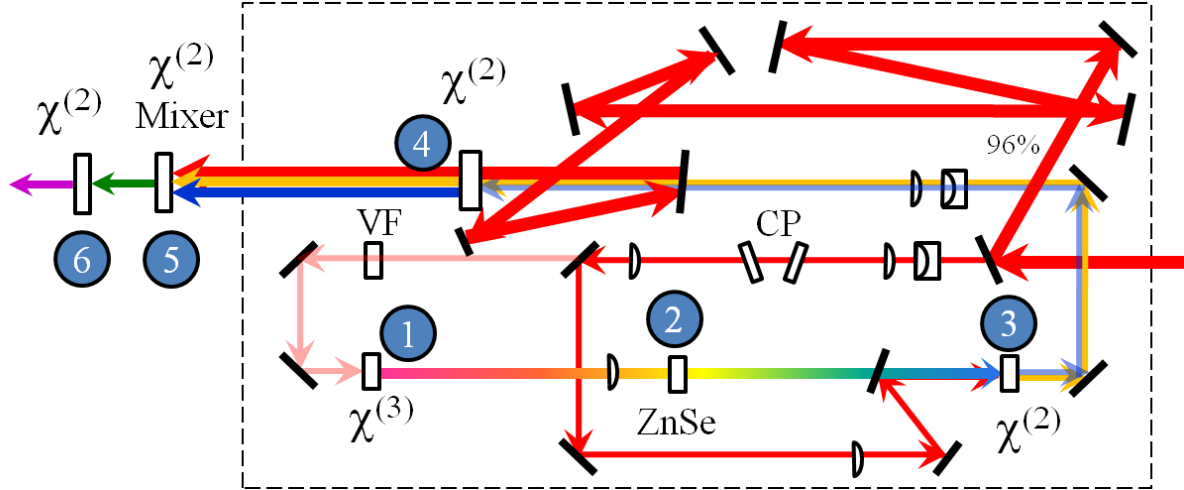


Figure 2.4. Setup of the Light Conversion TOPAS-C. (1) Sapphire plate for continuum generation; (2) ZnSe crystal to chirp the continuum; (3) BBO crystal for signal/idler generation/preamplification; (4) BBO crystal for main amplification; (5) BBO mixer for SFS/SFI/SHS/SHS generation; (6) External BBO crystal for ultraviolet generation.

continuum that is actually in the near IR. This occurs at element (1) in the figure. The continuum pulse is then temporally chirped by a ZnSe crystal (2) and spatially delayed with respect to the remaining fundamental (the “pre-amplifier”) before interacting in a nonlinear crystal (3). Because the continuum is temporally dispersed (~ 10 ps), the pre-amplifier will only overlap with a small portion of the seed in the crystal, so only specific frequency components will interact, thus allowing for tunable difference-frequency mixing to create the idler (and hence amplification of the pump by OPA). Additional tuning is achieved by changing the angle of (3) to maximize the phase-matching condition. The generated colors are then recombined with the majority ($\sim 96\%$) of the pump beam input into the TOPAS-C in a second nonlinear crystal (4) to amplify the signal and idler via DFG/OPA to useable powers, with total IR conversion efficiency (signal+idler) of $>35\%$. Because the amount of light used to seed the continuum is so small, the mismatch in the number of photons between the signal and idler is insignificant. The IR parametric light (1200-3000 nm) can be converted again using SFG with the residual fundamental pump to access the visible region by a computer-controlled mixer (5), and SHG of these colors or fourth-harmonic generation (twice sequential SHG) of the signal or idler via another external nonlinear crystal (6) can generate tunable ultraviolet light. The TOPAS-C introduces minimal temporal broadening of the pulses ($\sim 5\text{-}10\%$) when optimally compressed.

2.2.3 Tunable UV by four-wave mixing

Frequency conversion based on harmonic- and sum-frequency generation in a nonlinear crystal is convenient and relatively straightforward for much of the visible and infrared spectrum. However, due to the absorptive and refractive properties of the materials used to construct the nonlinear crystals, such as β -barium borate (BBO), generating frequencies in the deep ultraviolet becomes very inefficient at sufficiently short wavelengths (< 240 nm), leading to poor transmission and group-velocity walk-off. Increasing the interaction length by using thicker nonlinear crystals invariably leads to pulse stretching and thus is unsuited for femtosecond applications, so other methods must be utilized, such as degenerate four-wave mixing (FWM).

FWM takes two photons of one frequency and a third photon of lower frequency to generate a fourth color:

$$\omega_{FWM} = \omega_1 + \omega_1 - \omega_2, \quad (2.7)$$

In the case of using only the fundamental ($\omega_2 = \omega$) and second harmonic ($\omega_1 = 2\omega$), the third harmonic of the fundamental can be generated in this fashion: $3\omega = 2\omega + 2\omega - \omega$. This is called degenerate four wave mixing. By using the second harmonic of the Ti:sapphire fundamental as ω_1 , and tunable infrared light from an optical parametric amplifier for ω_2 , tunable ultraviolet light can be generated with conversion efficiencies of up to ~15%.^{12, 13} FWM of femtosecond pulses is typically carried out in a long capillary tube filled with a dilute gas, such as argon or neon, allowing for significant interaction lengths.

Because the capillary acts as a waveguide, the dispersion properties are different than for standard transmissive materials, so there is no need for a birefringent medium. To achieve efficient generation of a new frequency, Eq. 2.6 shows that the light's momenta must be matched. The magnitude of the wavevector for light propagating through a capillary filled with a gas with refractive index n_g can be expressed as:¹⁴

$$k = \frac{\omega n_g(\omega)}{c} \left\{ 1 - \frac{1}{2} \left(\frac{2\pi u_{nm}}{a\omega} \right)^2 \left[1 + \text{Im} \left(\frac{2c v_{EH}}{a\omega} \right) \right] \right\} \quad (2.8)$$

, where

$$v_{EH} = \frac{\nu^2 + 1}{2\sqrt{\nu^2 - 2}} \quad (2.9)$$

and $\nu = n_{cap}/n_g$, where n_{cap} is the refractive index of the capillary material, u_{nm} is the modal constant, and a is the core radius. The phase-matching criterion thus becomes one of matching the index of refraction and the transverse modes. These equations can be used to express the phase matching condition for four-wave mixing in a gas-filled capillary for any wavelength and any transverse mode.

Some control can be expressed over the refractive index to achieve better phase matching, such as the choice of gas and the pressure within the capillary. From the Lorentz-Lorenz equation, the refractive index of a dilute gas is related to its pressure by:

$$n_g(\omega) \approx \sqrt{1 + 4\pi\rho\alpha(\omega)\frac{P}{k_B T}} \approx 1 + 2\pi\rho\alpha(\omega)\frac{P}{k_B T} = 1 + pA_g(T, \omega), \quad (2.10)$$

where ρ is the gas density, α is the (frequency-dependent) atomic polarizability of the gas, p is the pressure, k_B is Boltzmann's constant, and T is the temperature; $A_g(T, \omega)$ is a temperature-, frequency- and gas-dependent constant. Thus controlling the pressure of the particular gas within the cell allows for phase matching to be maximized. Typical pressures of Argon are around 50-60 torr.¹²⁻¹⁴

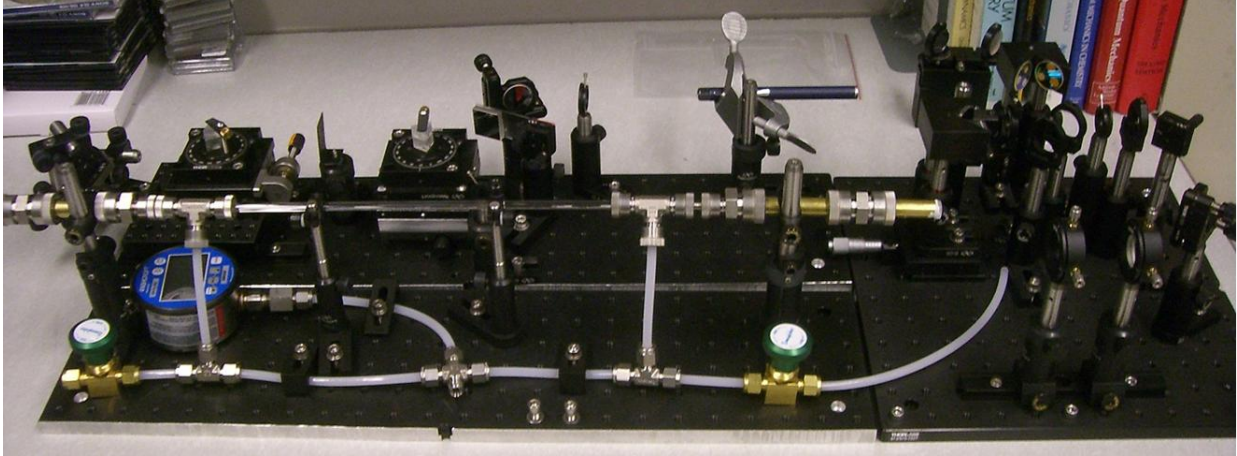


Figure 2.5. Tunable four-wave mixing (FWM) apparatus with prism compressor and delay matching stage.

The strong fields of the ultrashort pulses lead to self- and cross-phase modulation within the waveguide, leading to frequency generation around the central wavelength. This is one of the advantages of the FWM, as the broad spectral width of the generated light allows for compression beyond the transform limit of the *input* pulses using a secondary compressor. Consequently, the mixing apparatus is typically paired with a prism compressor.

A degenerate four-wave mixing device has been constructed based on the designs of Durfee, *et al.*¹² as well as a similar device constructed in the Bradforth group.¹³ The device is composed of three main pieces: the four-wave mixer (FWM), the beam path matcher (BPM) and the dispersion-compensating compressor (DCC). A photograph of the entire apparatus is shown in Figure 2.5. Instead of constructing the apparatus on one breadboard or on the laser table itself, the device was constructed on three separate, modular breadboards such that each piece could be used separately. The beam path matcher (BPM) can be easily converted into a third-harmonic generator (details below). The tunable prism compressor (DCC) can be utilized for a wide range of frequencies ranging from the ultraviolet light generated by standard harmonic conversion or the parametric/visible light from the TOPAS-C, or even the infrared fundamental, regardless of the four-wave mixer. This design also makes placement of the apparatus flexible and storage simple, requiring minimal alignment when needed again.

The main assembly comprises a ~30 cm fused silica (Schott Duran glass, 6mm OD, 0.4 mm ID) tube into which is threaded the hollow-core fused silica fiber (Polymicro 363 μm OD, 75-200 μm) of slightly longer length. The fiber should protrude ~1/4" on each side to increase coupling of the input light to the waveguide. The ends of the tube assembly are attached to 1/4" Ultra-Torr tee vacuum fittings which connect on one side to a 1/4"-1/2" Ultra-torr adapter to bridge it to the detachable windows (3mm thick, 1/2" diameter CaF_2 windows epoxied to 1/2" copper tubes) and to polyethylene tubing on the other. The tubing connects the mixing assembly to a vacuum system on one side and a controlled gas inlet on the other. Gas pressure is monitored with a positive-pressure gauge (Ashcroft 35053 digital pressure gauge). Optimal phase matching is achieved by alternating control of the inlet and vacuum valves until the desired pressure is reached.

The two colors being mixed inside the cell must be overlapped in space as well as time. Temporal overlap is achieved using a beamsplitter/delay line configuration almost identical to that of a third harmonic generator. First, the size is reduced 50% using a 1:2 Galilean telescope

(lens 1: $f = 10$ cm plano-convex, lens 2: $f = -5$ cm plano-concave, both BK7 for use with the 800 nm fundamental) to increase second harmonic generation efficiency in the BBO crystal (Crystech, BBO, $\theta = 29.6$, $\phi = 0$, 10×10 mm², 0.5 mm thick) immediately following. The thickness of the crystal is chosen to maximize second harmonic generation; the pulse-spreading within the thick crystal becomes irrelevant once the pulse begins to propagate within the fiber and spread further. The generated 400 nm light is selectively reflected using a beamsplitter onto a fixed-delay retro-reflector composed of two dielectric mirrors. Unconverted fundamental is directed through a 780 nm half waveplate (ThorLabs WPQ10M-780) onto an adjustable length retro-reflector made of two silver mirrors on a micrometer stage. The two colors are then recombined using a dichroic beam combiner. Each color is focused into the fiber using its own lens so as to maximize the conversion efficiency due to the wavelength-dependent focal length of a given lens. The beam path compensator can be converted into a third-harmonic generator by simply placing a sum-frequency crystal (Crystech, BBO, $\theta = 45.1$, $\phi = 0$, 10×10 mm², 0.09 mm thick) for mixing the 800 nm fundamental and the 400 nm second harmonic, producing 266 nm third harmonic at a reasonable conversion efficiency (~5-10% total conversion). The second harmonic crystal should also be replaced for this use with a thinner crystal to avoid inducing large GDD. Also, this part of the device becomes unnecessary when using tunable/parametric light from the TOPAS-C as the path length through the TOPAS is 165 cm and will thus the 400 nm second harmonic beam path must be lengthened significantly to compensate.

Reported pulse energies for this device are in the 5 μ J/pulse range using a 75 μ m fused silica fiber, which is on the low end for pulses in time-resolved photoelectron imaging of anions. Because the output intensity does not scale with the input power due to nonlinear effects and optical damage to the fused-silica fiber, the best way to tune the power is to vary the fiber inner diameter and scale the input power accordingly. The implementation of this device will be detailed more in-depth in the thesis of Madeline Elkins.

2.3 Velocity Map Imaging (VMI) electron detection

Once the appropriate ion mass is transmitted through the mass gate it is interrogated by the laser pulse(s) to produce photoelectrons which are collected by velocity-map imaging (VMI). VMI¹⁵ uses a cylindrically symmetric inhomogeneous electric field to accelerate the photoelectrons (indeed, all negatively charged particles) toward a two dimensional detector. The cylindrical plates are deployed in a repeller/extractor/ground configuration similar to the Wiley-McLaren mass spectrometer, however the shape and spacing of the plates are different, and the relative voltages are fixed. Because of the shape of the (total) electric field, each ejected electron with the same velocity *vector* is focused onto the same position on the detector, in essence connecting the laboratory frame to the electron center-of-mass frame. This enables the free electron wave's momentum to be mapped directly, and by conservation of angular momentum (for electric dipole transitions), information on the molecular orbital of origin to be obtained. The method is shown schematically in Figure 2.6.

The repeller plate is typically pulsed from -4000 V to ground, while the extractor plate is held at a constant (DC) potential of -2800 V, yielding a ratio of the extractor to repeller of 70%. This ratio yields the best focus for the photoelectron images; it is a constant for the apparatus, determined largely by the flight tube length. The magnitude of the VMI voltages, in conjunction with the flight tube length and detector diameter, determines the maximum measureable kinetic

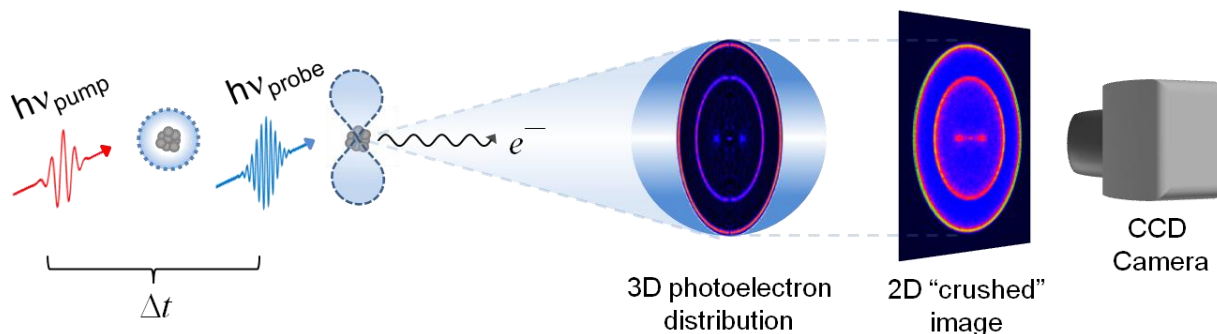


Figure 2.6. Schematic of photoelectron imaging collection process

energy of the photoelectrons. Images are amplified using a pair of chevron-mounted spatially-sensitive 70 mm microchannel plates (MCPs) with the resulting amplified electron signal further accelerated to a phosphor screen and collected by a charge-coupled device (CCD) camera which averages over detection events to produce an integrated photoelectron image. The front plate of the detector is pulsed to only amplify the photoelectrons and not the photo-produced neutrals (moving with enough kinetic energy to be amplified) and un-detached ions. Only the front plate of the detector is pulsed; the back plate and the phosphor screen are held at constant voltages (+1500 to +1600 V above ground and +4000 V, respectively). The front plate is pulsed from +700 V to ground for 180-250 ns at the appropriate time leading to the full 1500-1600 V potential difference across the plates at the time of the photoelectrons' arrival. The ~800-900 V potential difference across the MCPs for the majority of the experimental cycle is not enough to yield secondary electron formation/amplification, thus allowing for photoelectron detection collinear with the ion beam axis without damaging the detector.

In 2010 the CCD camera and framegrabber had to be upgraded to interface with the new LabView version of the image acquisition program (ImageDAQ 2.0, described in detail in Appendix 4). The old camera was replaced with a Dalsa (DS-21-01M60-10E) 1024 x 1024 pixel², 12-bit camera capable of capturing images at 30 Hz or 60 Hz. The camera is interfaced to the computer via a National Instruments (NI Vision PCIe 1427/PXI interface) framegrabber. The acquisition software samples images at 30 Hz and bins them to 512 x 512 pixel². Further details on processing and reconstruction are given in Appendix 4.

2.4 References

- 1 B. J. Greenblatt, University of California, Berkeley, 1999.
- 2 M. T. Zanni, University of California, Berkeley, 1999.
- 3 A. V. Davis, University of California, Berkeley, 2002.
- 4 A. E. Bragg, University of California, Berkeley, 2004.
- 5 U. Even *et al.*, *J. Chem. Phys.* **112** (18), 8068 (2000).
- 6 C. E. Klots, *Z. Phys. D* **20** (1), 105 (1991).
- 7 W. C. Wiley, and I. H. McLaren, *Rev. Sci. Instrum.* **26** (12), 1150 (1955).
- 8 G. R. Fowles, *Introduction to modern optics* (Dover Publications, 1989).
- 9 C. Rullière, *Femtosecond laser pulses: principles and experiments* (Springer, 2005).
- 10 A. E. Siegman, *Lasers* (University Science Books, 1986).
- 11 R. L. Fork, O. E. Martinez, and J. P. Gordon, *Opt. Lett.* **9** (5), 150 (1984).

- 12 C. G. Durfee Iii *et al.*, Opt. Lett. **24** (10), 697 (1999).
- 13 A. E. Jailaubekov, and S. E. Bradforth, Appl. Phys. Lett. **87**, 021107 (2005).
- 14 C. G. Durfee Iii *et al.*, Opt. Lett. **22** (20), 1565 (1997).
- 15 A. T. J. B. Eppink, and D. H. Parker, Rev. Sci. Instrum. **68** (9), 3477 (1997).

Chapter 3. Charge Carrier Dynamics in Semiconducting Mercury Cluster Anions $(\text{Hg})_n^-$ ($7 \leq n \leq 20$)

[Reprinted with permission from "Charge carrier dynamics in semiconducting mercury cluster anions" R. M. Young, G. B. Griffin, O. T. Ehrler, A. Kammarath, A. E. Bragg, J. R. R. Verlet, O. Cheshnovsky and D. M. Neumark, Phys. Scr. 80, 048102 (2009)]

We have examined size-dependent electronic relaxation dynamics in isolated semiconducting mercury cluster anions using time-resolved photoelectron imaging. Relaxation following excitation from within the conduction (p -) band occurs on a ~ 3 -40 ps timescale and is attributed to non-adiabatic relaxation through the p -band. Exciting an electron from the valence (s -) band into the conduction band creates an electron-hole pair that relaxes prior to Auger emission. The dynamics associated with this feature occur on a ~ 500 fs timescale and are attributed to either a hole-induced contraction of the cluster or electron-electron scattering.

3.1 Introduction

As nanotechnology becomes a more integral part of the broader technological landscape, it becomes increasingly important to gain a fundamental understanding of the electronic processes that occur at the nanoscale. For example, there has been considerable recent interest in the mechanisms of electronic relaxation in semiconductor quantum dots owing to the possible application of these species in solar cells¹. Much of this interest has focused on the creation and relaxation dynamics of multiple charge carriers in quantum dots, either by absorption of multiple photons by a single quantum dot or through the proposed mechanism of multiple exciton generation^{2,3}, in which a high-energy electron-hole pair created by a single photon decays into multiple electron-hole pairs.

Quantum dots are generally formed in solution and passivated with surface-capping groups, however, and some experiments have suggested that the surface-capping can have significant effects on the electronic dynamics of the quantum dots^{4,5}. Hence, studies of bare, gas-phase species that mimic the electronic structure of quantum dots can provide new perspectives into the relaxation dynamics that occur in these species. In this article, we present recent experimental work⁶⁻⁹ on mercury cluster anions using time-resolved photoelectron imaging (TRPEI) to monitor electronic relaxation dynamics after (independently) exciting electrons from either the conduction or valence band.

Mercury clusters are an ideal system to study in this respect. Upon aggregation of Hg atoms, the filled atomic $6s$ and empty $6p$ atomic orbitals form quasi-continuous "bands". These bands are well separated, having a distinct band gap (BG) that drops with increasing cluster size, similar to the situation in semiconductor quantum dots. Clusters of only a few Hg atoms will be bound in van der Waals (vdW) complexes¹⁰ before making a transition to a more covalent binding character characteristic of semiconductors, with increased delocalization of electrons throughout the cluster. This change in bond character has been studied extensively in both neutral¹¹⁻¹⁶ and charged¹⁷⁻²⁰ clusters. Eventually, the addition of orbitals to the bands leads to the closure of the BG, in a Kubo-type insulator-to-metal transition¹⁹.

Mercury cluster anions, $(\text{Hg})_n^-$, offer a natural way to probe the size-evolution of these trends. Since the clusters are charged, size-selection prior to spectroscopic interrogation is

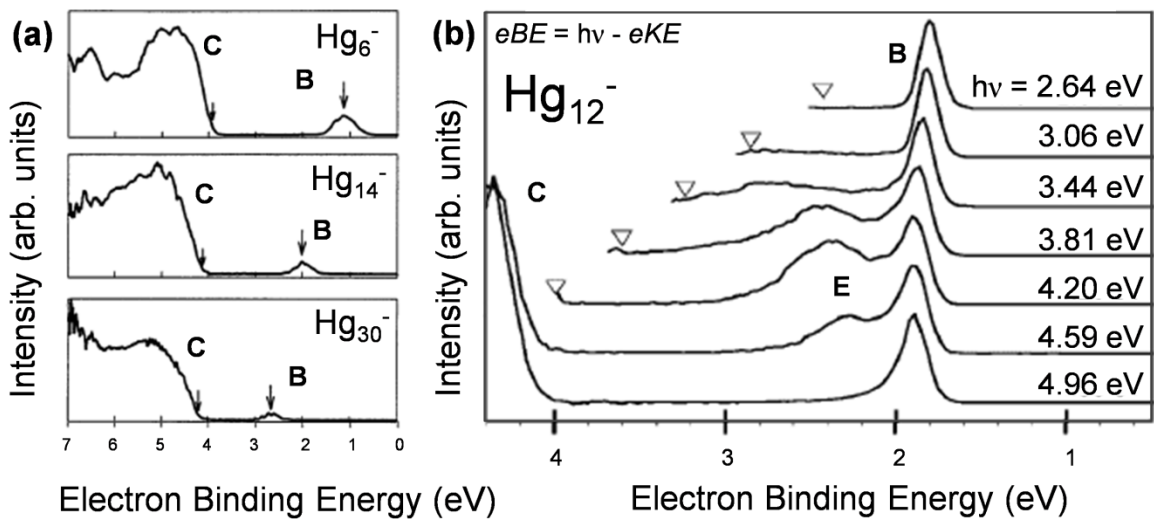


Figure 3.1a. Photoelectron spectra of $(\text{Hg})_n^-$ measured with 7.9 eV photons adapted from Busani, et al.²¹ The gap between the low eBE ($6p$ electrons) peak and the broad, high eBE shoulder ($6s$ electrons) decreases with cluster size. This corresponds to the band gap of the neutral $(\text{Hg})_n$ cluster.

Figure 3.1b. Photoelectron spectra measured using a tunable UV nanosecond laser, showing the $(\text{Hg})_n^-$ band gap (BG) and the wavelength-dependent appearance of a new feature due to delayed Auger emission, adapted from Busani, et al.²² The e^-h^+ pair could potentially relax much further (triangles) than the signal actually extends, indicating that there is some fast Auger emission that inhibits this process

straightforward. Moreover, in the cluster anions, the excess electron resides at the bottom of the p -band. Thus, as shown by Cheshnovsky and co-workers, photoelectron spectroscopy of $(\text{Hg})_n^-$ anions at photon energies high enough to detach electrons from both the p - and s - bands can directly yield the BG as a function of cluster size.²¹⁻²³ Characteristic photoelectron spectra are shown in Figure 3.1a. Basic processes yielding these features are shown schematically on the left part of Figure 3.2. In this case, direct UV detachment from the p - and s -bands (corresponding to Features B and C) yields the BG in the photoelectron spectrum. Extrapolation of extracted BG energies indicates that the transition to metallic bonding (i.e. $\text{BG} \sim 0$) occurs around $n = 400 \pm 30$ Hg atoms.

An interesting effect in the photoelectron spectra of $(\text{Hg})_n^-$ anions is shown in Figure 3.1b, where photoelectron spectra for Hg_{12}^- are shown as a function of photon energy. In addition to the direct detachment features B and C, an additional feature (E) appears at slightly higher electron binding energies than feature B at selected photon energies. This results from resonant excitation of an electron from the s -band to the p -band, creating an electron-hole (e^-h^+) pair in the cluster. This e^-h^+ pair can decay by an Auger process, in which recombination releases enough energy to eject the excess electron originally lying at the bottom of the p -band (process E in Figure 3.2). Because these electrons appear at lower electron kinetic energies than the direct detachment feature B, some relaxation of the nascent e^-h^+ pair must occur prior to Auger emission.

These observations raise questions about the rate of this Auger process and the nature of the relaxation prior to electron emission. We address these questions here using TRPEI. In these experiments, we use one femtosecond laser pulse to excite an electron within the cluster to a higher electronic state and then a second such pulse to detach the electron after a variable time-

delay. We have monitored the dynamics following two types of excitation: “intra-band” ($6p \rightarrow 6p^*$) and “inter-band” ($6s^{2n}6p^1 \rightarrow 6s^{2n-1}6p^16p^*$) excitation.

3.2 Experimental Setup

The experimental setup for TRPEI has been described in detail elsewhere²⁴; a brief summary is given here. Mercury clusters are produced via a seeded supersonic expansion of argon and Hg vapor (over 230 °C liquid Hg) into a vacuum chamber using a pulsed solenoid valve²⁵ and ionized with a pulsed ring electrode. Anions are then injected into a Wiley-McLaren²⁶ type time-of-flight (TOF) mass spectrometer. The cluster size of interest is isolated using a pulsed electrostatic switch. The size-selected ion packet is then crossed with femtosecond pump and probe laser pulses. The pump pulse electronically excites the anion, and at a designated time delay the probe pulse detaches electrons that are energetically accessible. Ejected photoelectrons are collected and analyzed by velocity-map imaging (VMI)²⁷ giving both velocity and angular information. The photoelectrons are accelerated towards a stack of microchannel plates (MCPs) coupled to a phosphor screen, creating an image that is captured in real time using a CCD camera. The raw images are four-way symmetrized to account for inhomogeneities in the detector, and then inverted using the BASEX transformation²⁸ to recover the three-dimensional photoelectron distribution. Angular integration yields the speed distribution of the electrons, from which we extract either the electron kinetic energy (eKE) or binding energy (eBE) distributions reported here ($eBE = h\nu_{probe} - eKE$).

Laser pulses in these experiments are produced with a commercial Ti:sapphire femtosecond oscillator, amplified through regenerative chirped-pulse amplification (Clark-MXR NJA-5 and CPA-1000) to yield ~100 fs pulses with 1 mJ pulse energy at a fundamental wavelength of ~800 nm/1.55 eV. Second and third harmonics of this wavelength at 400 nm/3.10 eV, and 266 nm/4.65 eV, respectively, are generated in nonlinear BBO crystals, with typical pulse energies of 100 μJ/pulse. Infrared pulses at 1.0 eV are generated using an optical parametric amplifier (TOPAS 4-800, Light-Conversion, Ltd.), resulting in ~1 μJ/pulse. The time-resolution, given by the cross-correlation of the pump and probe laser pulses, is ~150 fs.

In the intra-band experiments,^{6,7} a pump pulse at either 1.55 or 1.0 eV is used to excite an electron from the bottom of the p -band to a higher-lying p -state and a 3.10 eV probe pulse detaches at a prescribed time-delay. Inter-band experiments^{8,9} utilize a 4.65 eV pump/1.55 eV probe scheme, where the UV pump excites an electron from the s -band into the p -band, and the 1.55 eV probe pulse detaches electrons from the p -band.

3.3 Dynamics in Mercury Cluster Anions

3.3.1 Results

Figure 3.3 shows representative photoelectron images and associated spectra for an *intra-band* excitation experiment of Hg_{15}^- at a pump energy of 1.55 eV⁶. Peak F at ~2.6 eV at the zero-of-time delay (t_0) in the progression results from detachment of the initially prepared excited state. At later time delays, the peak shifts to lower eKE until it almost coincides with the detachment of ground state electrons at the bottom of the p -band (Feature A), at which point the dynamics are complete. For the cluster size range studied here ($n = 11-16, 18$), these dynamics

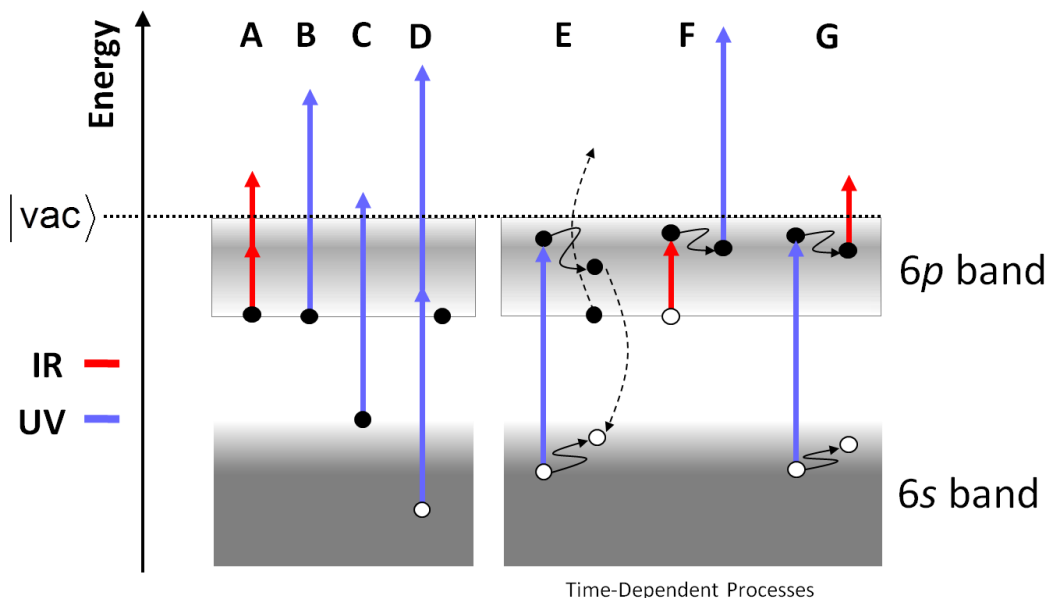


Figure 3.2. Schematic of possible photoinduced electronic processes in $(\text{Hg})_n^-$ for the experiments described in the text. Processes A-D show no time dependence beyond cross-correlation limited depletion effects. Process E describes Auger emission, which is detectable only after some relaxation of the excited electron or hole (or both); Process F is the intraband excitation and relaxation prior to detachment; and Process G describes the transient interband population. Red denotes IR wavelengths, Blue denotes UV wavelengths. See text for exact combinations used in each experiment.

occur on a timescale of $\sim 10\text{-}40$ ps. Because there are no other mobile charge carriers present, electronic relaxation can only occur via sequential radiationless transitions through the p -band. Analogous experiments using 1.0 eV pump photons⁷ were conducted in similarly sized clusters ($n = 7\text{-}13, 15, 18$) and the resulting relaxation rates of $\sim 4\text{-}9$ ps were observed to be faster, on average, by a factor of 3 to 4.

A second set of experiments was performed to investigate the dynamics following *interband* excitation, pumping with 4.65 eV and probing with 1.55 eV. Figure 3.4 shows time-resolved photoelectron spectra for Hg_{19}^- over a 3 ps delay range. The integrated intensity of each feature is plotted as a false-color map over its respective energy range as a function of time-delay. Features A, B and F in Figure 3.4 show only trivial depletion-related dynamics. These coincide to the same processes observed in the original one-color work of Cheshnovsky^{21, 22}, with the exception of feature A, which requires intensities associated with femtosecond lasers. However, the Auger feature E has time-dependence that extends well beyond the cross-correlation of the pump and probe pulses, and is therefore of interest dynamically. In addition, there is another feature (G) around 0.6 eV that only appears in the time-resolved spectra. This feature appears in an energy range consistent transient $[1+1']$ detachment of excited electrons high enough in the p -band. It disappears slightly faster than the recovery of the Auger feature E, but lasts significantly longer than the cross-correlation.

The integrated intensities of each of these features for Hg_{13}^- are displayed in Figure 3.5a. The Auger emission signal is fit to an exponential recovery and occurs over approximately 490 ± 55 fs (τ_E). Changes in intensity before t_0 are due to depletion effects from the cross-correlation of the two pulses, as at negative time-delays, the probe pulse arrives before the pump, depleting the excess electron (via channel A) prior to Auger ejection; these effects are discussed in detail in

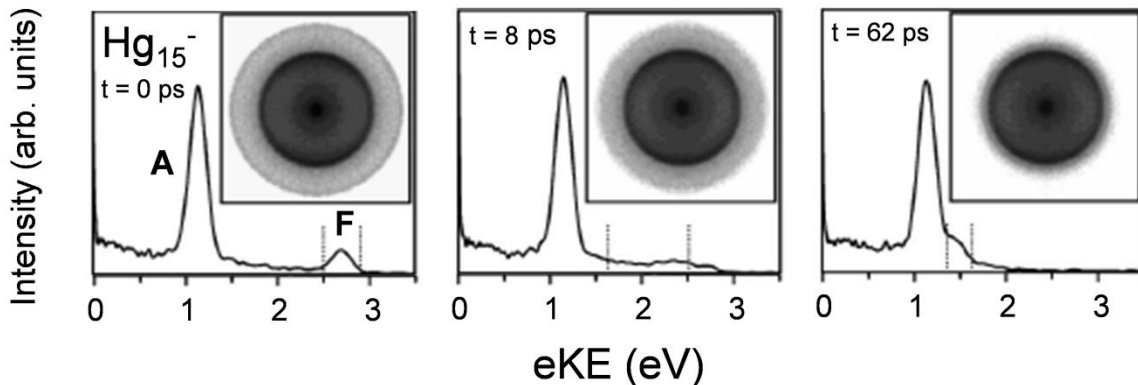


Figure 3.3. Photoelectron Images and their associated spectra for Hg_{15}^- at $\Delta t=0, 8,$ and 62 ps following intraband excitation. The direct-detachment peak from the p -band (Feature F) moves to lower eKE with increasing time-delay as the excited electron non-adiabatically cascades through the states in the band⁶.

our previous work.⁸ The transient p -state population must first be created by the pump pulse before being detached by the probe, thus the population is fit to a convolution of an exponential decay with a Gaussian with a width equal to the cross-correlation time. The recovered time constant is 400 ± 55 fs (τ_G). Both processes show complementary dynamics: they occur over similar timescales and the recovery of Auger signal is concomitant with decay of the transient population. The complementary nature of the dynamics suggests that these features are probing the same dynamical process and fully account for the transient electron population.

Timescales for the intraband and interband experiments are shown as a function of cluster size in Figure 3.6 on a logarithmic scale. Notable features are that (a) intraband relaxation is faster for excitation at 1.0 eV than at 1.55 eV, (b) relaxation subsequent to interband relaxation is typically an order of magnitude faster than intraband relaxation, and (c) the timescale for recovery of the Auger signal (feature E in Figure 3.6) rises abruptly at $n = 13$.

3.3.2 Discussion

In the case of intraband excitation, the lone electron at the bottom of the p -band is excited to a higher-lying p -state (process F in Figure 3.2) using a low energy IR pump photon. Since there are no other charge carriers present in the conduction band, the electron can only relax via the cluster equivalent of electron-phonon coupling. The overall shape of the eKE progressions suggests that the electron relaxes from one electronic state to another, cascading non-adiabatically through the p -band, a mechanism reinforced by kinetic modeling with a simple master equation approach of the observed dynamics⁶. In this size range, the electronic states within the p -band are spaced by ~ 0.1 eV¹⁰, and each non-adiabatic transition results in transfer of electronic energy into vibrational modes of the cluster.

The observed relaxation rates corresponding to the timescales reported in Figure 3.6 ($1/\tau$) generally increase with cluster size, but not in a simple monotonic fashion. In contrast, rates obtained from the described kinetic model [which does not incorporate any quantum effects and assumes equal coupling over a uniform density of states (DOS)] scale linearly⁶; each Hg atom contributes 3 unoccupied p -states, so the DOS (and thus the rate) should increase linearly with

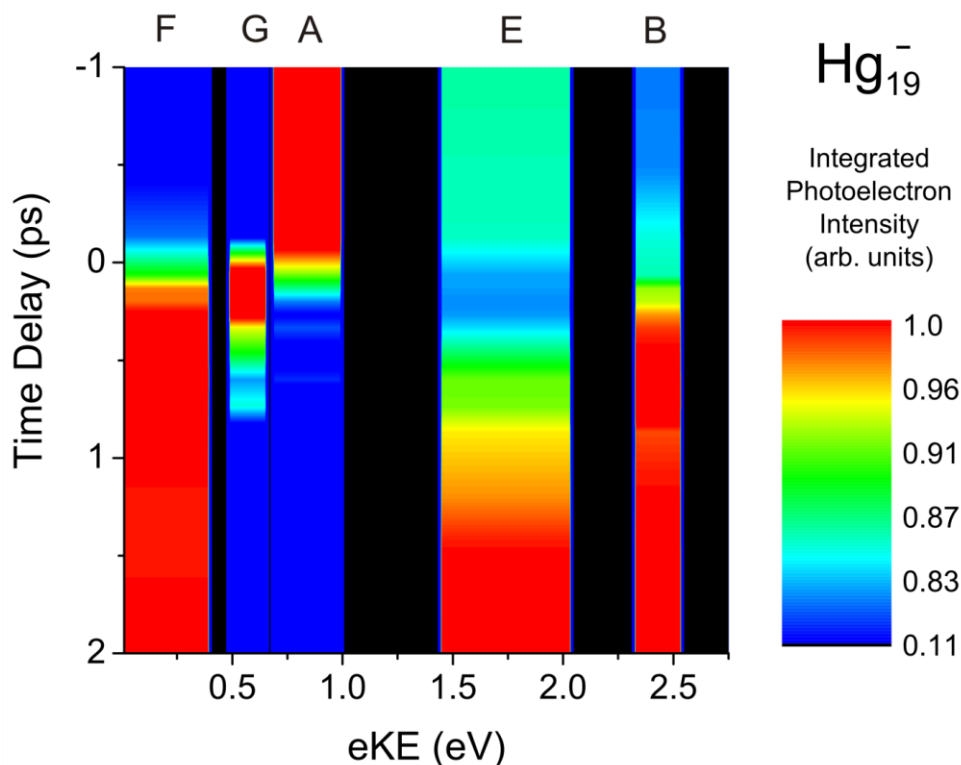


Figure 3.4. Time-resolved photoelectron spectra following interband excitation of Hg_{19}^- . Each of the features is labeled according to the processes presented in Figure 3.2. Feature E is the Auger tail described in the text and seen in previous one-color studies, seen here to evolve in time. Feature G at ~ 0.6 eV belongs to the transient interband electron population.

cluster size. Quantum and surface effects inherent to the molecularity and high fraction of surface atoms in this size range thus still have a strong influence on the relaxation rate. The somewhat faster relaxation at 1.0 eV is rather surprising, since one generally expects more rapid relaxation for higher excitation energies, since more relaxation pathways are accessible.

A possible explanation for faster relaxation is that the electronic DOS is not uniform across the p -band, an idea that is supported by calculations¹⁰ of neutral clusters. A higher DOS closer to the bottom of the p -band, for example, would require less energy being transferred into cluster vibrational modes for each radiationless transition, thereby increasing the relaxation rate. However, more detailed theory is needed to confirm this hypothesis.

From Figure 3.6, it can easily be seen that the recovery of the Auger (E) and the decay time of the $[1+1']$ features (G) in the interband excitation experiments are significantly faster than the intraband relaxation at either pump energy. Both the Auger and transient timescales show an overall increase with cluster size, though there is also a high degree of variation over this small size range, again highlighting the molecular nature of these clusters. The faster dynamics subsequent to interband excitation reflect the presence of multiple charge carriers, i.e. two electrons and one hole, and the accompanying larger variety of decay channels accessible to the excited state created by the pump pulse. While the excited p -electron can decay by electronic \rightarrow vibrational energy transfer in both cases, the Auger decay pathway is accessible only upon interband excitation. This situation is similar to that in quantum dots, in which excited states with multiple excitons decay much more rapidly than states with a single e^-h^+ pair^{29,30}.

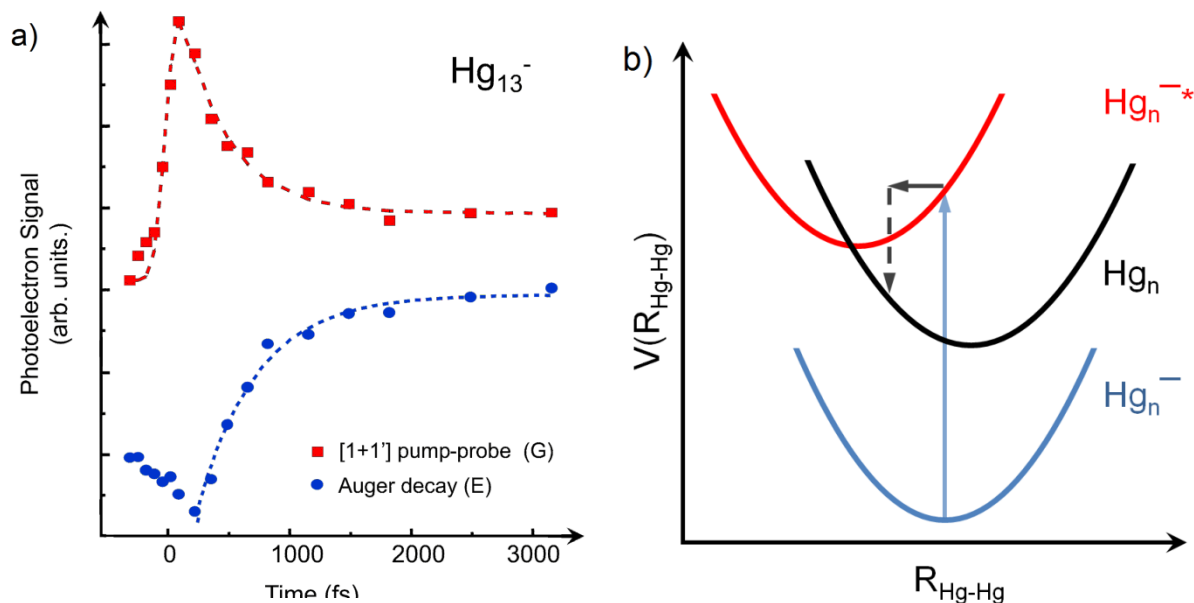


Figure 3.5a. Integrated intensities of the Auger feature (E, blue) and the transient interband electron intensity (G, red) for $(\text{Hg})_{13}^-$. Feature E is fit to an exponential recovery with a time constant of 490 ± 55 fs; Feature G is fit to a convolution of a Gaussian (for the laser profile) and an exponential decay, with an extracted time constant of 400 ± 55 fs.

Figure 3.5b. Schematic potential energy surfaces showing the hole-contracted excited state. The reduction in nearest-neighbor bond distances allows the electron to dissipate its energy via vibrational relaxation to the lowest-energy geometry.

The marked jump in τ_E towards longer lifetimes at $n = 13$ coincides with various other observations in both experiments and calculations on neutral and charged Hg clusters which indicate a transition from vdW to covalent bonding.¹⁰⁻¹⁹ It should be noted that the $n = 13$ geometry is predicted to be a Hg atom encapsulated by an icosahedral shell¹⁴. This combined with the reduced surface area of such a symmetric structure and the heightened number of nearest neighbors would lead to an increase in sharing of the electrons and mixing/hybridization of the s - and p -orbitals. Also, the high symmetry of this shape will facilitate delocalization of the excess charge, which could explain why the transient times are less sensitive to the size change at $n \geq 13$.

As mentioned above, Auger emission occurs with lower eKE than the direct detachment feature, which means the e^-h^+ pair must relax before recombining. This relaxation must be due to something other than the stepwise non-adiabatic transitions inferred from the intraband experiments, as the Auger timescale is more than an order of magnitude faster than the timescales in Figure 3.6. Calculations¹⁵ using the Diatomics-in-Molecules (DIM) approach suggest that in neutral Hg clusters the creation of an e^-h^+ pair leads to a contraction of the nearest-neighbor bond lengths. This hole-induced contraction likely occurs in the anionic clusters as well. Such a process would have substantial effects on the relaxation dynamics, as the s -electron is now excited to a highly perturbed electronic state, far from the equilibrium bond distance at the minimum of the potential energy surface. The excited cluster can then undergo vibrational relaxation toward the equilibrium geometry, leading to dissipation along the nuclear coordinates such that that energy is no longer available to the electron. The potential energy surfaces involved in this process are schematized in Figure 3.5b.

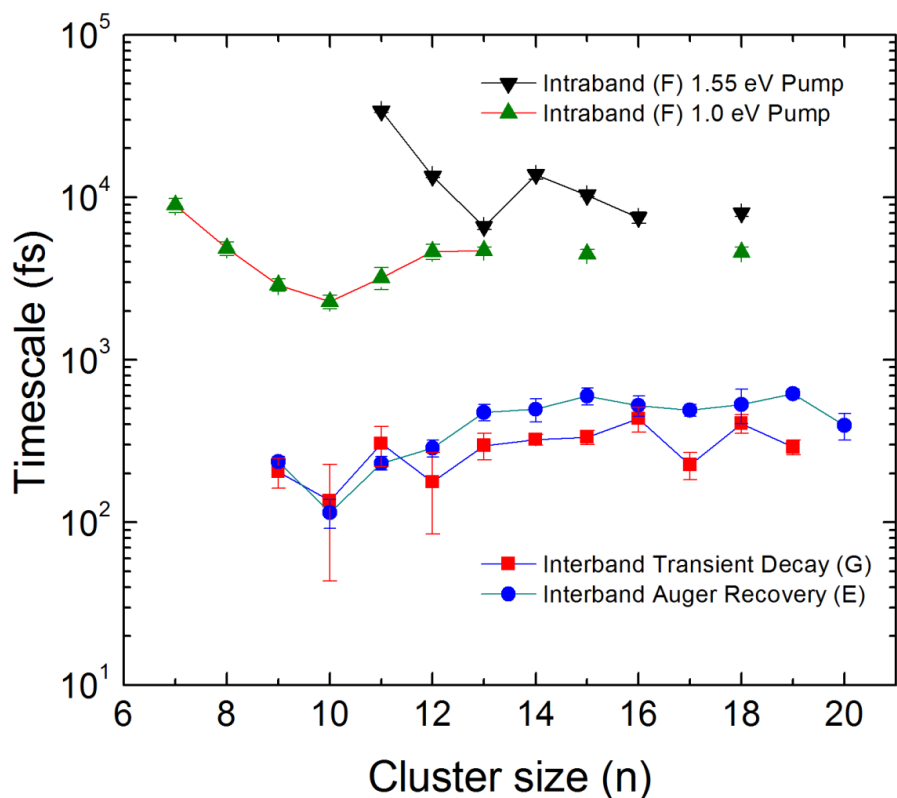


Figure 3.6. Timescales for non-adiabatic relaxation through the p -band following intraband excitation (1.55 eV in Black and 1.0 eV in Green) as a function of cluster size; this relaxation occurs on a ~ 10 ps timescale. Auger emission timescales (Feature E in Blue) and Transient interband electron decay timescales (Feature G in Red) as a function of cluster size, on a femtosecond timescale

Moreover, because there are two electrons in the p -band and one hole in the s -band in the interband experiments, the excited electron can relax by multiple pathways, moving lower in energy through the manifold of anion excited states, with the energy difference being made up via inelastic electron-electron and/or electron-hole scattering. Indeed, electron-electron scattering has been invoked to explain the rapid timescales seen for ultrafast electron relaxation in transition metal clusters as well.³¹⁻³³ The manifold of anion states is much denser than that belonging to those excited states where there is only one p -band electron and no hole in the s -band; relaxation along this manifold can also occur as the hole rises in energy. Through either mechanism, the emitted Auger electron has less energy available to it than before relaxation, and thus will be detected at lower kinetic energy, which must occur before the electrons are emitted. Thus the timescales extracted from each process represent upper bounds to the actual relaxation times, which, again, are an order of magnitude faster than the non-adiabatic relaxation of a single electron in the p -band seen in the intraband excitation experiments.

3.4 Outlook

Our extensive experiments have determined the timescales of various electronic relaxation processes in isolated semiconducting clusters. A single mobile electron within the conduction band will relax via interactions with the phonon bath over tens of picoseconds as it

falls through the energy levels of the conduction band. However, the presence of additional charge carriers is seen to have a dramatic effect on the decay of the electronic excitation. A change in geometry induced by a hole in the valence band and/or electron-electron scattering causes a substantial increase in the rate of energy transfer, into the femtosecond regime.

At present, however, it is unclear whether it is the electron or the hole, or both in conjunction that are responsible for the relaxation in $(\text{Hg})_n^-$. The analogous process creating the e^-h^+ pair from the d -band could elucidate the role of the hole in the overall relaxation. The density of p -states would remain the same but the density of hole states would presumably be much larger and thus the hole could relax much faster, increasing the rate of Auger decay.

Investigating both the intra- and interband excitation studies over a broader size range is the next natural step, as the clusters become more similar to their quantum dot analogs and structural differences between anions and neutrals should be reduced. Figure 3.6 seems to suggest convergence toward a large-size limit for the timescales of the processes involved, at least over the size-range of the vdW-to-covalent transition. At much larger cluster sizes, the effect of the insulator-to-metal transition on the relaxation rates would also be of considerable interest. Experiments to probe these effects are planned in our laboratory.

Varying the pump energy should also yield interesting results. In addition to being able to access the d -band electrons in larger clusters, pumping with higher frequency light could generate multiple excitons through charge-carrier multiplication [2-3]. The effect on the observable relaxation rates would yield more insight into the nature of the relaxation and provide a clear parallel to studies on larger quantum dots.

Central to all of these experiments is a detailed knowledge of the band structure. An explicit mapping of the DOS with higher energy resolution over the cluster size regime studied would aid in the interpretation of these results, especially for the pump energy-dependent intraband relaxation rates. This information could be obtained through a combination of experiment and improved electronic structure calculations. In addition, experiments that probe the geometric evolution of neutral and charged mercury clusters with size would be exceedingly valuable in understanding the trends seen here. Electron diffraction experiments on size-selected clusters³⁴ may be very useful in addressing this issue.

3.5 References

- 1 W. U. Huynh, J. J. Dittmer, and A. P. Alivisatos, *Science* **295** (5564), 2425 (2002).
- 2 R. D. Schaller, V. M. Agranovich, and V. I. Klimov, *Nature Phys.* **1**, 189 (2005).
- 3 R. J. Ellingson *et al.*, *Nano Lett.* **5** (5), 865 (2005).
- 4 P. Guyot-Sionnest, B. Wehrenberg, and D. Yu, *J. Chem. Phys.* **123** (7), 074709 (2005).
- 5 A. Pandey, and P. Guyot-Sionnest, *J. Chem. Phys.* **127**, 111104 (2007).
- 6 J. R. R. Verlet *et al.*, *J. Chem. Phys.* **121** (20), 10015 (2004).
- 7 A. E. Bragg *et al.*, *J. Chem. Phys.* **122**, 054314 (2005).
- 8 G. B. Griffin *et al.*, *Chem. Phys.* **350**, 69 (2008).
- 9 G. B. Griffin *et al.*, *J. Chem. Phys.* **130** (23), 231103 (2009).
- 10 G. M. Pastor, and K. H. Bennemann, in *Clusters of Atoms and Molecules*, edited by H. Haberland (Springer-Verlag, Berlin, 1994), pp. 86.
- 11 K. Rademann *et al.*, *Phys. Rev. Lett.* **59** (20), 2319 (1987).
- 12 H. Haberland *et al.*, *J. Chem. Soc. Faraday Trans.* **86** (13), 2473 (1990).

- 13 C. Brechignac *et al.*, Phys. Rev. Lett. **60** (4), 275 (1988).
- 14 G. E. Moyano *et al.*, Phys. Rev. Lett. **89** (10) (2002).
- 15 H. Kitamura, Eur. Phys. J. D **43**, 33 (2007).
- 16 H. Kitamura, Chem. Phys. Lett. **425** (4-6), 205 (2006).
- 17 N. Gaston, P. Schwerdtfeger, and B. v. Issendorf, Phys. Rev. A **74**, 043203 (2006).
- 18 H. Haberland *et al.*, Phys. Rev. Lett. **69** (22), 3212 (1992).
- 19 B. von Issendorf, and O. Cheshnovsky, Annu. Rev. Phys. Chem. **56**, 549 (2005).
- 20 Y. Wang, H. Flad, and M. Dolg, Int. J. Mass Spectrom. **201**, 197 (2000).
- 21 R. Busani, M. Folkers, and O. Cheshnovsky, Phys. Rev. Lett. **81** (8), 3836 (1998).
- 22 R. Busani *et al.*, Phys. Rev. Lett. **90** (8), 083401 (2003).
- 23 R. Busani, and O. Cheshnovsky, J. Phys. Chem. C **111** (48), 17725 (2007).
- 24 A. V. Davis *et al.*, J. Chem. Phys. **118** (3), 999 (2003).
- 25 U. Even *et al.*, J. Chem. Phys. **112** (18), 8068 (2000).
- 26 W. C. Wiley, and I. H. McLaren, Rev. Sci. Instrum. **26** (12), 1150 (1955).
- 27 A. T. J. B. Eppink, and D. H. Parker, Rev. Sci. Instrum. **68** (9), 3477 (1997).
- 28 V. Dribinski *et al.*, Rev. Sci. Instrum. **73** (7), 2634 (2002).
- 29 A. L. Efros, V. A. Kharchenko, and M. Rosen, Solid State Commun. **93** (4), 281 (1995).
- 30 V. I. Klimov *et al.*, Science **287** (5455), 1011 (2000).
- 31 E. Knoesel, A. Hotzel, and M. Wolf, Phys. Rev. B **57** (20), 12812 (1998).
- 32 N. Pontius, M. Neeb, and W. Eberhardt, Phys. Rev. B **67**, 035425 (2003).
- 33 N. Pontius *et al.*, Phys. Rev. Lett. **84** (6), 1132 (2000).
- 34 E. Oger *et al.*, J. Chem. Phys. **130**, 124305 (2009).

Chapter 4. Time-Resolved Dynamics in Acetonitrile Cluster Anions $(\text{CH}_3\text{CN})_n^-$ ($20 \leq n \leq 50$)

[Reprinted with permission from "Time-resolved dynamics in acetonitrile clusters anions $(\text{CH}_3\text{CN})_n^-$ " R. M. Young, G. B. Griffin, A. Kammrath, O. T. Ehrler, and D. M. Neumark, Chem. Phys. Lett. 485, 59 (2010)]

Excited state dynamics of acetonitrile cluster anions, $(\text{CH}_3\text{CN})_n^-$, were investigated using time-resolved photoelectron imaging (TRPEI) for $20 \leq n \leq 50$. The clusters were excited and then photodetached with femtosecond pump and probe pulses at 790 and 395 nm, respectively. Excited state lifetimes varied between 200 fs and 270 fs over this size range, showing no obvious size trend. Experimental evidence indicates that we are exciting "isomer II" clusters in which the excess electron is valence-bound to a solvated anionic dimer core. The absence of an obvious size-dependence in the excited state lifetimes is consistent with such a structure.

4.1 Introduction

Solvated electrons are important species in chemistry, biology, and physics. A solvated electron is a purely quantum mechanical solute and is therefore of fundamental interest in condensed phase chemistry. From a more practical perspective, solvated electrons are formed by ionizing radiation and are thus key players in radiation chemistry and biology.^{1, 2} While much interest has focused on hydrated electrons³, i.e. electrons in aqueous solution, solvated electrons have been observed in numerous inorganic and organic solvents. The properties of solvated electrons depend significantly on the solvent in which they are formed, and the nature of the electron-solvent interaction responsible for these properties has been the focus of numerous experimental and theoretical studies. Many aspects of the electron-solvent interaction are controversial. Even in water, the most thoroughly studied solvent, unresolved questions remain concerning structural issues centered on whether the electron exists in a solvent cavity⁴ or in a chemically bound form⁵, as well as dynamical issues related to the mechanism by which delocalized and/or electronically excited electrons relax to their ground state.⁶

These considerations have motivated studies of gas phase clusters of the type $(\text{S})_n^-$, in which an excess electron is bound to a known number of solvent species S, with the goal of applying the powerful experimental tools developed for gas phase spectroscopy and dynamics to these clusters and then extrapolating the results to the infinite size limit to shed light on the properties of electrons in bulk solvents.⁷ Several laboratories have reported one-photon⁸⁻¹¹ and time-resolved¹²⁻¹⁴ photoelectron (PE) spectra of $(\text{H}_2\text{O})_n^-$ clusters, while we have carried out both types of studies on $(\text{CH}_3\text{OH})_n^-$ clusters.^{15, 16} This line of inquiry is continued here, where we report time-resolved PE spectra for $(\text{CH}_3\text{CN})_n^-$ clusters.

Electrons dissolved in bulk CH_3CN show two broad absorption bands, one in the near-infrared, peaking from 1200-1400 nm, and the other in the visible around 500 nm.¹⁷ Recent studies by Shkrob¹⁸ and Kohler¹⁹ have attributed the near-IR band to a solvated electron located within a solvent cavity, and the visible band to an electron localized on a monomer or (more likely) a dimer of CH_3CN . The dimer unit, $(\text{CH}_3\text{CN})_2^-$, is a valence-bound species in which the excess electron is distributed over the π^* orbitals of two bent, antiparallel solvent molecules.^{19, 20}

Evidence for two electron solvation motifs in acetonitrile also comes from PE spectra of $(\text{CH}_3\text{CN})_n^-$ ($n = 10-100$) clusters measured by Kaya and co-workers.²¹ These studies show the existence of two cluster isomers: a weakly bound isomer (isomer I) with vertical detachment energies (VDE's) ranging from 0.4-1.0 eV, and a more strongly bound isomer (isomer II) with VDE's from 2.2-2.8 eV. Isomer II dominates starting at $n = 13$, but both are seen out to $n = 100$. Based on comparison with the bulk results, isomer II was attributed to clusters with a valence-bound, $(\text{CH}_3\text{CN})_2^-$ core, while the more weakly bound isomer I was assigned to an electron within a solvent cavity. Recent electronic structure calculations^{20, 22} on small $(\text{CH}_3\text{CN})_n^-$ clusters support the existence of the two isomers along these lines. The calculations by Takayanagi²² are particularly relevant as they show that the $(\text{CH}_3\text{CN})_2^-$ anion core, which is unstable in the gas phase with respect to autodetachment, becomes thermodynamically stable with the addition of only a few solvent molecules.

Time-resolved experiments on electrons in liquid acetonitrile were performed by Kohler,¹⁹ who excited the charge-transfer-to-solvent (CTTS) band of the iodide anion in CH_3CN at 265 nm and monitored the resulting electron solvation dynamics with transient absorption. The overall dynamics were described by three time-constants, 1.9 ps, 29 ps, and 257 ps, attributed respectively to initial solvation dynamics, geminate recombination of the free electron with the I atom, and scavenging of the electron by CH_3CN monomer or dimer. The cluster analog to this experiment was performed in our group,^{23, 24} in which we measured time-resolved PE spectra of $\text{I}^-(\text{CH}_3\text{CN})_n$ clusters subsequent to ejection of the electron from the iodide to the surrounding solvent network. The VDE dropped abruptly within 300-400 fs, followed by a bi-exponential increase that was complete by ~ 10 ps. Previous theoretical work²⁵ found that the iodide is internally solvated, and that photodetachment results in formation of a diffuse electron cloud in a confined cavity. We interpreted the initial drop in VDE as a combination of expansion of the cavity and localization of the excess electron on one or two solvent molecules. The subsequent increase in VDE was attributed to a combination of the I atom leaving the cavity and rearrangement of the acetonitrile molecules to solvate the electron.

In this study, we use time-resolved photoelectron imaging (TRPEI)²⁶ to investigate the relaxation dynamics of electronically excited $(\text{CH}_3\text{CN})_n^-$ isomer II clusters in the size range $n = 20-50$. These experiments complement our previous work on $\text{I}^-(\text{CH}_3\text{CN})_n$ clusters, in the same way that our TRPEI studies on $\text{I}^-(\text{H}_2\text{O})_n$ and $(\text{H}_2\text{O})_n^-$ clusters complemented one another.²⁷ There is reasonably strong evidence that in CH_3CN clusters, both the iodide and excess electron are internally solvated.^{20, 22, 25, 28, 29} In contrast, small water clusters ($n \leq 25$) favor surface solvation for both species,^{30, 31} while the nature of electron solvation in larger clusters is being actively investigated.^{11, 32, 33} Hence, the experiments presented here provide an opportunity to investigate the dynamics of internally solvated electrons and to compare the results to other solvent clusters where the solvation motif is less settled. We find that the excited state of isomer II after 790 nm excitation has a lifetime of 200-270 fs for the size range studied here with no obvious dependence on cluster size. The absence of size dependence is consistent with the assignment of isomer II as a having a valence-bound anion core solvated by the remaining solvent molecules.

4.2 Experimental

Details of our experiment setup have been presented previously,³⁴ only a brief summary will be given here. A seeded supersonic expansion was created by passing argon gas at 35 psig

over room temperature liquid acetonitrile. The resulting gas mixture was sent through a solenoid valve³⁵ pulsed at 87 Hz into the vacuum chamber. Anion clusters were formed by secondary electron attachment to neutral $(\text{CH}_3\text{CN})_n$ clusters³⁶ from a pulsed ring ionizer attached to the valve. The resulting anions were extracted perpendicularly into a Wiley-McLaren time-of-flight mass spectrometer³⁷ where ions of the desired mass were transmitted by an electrostatic switch pulsed at the appropriate time. This ion packet was interrogated by femtosecond pump and probe laser pulses that induced electronic excitation and photodetachment, respectively. The detached photoelectrons were accelerated by velocity-map imaging³⁸ onto microchannel plates coupled to a phosphor screen. A CCD camera converted this to a digital image that was four-way symmetrized and inverted using the BASEX method³⁹ to recover the photoelectron velocity distribution.

Photoelectron kinetic energy spectra were obtained via angular integration. The images also yielded photoelectron angular distributions (PADs) as a function of electron kinetic energy (eKE), which, for one-photon processes, are given by⁴⁰

$$I(\theta, eKE; n) = \frac{\sigma_{total}}{4\pi} [1 + \beta_2(eKE; n)P_2(\cos \theta)], \quad (4.1)$$

where θ is the angle between the emitted electron and the laser polarization, n is the cluster size, σ_{total} is the total photodetachment cross section, and β_2 is the anisotropy parameter for the feature of interest.

The pump and probe laser pulses were created by a commercial Ti:sapphire femtosecond oscillator and amplified by chirped-pulse multipass amplification (KM Labs Griffin oscillator/Dragon amplifier), yielding pulses at a center wavelength of 790 nm (1.57 eV) with a pulse duration of 35 fs. Some of this light was directed through a BBO crystal to generate probe pulses at the second harmonic wavelength, 395 nm (3.14 eV), yielding 120 μJ pulses with minimal temporal broadening. The remaining fundamental was attenuated to $< 20 \mu\text{J/pulse}$ and used as the pump. The cross-correlation time within the vacuum chamber was ~ 70 fs FWHM as measured separately by above-threshold detachment of negative ions.

4.3 Results and Analysis

Reconstructed single photon photoelectron images and their associated normalized kinetic energy spectra are shown in Figure 4.1 for $(\text{CH}_3\text{CN})_{40}^-$. Kinetic energy spectra are shown in Figure 4.1a for photon energies $h\nu = 1.57$ eV (red) and $h\nu = 3.14$ eV (blue). The red curve in Fig. 4.1a is multiplied by a factor of 20. Figures 4.1b and 4.1c show the associated photoelectron Newton spheres for the red and blue curves, respectively.

For photodetachment at 1.57 eV, peak B, centered at an eKE of 1.0 eV, is from direct detachment of isomer I. Peak C, seen from photodetachment at 3.14 eV, is from direct detachment of isomer II; these features yield VDE's of 0.6 and 2.6 eV for isomers I and II, respectively. At 3.14 eV, virtually no signal is seen from isomer I for this cluster size. The very slow peak A is attributed to vibrational autodetachment of isomer II excited at 1.57 eV, since this

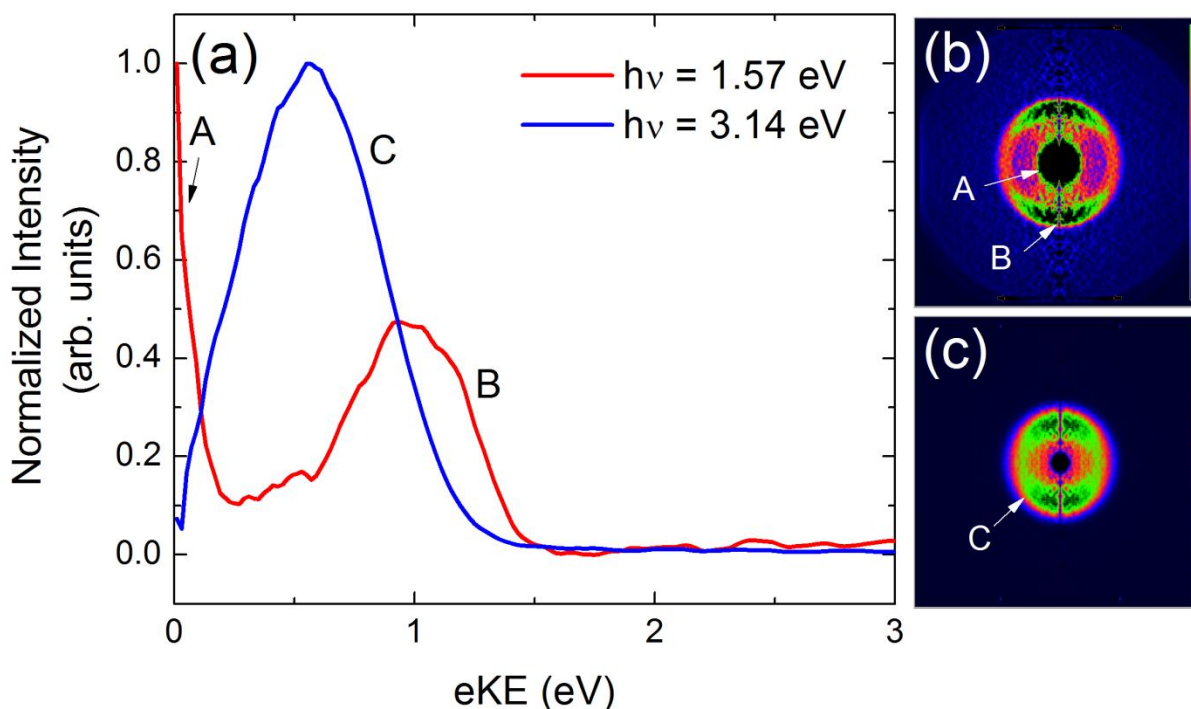


Figure 4.1a. One-photon photoelectron spectra of $(\text{CH}_3\text{CN})_{40}^-$ taken at $h\nu = 1.57$ eV (red) and 3.14 eV (blue). The red spectrum is scaled up by a factor of 20. Feature A is excited state autodetachment from isomer II and feature B is direct detachment of isomer I. Feature C, at 3.14 eV, is from direct detachment of isomer II. BASEX reconstructed photoelectron Newton spheres are shown at (4.1b) $h\nu = 1.57$ eV and (4.1c) $h\nu = 3.14$ eV, with the intensity of image (4.1b) scaled up by a factor of 5 and false color mapped. Note: black on the image intensity if off the scale. See text for details and extracted anisotropy parameters.

photon energy lies well above the VDE of isomer I. While the energetics and relative isomer intensities are consistent with the PE spectra measured by Kaya at 3.50 eV²¹, the slow autodetachment feature was not seen previously; its observation here results from using photoelectron imaging for detection, which is considerably more sensitive to slow electrons than time-of-flight photoelectron spectroscopy. The photoelectron image for feature B from isomer I shows significant anisotropy in the PAD. We find that $\beta_B = 0.60 \pm 0.07$ for the outer feature. Isomer II has a more symmetric photoelectron image, with feature C having $\beta_C = 0.35 \pm 0.09$.

Time-resolved photoelectron images of $(\text{CH}_3\text{CN})_n^-$ were recorded for $20 \leq n \leq 50$, with pump and probe photon energies of 1.57 and 3.14 eV, respectively. Representative photoelectron spectra for $n = 20$ and $n = 39$ extracted from these images are displayed in Figures 4.2 and 4.3, respectively, with pump-probe delay increasing nonlinearly from back to front and feature C scaled down by a factor of 8. These spectra show a weak, short-lived transient between 2.4 - 3.4 eV, feature D, attributed to excited state dynamics induced by the pump pulse.

The intensity of the excited state feature D is shown for $n = 39$ in Figure 4.4, integrated from 2.45 - 3.20 eV. The fitting procedure involves convoluting an exponential decay with lifetime τ beginning at t_0 ,

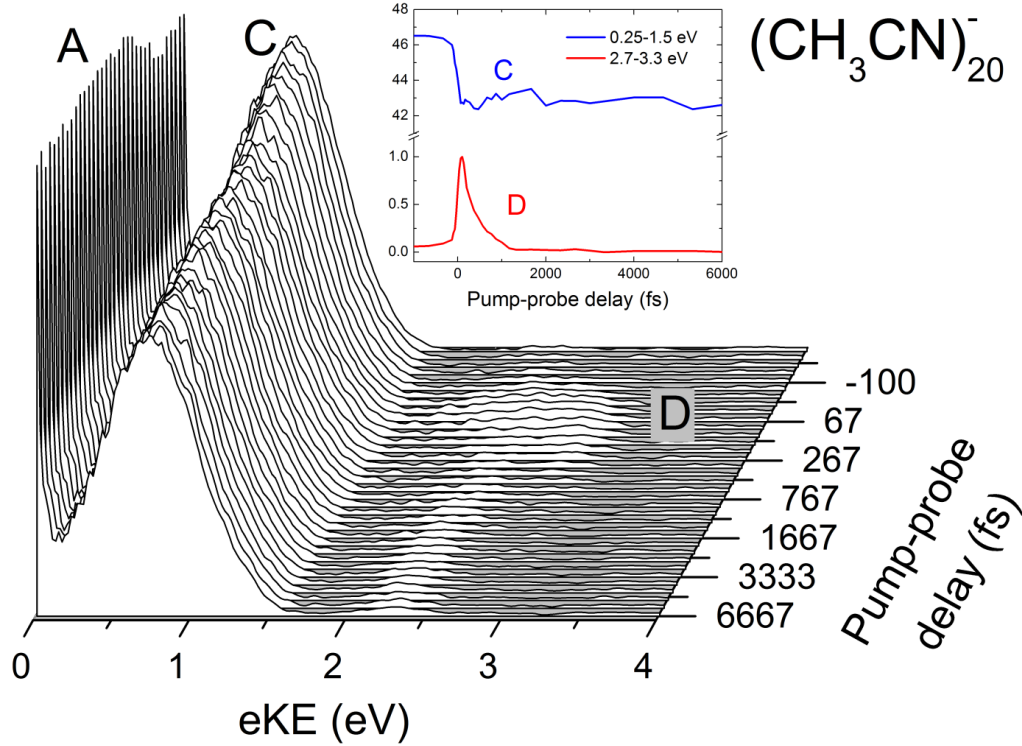


Figure 4.2. Time-resolved photoelectron spectra displayed as a waterfall plot for $(\text{CH}_3\text{CN})_{20}^-$ with $h\nu_{\text{pump}} = 1.57$ eV and $h\nu_{\text{probe}} = 3.14$ eV, with pump-probe delay increasing from front to back. Inset: Integrated intensities of features C and D.

$$P(t) = \begin{cases} I_0 & t < t_0 \\ I_0 + A_1 e^{-t/\tau} & t \geq t_0 \end{cases}, \quad (4.2)$$

with a Gaussian instrument response function of width σ (given by $\text{FWHM} = 2\sigma\sqrt{2\ln 2}$), yielding^{41, 42}

$$I(t) = I_0 + A_2 \left\{ 1 - \text{erf} \left(\frac{\sigma}{2\tau} - \frac{t-t_0}{\sigma} \right) \right\} e^{\left[\left(\frac{\sigma}{2\tau} \right)^2 - \frac{t-t_0}{\tau} \right]}, \quad (4.3)$$

where the A's are scaling factors and I_0 is an offset. Integration is performed on the higher eKE side of feature D in order to minimize contamination from isomer I, from which instrument-limited above-threshold detachment can occur and obscure the dynamics. The extracted decay constant for the excited state in $n = 39$ is $\tau = 226 \pm 19$ fs. Excited state lifetimes as a function of cluster size are shown in Figure 4.5; each point is the average of multiple experiments on the same cluster size, with the error bars representing the standard deviation of the mean, or in the case of only a single data set, the standard error associated with the fit. The lifetime of the excited state is relatively constant over the cluster size range, varying from 208-266 fs, with no clear size-dependent trend.

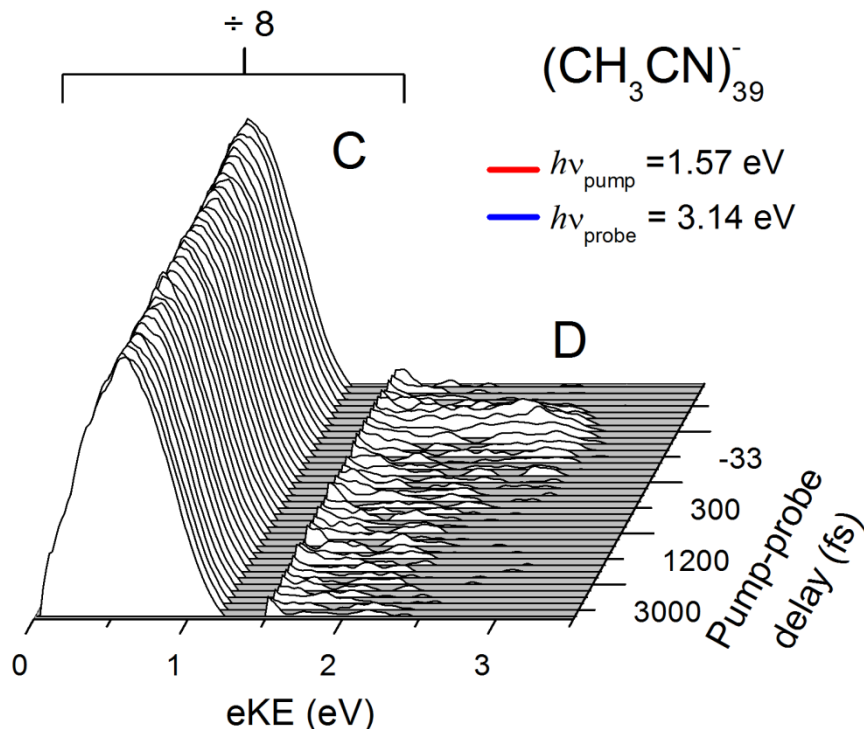


Figure 4.3. Time-resolved photoelectron spectra displayed as a waterfall plot for $(\text{CH}_3\text{CN})_{39}^-$ with $h\nu_{\text{pump}} = 1.57$ eV and $h\nu_{\text{probe}} = 3.14$ eV, with pump-probe delay increasing from front to back. The time-dependent feature D occurs at the zero of pump-probe delay, in the energy range 2.45-3.20 eV. Feature C is scaled down by a factor of 8. The autodetachment feature A is not seen as it is likely obscured by the direct detachment feature C.

Peak C, from probe-photon detachment of isomer II, exhibits a small but rapid decrease at positive pump-probe delays, displayed in the insets of Figures 4.2 and 4.4, showing that the probe pulse depletes the ground state population of isomer II. It is unclear if there is any recovery of the ground state population for larger cluster sizes; recovery has been observed for $n \geq 40$, but the signal is not reproducible in every experiment, most likely reflecting the difficulty in accurately measuring a small pump-induced depletion signal ($\sim 2\%$, see insets of Figs. 4.2 and 4.4) on top of a large background.

4.4 Discussion

The one-photon photoelectron kinetic energy spectra in Fig. 4.1 and the time-resolved photoelectron spectra can be interpreted with reference to Fig. 4.5, which shows the vertical detachment energy for isomer II of $(\text{CH}_3\text{CN})_{40}^-$. Isomer I is not shown on this diagram, because its energetics relative to isomer II are unknown. While the difference in the VDE's between the two isomers is known, vertical detachment accesses rather different neutral species in each case; the two bent CH_3CN molecules comprising the dimer anion core in isomer II represent a particularly high energy configuration for the neutral cluster, for example. The photoelectron spectrum associated with isomer II (peak C, Fig. 4.1) is superimposed on this diagram, and as such it represents the spectrum of electron binding energies given by $h\nu - \text{eKE}$. Note that this spectrum extends down to 1.57 eV, the photon energy used to generate the red spectrum in Fig.

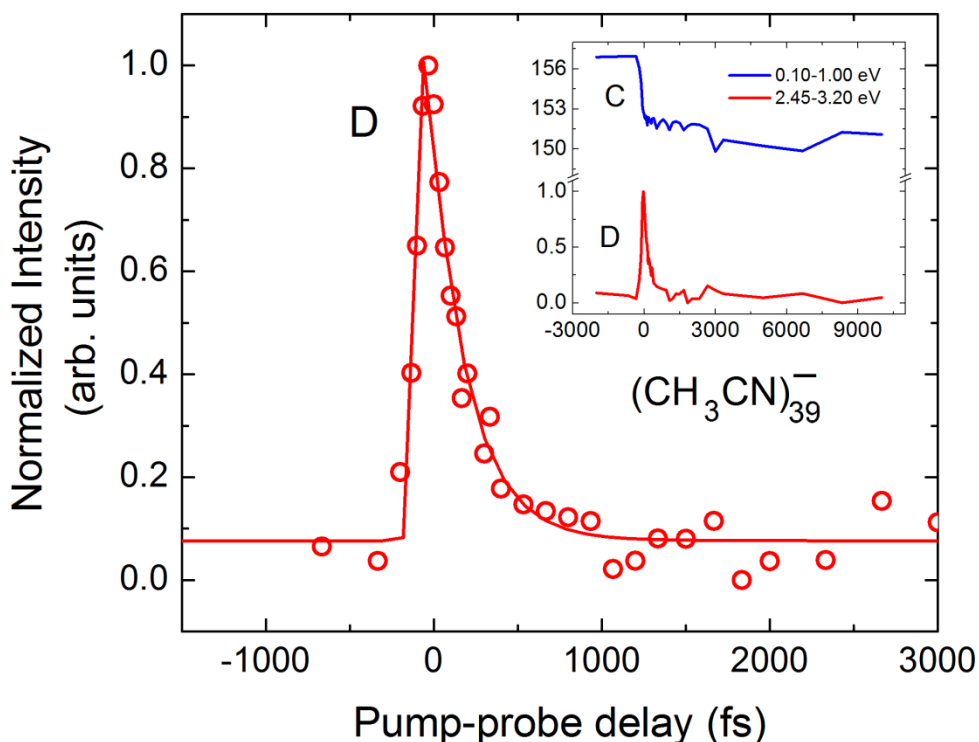


Figure 4.4. Integrated intensity for $(\text{CH}_3\text{CN})_{39}^-$ feature D upon 1.57 eV excitation. Data are integrated from 2.45-3.20 eV. The excited state reaches its maximum shortly after t_0 , and decays back to its initial value with a time constant of $\tau = 226 \pm 19$ fs. Inset: depletion of feature C, normalized to the maximum of feature D, showing no recovery out to 10 ps.

4.1. Hence, an excited state of isomer II produced at this photon energy will have sufficient energy to undergo autodetachment, producing the very slow electrons (peak A) in Fig. 4.1.

The one-photon images in Figures 4.1b and 4.1c provide additional insight into the nature of the excess electron in isomers I and II of $(\text{CH}_3\text{CN})_n^-$ clusters. The PAD's associated with detachment from the two isomers are distinctly different, with peak B from isomer I showing more anisotropy than peak C from isomer II ($\beta_C = 0.60 \pm 0.07$ vs. 0.35 ± 0.09). The PAD is sensitive to the shape of the orbital from which detachment occurs⁴³, so our results are consistent with quite different electronic wavefunctions for the excess electron in the two isomers. Moreover, the more positive value of β for isomer I suggests more s-like character for the excess electron than in isomer II, which is again consistent with the notion that the excess electron in isomer I resides in a solvent cavity as opposed to a more structured π^* orbital expected for localization on a CH_3CN dimer unit²⁰. Hence, the PAD's offer some support for previous assignments of the two isomers.

We next consider the interpretation of the transient feature D in our experiments. The pump laser wavelength of 790 nm is on the red edge of the electronic absorption band of electrons in liquid acetonitrile localized on solvent dimers.^{17, 19} Since this dimer-localized motif is calculated to lie at the core of isomer II cluster anions²², it is reasonable to assign feature D to pump-probe signal via the isomer II excited state, labeled II* in Fig. 4.6, and its decay to the lifetime of this excited state. Several specific observations from our results support this interpretation. First, the observation of autodetachment (Fig. 4.1) implies that the 790 nm pump

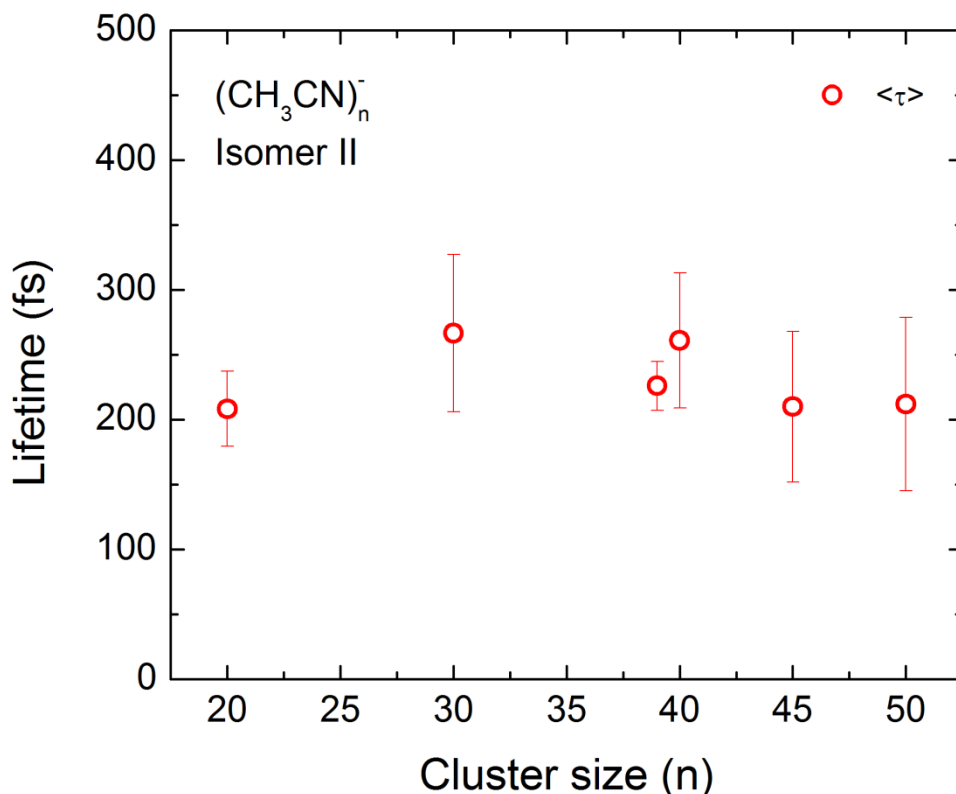


Figure 4.5. Isomer II excited state lifetime as a function of cluster size. All timescales reported lie between 200 fs and 270 fs.

pulse overlaps an electronic transition of $(\text{CH}_3\text{CN})_{40}^-$. Secondly, while the measured lifetime of feature D is quite short, ~ 200 fs over the size-range considered here, it is significantly longer than the temporal width of the laser pulses (~ 70 fs). This measurement therefore rules out feature D originating from, for example, two-color above threshold detachment of isomer I or isomer II, since either process would result in symmetric transients persisting only during the cross-correlation of the pump and probe laser pulses. Finally, the pump-induced depletion of peak C, the isomer II ground state feature, for all clusters shows that the pump pulse is exciting isomer II. This result also confirms the proposed association of the bulk 500 nm electronic transition with isomer II.²¹

The excited state lifetimes for $n = 20$ -50 shown in Fig. 4.5 all lie between 200 and 270 fs and show no obvious size dependence. This result differs from the excited state lifetimes in comparably-sized water cluster anions¹³ which, for example, drop from 400 fs for $(\text{D}_2\text{O})_{25}^-$ to 200 fs for $(\text{D}_2\text{O})_{50}^-$. Such a result is consistent with the attribution of isomer II clusters built around a valence-bound $(\text{CH}_3\text{CN})_2^-$ dimer core, whose properties are relatively insensitive to solvent molecules beyond those in direct contact with this moiety. The calculations by Takayanagi²² find that in isomer II of $(\text{CH}_3\text{CN})_8^-$, there are three solvent molecules bound to each N atom of the dimer anion core, and eight molecules on each core N atom for $(\text{CH}_3\text{CN})_{10}^-$. The first solvent shell would continue to build in this manner until it is closed, encapsulating the dimer anion. Over the size range studied here, it is reasonable to assume that the number of strong binding sites on the dimer core is saturated.

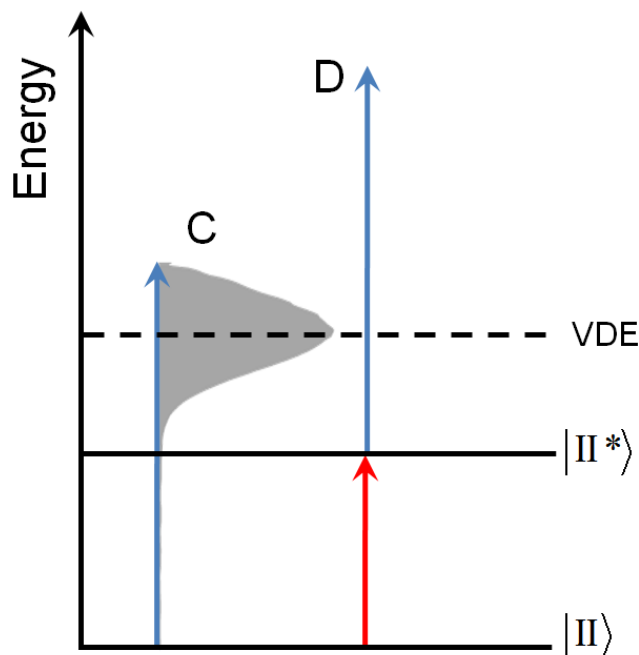


Figure 4.6. Energetics for electronic states of isomer II in $(\text{CH}_3\text{CN})_{40}^-$, with photoelectron spectrum from Fig. 4.1 at 3.14 eV superimposed. State II^* is formed by excitation at 1.57 eV. Autodetachment from this state is energetically allowed.

While our experiments yield excited state lifetimes, the relaxation pathway for the cluster excited state is less clear. In water cluster anions, the time constants for excited state decay and ground state recovery were nearly the same over a wide cluster size range,^{13,42} indicating that the excited state decayed by internal conversion to the ground state. The situation is more complicated for acetonitrile, given that no recovery of the ground state feature C is seen for cluster sizes below $n = 40$. While there are hints of recovery for larger clusters, we have not been able to observe this reliably. We also searched for recovery in the energy region where probe-induced detachment from isomer I would occur, around 2.4-2.5 eV, with the idea that isomer I might be formed as an intermediate decay product from the excited state II^* , but no evidence for this was seen, either. It is possible that excited-state autodetachment is the primary decay channel for state II^* . This channel is open, as evidenced by peak A, and autodetachment was observed to compete with internal conversion for excited $(\text{H}_2\text{O})_n^-$ clusters with $n < 25$, although the autodetachment yield never exceeded 25%.⁴² Future studies on larger clusters than those reported here at wavelengths closer to the bulk absorption band at 500 nm may provide additional insights into the excited state decay channels.

The results presented here show that the excited state decay dynamics in $(\text{CH}_3\text{CN})_n^-$ clusters are quite different from those in water and methanol cluster anions²⁷, showing a much weaker and possibly non-existent size-dependence in the $n = 20$ -50 size regime. It will be of considerable interest to see if these lifetimes carry over into electrons in liquid acetonitrile, and we hope our results will stimulate such investigations in other laboratories.

Since the publication of this research in 2010, high-level quantum chemical calculations on the acetonitrile dimer anion and its excited state have elucidated the nature of the excitation and the symmetry of the excited state. As mentioned above, the ground states of the neutral and

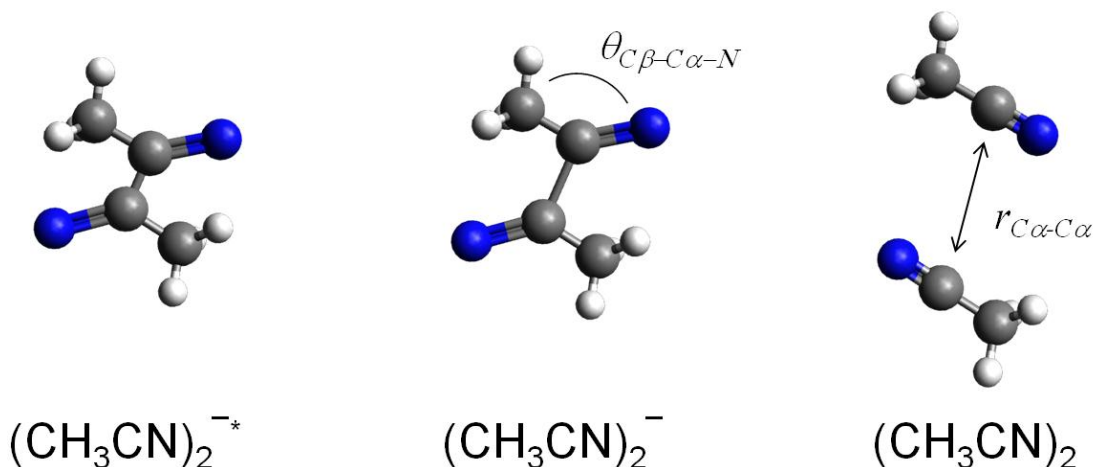


Figure 4.7. Minimum energy structures for the unsolvated acetonitrile dimer anion excited state, anion ground state, and neutral ground state. Ground state structures were calculated using DFT at the ω B97/6-311++G** level of theory; the excited state was calculated using SOS-CIS(D₀) with the 6-311++G** basis. These states are connected along two coordinates: the C_α-C_α distance and the C_βC_αN bond angle. Adapted from Azar, *et al.* 2011.⁴⁴

anionic dimer have been investigated by numerous methods; however until recently there had been no extensive study of the bound excited state of the anion. In 2011, Azar and Head-Gordon⁴⁴ published a study motivated by the experiments presented here to investigate this state and the nature of the excitation. They showed that a low-lying excited state of the radical anion was at least metastable in the bare dimer, about 2 eV above the anion ground state. The equilibrium structures for the acetonitrile dimer anion excited state, anion ground state and neutral ground state are shown in Figure 4.7.

The geometry of the dimer anion changes upon excitation; the adiabatic structure of the excited dimer anion is similar to the bent anti-parallel configuration of the anion ground state. Most bond lengths and angles are roughly the same as in the ground states of both the anion and neutral dimers, however the C_α-C_α bond is contracted by ~14% and the C_βC_αN bond angle is about 7° smaller. Because the ground states of the neutral and anion dimers are also connected by motion along these coordinates, the configuration of the excited state suggests a possible set of coordinates leading to dissociation. Indeed, calculated potential energy surfaces along these coordinates for all three species were shown to intersect such that vertical excitation from the anion ground state deposited ~0.5 eV of excess energy into the excited state, making the excited dimer vibrationally hot, populating the $\nu = 5$ vibrational state. Integrating the nuclear wavefunction beyond the seam of the potential energy surface yields an estimate of the autodetachment lifetime of about 200-270 fs, in excellent agreement with those observed experimentally.

The solvation of this species was also examined. Solvation of the dimer anion core by up to 8 additional acetonitrile molecules drives the excitation energy from 2 eV to about 1.63 eV by $n = 10$ where it appears fairly level. This energy is in good agreement with the experimental excitation energy of 1.57 ± 0.05 eV for the much larger clusters ($n = 20$ -50) studied here.

4.6 Conclusions

Time-resolved photoelectron imaging was used to investigate excited state dynamics in acetonitrile cluster anions $(\text{CH}_3\text{CN})_n^-$ over the size range $20 \leq n \leq 50$. These experiments were performed using femtosecond pump and probe laser pulses at 790 and 395 nm, respectively, in which the pump pulse electronically excited the clusters and the probe pulse photodetached them. In this cluster size regime, isomer II cluster anions, in which the excess electron is valence-bound to a solvated dimer anion core, are the dominant species. We observed pump-probe signal yielding excited state lifetimes of isomer II clusters with decay times varying between 208 fs and 266 fs with no obvious size-dependent trend. Depletion of the ground state population was observed for all clusters, which signifies that the visible absorption band in the bulk is associated with isomer II, as proposed in the literature. The absence of a clear size-dependence, in contrast to earlier work on water and methanol cluster anions, is consistent with a highly localized excess electron that is only weakly perturbed by solvent molecules beyond the first solvation shell.

4.7 References

- 1 D. M. Bartels *et al.*, *J. Phys. Chem. A* **104** (8), 1686 (2000).
- 2 J. Simons, *Accts. Chem. Res.* **39** (10), 772 (2006).
- 3 E. J. Hart, and M. Anbar, *The Hydrated Electron* (Wiley-Interscience, New York, 1970).
- 4 P. J. Rossky, and J. Schnitker, *J. Phys. Chem.* **92** (15), 4277 (1988).
- 5 H. F. Hameka, G. W. Robinson, and C. J. Marsden, *J. Phys. Chem.* **91** (12), 3150 (1987).
- 6 C. Silva *et al.*, *Phys. Rev. Lett.* **80**, 1086 (1998).
- 7 J. V. Coe, S. M. Williams, and K. H. Bowen, *Int. Rev. Phys. Chem.* **27** (1), 27 (2008).
- 8 J. V. Coe *et al.*, *J. Chem. Phys.* **92** (6), 3980 (1990).
- 9 J. Kim *et al.*, *Chem. Phys. Lett.* **297** (1-2), 90 (1998).
- 10 J. R. R. Verlet *et al.*, *Science* **307** (5706), 93 (2005).
- 11 L. Ma *et al.*, *J. Chem. Phys.* **131** (14), 144303 (2009).
- 12 J. M. Weber *et al.*, *Chem. Phys. Lett.* **339** (5-6), 337 (2001).
- 13 A. E. Bragg *et al.*, *Science* **306** (5296), 669 (2004).
- 14 D. H. Paik *et al.*, *Science* **306**, 672 (2004).
- 15 A. Kammrath *et al.*, *J. Chem. Phys.* **125** (17), 171102 (2006).
- 16 A. Kammrath *et al.*, *J. Chem. Phys.* **126**, 244306 (2007).
- 17 I. P. Bell, M. A. J. Rodgers, and H. D. Burrows, *J. Chem. Soc. Faraday Trans. I* **73**, 315 (1977).
- 18 I. A. Shkrob, and M. C. Sauer, *J. Phys. Chem. A* **106** (39), 9120 (2002).
- 19 C. G. Xia, J. Peon, and B. Kohler, *J. Chem. Phys.* **117** (19), 8855 (2002).
- 20 Q. K. Timerghazin, and G. H. Peslherbe, *J. Phys. Chem. B* **112** (2), 520 (2008).
- 21 M. Mitsui *et al.*, *Phys. Rev. Lett.* **91** (15), 153002 (2003).
- 22 T. Takayanagi, T. Hoshino, and K. Takahashi, *Chem. Phys.* **324** (2-3), 679 (2006).
- 23 O. T. Ehrler *et al.*, *J. Phys. Chem. B* **113** (13), 4031 (2009).
- 24 O. T. Ehrler, and D. M. Neumark, *Accts. Chem. Res.* **42** (6), 769 (2009).
- 25 T. Takayanagi, *J. Phys. Chem. A* **110** (22), 7011 (2006).
- 26 A. Stolow, A. E. Bragg, and D. M. Neumark, *Chem. Rev.* **104** (4), 1719 (2004).

- 27 D. M. Neumark, *Mol. Phys.* **106** (16-18), 2183 (2008).
28 G. Markovich *et al.*, *J. Chem. Phys.* **105** (7), 2675 (1996).
29 T. N. V. Nguyen, and G. H. Peslherbe, *J. Phys. Chem. A* **107** (10), 1540 (2003).
30 D. M. Koch, and G. H. Peslherbe, *Chem. Phys. Lett.* **359** (5-6), 381 (2002).
31 J. R. Roscioli, N. I. Hammer, and M. A. Johnson, *J. Phys. Chem. A* **110** (24), 7517 (2006).
32 K. R. Asmis *et al.*, *J. Chem. Phys.* **126** (19), 191105 (2007).
33 A. Madarasz, P. J. Rossky, and L. Turi, *J. Chem. Phys.* **130** (12) (2009).
34 A. V. Davis *et al.*, *J. Chem. Phys.* **118** (3), 999 (2003).
35 U. Even *et al.*, *J. Chem. Phys.* **112** (18), 8068 (2000).
36 K. Mitsuke, T. Kondow, and K. Kuchitsu, *J. Phys. Chem.* **90** (8), 1505 (1986).
37 W. C. Wiley, and I. H. McLaren, *Rev. Sci. Instrum.* **26** (12), 1150 (1955).
38 A. T. J. B. Eppink, and D. H. Parker, *Rev. Sci. Instrum.* **68** (9), 3477 (1997).
39 V. Dribinski *et al.*, *Rev. Sci. Instrum.* **73** (7), 2634 (2002).
40 J. Cooper, and R. N. Zare, *J. Chem. Phys.* **48**, 942 (1968).
41 T. E. Dermota *et al.*, *J. Phys. Chem. A* **109** (37), 8254 (2005).
42 G. B. Griffin *et al.*, *J. Chem. Phys.* **131** (19), 194302 (2009).
43 K. L. Reid, *Annu. Rev. Phys. Chem.* **54**, 397 (2003).
44 J. Azar, W. Kurlancheek, and M. Head-Gordon, *Phys. Chem. Chem. Phys.* (2011).

Chapter 5. Dynamics of Electron Solvation in $I^-(CH_3OH)_n$ ($4 \leq n \leq 11$)

[Reprinted with permission from "Dynamics of electron solvation in $I^-(CH_3OH)_n$ clusters ($4 \leq n \leq 11$)" R. M. Young, M. A. Yandell, D. M. Neumark, J. Chem. Phys. 134, 124311 (2011)]

The dynamics of electron solvation following excitation of the charge-transfer-to-solvent (CTTS) precursor state in iodide-doped methanol clusters, $I^-(CH_3OH)_{n=4-11}$, are studied with time-resolved photoelectron imaging (TRPEI). This excitation produces a $I^{\cdot-}(CH_3OH)_n^-$ cluster that is unstable with respect to electron autodetachment, and whose autodetachment lifetime increases monotonically from ~ 800 fs to 85 ps as n increases from 4-11. The vertical detachment energy (VDE) and width of the excited state feature in the photoelectron spectrum show complex time dependence during the lifetime of this state. The VDE decreases over the first 100-400 fs, then rises exponentially to a maximum with a ~ 1 ps time constant, and finally decreases by as much as 180 meV with timescales of 3-20 ps. The early dynamics are associated with electron transfer from the iodide to the methanol cluster, while the longer-time changes in VDE are attributed to solvent reordering, possibly in conjunction with ejection of neutral iodine from the cluster. Changes in the observed width of the spectrum largely follow those of the VDEs; the dynamics of both are attributed to the major rearrangement of the solvent cluster during relaxation. The relaxation dynamics are interpreted as a reorientation of at least one methanol molecule and the disruption and formation of the solvent network in order to accommodate the excess charge.

5.1 Introduction

How chemical environments stabilize excess charges is of critical importance in biology, solution phase chemistry, and condensed matter physics. The solvated electron is perhaps one of the best-studied species in this area as it is the simplest quantum solute^{1,2} with only electronic degrees of freedom. Solvated electrons can be produced from the charge-transfer-to-solvent (CTTS) bands of solvated anions,³ typically halide species such as iodide, I^- . Though most attention has been focused on CTTS dynamics in water,^{4,5} solvated electrons have been produced from CTTS excitations in a variety of other solvents, such as ethylene glycol,⁶ tetrahydrofuran,^{7,8} acetonitrile,⁹ and many alcohols, including methanol.¹⁰ In the gas phase, iodide has no bound excited states and photoexcitation leads directly to detachment into the vacuum. However, upon solvation by only a few solvent molecules, an excited state can be observed as a broad feature in the electronic absorption spectrum of the gas-phase cluster.¹¹ Excitation then leads to ejection of the charge from the iodide onto the solvent network, which then begins to relax around it. Hence, time-resolved studies of halide-solvent clusters¹²⁻¹⁴ provide complementary insights when compared with experiments performed in solution. In this study, we investigate electron solvation dynamics in $I^-(CH_3OH)_n$ clusters subsequent to CTTS excitation.

Methanol is similar to water in that it is polar and it can participate in hydrogen bonding, but it also has an aliphatic end more suited for non-polar interactions. In many ways it is the closest solvent to water and can be thought of as its "methylated" counterpart. Methanol differs significantly, however, in that it can participate in only half as many hydrogen bonds. Its similarities and differences compared to water allow for a better understanding of how the local

solvent environment affects electron solvation and solvent relaxation. To this end, numerous experimental¹⁵⁻²¹ and theoretical²²⁻²⁴ investigations have been carried out on the dynamics of electron solvation in methanol. For example, ultrafast transient absorption experiments have been utilized by Bradforth and co-workers^{5, 25} to probe the CTTS dynamics from iodide in water, methanol and the lower alcohols. By monitoring the absorbance of the nascent solvated electron, they find that the electron is ejected from the iodide into the primary solvent cavity, forming a contact pair with the neutral iodine during the first ~300 femtoseconds. From there, it either undergoes geminate recombination or diffuses out of the solvent cavity. The recombination and escape dynamics in methanol are both slower than those in water, which is explained in their model as a result of the higher viscosity of methanol.

As a complement to the work in solution, experiments on halide-solvent clusters examine electron solvation dynamics as a function of size and reveal details of the molecular processes behind charge transfer and subsequent stabilization.^{11, 12, 26, 27} Time-resolved photoelectron spectroscopy experiments on $I^-(CH_3OH)_n$ ($n = 5-8$) by Davis *et al.*²⁸ showed that after electron transfer, the excited state of the cluster is metastable, with the population decaying within ~22 ps for the largest cluster studied. The ultimate fate of the excess electron was attributed to ‘thermionic emission’, or more specifically, vibrational autodetachment, as geminate recombination of the electron with the neutral iodine would release enough energy to fracture the cluster, which was not observed. However, the low energy electrons expected from autodetachment were not detectable with the magnetic bottle analyzer used in those experiments. Davis also noted the unique evolution of the shape of the photoelectron spectrum, which was markedly broader and asymmetric than in similar experiments with other solvents. The asymmetry of the spectra was speculatively attributed to evaporative loss of either iodine or a solvent monomer or from the contribution of another state with a shorter lifetime. However, little was known at the time about the structure of the initial and final state geometries or the energetics of bare methanol cluster anions, so no definitive assignment could be made.

Recent experimental and theoretical investigations into methanol clusters have caused us to revisit the dynamics of $I^-(CH_3OH)_n$. Infrared (IR) predissociation studies on small ($n \leq 12$) $X^-(CH_3OH)_n$ clusters ($X^- = F^-, Cl^-, I^-$) by Lisy, Johnson, and co-workers,^{27, 29-31} and accompanying quantum chemical calculations³² have provided the first structural probes of these clusters, in particular probing whether the halide anion is solvated internally or resides at the surface of the cluster. The experiments find that the halide anion is hydrogen-bonded to one or more OH groups on adjacent methanol molecules. However, evidence for methanol-methanol binding is seen for clusters as small as $I^-(CH_3OH)_2$, indicating a propensity for the methanol molecules to bind to one another as opposed to binding to the halide and leaving the anion at the cluster surface. Interestingly, molecular dynamics simulations predict little or no enhancement of iodide at the liquid-vapor interface of bulk methanol^{33, 34} because the methanol surface is covered by hydrophobic methyl groups with the OH groups pointed inward; this situation differs substantially from water, which exhibits considerable iodide enhancement at its surface.³⁵ Some sample structures for $I^-(CH_3OH)_6$ and $I^-(CH_3OH)_8$ at the DFT level of theory are shown in Figure 5.1.

Additional motivation for revisiting CTTS dynamics in $I^-(CH_3OH)_n$ clusters comes from recent experimental and theoretical work on $(CH_3OH)_n^-$ cluster anions. These clusters are, in essence, the final states expected in our CTTS experiments. Methanol cluster anions comprising 70-460 solvent molecules were studied in our research group by one-photon³⁶ and time-resolved³⁷ photoelectron imaging. The absence of anion clusters with fewer than 70 methanol

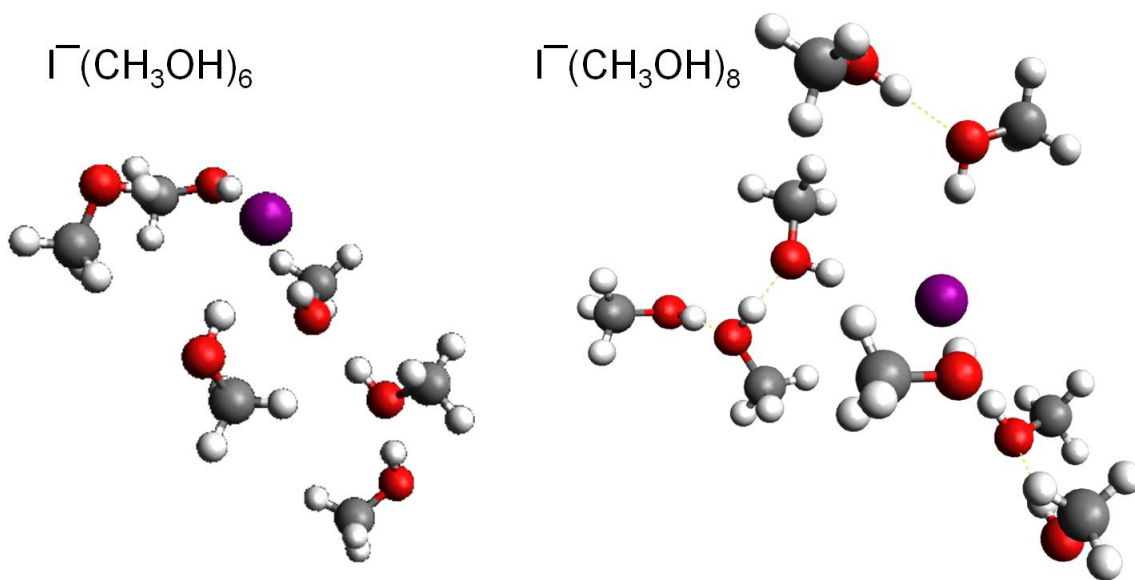


Figure 5.1. A sampling of calculated structures for $\text{I}^-(\text{CH}_3\text{OH})_6$ and $\text{I}^-(\text{CH}_3\text{OH})_8$ using density functional theory [B3LYP / 6-31++G** I ECP(LANL2DZ)]. These are among many nearly isoenergetic structures for clusters of this size. Note the disrupted hydrogen bond network and the propensity for I^- to reside at the cluster surface. The authors thank Julian Azar and the Head-Gordon group for assistance with these structures.

molecules in the mass spectrum suggested that these smaller clusters were unstable on the time scale of our experiment. The one-photon studies demonstrated the existence of two distinct electron solvation motifs (isomers).³⁶ The first is a weakly-bound state (isomer II) that appears at higher ion source backing pressures. Isomer II clusters exhibit narrow photoelectron spectra and were assigned to clusters with surface-bound electrons. The other isomer (isomer I) is more strongly bound, with a broader photoelectron spectrum, and is favored at lower ion source backing pressures. We proposed that isomer I is the more “bulk-like” state, possibly being internally solvated. Time-resolved experiments on this isomer³⁷ yielded internal conversion lifetimes that extrapolated reasonably well to the timescales from transient absorption experiments on electrons in bulk methanol by Thaller *et al.*²¹ On the theoretical side, a new electron-methanol pseudopotential has recently been developed by Turi^{24,38} and applied to large methanol cluster anions ($n = 50-500$). This work found diffuse, weakly-bound surface states with surface methyl groups oriented toward the excess electron, similar to the isomer II structure inferred from our photoelectron spectra.³⁶

With better knowledge of the initial and final states, we reexamine here the dynamics of $\text{I}^-(\text{CH}_3\text{OH})_n$ following CTTS excitation with time-resolved photoelectron imaging (TRPEI) over a larger size range ($n = 4-11$) than previously reported. Photoelectron imaging yields the photoelectron kinetic energy and angular distribution. As has been demonstrated for $\text{I}^-(\text{H}_2\text{O})_n$ clusters,^{39,40} the near-unity collection efficiency of charged particle imaging enables tracking of the autodetachment channel that cannot be observed with a magnetic bottle analyzer. We find this channel to be the dominant pathway for population decay for $\text{I}^-(\text{CH}_3\text{OH})_n$ clusters, as $(\text{CH}_3\text{OH})_n^-$ are unstable in this size regime. Short time dynamics (100-400 fs) not previously observed are attributed to the electron associating with the solvent moiety immediately following excitation. The cluster response to this charge distribution can be monitored by the evolution of

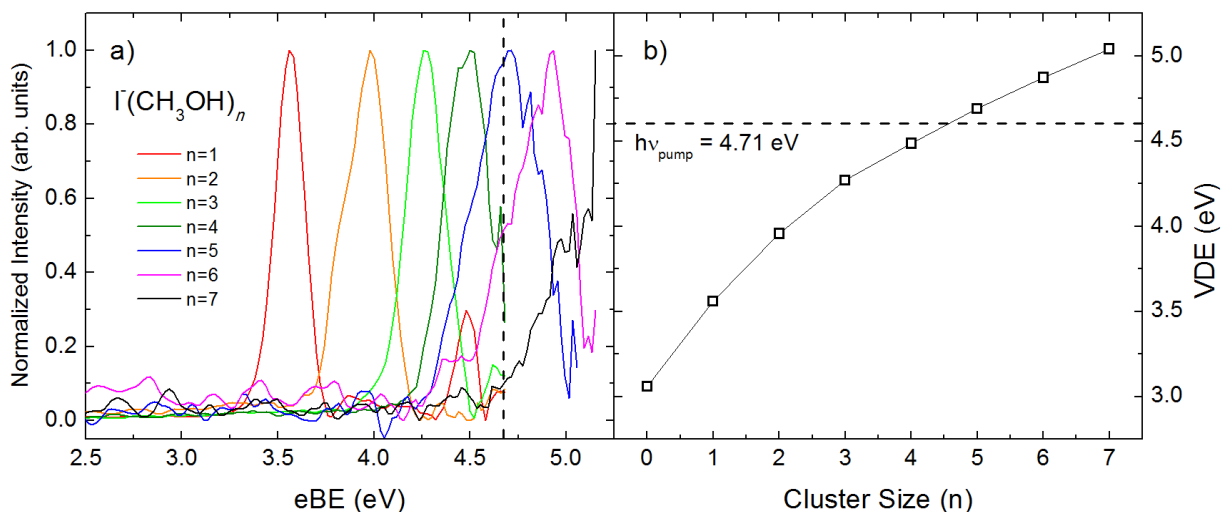


Figure 5.2a. One-photon detachment spectra for $I^-(CH_3OH)_n$ ($n = 1-7$) using 263 nm and 238 nm light. Dashed lines indicate the maximum binding energy accessible by the 263 nm pump pulse. Autodetachment is possible at this wavelength beginning at $n = 4$ but delayed until $n = 7$ for 238 nm excitation.

Figure 5.2b. Vertical detachment energies (VDEs) derived from the spectra in Fig. 5.2a by Gaussian fit to the eBE distribution of the $^2P_{3/2}$ peaks.

the photoelectron spectrum. The observed changes in the binding energy of the electron (3-20 ps) and the width of the spectrum (5-30 ps) are evidence for a major rearrangement of the solvent geometry near the halide and the excess electron.

5.2 Experimental

The femtosecond time-resolved photoelectron imaging apparatus has been described in detail elsewhere.³⁹ Briefly, argon carrier gas at ~20 psig was flowed over reservoirs of liquid methanol and methyl iodide at room temperature into a pulsed solenoid valve⁴⁰ operating at 100 Hz. The resulting pulsed jet then passed through a ring electrode ionizer. Secondary electrons from the ionization process formed I^- via dissociative electron attachment to CH_3I , which could either be picked up by methanol clusters in the jet or act as a nucleation site for cluster formation. The anion beam was injected into a Wiley-McLaren time-of-flight mass spectrometer,⁴¹ configured so that only ions of the desired mass interacted with the pump and probe laser pulses. Additional size selectivity was accomplished by an electrostatic switch at the entrance to the interaction region pulsed at the appropriate time. Ejected photoelectrons were accelerated by velocity-map imaging⁴² onto a pair of chevron-mounted 75 mm microchannel plates coupled to a phosphor screen. Intensified images were collected at 30 Hz with a CCD camera and four-way symmetrized to ensure homogeneity.

Images were reconstructed using the BASEX method⁴³ for photoelectron kinetic energy (eKE) spectra or the pBASEX method⁴⁴ for the photoelectron angular distributions (PADs). The PADs were fit to an even series of Legendre polynomials:⁴⁵

$$I(\theta, eKE; n) = \frac{\sigma_{\text{total}}}{4\pi} [1 + \beta_2(eKE; n)P_2(\cos \theta) + \beta_4(eKE; n)P_4(\cos \theta)] \quad (5.1)$$

where I is the intensity, θ is the angle between the photoelectron wave vector and the laser polarization, n is the cluster size, σ_{total} is the total photodetachment cross section, and $\beta_{2,4}$ are anisotropy parameters which contain information about the excess electron's angular momentum.

Pump and probe laser pulses were generated in a commercial Ti:sapphire oscillator and then amplified by chirped-pulse multipass amplification (KM Labs Griffin oscillator/Dragon amplifier), resulting in pulses of 35 fs duration (full width at half maximum, FWHM) at 790 nm (1.57 eV). 75% of this light was directed into a third-harmonic generator, yielding pulses at 263 nm (4.71 eV) with 30 $\mu\text{J}/\text{pulse}$ to be used to excite the CTTS transition. The remaining fundamental was attenuated and used as the probe pulse, with a pulse energy at the entrance to the vacuum chamber of 120-200 $\mu\text{J}/\text{pulse}$. Time resolution at the vacuum chamber was measured *in situ* by above threshold detachment of iodide as ~ 80 fs. Ultraviolet pulses for one-photon photodetachment studies were produced with an optical parametric amplifier (Light Conversion TOPAS-C) at 238 nm (5.21 eV).

5.3 Results

One-photon UV photoelectron spectra are shown in Figure 5.2a for $n = 1-7$. TRPEI was carried out for $\text{I}^-(\text{CH}_3\text{OH})_n$ clusters with $n = 4-11$ and their deuterated analogs (*-d1*) and (*-d4*). Figure 5.3 shows the time-resolved photoelectron spectrum for $\text{I}^-(\text{CH}_3\text{OH})_4$, with eKE decreasing from left to right and pump-probe delay increasing nonlinearly from front to back. Four prominent features are seen: an intense, time dependent signal at eKE ~ 0 (Feature A), a peak from 1.5-1.8 eV that appears near the zero of pump-probe delay (B), a broad peak around 0.25 eV (C), and a low-intensity feature around 1.5 eV which shows no time-dependence (D). These last two features are only seen for $n = 4$. Figure 5.4 and 5.5 show TRPE spectra for $\text{I}^-(\text{CH}_3\text{OH})_7$ and its singly-deuterated isotopologue, respectively; these spectra are representative of cluster sizes with $n \geq 5$. There are no qualitative differences in the TRPES for any isotopes presented here. They are similar to those previously presented by Davis,²⁸ but the sharp, intense feature (A) near eKE = 0 was not seen in that work owing to the poor transmission of the magnetic bottle analyzer for very low eKE. Feature A dominates the spectra for all cluster sizes $n \geq 5$ but becomes less intense overall for the largest cluster sizes as the CTTS band blue-shifts away from 263 nm. Integrated intensities of Features A and B are shown in the insets of Figs. 5.3-5.5.

For all cluster sizes, Features A and B exhibit a strong and complementary dependence on the pump-probe delay. The intensities of both features change abruptly near the zero of pump-probe delay, t_0 ; Feature A is depleted by the probe pulse from its pump-only value at negative time delays, whereas Feature B is not seen until the pump and probe pulses overlap. Both features then return more slowly to their initial values on a time scale that increases with cluster size, ranging from 1-2 ps for $n = 4$ to nearly 100 ps for $n = 11$. For $n \geq 6$, Features A and B reach their respective minimum or maximum intensities 1-3 ps after the cross-correlation time of the two laser pulses.

Based on our previous work on $\text{I}^-(\text{H}_2\text{O})_n$ and $\text{I}^-(\text{CH}_3\text{CN})_n$ clusters,^{46, 47} we assign Feature A to vibrational autodetachment (VAD) of the $\text{I}^-(\text{CH}_3\text{OH})_n$ clusters after pump excitation. Likewise, Feature B is assigned to the [1+1'] pump-probe signal from the excited state of the cluster. These assignments explain the complementary time-dependence of Features A and B,

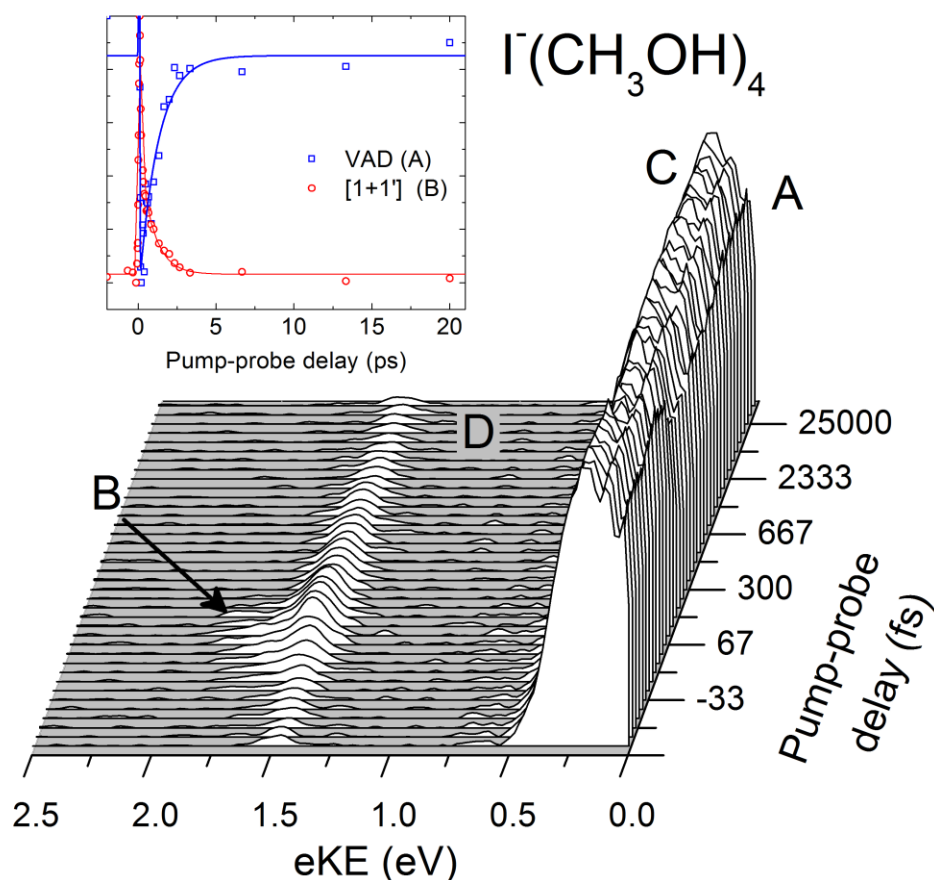


Figure 5.3. Time-resolved photoelectron spectrum for $\text{I}^-(\text{CH}_3\text{OH})_4$ with pump-probe delay increasing nonlinearly from front to back. Feature A is due to vibrational autodetachment (VAD); Feature B is the resonant two-photon $[1+1']$ signal; Feature C is from UV direct detachment to the $^2\text{P}_{3/2}$ state of iodine; and Feature D is from 4-photon IR detachment to the $^2\text{P}_{3/2}$ state. Normalized intensities of Features A (blue) and B (red) are shown in the inset, with fits shown as solid lines.

since the excited state either undergoes autodetachment or is photodetached by the probe pulse.^{46, 47} For all sizes studied here, both the peak and width of the eKE distribution for Feature B change significantly with pump-probe delay, with the extent of this variation changing with cluster size. Partial ($-d1$) and full ($-d4$) deuteration result only in small effects on the time-dependent intensities, binding energies, and spectral shapes. The detailed time-dependence of Features A and B is explored in Section 4.

For $n = 4$, Feature C is also seen with only the UV pulse and is due to direct detachment of I^- to the $^2\text{P}_{3/2}$ state of iodine. Similarly, Feature D is also seen with only the infrared pulse and is attributed to 4-photon IR detachment of I^- to the $^2\text{P}_{3/2}$ state of neutral iodine, shifted to slightly higher binding energy due to the ponderomotive effect of the high-intensity laser field.⁴⁸ A small ridge on the low eKE side of Feature C is at approximately the correct energy for 3 photon detachment to the $^2\text{P}_{3/2}$ state as well. These features are not seen for larger cluster sizes or at lower pulse energies.

Feature A is a one-photon process and can be fit with a single anisotropy parameter. For the sizes studied here, the feature was symmetric and β_2 was ~ 0 for all delays. The pump-probe Feature B was fit to Eq. 5.1. For clusters sizes with sufficient signal-to-noise, the two-photon

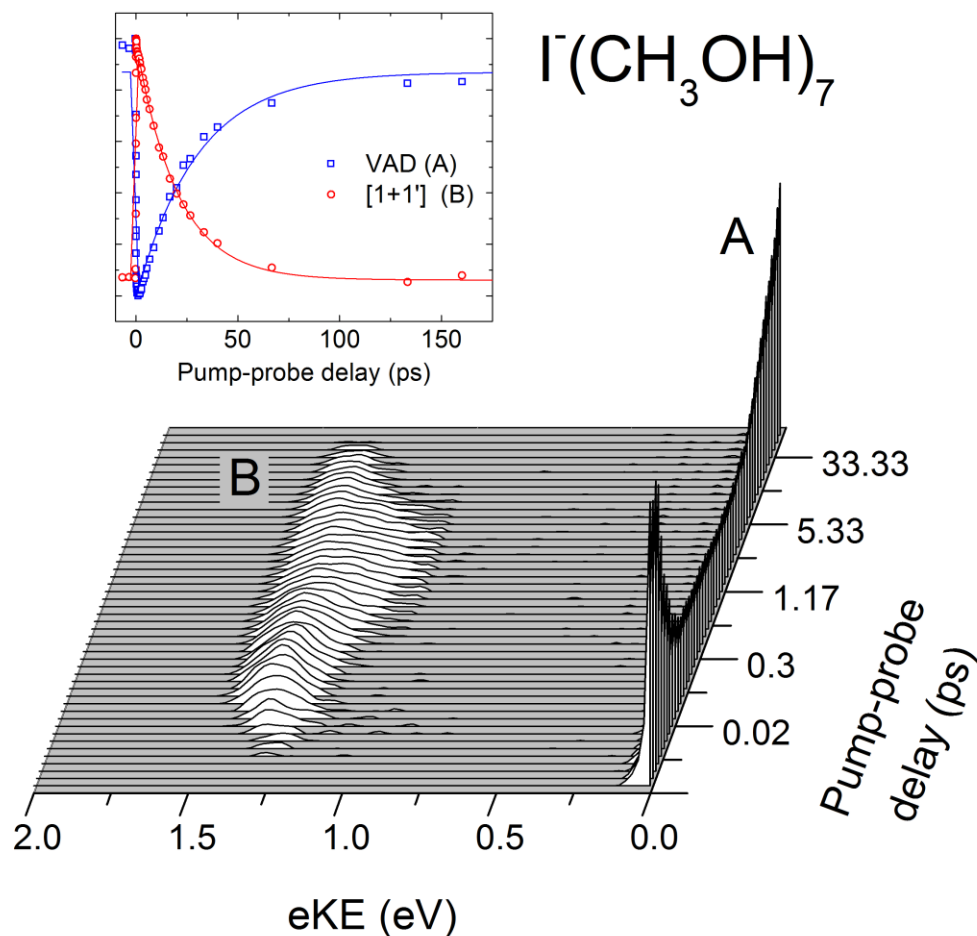


Figure 5.4. Time-resolved photoelectron spectrum for $\text{I}^-(\text{CH}_3\text{OH})_7$ with pump-probe delay increasing nonlinearly from front to back. Feature A is due to vibrational autodetachment; Feature B is the resonant two-photon $[1+1']$ signal. Normalized intensities of Features A (blue) and B (red) are shown in the inset, with fits shown as solid lines.

anisotropy parameter β_4 was observed to be close to zero (-0.1 to 0.3) at all pump-probe delays, while β_2 showed marked temporal evolution. The sensitivity of the pBASEX algorithm to both signal levels and to noise makes the time-dependent feature more difficult to fit, but general observations can be made about the anisotropy near t_0 and very long pump-probe delays. The images begin with a significant anisotropy for feature B ($\beta_2 \sim 0.7$ – 1.0) and then become more isotropic ($\beta_2 \sim 0$ – 0.4) before the signal fades. No obvious size-dependent trends in the anisotropy parameters were observed. A progression of reconstructed photoelectron Newton spheres is shown in Figure 5.6.

5.4 Analysis

In this section, we analyze the temporal evolution of the photoelectron spectra in detail. Time-dependent intensities for each feature are fit to retrieve the lifetime of the excited cluster, and the eKE distribution itself is fit at each delay to extract vertical detachment energies (VDEs) and the FWHM of the excited state feature.

First, we focus on the lifetime of the excited state and autodetachment process. The

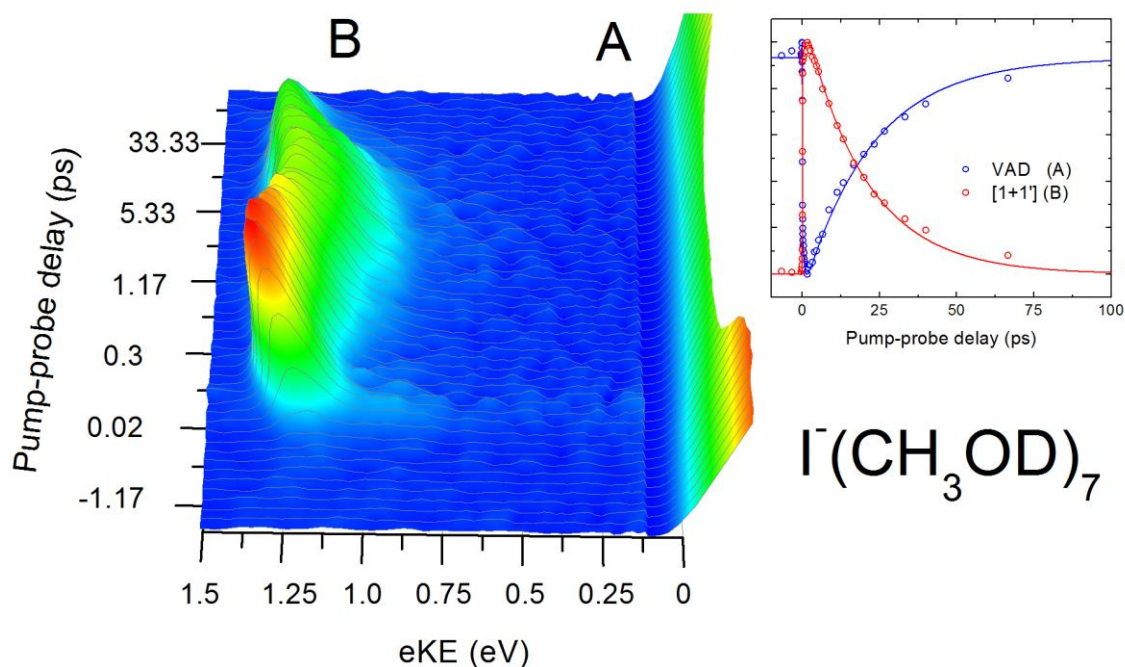


Figure 5.5. Time-resolved photoelectron spectra for $\text{I}^-(\text{CH}_3\text{OD})_7$: with pump-probe delay increasing nonlinearly from front to back and intensity false-color mapped. Feature A is due to vibrational autodetachment; Feature B is the resonant two-photon $[1+1']$ signal. Normalized intensities of Features A (blue) and B (red) are shown in the inset, with fits shown as solid lines.

intensities of Features A and B are determined by integrating over the respective range of the eKE distribution at each time delay. The resultant intensities are then fit to Eq. 5.2, representing the convolution of a Gaussian instrumental response function of temporal width σ with the sum of (i) a multi-exponential function characterized by time constants τ_{Xi} where X is either A or B, (ii) a delta function centered at t_0 (to account for coherence artifacts during the cross-correlation time), and (iii) an offset, I_0 :

$$I_X = e^{-t^2/\sigma^2} * \begin{cases} I_0 & t < t_0 \\ I_0 + a_0\delta(t-t_0) + \sum_i a_i \exp[-(t-t_0)/\tau_{Xi}] & t \geq t_0 \end{cases} \quad (5.2)$$

where $i = 1$ for $n = 4, 5$ and $i = 1, 2$ for larger clusters. The time resolution of the apparatus is given by $\tau_{\text{FWHM}} = 2\sigma\sqrt{\ln 2} = 70\text{-}90$ fs. For clusters larger than $n = 5$, the integrated intensity of the excited state feature rises and falls in a bi-exponential fashion; the rise time τ_{B1} is around 1 ps for $6 \leq n \leq 11$.

Features A and B can be described by the same equation with opposite signs for the coefficients a_i ; the recovery of Feature A is systematically slower than the decay of Feature B by a few percent, though within the error bars. This small discrepancy is attributed to the intrinsic difficulty in measuring small changes in Feature A atop a large background. Hence, we report

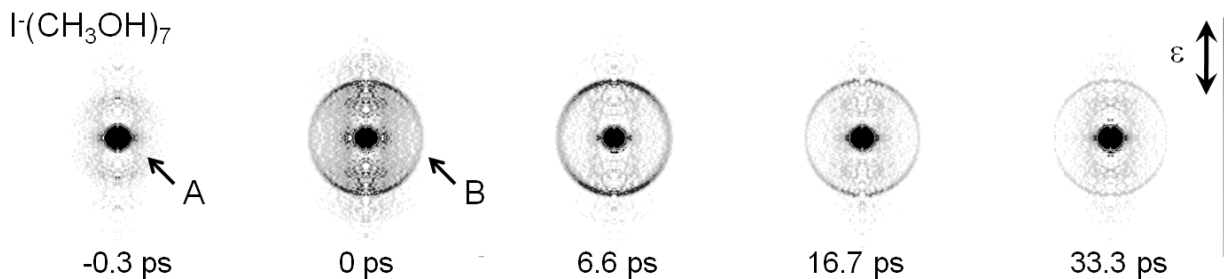


Figure 5.6. Reconstructed photoelectron Newton circles for $\text{I}^-(\text{CH}_3\text{OH})_7$ at -0.3 ps through 33 ps pump-probe delay, with laser polarization and scale indicated on the right. Feature A appears isotropic at all pump-probe delays, while Feature B is maximal along the laser polarization axis, appearing at t_0 and decaying with increasing delay.

the time constants τ_{B1} and τ_{B2} as the lifetimes of the excited clusters for $n \leq 5$ and $n \geq 6$, respectively. These time constants are listed in Table 5.1.

Excited state VDEs are determined by fitting an asymmetric Gaussian function to the eKE spectrum over the range of Feature B to monitor the time-dependent energetics of the excited state for each cluster size and at each pump-probe delay. The kinetic energy profile for cluster n is fit to:

$$I_n(eKE; t) = \begin{cases} I_0 + be^{-[eKE - E_0(t)]^2 / w_1^2(t)} & eKE < E_0 \\ I_0 + be^{-[eKE - E_0(t)]^2 / w_2^2(t)} & eKE \geq E_0 \end{cases} \quad (5.3)$$

where b is a scaling parameter, E_0 is the peak of the eKE distribution, and w_1 and w_2 are the width parameters on either side of the peak. Eq. 5.3 is a phenomenological lineshape that has been observed previously for halide-solvent clusters.⁴⁷ The FWHM of the kinetic energy profile is $(w_1 + w_2) \times \sqrt{\ln 2}$. For $n = 4$ only, where direct detachment leading to Features C and D competes with CTTS excitation, the eKE spectrum at $\Delta t = -1$ ps is first subtracted before fitting to avoid contamination. Figure 5.7 shows the eKE distribution and accompanying fits for

Cluster size (n)	Lifetime	VDE		FWHM	
	τ_{B2}	t_{max}	τ_2	T_{max}	T_2
4	$0.80 \pm 0.07^*$	n/a	n/a	n/a	n/a
5	$4.10 \pm 0.02^*$	1.5 ± 0.2	3.1 ± 0.3	1.4 ± 0.2	5.6 ± 0.3
6	9.40 ± 0.52	1.8 ± 0.2	4.5 ± 1.1	2.8 ± 0.3	8.0 ± 2.9
7	19.6 ± 0.49	1.7 ± 0.2	7.5 ± 1.4	2.7 ± 0.3	7.5 ± 1.1
8	32.6 ± 0.44	3.5 ± 0.3	9.5 ± 0.3	2.4 ± 0.3	9.3 ± 1.0
9	49.7 ± 0.79	3.6 ± 0.3	16.7 ± 3.9	4.4 ± 0.7	23 ± 9.3
10	70.9 ± 2.59	2.4 ± 0.7	20.1 ± 7.6	5.2 ± 0.3	30 ± 12
11	85.5 ± 6.30	n/a	n/a	n/a	n/a

*Lifetime given by τ_{B1} .

Table 5.1. Timescales for excited state lifetime, VDE and FWHM dynamics, in picoseconds. Values represent averages over data sets and errors represent the standard deviation of the mean. Only population information is available for $n = 4$ due to the short lifetime of the cluster, and for $n = 11$ due to signal levels.

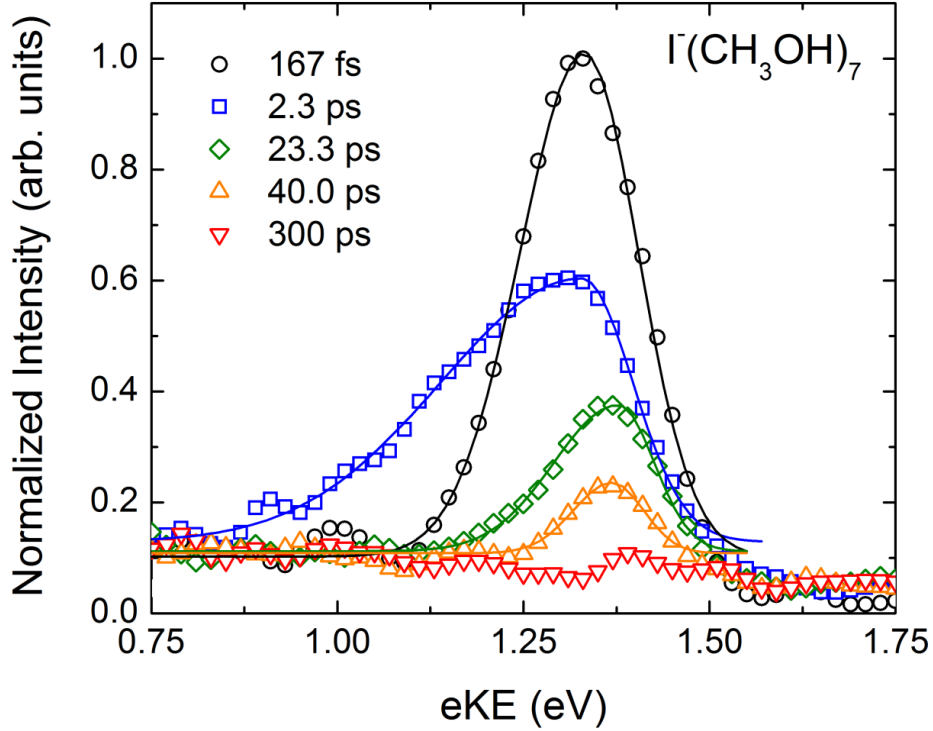


Figure 5.7. Photoelectron spectra at the following pump-probe delays for $\text{I}^-(\text{CH}_3\text{OH})_7$: Black circles: 167 fs; Blue squares: 2.3 ps; Green diamonds: 23.3 ps; Orange upward triangles: 40.0 ps; Red downward triangles: 300 ps. Spectra at each delay are normalized to the peak intensity of the spectrum at $t = 167$ fs.

$\text{I}^-(\text{CH}_3\text{OH})_7$ at various delays, showing how both the peak energy and the width of the spectrum change significantly over time.

The time-dependent peak of the eKE distribution, $E_0(t)$ yields the vertical detachment energy:

$$VDE(t) = h\nu - E_0(t). \quad (5.4)$$

VDEs vs. delay are shown for $\text{I}^-(\text{CH}_3\text{OH})_7$ in Figure 5.8. Following CTTS excitation, the VDEs quickly fall to a minimum value, VDE_{\min} , during the first 100-400 fs (t_{\min}) with no clear size dependence over the range studied here. For $n \geq 5$, over the next ~ 1 -3 ps, the VDE rises to a maximum, VDE_{\max} , before falling again for the remainder of the excited state lifetime, typically approaching a value lower than the initial local minimum at t_{\min} . Time-dependent VDEs after VDE_{\min} can be fit to a bi-exponential process:

$$VDE_n(t) = VDE_n(\infty) + c_2^{(n)} e^{-(t-t_0)/\tau_1^{(n)}} + c_3^{(n)} e^{-(t-t_0)/\tau_2^{(n)}} \quad (5.5)$$

where τ_i is the relaxation time for each term and $VDE_n(\infty)$ is an estimate of the asymptotic VDE. The second term applies to the rise ($c_2 < 0$) while the third describes the decrease in VDE ($c_3 > 0$). The increase to maximum VDE takes place on a timescale τ_1 ranging from 0.7-2 ps,

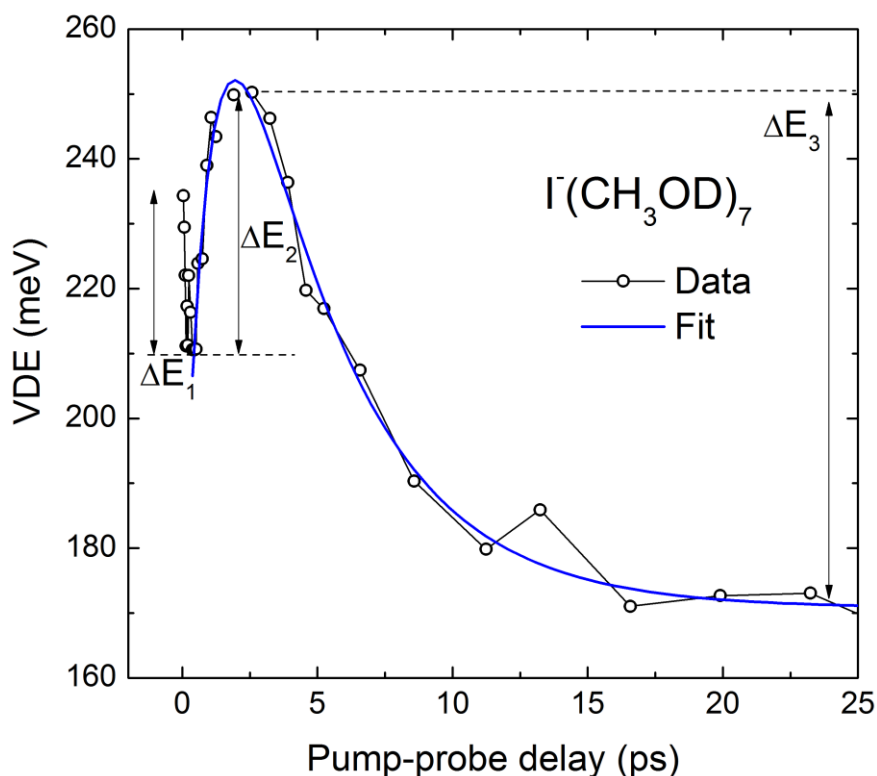


Figure 5.8. VDE as a function of pump-probe delay for $\text{I}^-(\text{CH}_3\text{OD})_7$ showing ΔE_1 , ΔE_2 , and ΔE_3 .

generally increasing with cluster size. The pump-probe delay t_{max} corresponding to VDE_{max} is taken directly from the spectra. The relaxation time τ_2 toward $\text{VDE}(\infty)$ increases from 3 ps to 20 ps from $n = 5$ to 10. The decay of the excited state signal leads to the increased errors associated with the fitting of the long-time tails of the exponential decay. The time constants t_{max} and τ_2 are listed in Table 5.1, while VDE_{min} , VDE_{max} , and $\text{VDE}(\infty)$ for each cluster are given in Table 5.2.

While the relaxation times and $\text{VDE}(\infty)$ are taken from the least-squares fitting, changes in the VDE, ΔE_i ($i = 1-3$), are taken directly from the spectra and are shown graphically in Figure 5.8. The initial change in energy between the first appearance of the excited state and VDE_{min} , $\Delta E_1 = \text{VDE}_{min} - \text{VDE}(0)$, becomes more pronounced with cluster size, varying from -40 meV at $n = 5$ to -115 meV for $n = 11$. $\Delta E_2 = \text{VDE}_{max} - \text{VDE}_{min}$ ranges from +45 meV to +165 meV over these sizes, and the long-time relaxation, $\Delta E_3 = \text{VDE}(\infty) - \text{VDE}_{max}$, varies from -60 meV to -220 meV, generally decreasing with cluster size. There is no strong isotope effect observed. Energy changes are listed in Table 5.2, and are shown in Figure 5.10.

The width of Feature B changes significantly with pump-probe delay, as can be seen in Figures 5.3-5.5 & 5.7. After the excited state is first populated, the width of this feature rises to a maximum (as much as $\text{FWHM} = 550$ meV for $n = 11$); the corresponding delay time T_{max} ranges from 1-5 ps. The width then decreases as the excited state decays. The width at each pump-probe delay can be fit to:

$$\text{FWHM}_n(t) = \text{FWHM}_n(\infty) + d_2^{(n)} e^{-(t-t_0)/T_1^{(n)}} + d_3^{(n)} e^{-(t-t_0)/T_2^{(n)}} \quad (5.6)$$

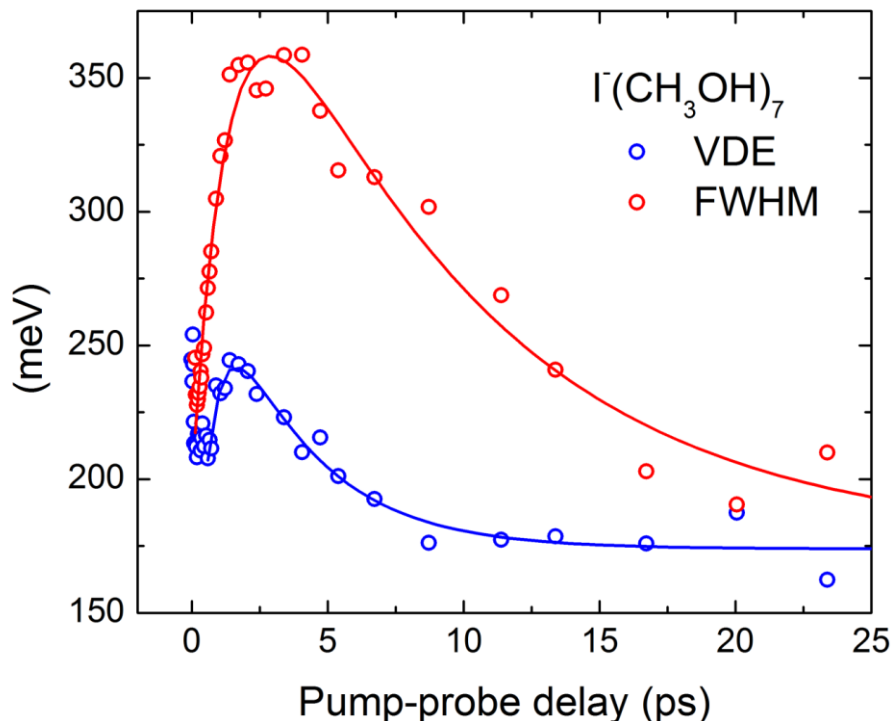


Figure 5.9. VDE (blue) and FWHM (red) as a function of pump-probe delay for $\text{I}^-(\text{CH}_3\text{OH})_7$.

where T_1 and T_2 describe the rise ($d_2 < 0$) and fall ($d_3 > 0$) times of the spectral width, respectively. The FWHM of $\text{I}^-(\text{CH}_3\text{OH})_7$ at each delay is also shown in Figure 5.9 alongside the VDE to their similar dynamics. As shown in the figure, the maximum width of the $[1+1']$ feature is reached slightly after VDE_{max} ; this is seen for all cluster sizes. The time constants T_{max} and T_2 are listed in Table 5.1.

Figure 5.11 compares the time-dependent FWHM of feature B in representative halide clusters with CH_3OH , H_2O , and CH_3CN .^{46,47} In all three solvents, the spectra broaden during the first 1-2 ps. However, for the latter two solvent species, the spectra rapidly narrow after only a few ps and their width remains constant throughout the remainder of the experimental window. In methanol, this decrease from maximal width occurs over a much longer timescale, as long as 30 ps for $n = 10$. The origin of this difference is considered in Section 5.

5.5 Discussion

In these experiments, the pump pulse ejects an electron from the iodide anion onto nearby solvent molecules, creating a cluster comprising several methanol molecules, an excess electron, and a neutral iodine atom. The initial configuration of the methanol molecules is set up to stabilize the iodide anion, and, as discussed below, significant rearrangement is expected to best accommodate the neutral iodine atom and excess electron. However, this accommodation is quite short-lived, because the electron leaves the cluster on a time scale varying from ~1- 85 ps over the cluster size range studied here. The TRPE spectra present a wealth of information that can shed light on these dynamics. The integrated intensities of Features A and B yield the population dynamics of the excited state, specifically the lifetime of the nascent anionic methanol cluster created by the pump pulse. The time-varying vertical detachment energy and

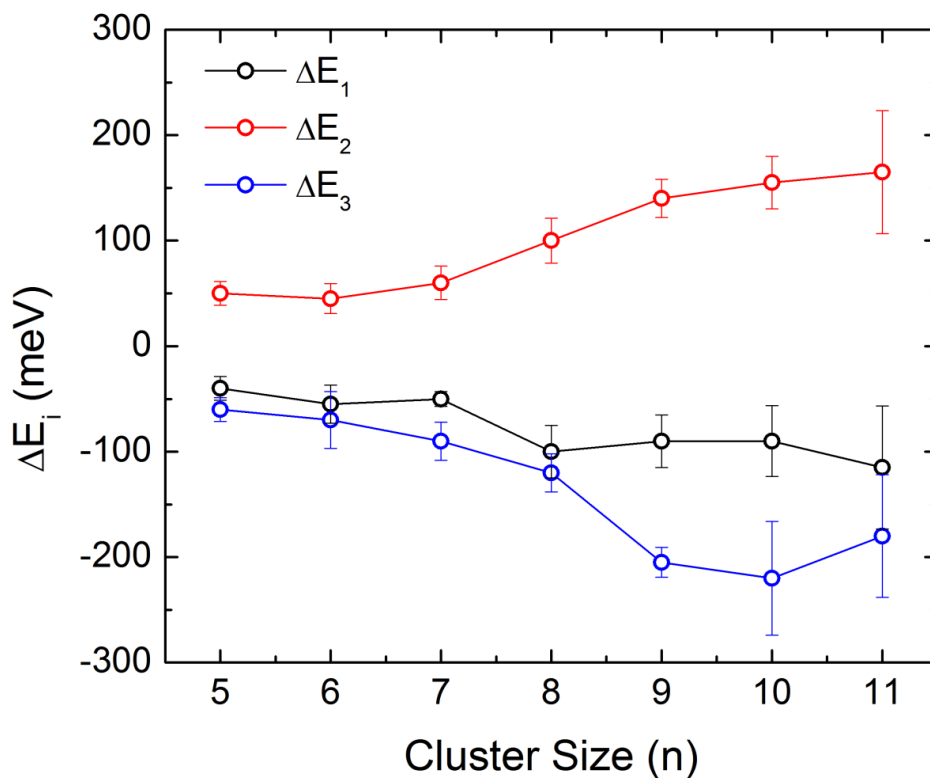


Figure 5.10. Changes in vertical detachment energies as a function of cluster size: $\Delta E_1 = VDE_{\min} - VDE(0)$ is shown as black circles, $\Delta E_2 = VDE_{\max} - VDE_{\min}$ is shown as red circles, and $\Delta E_3 = VDE(\infty) - VDE_{\max}$ is shown as blue circles. See text for details.

width of Feature B probe the response of the $I^-(CH_3OH)_n$ cluster to the ejection of an electron from the iodide anion. Each of these quantities and their evolution with time and cluster size provide insight into how small methanol clusters accommodate an excess charge. Comparison of these results with those obtained for iodide clustered with other solvents reveals significant differences in the overall dynamics.

Cluster size (n)	VDE(0)	VDE _{min}	VDE _{max}	VDE(∞)	ΔE_1	ΔE_2	ΔE_3
5	130 ± 10	90 ± 5	140 ± 10	80 ± 5	-40 ± 10	50 ± 15	-60 ± 10
6	195 ± 15	140 ± 10	185 ± 10	115 ± 25	-55 ± 15	45 ± 10	-70 ± 20
7	250 ± 5	200 ± 5	260 ± 15	170 ± 10	-50 ± 10	60 ± 20	-90 ± 10
8	330 ± 20	230 ± 15	330 ± 15	210 ± 10	-100 ± 30	100 ± 25	-120 ± 25
9	325 ± 10	235 ± 15	375 ± 10	170 ± 10	-90 ± 25	140 ± 30	-205 ± 20
10	345 ± 30	255 ± 15	410 ± 20	190 ± 50	-90 ± 15	155 ± 15	-220 ± 50
11	450 ± 50	335 ± 30	500 ± 50	320 ± 30	-115 ± 50	165 ± 50	-180 ± 50

Table 5.2. Vertical Detachment Energies (VDEs) at various time delays and associated changes for each cluster size for non-deuterated methanol, in meV. Values represent averages over data sets and errors represent the standard deviation of the mean.

5.5.1 Population dynamics

The “excited state” of the $\text{I}^-(\text{CH}_3\text{OH})_n$ clusters in these experiments approximately corresponds to charge transfer from the anion to the solvent network. After CTTS excitation, the electron is associated with the methanol cluster moiety in a perturbed, unequilibrated geometry. Bare methanol clusters have been shown to support anion states for clusters only as small as $n = 71$, well beyond the size range studied here.³⁶ In the absence of a stable final state, the excess electron in the $\text{I}^-(\text{CH}_3\text{OH})_n^-$ cluster created by the pump pulse cannot be supported and will autodetach. This interpretation is supported by the observation that the decay of the pump-probe signal, Feature B, and recovery of the autodetachment signal, Feature A, occur on essentially the same time scale, as discussed in Section 4. The integrated intensity of Feature B and the depletion of Feature A both represent the population of the excited state created by the pump pulse, so the two signals exhibit complementary temporal character. Direct observation of this channel and its complementary nature to Feature B allow us to fully account for the electron population after CTTS excitation. In the previous study by Davis, the fate of the electron could only be inferred from the data but could not be conclusively determined. Here we can confirm the mechanism for the ultimate decay of the excess electron, and can unequivocally say, for example, that it does not occur by recombination with the iodine atom.

The decay dynamics in this experiment are very different from those in our work on bare methanol cluster anions.³⁷ In those experiments, the excess electron associated with the methanol cluster is electronically excited, and decay of the excited state occurs by rapid (150-300 fs) internal conversion back to the ground electronic state of the anion, not by autodetachment. Here, in contrast, the perturbed methanol cluster anion created by CTTS excitation can be considered to be in its electronic ground state, so rapid internal conversion to a lower state is not possible. For smaller clusters, $n < 6$, only a single decay constant is needed to fit the integrated intensities. Larger clusters ($n \geq 6$) show a delayed rise with a time constant on the order of 1 ps. This delayed rise is commensurate with early evolution of the VDE and peak width that are discussed in more detail in Section 5.2. It most likely arises from rapid changes in the photodetachment cross section as the excess electron starts interacting more with the solvent network and less with the iodine atom.

The thermionic emission rate should depend on the initial cluster temperature, which we estimate to be 100-150K based on the evaporative ensemble model.⁴⁹ It would be of interest to perform these experiments on ions that have been actively cooled to much lower temperatures,⁵⁰ but we have not systematically varied the temperature thus far. The lifetimes measured here are in good agreement with those reported by Davis, with the exception of $n = 8$, the largest cluster considered in that work, for which they obtained a lifetime of 22 ps vs. 33 ps here. Owing to the improved signal-to-noise in the current experiment, and the observation that the newer value fits well within the size trend of the other clusters studied here (a larger range), we consider the new value to be more accurate.

The excited state lifetimes in these clusters as measured by decay of the pump-probe signal are much shorter than in $\text{I}^-(\text{H}_2\text{O})_n$ and $\text{I}^-(\text{CH}_3\text{CN})_n$,^{28, 46, 47} but are comparable with lifetimes in similarly-sized $\text{I}^-(\text{NH}_3)_n$ clusters.⁵¹ For example, the analogous lifetimes in $\text{I}^-(\text{H}_2\text{O})_7$ and $\text{I}^-(\text{H}_2\text{O})_{10}$ are 300 ps and least 3 ns, respectively. These differences may reflect the fact that $(\text{H}_2\text{O})_n^-$ and $(\text{CH}_3\text{CN})_n^-$ clusters are stable in this size range,^{52, 53} whereas $(\text{CH}_3\text{OH})_n^-$ and $(\text{NH}_3)_n^-$ clusters are not.⁵⁴

5.5.2 VDE's and peak widths

VDEs directly measure the difference in energy between the anion and neutral states at the instantaneous nuclear geometry as the cluster relaxes. These values show the same characteristics for all cluster sizes larger than $n \geq 5$, with individual values summarized in Tables 5.1 and 5.2. The excited state lifetime of the $n = 4$ cluster is too short for any significant relaxation to occur, and is not discussed further. The fast decrease in VDE, ΔE_1 , shown in Figures 5.8 and 5.9, is complete after the first 100-400 fs. It is unlikely that significant rearrangement of the cluster occurs this rapidly. Thus we attribute this portion of the relaxation to the electron interacting with both the solvent cluster and the iodine atom, forming the cluster analog of the “contact pair” that is proposed to form in the bulk. This fast change in the electron wavefunction contributes to the modulation in the photodetachment cross section observed in the early stages of the population dynamics. This modulation was not seen in the study by Davis but has been seen in studies of other halide-solvent clusters.^{46,47}

Similar to the situation in iodide-water clusters, the subsequent change in energy ΔE_2 is attributed to the solvent response to the newly established charge distribution. However, in $\text{I}^-(\text{H}_2\text{O})_n$ clusters, the longer time modulation ΔE_3 was ~ -50 meV, independent of cluster size, whereas in $\text{I}^-(\text{CH}_3\text{OH})_n$ clusters, ΔE_3 generally increases in magnitude with cluster size, from -60 to -220 meV over the size range considered here. The constant ΔE_3 in $\text{I}^-(\text{H}_2\text{O})_n$ clusters was attributed to the loss of the iodine atom from the water cluster anion, to which it is only weakly bound,⁵⁵ but here it seems unlikely that loss of an iodine atom is solely responsible for the strongly size-dependent ΔE_3 values in $\text{I}^-(\text{CH}_3\text{OH})_n$ clusters. Instead, we attribute these longer-time dynamics to solvent reorganization that destabilizes the anion relative to the neutral cluster.

The changing nature of the lineshape of Feature B is also shown in Figure 5.7 and the top panel of Figure 5.11. In photoelectron spectra where no vibrational structure is resolved, peak widths are dictated by the Franck-Condon factors reflecting the nuclear wavefunction overlap of the anion and neutral states; larger displacements of the anion geometry from the equilibrium geometry of the neutral yield more vibrational activity upon photodetachment and hence broader peaks. Therefore, the width of Feature B allows us to track the anion cluster geometry in relation to that of the neutral. This feature is widest around 2-5 ps, indicating maximal displacement from the neutral equilibrium geometry, and then narrows at longer times, indicating that the anion solvent configuration is approaching the geometry of the neutral methanol cluster.

Figure 5.12 shows a set of one dimensional potential energy curves that are consistent with our time-dependent VDE's and peak widths. These curves are loosely based on theoretical and experimental results on neutral^{56, 57} and anionic^{38, 58} methanol clusters, as well as halide-doped methanol clusters.^{27, 29-31} The x-axis represents the angle between the CO bond of a solvent molecule (the average OH dipole direction) and the cluster center. The minimum energy geometry of the anion has one or more OH groups directed at the I^- ion ($\theta_{\text{CO}} \sim 180^\circ$). Vertical excitation accesses the anion charge-transfer state. Both this state and the neutral methanol cluster have their lowest energy structures with the OH groups directed inward, maximizing the number of hydrogen bonds, so both of these surfaces will have minima at $\theta_{\text{CO}} \sim 0^\circ$. Due to the attractive nature of the $\text{OH} \cdots e^-$ interaction (~ 90 meV),⁵⁸ the anion surface may have a shallow minimum where the hydroxyl group is directed toward the electron center of mass. However this is not the global minimum, as the hydrogen bonds in methanol are each around 200 meV⁵⁹, leading to the deeper well at $\theta_{\text{CO}} \sim 0^\circ$. The reorientation of only one methanol is shown for

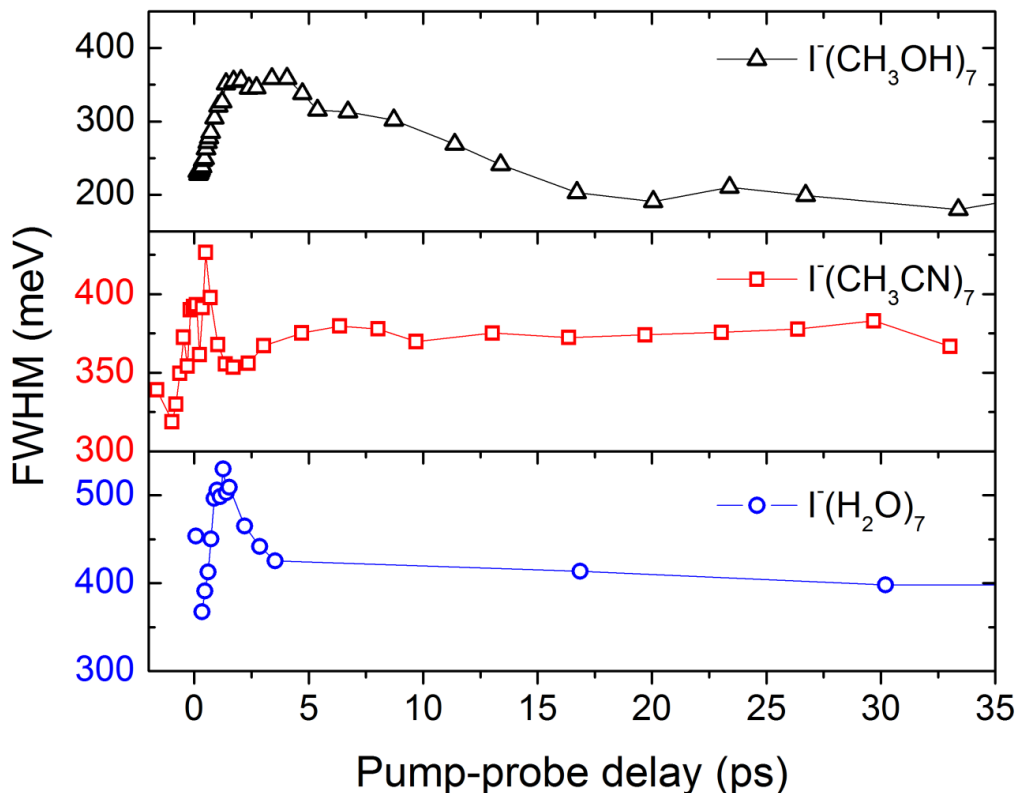


Figure 5.11. Spectral FWHM for the excited state feature of the $n = 7$ cluster of iodide-doped methanol (black triangles), acetonitrile (red squares), and water (blue circles).

simplicity, although the actual dynamics presumably involve collective solvent motion.

These curves, as drawn, are consistent with the salient features of our data. Specifically, the gap between the excited anion and neutral (the VDE of Feature B) first increases then rapidly decreases as the cluster relaxes along the reaction coordinate, explaining the positive value of ΔE_2 and the negative value of ΔE_3 . In addition, the initially prepared excited anion state lies above the minimum of the neutral curve, so autodetachment is energetically possible. In this one-dimensional picture, the widths of the photoelectron peaks are determined by the relative slopes of the potential energy curves at a given angle (the “reflection” principle of photodissociation⁶⁰). Here again, these curves show that the width will increase to a maximum before decreasing again as θ_{CO} approaches 0° . We emphasize, however, that the curves in Figure 5.12 are drawn to show that a simple and reasonable one-dimensional picture can explain our data; electronic structure calculations are needed to validate them.

The timescales observed in these experiments are in keeping with the proposed mechanism. Specifically, one expects those CH_3OH molecules with their OH bonds initially oriented towards the iodide at the surface of the cluster to undergo a half-rotation, resulting in more hydrogen bonds with other solvent molecules. A lower bound for the time associated with this rotation can be estimated as half of the $J = 1$ end-over-end rotational period for free methanol under the rigid rotor approximation for an asymmetric top,⁶¹ which is ~ 9 -10 ps. This motion will be hindered and slowed due to interactions with the other methanol molecules in the cluster, especially if the hydrogen bonds in the remainder of the cluster need to be broken in order to accommodate the additional contribution to the solvent network. Preliminary results on

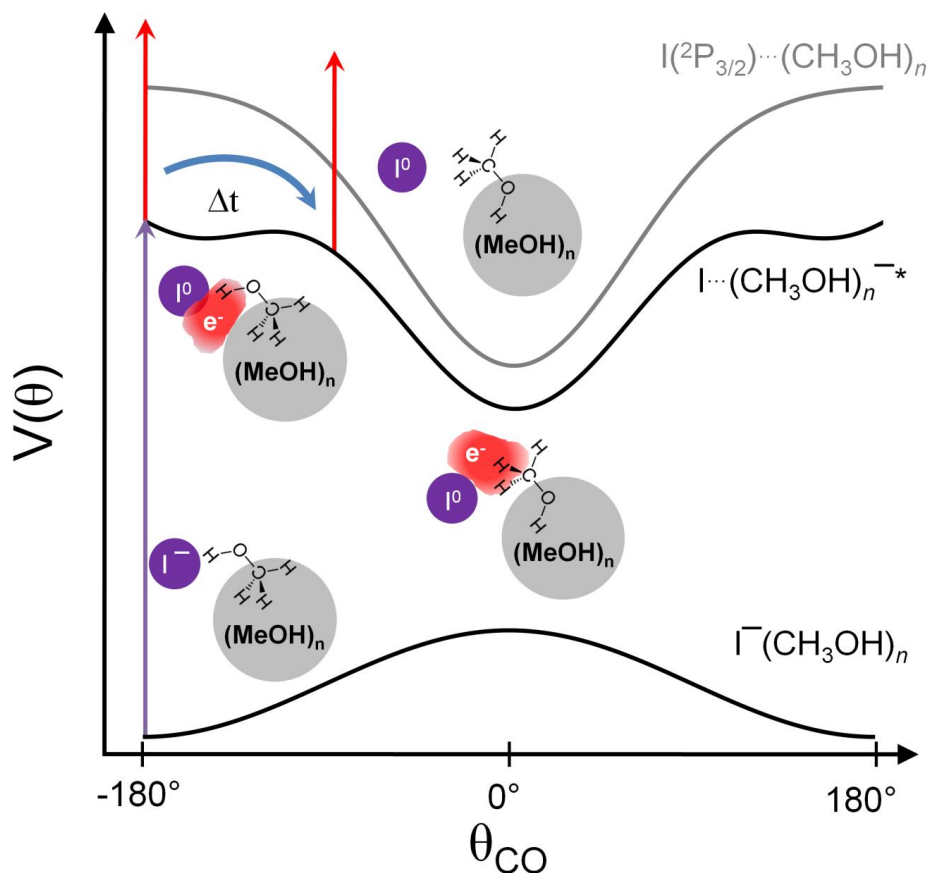


Figure 5.12. Schematic potential energy surfaces for $\text{I}^-(\text{CH}_3\text{OH})_n$ with associated geometries inferred from the spectra. Motion of one methanol molecule is shown for simplicity; the remaining solvent moiety is depicted as $(\text{MeOH})_n$. See text for details.

$\text{I}^-(\text{ethanol})_n$ clusters show similar behavior, however the relaxation of the width takes ~ 1.4 times longer, roughly consistent with the ratio of rotational constants of the two molecules, and supporting this interpretation.

This relaxation mechanism is quite different than that proposed for halide-water clusters. $\text{I}^-(\text{H}_2\text{O})_n$ clusters have been predicted to solvate iodide on their surface until at least $n \sim 55$.⁶² Excess electrons in water clusters have been shown to exist in a variety of binding motifs,^{50, 63} with surface-bound states dominating at smaller sizes.⁶⁴ However, in contrast to methanol clusters, these surface-bound electrons interact with free OH bonds at the cluster surface. The ability to form only one hydrogen bond makes the energetics of the $\text{OH}\cdots\text{e}^-$ and $\text{OH}\cdots\text{O}$ interaction much more important in methanol than in water. Hence, relaxation of the solvent network certainly occurs upon CTTS excitation of $\text{I}^-(\text{H}_2\text{O})_n$ clusters, but with less disruption to the cluster geometries compared to methanol clusters, as indicated by the constant widths at longer times of the excited state photoelectron spectra of $\text{I}^-(\text{H}_2\text{O})_n$ clusters (see Figure 5.11). In a similar vein, there is reasonably strong evidence that both iodide^{65, 66} and excess electrons^{53, 67-69} are internally solvated in $\text{I}^-(\text{CH}_3\text{CN})_n$ and $(\text{CH}_3\text{CN})_n^-$ clusters, respectively. Thus both the initial and final states lie within the same solvent cavity, again reducing the extent of solvent reorientation needed upon excitation of $\text{I}^-(\text{CH}_3\text{CN})_n$ clusters. Despite being chemically similar to both water and acetonitrile, the ability of methanol to both hydrogen bond and to stabilize a

charged species with its methyl terminus cause it to have significantly different dynamics than either solvent.

5.5.3 Comparison to larger systems

A key question raised by these cluster studies is how the energetics and dynamics observed here correlate with those seen larger methanol cluster anions and with electrons in liquid methanol. We first compare the long-time VDEs measured here to the those seen in one-photon PE spectra of $(\text{CH}_3\text{OH})_n^-$ clusters. As the cluster size increases, the binding energy of the nascent methanol cluster anion should increase, eventually approaching that of the appropriate stable cluster anion isomer. As seen in Table 5.2, $\text{VDE}(\infty)$ does increase with cluster size; by $n = 11$ it is 320 meV, already larger than the VDE of 190 meV of $(\text{CH}_3\text{OH})_{73}^-$ isomer II, the smallest isomer II cluster seen previously.³⁶ It thus appears that in the current work, the excess electron in the asymptotic cluster configuration (i.e. just prior to autodetachment) is more tightly bound than in an isomer II cluster.

A similar picture arises from the photoelectron angular distribution, where we observe Feature B to have a sizeable anisotropy (~ 0.7 - 1.0) near t_0 that becomes much more isotropic prior to its decay. Our previous one photon study on large methanol cluster anions ($n \sim 70$ - 460) found smaller anisotropy parameters ($\beta_2 \sim 0.25$ - 0.16) for the more tightly bound isomer I clusters, while higher values ($\beta_2 \sim 0.90$ - 0.72) were seen for isomer II clusters.³⁶ Hence, while there is a significant difference between clusters of 70+ and clusters of 10 molecules, the photoelectron angular distributions also suggest that isomer II clusters are not the appropriate asymptotic limit in the $\text{I}^-(\text{CH}_3\text{OH})_n$ experiments. This is not to say that the picture of solvent re-orientation in Figure 5.12 is incorrect; instead the implication is that the excess electron interacts more strongly with the solvent network in these clusters than in the very diffuse surface state of an isomer II cluster.

It would be of considerable interest to extend the $\text{I}^-(\text{CH}_3\text{OH})_n$ experiments to much larger clusters to see if the long-time VDEs approached those of isomer I methanol cluster anions. This would provide for a continuous evolution to the structure of the solvated electron in liquid methanol whose suggested structure is for the OH groups of the alcohol to be directed toward the electron's center of mass.^{19, 22, 70}

Time-resolved experiments²⁵ on photodetachment of I^- in bulk methanol and related theoretical treatments^{71, 72} indicate that CTTS excitation leads to formation of an I: e^- "contact pair" on a time-scale of 200-300 fs. The newly formed electron can undergo either diffusive escape to form a solvated electron or geminate recombination with the iodine atom.^{5, 25, 73} Diffusion is not applicable to an isolated cluster of 4-11 molecules, and likewise recombination is not expected or even possible if the iodine evaporates from the cluster after relaxation. On the other hand, the time scale for contact pair formation in solution is similar to that associated with the initial drop in VDE to VDE_{min} in the cluster experiments (see Figure 5.8). As pointed out by Vilchiz *et al.*,²⁵ the contact pair in methanol does not decay to a thermalized solvated electron. Instead, the electron is initially formed in a "trapped" or "hot" state after it is injected into the liquid. The authors monitored its subsequent relaxation by shifts in the transient absorption spectrum of the electron in the spectral range of 500-700 nm. This relaxation occurred on a time scale of 10 ps for electrons in methanol, after which no further spectral evolution was observed. Spectral shifting on a similar time scale is also seen in experiments in which electrons in methanol are electronically excited.^{16-18, 21} In both types of experiments, this relaxation is

associated with the characteristic rotational time scale of a methanol molecule in solution.^{15, 25, 74} In the cluster experiments, we see relaxation of the VDEs on a 10 ps time scale and have attributed this process to solvent rotational motion based on consideration of initial and final states of the cluster. Hence, it appears that solvent rotation is playing a key role in relaxation phenomena seen both in solution and in our anion clusters.

Recent theoretical work on electron solvation in large methanol clusters following electron attachment were published just after these results by Mones, *et al.*⁷⁵ In that study, an electron was attached to a large, equilibrated methanol cluster and the dynamics of solvation were calculated using mixed-quantum classical molecular dynamics in a newly developed electron-methanol pseudopotential. The electrons were shown to reside on the surface of the cluster until a thermally-driven fluctuation ($T \sim 200$ K) brought the hydroxyl group of one methanol molecule to the surface near the electron density. The more favorable interaction between the -OH group compared to the -CH₃ groups at the surface causes the electron to follow the motions of that fluctuating methanol molecule as it moves to pointing the OH group back toward the cluster center, thus internalizing the electron, in a similar manner to the dynamics proposed in the study presented here. The internalization process occurs over a ~ 50 ps timescale. The similarity in the two studies is striking, however, there are notable differences. The clusters in the simulations were much larger than those presented here (50-500 molecules/cluster) and the bath temperature was also higher than the estimate for our clusters. Moreover, the mechanism of charge injection is fundamentally different; the electron ejected from the iodide will have a certain amount of excess energy following CTTS excitation, which has been shown to affect its autodetachment lifetime⁷⁶ and could conceivably affect its relaxation dynamics. However, that the fundamental mechanism for relaxation is the same in both studies and achieved through very different methods suggests the general picture is correct.

5.6 Conclusions

We have measured the charge-transfer-to-solvent dynamics of $\text{I}^-(\text{CH}_3\text{OH})_n$ clusters from $n = 4$ -11 with time-resolved photoelectron imaging. Vibrational autodetachment is observed to be the primary decay pathway, occurring over ~ 1 -100 ps for this size range. The changes in the vertical detachment energies and the shapes of the spectra have been interpreted in light of newly investigated geometries of the initial and final states. Excitation of the charge transfer band leads to ejection of the excess electron from iodide onto a part of the solvent cluster, forming an unequilibrated methanol cluster anion. These clusters then relax towards the equilibrium geometry of bare anionic methanol clusters which have been shown by previous studies to have their OH bonds directed inward and their methyl groups pointing toward the surface. This relaxation is reflected in the changes in VDE and width of the excited state feature of the photoelectron spectrum and occurs over ~ 10 -20 ps, a timescale consistent with end-over-end rotation of methanol. The contribution to the long-time destabilization from iodine loss or solvent evaporation cannot be entirely ruled out. Simulations and *ab initio* geometries would be invaluable in investigating the proposed relaxation mechanism. Complementary infrared photodissociation studies on larger $\text{I}^-(\text{CH}_3\text{OH})_n$ ($n > 2$) would also be of use in determining the initial halide-solvent cluster geometries. Time-resolved CTTS experiments on higher alcohol clusters, specifically ethanol, will also be of interest, as these clusters should undergo a similar relaxation mechanism; these studies are currently underway in our laboratory.

5.7 References

- 1 E. J. Hart, and M. Anbar, *The Hydrated Electron* (Wiley-Interscience, New York, 1970).
- 2 J. Schnitker, and P. Rossky, *J. Chem. Phys.* **86** (6), 3471 (1987).
- 3 J. Jortner, M. Ottolenghi, and G. Stein, *J. Phys. Chem.* **68**, 247 (1964).
- 4 S. E. Bradforth, and P. Jungwirth, *The Journal of Physical Chemistry A* **106** (7), 1286 (2002).
- 5 X. Chen, and S. E. Bradforth, *Annu. Rev. Phys. Chem.* **59**, 203 (2007).
- 6 N. Chandrasekhar, and P. Krebs, *J. Chem. Phys.* **112** (13), 5910 (2000).
- 7 A. E. Bragg, and B. J. Schwartz, *J. Phys. Chem. B* **112**, 483 (2008).
- 8 A. E. Bragg, and B. J. Schwartz, *J. Phys. Chem. A* **112**, 3530 (2008).
- 9 C. Xia, J. Peon, and B. Kohler, *J. Chem. Phys.* **117** (19), 8855 (2002).
- 10 M. F. Fox, and E. Hayon, *Chem. Phys. Lett.* **25** (4), 511 (1974).
- 11 D. Serxner, C. E. H. Dessent, and M. A. Johnson, *J. Chem. Phys.* **105** (16), 7231 (1996).
- 12 L. Lehr *et al.*, *Science* **284**, 635 (1999).
- 13 D. M. Neumark, *Mol. Phys.* **106** (16-18), 2183 (2008).
- 14 O. T. Ehrler, and D. M. Neumark, *Acc. Chem. Res.* **42** (6), 769 (2009).
- 15 W. J. Chase, and J. W. Hunt, *J. Chem. Phys.* **79** (26), 2835 (1975).
- 16 C. Pepin *et al.*, *J. Phys. Chem.* **98**, 7009 (1994).
- 17 X. Shi *et al.*, *J. Phys. Chem.* **99**, 6917 (1995).
- 18 C. Silva *et al.*, *J. Phys. Chem. A* **102** (28), 5701 (1998).
- 19 M. J. Tauber, C. M. Stuart, and R. A. Mathies, *J. Am. Chem. Soc.* **126** (11), 3414 (2004).
- 20 T. Scheidt, and R. Laenen, *Chem. Phys. Lett.* **371**, 445 (2003).
- 21 A. Thaller, R. Laenen, and A. Laubereau, *J. Chem. Phys.* **124** (2006).
- 22 L. Turi, A. Mosyak, and P. Rossky, *J. Chem. Phys.* **107** (6), 1970 (1997).
- 23 P. Minary, L. Turi, and P. J. Rossky, *J. Chem. Phys.* **110** (22), 10953 (1999).
- 24 L. Mones, and L. Turi, *J. Chem. Phys.* **132** (15), 154507 (2010).
- 25 V. H. Vilchiz *et al.*, *Radiation Physics and Chemistry* **72** (2-3), 159 (2005).
- 26 C. E. H. Dessent, C. G. Bailey, and M. A. Johnson, *J. Chem. Phys.* **103** (6), 2006 (1995).
- 27 W. H. Robertson *et al.*, *J. Chem. Phys.* **116** (12), 4853 (2002).
- 28 A. V. Davis *et al.*, *J. Electron Spec.* **108**, 203 (2000).
- 29 O. M. Cabarcos *et al.*, *J. Chem. Phys.* **110** (19), 9516 (1999).
- 30 C. A. Corbett, T. J. Martinez, and J. M. Lisy, *J. Phys. Chem. A* **106** (42), 10015 (2002).
- 31 J. P. Beck, and J. M. Lisy, *J. Phys. Chem. A* **114**, 10011 (2010).
- 32 R. Ayala *et al.*, *J. Phys. Chem. A* **104**, 2799 (2000).
- 33 L. X. Dang, *J. Phys. Chem. A* **108** (42), 9014 (2004).
- 34 L. Cwiklik *et al.*, *Chemphyschem* **8** (10), 1457 (2007).
- 35 P. Jungwirth, and D. J. Tobias, *J. Phys. Chem. B* **106** (25), 6361 (2002).
- 36 A. Kammrath *et al.*, *J. Chem. Phys.* **125**, 171102 (2006).
- 37 A. Kammrath *et al.*, *J. Chem. Phys.* **126**, 244306 (2007).
- 38 L. Mones, P. J. Rossky, and L. Turi, *J. Chem. Phys.* **133** (14), 144510 (2010).
- 39 A. V. Davis *et al.*, *J. Chem. Phys.* **118** (3), 999 (2003).
- 40 U. Even *et al.*, *J. Chem. Phys.* **112** (18), 8068 (2000).
- 41 W. C. Wiley, and I. H. McLaren, *Rev. Sci. Instrum.* **26** (12), 1150 (1955).
- 42 A. T. J. B. Eppink, and D. H. Parker, *Rev. Sci. Instrum.* **68** (9), 3477 (1997).
- 43 V. Dribinski *et al.*, *Rev. Sci. Instrum.* **73** (7), 2634 (2002).

- 44 G. A. Garcia, L. Nahon, and I. Powis, *Rev. Sci. Instrum.* **75** (11), 4989 (2004).
45 K. L. Reid, *Annu. Rev. Phys. Chem.* **54**, 397 (2003).
46 A. Kammrath *et al.*, *J. Phys. Chem. A* **109**, 11475 (2005).
47 O. T. Ehrler *et al.*, *J. Phys. Chem. B* **113**, 4031 (2009).
48 R. Reichle, H. Helm, and I. Y. Kiyan, *Phys. Rev. Lett.* **87** (24), 243001 (2001).
49 C. E. Klots, *Z. Phys. D* **20** (1), 105 (1991).
50 L. Ma *et al.*, *J. Chem. Phys.* **131** (14), 144303 (2009).
51 C. Frischkorn *et al.*, *Faraday Disc.* **115**, 49 (2000).
52 J. V. Coe *et al.*, *J. Chem. Phys.* **92** (6), 3980 (1990).
53 M. Mitsui *et al.*, *Phys. Rev. Lett.* **91** (15), 153002 (2003).
54 G. H. Lee *et al.*, *Z. Phys. D* **20** (1-4), 9 (1991).
55 H. M. Lee, S. B. Suh, and K. Kim, *J. Chem. Phys.* **119**, 7685 (2003).
56 R. A. Provencal *et al.*, *J. Chem. Phys.* **110** (9), 4258 (1999).
57 I. Natkaniec *et al.*, *Chem. Phys.* **317**, 171 (2005).
58 L. Turi, *J. Chem. Phys.* **110** (21), 10364 (1999).
59 G. C. Pimentel, and A. L. McClellan, *The Hydrogen Bond* (Reinhold Publishing Corporation, New York, N.Y., 1960).
60 R. Schinke, *Photodissociation Dynamics* (Cambridge University Press, New York, NY, 1993), Cambridge Monographs on Atomic, Molecular, and Chemical Physics.
61 T. Iijima, *Journal of Molecular Structure* **212**, 137 (1989).
62 D. M. Koch, and G. H. Peslherbe, *Chem. Phys. Lett.* **359** (5-6), 381 (2002).
63 J. R. R. Verlet *et al.*, *Science* **307**, 93 (2005).
64 N. I. Hammer *et al.*, *Science* **306**, 675 (2004).
65 G. Markovich *et al.*, *J. Chem. Phys.* **105** (7), 2675 (1996).
66 T. Takayanagi, *J. Phys. Chem. A* **110** (22), 7011 (2006).
67 T. Takayanagi, *Chem. Phys.* **302**, 85 (2004).
68 T. Takayanagi, *J. Chem. Phys.* **122**, 244307 (2005).
69 T. Takayanagi, T. Hoshino, and K. Takahashi, *Chem. Phys.* **324**, 679 (2006).
70 L. Kevan, *Chem. Phys. Lett.* **66** (3), 578 (1979).
71 W.-S. Sheu, and P. J. Rossky, *J. Phys. Chem.* **100**, 1295 (1996).
72 A. Staib, and D. Borgis, *J. Chem. Phys.* **104**, 9027 (1996).
73 J. A. Kloepfer *et al.*, *Chem. Phys. Lett.* **298**, 120 (1998).
74 T. Goulet *et al.*, *Radiation Physics and Chemistry* **54** (5), 441 (1999).
75 L. Mones, P. J. Rossky, and L. Turi, **135** (8), 084501 (2011).
76 M. A. Yandell *et al.*, *The Journal of Physical Chemistry A* (2011).

Chapter 6. Photoelectron Imaging of Tetrahydrofuran Cluster Anions $(\text{THF})_n^-$ ($1 \leq n \leq 100$)

[Reprinted with permission from "Photoelectron imaging of tetrahydrofuran cluster anions $(\text{THF})_n^-$ ($1 \leq n \leq 100$)" R. M. Young, M. A. Yandell, M. Niemeyer, D. M. Neumark, J. Chem. Phys. 133, 154312 (2010)]

Anionic tetrahydrofuran clusters $(\text{THF})_n^-$ ($1 \leq n \leq 100$) are studied with photoelectron imaging as gas-phase precursors for electrons solvated in THF. Photoelectron spectra of clusters up to $n = 5$ show two peaks, one of which is attributed to a solvated open chain radical anion and the other to the closed THF ring. At $n = 6$, the spectra change shape abruptly, becoming more characteristic of $(\text{THF})_n^-$ clusters containing solvated electrons. From $n = 6$ -100, the vertical detachment energies (VDEs) of these solvated electron clusters increase from 1.96 eV to 2.71 eV, scaling linearly with $n^{-1/3}$. For fully deuterated $(\text{THF-d8})_n^-$ clusters, the apparent transition to a solvated electron cluster is delayed to $n = 11$. Extrapolation of the VDEs to infinite cluster size yields a value of 3.10 eV for the bulk electron detachment energy. The relatively large VDEs at onset and small stabilization with increasing cluster size compared to other solvated electron clusters may reflect the tendency of the bulk solvent to form preexisting voids that can readily solvate a free electron.

6.1 Introduction

The solvated electron has long been of interest to physical scientists as it plays a key role in diverse phenomena including quantum interactions in condensed phases,^{1, 2} the atmospheric chemistry of aerosols,³ and low-energy radiation damage of DNA.⁴ Solvated electrons are the simplest quantum mechanical solute, and studies of electron solvation phenomena probe fundamental aspects of this solute-solvent interaction.^{1, 5, 6} While solvated electrons are most frequently studied in aqueous solution,^{1, 7} they exist in a multitude of organic and inorganic solvents.^{8, 9, 10} Experiments in solution have been complemented by studies of gas phase water cluster anions¹¹⁻¹⁴ and clusters comprising electrons bound to other solvent molecules such as acetonitrile,^{15, 16} benzene,¹⁷ methanol,^{18, 19} and formamide.²⁰ The cluster work has yielded a great deal of insight into how excess electrons interact with small numbers of molecules and how this interaction evolves toward that of the bulk solution as the number of solvent molecules increases.^{21, 22} In this study, we report experiments in which tetrahydrofuran cluster anions $(\text{THF})_n^-$ are observed for the first time and are characterized using photoelectron spectroscopy in order to study the solvation of excess electrons in a weakly polar medium.

The interaction of THF with electrons has been studied in both gas phase and condensed phase environments. The gas phase experiments and accompanying theory have considered electron scattering total and differential cross sections,²³⁻²⁵ the ion mass distribution resulting from dissociative electron attachment,^{26, 27} and the electron energy loss spectrum.²⁸ These investigations are motivated by the notion that THF is a model system for the ribose ring in nucleic acids, and that electron scattering from THF can thus provide insight into the radiation damage induced in DNA by low energy electrons.

More relevant to the work reported here are the extensive experimental and theoretical studies by Schwartz²⁹⁻³³ and Ruhman³⁴ on the spectroscopy and dynamics of solvated electrons in liquid THF. Most of these experiments have focused on forming the sodide (Na^-) anion in THF, ejecting an electron into the solvent by excitation of the charge-transfer-to-solvent (CTTS) transition with a femtosecond laser pulse, and monitoring the ensuing dynamics with one or two femtosecond probe pulses. The CTTS transition for the sodide anion, which is easily formed in THF, is centered around 780 nm, making it readily accessible to Ti:sapphire laser excitation, while the absorption spectrum of solvated electrons in THF peaks around 2000 nm and is hence well-separated from the CTTS transition. The overall experimental arrangement is similar to that used for the CTTS excitation of halide anions in aqueous solution,³⁵ but both the CTTS and solvated electron transitions are substantially red-shifted in the sodide/THF experiments.

Simulations by Schwartz^{30,31} and neutron diffraction experiments by Soper³⁶ have shown that liquid THF has unusual aspects that can significantly affect electron solvation. Specifically, there appear to be pre-existing voids with diameters in the range of 2.5-5 Å within the solvent network. Moreover, the simulations and experiments suggest that these empty spaces are partially positively polarized and can therefore act as traps for solvated electrons, allowing for solvation with little nuclear rearrangement. The presence of these voids has been invoked by Sanche³⁷ to explain the very high trapping efficiency of low energy electrons by thin films of THF. This picture of electron solvation in THF is in sharp contrast to the widely accepted cavity model for electrons in water,¹ in which the electrons have to push water molecules aside to form a cavity with a radius of ~2.5 Å. Moreover, in water, the low-lying excited states of the hydrated electron are quite localized with respect to its ground state, whereas in THF the excited states have amplitude not only in the pre-formed cavity in which the electron originally resides, but also in nearby unoccupied cavities.³⁰

The condensed phase results on electrons in THF raise the question of how the properties of liquid THF might manifest themselves in negatively charged cluster anions. Specifically, it is of considerable interest to determine if the tendency of bulk THF to form pre-existing voids that can readily accommodate excess electrons translates into measurable trends in the energetics, spectroscopy, and dynamics of $(\text{THF})_n^-$ clusters. As a first step in this direction, we report the first observation of $(\text{THF})_n^-$ clusters in the gas phase and their one-photon photoelectron spectra. The experiments yield vertical detachment energies (VDEs) for clusters up to $n = 100$, and provide evidence that a minimum of six THF molecules is needed to form a “solvated electron cluster”.

6.2 Experimental

The experiments were performed on our time-resolved anion photoelectron imaging apparatus,³⁸ although the work described here did not involve any explicitly time-resolved measurements. Briefly, argon gas at 20 psig was flowed over THF at room temperature, where it picked up the vapor over the liquid and was co-expanded into a vacuum chamber through a pulsed solenoid valve³⁹ operating at 100 Hz. Collisions within the expansion cooled the gas and induced clustering of the THF molecules. Ionization occurred via secondary attachment of electrons from a ring-electrode ionizer that intercepted the gas during expansion. The resulting ions were then injected perpendicularly into a Wiley-McLaren time-of-flight (TOF) mass spectrometer.⁴⁰ An electrostatic switch pulsed at the appropriate delay time acted as a mass gate, allowing ions of the desired mass to pass into the interaction region where a laser pulse

photodetached the electrons. Mass spectra were collected with a retractable microchannel plate (MCP) detector within the interaction region and recorded on a digital oscilloscope (Tektronix DPO3034).

The photodetachment light pulse was generated by a commercial Ti:sapphire oscillator and multipass chirped pulse amplifier (KM Labs Griffin oscillator, Dragon amplifier), yielding 30 fs pulses at 790 nm (1.57 eV). A fraction of this light was then directed into a 29.2° BBO crystal to generate the second harmonic at 395 nm (3.14 eV, 100 μJ/pulse at 600 Hz) which was used to photodetach the anions. For photodetachment cross section measurements, the visible output (sum-frequency idler) of an optical parametric amplifier (Light Conversion TOPAS-4 800) was used.

The resulting photoelectrons were accelerated, detected and analyzed using velocity map imaging (VMI),⁴¹ yielding their kinetic energy and angular distributions. The imaging detector comprised a chevron-mounted dual MCP stack coupled to a phosphor screen. 12-bit images were recorded at 30 frames per second with a CCD camera. Images were integrated over ~10⁵ laser pulses, with 5-10 photoelectrons/pulse. The resulting images were then four-way symmetrized to account for detector inhomogeneities and transformed with the basis-set expansion (BASEX) method,⁴² recovering the full velocity distribution. The VMI/camera system was calibrated by photodetachment of O₂⁻ anions⁴³ with 395 nm laser pulses.

Angular integration of the transformed images yielded the electron speed distribution, from which one derives the distribution of electron kinetic energies (eKE) and electron binding energies (eBE), where eBE = $h\nu - eKE$. Single photon photoelectron angular distributions (PADs) were recovered by fitting the transformed images to^{44, 45}:

$$I(\theta, eKE; n) = \frac{\sigma_{total}}{4\pi} [1 + \beta_2(eKE; n)P_2(\cos \theta)] \quad (6.1)$$

Here θ is the angle between the ejected photoelectron wave and the laser polarization, σ_{total} is the total photodetachment cross section, n is the cluster size, $P_2(\cos \theta)$ is the second-order Legendre polynomial. The anisotropy parameter β_2 , which lies between 2 and -1, specifies the nature of the PAD at each value of the eKE.

To aid in assigning the photoelectron spectra, electronic structure calculations were performed using Density Functional Theory (DFT) with the B3LYP functional and the 6-311++G** basis set for correlation in the Gaussian '03⁴⁶ software package. The VDEs for species of interest were computed as the difference in absolute energies between anion and neutral molecules frozen at the optimized anion geometry.

6.3 Results and Analysis

6.3.1 Mass spectrum

A representative anion mass spectrum is shown in Figure 6.1. Nearly all peaks in the spectrum fit a (THF)_{*n*}⁻ cluster distribution beginning at $n = 1$ ($m/z = 72$), with single-size resolution extending to $n \sim 55$, beyond which clusters can still be isolated to within $\Delta m/m \sim 1\%$ using the calibration method described previously.^{13, 18} The inset of Figure 6.1 shows the first few peaks of the mass distribution. The signal near $n = 1$ is split into two peaks with $m/z = 71$ and 72, both of which are discussed in more detail below. Ions generated from fully deuterated

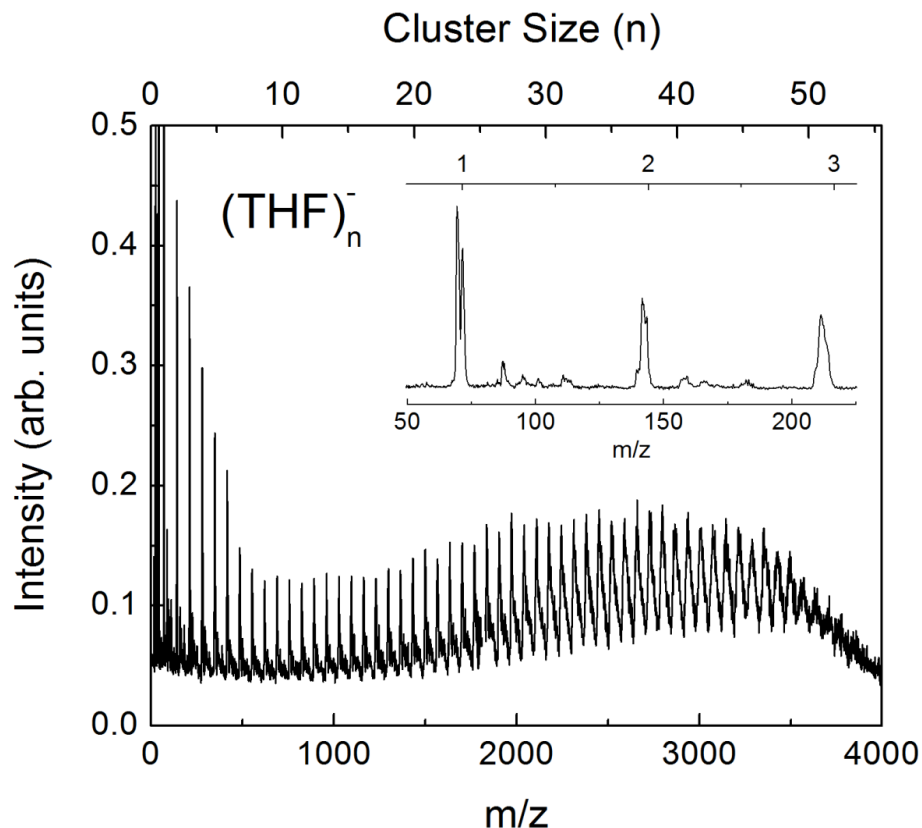


Figure 6.1. Time-of-Flight mass spectrum of $(\text{THF})_n^-$ cluster anions. Inset shows mass spectrum in the range $n = 1-3$. The first peak is split by the presence of $(1,2)\text{-}s\text{-C}_4\text{H}_7\text{O}^-$ at $m/z = 71$. Cluster number assignments are assigned based on flight times relative to this peak.

THF-d8 show the analogous pattern of peaks (with different peak separations), while ions generated from a different constitutional isomer of $\text{C}_4\text{H}_8\text{O}$, butyraldehyde, yield a very different mass spectrum. These additional measurements support assignment of the main pattern of peaks in Fig. 6.1 to $(\text{THF})_n^-$ clusters.

6.3.2 Photoelectron spectra

Fig. 6.2 shows the photoelectron (PE) spectrum of the anion at $m/z = 72$ (blue curve), where it is compared to that of the anion at $m/z = 71$ (red curve). The PE spectrum of the $m/z = 71$ peak corresponds to that of the *sec*-butyraldehyde enolate $[(1,2)\text{-}s\text{-C}_4\text{H}_7\text{O}^-]$ as observed by Continetti *et al.*⁴⁷ The spectrum for $m/z = 72$ has two clear peaks at VDE = 1.12 eV (Feature A) and VDE = 1.87 eV (Feature B). Feature A is structureless and narrow, with a full-width at half-maximum (FWHM) of 130 meV, larger than the experimental resolution of 45 meV set by the bandwidth of the femtosecond laser pulse. The anisotropy parameter β associated with this feature is 1.60 ± 0.10 , signifying that this feature originates from a highly symmetric *s*-like molecular orbital. The shape of Feature B suggests underlying vibrational structure, and its PAD is isotropic, with $\beta \sim 0$. The PE spectrum of the anion with $m/z = 80$ from THF-d8 is also shown in Fig. 6.2; Feature B is the same in this spectrum, but Feature A is much less intense.

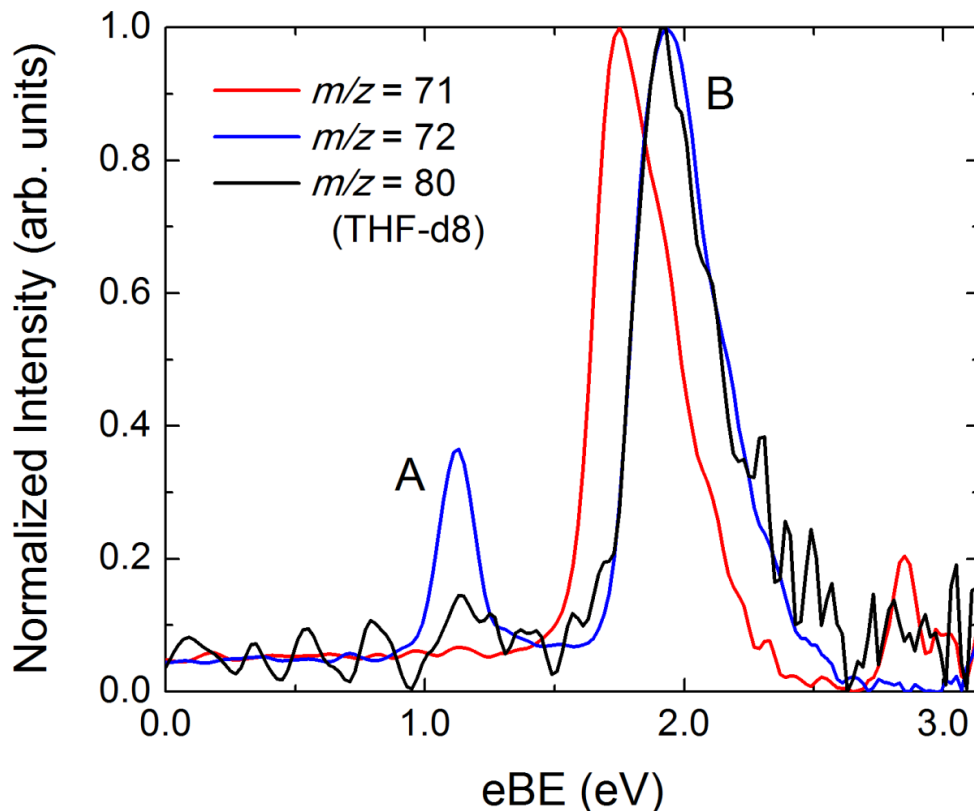


Figure 6.2. Photoelectron spectrum of $m/z = 71$ (red), $m/z = 72$ (blue), and $m/z = 80$ (black) taken at a photon energy of 3.14 eV. The curve for $m/z = 72$ shows two peaks: Feature A at 1.12 eV and Feature B at 1.87 eV.

Fig. 6.3 shows normalized photoelectron spectra for selected members of the $(\text{THF})_n^-$ progression from $n = 1$ to $n = 100$. The two sharp features seen in Fig. 6.2, A and B, are apparent up to $n = 5$, and progressively shift to higher binding energies with increasing cluster size. By $n = 5$, feature B is barely accessible at our photodetachment energy of 3.14 eV. The relative intensities of both features remain constant over $n = 1-5$.

At $n = 6$, the PE spectral shape changes dramatically compared to the smaller clusters, becoming markedly broader and less symmetric. From $n = 6-100$, the vertical detachment energies (VDEs) increase monotonically from 1.96 eV to 2.71 eV; VDEs at each cluster size are determined by fitting the binding energy spectrum to a Gaussian distribution peaked at the VDE with width w_G (FWHM = $2w_G\sqrt{\ln 2}$). For larger cluster sizes ($n \geq 50$), the asymmetry becomes more pronounced and the spectra are best fit to a Gaussian-Lorentzian profile²¹ where the low and high binding energy sides of the peak energy (VDE_{*n*}) are fit by a Lorentzian with width w_L and a Gaussian with width w_G , respectively:

$$I(eBE; n) = \begin{cases} I_0 + A \left[\frac{w_L^2}{(eBE - \text{VDE}_n)^2 + w_L^2} \right] & eBE < \text{VDE}_n \\ I_0 + Ae^{-\frac{(eBE - \text{VDE}_n)^2}{w_G^2}} & eBE \geq \text{VDE}_n \end{cases} \quad (6.2)$$

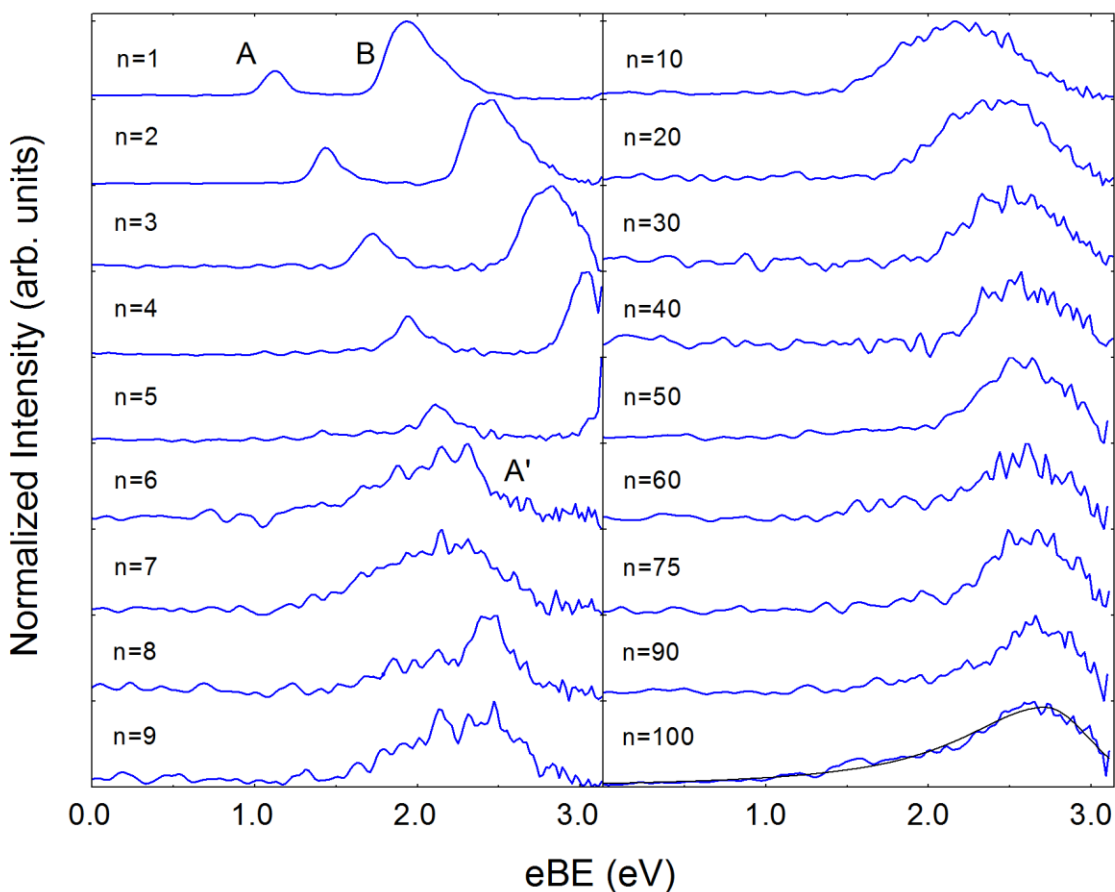


Figure 6.3. Selected normalized photoelectron spectra of $(\text{THF})_n^-$ cluster anions taken with $h\nu = 3.14$ eV from $n = 1$ to 100. Features A and B from Figure 2 are seen through $n = 5$. Starting at $n = 6$, the single remaining feature is re-labeled as Feature A'. A Gaussian-Lorentzian profile (black curve) is imposed on $n = 100$ for comparison of the fit function.

($\text{FWHM} = w_G \sqrt{\ln 2} + w_L$). A fit to Eq. 6.2 (black curve) is superimposed on the data for $n = 100$ in Figure 6.3 to demonstrate the appropriateness of this choice of fit function for this size regime.

Fig. 6.4 shows peak widths and photoelectron anisotropy parameters β for Feature A in anions with $n = 1-5$ and for the single peak seen for the larger clusters. The peak width more than doubles going from $n = 5$ to $n = 6$, after which it remains relatively constant. Similarly, β shows a large drop from $n = 5$ to 6, then shows little variation from $n = 6-25$. This abrupt transition suggests that the nature of the electron-solvent interaction changes around $n = 6$. Hence, for this and larger clusters, the single observed feature is re-labeled as Feature A'.

Varying the ion source conditions by adjusting the argon backing pressure from 20-35 psig does not change the photoelectron spectra for the $n = 1$ and $n = 26$ anions, suggesting that there are no other markedly different binding motifs (isomers) of the solvent cluster anions over this size range. Examination of the deuterated clusters $(\text{THF-d8})_n^-$ at an Ar backing pressure of 20 psig shows similar trends with a few important differences. Feature A is present, but is significantly less intense relative to Feature B in small clusters, as shown in Figure 6.2 for $n = 1$. Moreover, the shape of Feature A does not change until $n = 11$, at which point the abrupt

transition analogous to that seen in THF occurs (see Fig. 6.4). For $n \geq 11$, the VDEs of $(\text{THF-d8})_n^-$ clusters are identical to those in Fig. 6.3.

6.4 Discussion

In this section, we examine the photoelectron spectra in detail, focusing first on the larger size regime beyond the transition to Feature A'. The measured VDEs in this size regime are compared to those of other solvated electron clusters. These results are also considered within the context of dielectric continuum theory. We then consider the smaller clusters and the possible origins of Features A and B. Finally, we speculate on the structure of THF clusters with excess electrons.

6.4.1 Large clusters

The PE spectra of the anion clusters with $n \geq 6$ comprise a single feature, A', which undergoes only gradual changes with increasing cluster size. More specifically, this feature is very broad (FWHM = 0.77 eV for $n = 6$, and 1.04 eV for $n = 100$), its shape is relatively constant with cluster size over the size range of $n = 6$ -100, and it shifts only gradually toward higher VDE with increasing cluster size. Fig. 6.5 shows that a plot of the Feature A' VDEs as a function of $n^{-1/3}$ yields a straight line, as it does for the VDEs of $(\text{C}_6\text{H}_6)_n^-$ clusters¹⁷ and isomer I of $(\text{H}_2\text{O})_n^-$ and $(\text{CH}_3\text{OH})_n^-$ clusters,^{11, 18, 48} all of which are shown in the figure. These attributes of Feature A' are characteristic of "solvated electron clusters", in which the excess electron is bound to multiple intact solvent molecules.^{22, 49} Hence, we assign Feature A' to $(\text{THF})_n^-$ clusters, in which the excess electron is solvated by intact THF molecules.

Comparison among the solvating species in Fig. 6.5 indicates several notable trends. First, the VDEs for $(\text{THF})_n^-$ clusters are noticeably higher than those for other solvated electron clusters in the same size regime, even for isomer I water cluster anions. Secondly, the minimum size at which an assignable THF solvated electron cluster is identified is comparable to that of water but much smaller than for benzene ($n = 53$) and methanol ($n = 143$ for isomer I, $n = 70$ for the more weakly bound isomer II). Interestingly, the solvated electron feature in perdeuterated THF-d8 clusters appears at $n = 11$ instead of $n = 6$. This delayed onset is also seen in ammonia cluster anions, where the smallest observed clusters are $n = 37$ and $n = 43$ for $(\text{NH}_3)_n^-$ and $(\text{ND}_3)_n^-$, respectively, where it was attributed to changes in the electron attachment cross section due to coupling to the motion of a hydrogen atom.⁵⁰ The slope of the VDEs for $(\text{THF})_n^-$ clusters in Fig. 6.5 is comparable to that for methanol and benzene cluster anions but considerably less than that for water cluster anions. Finally, the value of the y-intercept is of considerable interest, since it should, in principle, yield the binding energy of the electron in the bulk solvent. The validity of this extrapolation has recently been demonstrated for water cluster anions through measurement of the VDE of hydrated electrons in liquid water microjets,⁵¹⁻⁵³ yielding values ranging from 3.3-3.6 eV. Fig. 6.5 implies that a similar measurement for THF would yield a bulk electron detachment energy of 3.10 eV.

The linear variation of the VDEs vs. $n^{-1/3}$ is predicted by dielectric continuum (DC) theory,^{54, 55} which is an appropriate first approximation for the energetics of solvated electron clusters. If it is assumed that the electron resides inside a spherical cluster consisting of a uniform dielectric material, DC theory finds that

$$VDE(n) = VDE(\infty) - \frac{e^2}{8\pi\epsilon_0 r_0} \left(1 + \frac{1}{\epsilon_\infty} - \frac{2}{\epsilon_s}\right) n^{-1/3} \quad (6.3)$$

$$VDE(\infty) = \frac{e^2}{8\pi\epsilon_0 a_0} \left(1 + \frac{1}{\epsilon_\infty} - \frac{2}{\epsilon_s}\right) \quad (6.4)$$

Here n is the cluster size, $VDE(\infty)$ is the bulk electron binding energy, r_0 is the average molecular radius, a_0 is the bulk cavity radius for the solvated electron, ϵ_0 is the permittivity of free space, and ϵ_∞ and ϵ_s are the optical and static dielectric constants, respectively. Moment analysis of the solvated electron absorption spectrum of THF is used to estimate the cavity radius of the electron.^{56, 57} The molecular radius is estimated from the molar volume of liquid THF,⁵⁸ and the optical dielectric constant is taken to be the square of the refractive index.⁵⁹ The temperature dependence of these values, as well as that of the static dielectric constant⁶⁰ has been accounted for by using two temperatures which should bracket that of (THF) n^- clusters in our ion beam. Values and results are summarized in Table 6.1.

The experimental VDEs show qualitative agreement with the DC model, as they scale linearly with the radius of the cluster ($\sim n^{-1/3}$), with a slope of -1.74 ± 0.08 eV and an intercept of $+3.10 \pm 0.03$ eV. This value has recently been verified by photoelectron spectroscopy of liquid THF jets at ~ 250 K, suggesting the clusters studied here are indeed liquid like and precursors to the solvated electron in THF.⁶¹ The disagreement between the experimental and predicted values for the slope and intercept highlights the simplicity of this model, which neglects molecularity and the disorder associated with solvent packing. For example, the effective molecular radius necessary to yield the experimental value for the slope would be 4.8 \AA , which is larger than the experimentally determined electron cavity radius of $\sim 4 \text{ \AA}$ in bulk THF.⁵⁶

As noted previously,^{11, 17, 18} DC theory reproduces the experimental slopes and intercepts for water and benzene quite well with little or no adjustment of the input parameters, but predicts a considerably larger slope for methanol, 4.3 eV vs. the experimental value of 2.25 eV for (CH₃OH) n^- clusters. The agreement between experiment and DC theory is better for THF than for methanol, but not as good as for water or benzene. It is not entirely surprising that a purely electrostatic model such as DC theory does not yield quantitative agreement for electrons in THF, given the complexity of the neat solvent and its interactions with solvated electrons.^{30, 36}

	150 K	200 K	Experimental
r_0 (Å) ^a	3.03	3.08	
a_0 (Å) ^b	3.46	3.86	
ϵ_∞ ^c	2.201	2.128	
ϵ_s ^d	16.17	11.75	
eBE(∞) (eV)	2.77	2.42	3.10 ± 0.03
Slope (eV)	-3.16	-3.04	-1.74 ± 0.09
<i>a.</i>	Ref ⁵⁸		
<i>b.</i>	Refs ^{56, 57}		
<i>c.</i>	Ref ⁵⁹		
<i>d.</i>	Ref ⁶⁰		

Table 6.1. Dielectric continuum (DC) theory values. The temperatures represent bounds for that of our anion beam.

6.4.2 Small anions

We next consider the PE spectra for anions with masses corresponding to $(\text{THF})_n^-$, $n = 1-5$. The PE spectrum of $m/z = 72$ (Figure 6.2) deserves special attention. Although this mass nominally corresponds to THF^- , THF has a closed-shell electronic configuration and a large HOMO-LUMO gap,^{62, 63} so a thermodynamically stable anion with the excess electron residing in a valence orbital is unlikely. The dipole moment of THF in the gas phase is between 1.64⁶⁴ and 1.75 D.⁶⁵ These values lie just above the minimum dipole moment of 1.62 D needed to support an anionic dipole-bound state,⁶⁶ but such states are typically bound by $\sim 10-100$ meV,⁶⁷⁻⁷⁰ much less than the VDE of either Feature A or B. Our computational investigations have revealed no valence-bound states for THF anion geometries starting from the C_1 , C_2 or C_s symmetries. However, higher-level treatments may be necessary to fully characterize a valence-bound THF anion theoretically.

To the best of our knowledge, the only observation of an anion with the mass of THF is from an electron scattering experiment by Sulzer *et al.*²⁶ A weak negative ion signal of mass 72 was observed upon bombardment of THF in an effusive molecular beam with 1.25 eV electrons. Since parent ions formed by electron attachment to isolated molecules are generally unstable with respect to dissociation or autodetachment, this signal was attributed to a metastable anion of unknown structure. Subsequent electron scattering studies on THF by Ibanescu *et al.*²⁷ did not reveal a negative ion signal at $m/z = 72$; only smaller anion fragments formed by dissociative electron attachment were observed starting at electron energies of 6 eV. It is possible that the parent ion signal seen by Sulzer *et al.*²⁶ came from low energy dissociative attachment to a THF cluster. Such a process is likely to occur in our ion source as well, given the relatively high concentration of neutral clusters produced in a pulsed molecular beam.

Focusing next on the anion structures associated with Features A and B in the anion PE spectrum in Fig. 6.2, we note that the PE spectrum of Feature B is very similar to that of the anion with $m/z = 71$ which, as mentioned above, is the open-chain *sec*-butyraldehyde enolate anion [(1,2)-*s*- $\text{C}_4\text{H}_7\text{O}^-$] previously observed by Continetti *et al.*⁴⁷ This species is presumably formed in the ion source by electron-induced opening of the ether ring and proton loss. It is therefore reasonable to explore whether Feature B with $m/z = 72$ is an open chain radical isomer of $\text{C}_4\text{H}_8\text{O}^-$. The most stable such isomer is expected to be the butoxyl radical anion, with the excess electron localized on the oxygen atom. Similar structures have comparable binding energies to that of Feature B (1.87 eV), such as the *tert*-butoxyl radical, 1.91 eV⁷¹, and the neopentoxyl radical, 1.93 eV.⁷²

There are several candidate structures for the butoxyl anion radical structure that can be evaluated because sigmatropic hydride shifting along the carbon chain causes significant changes in the VDE. DFT calculations are used to determine which radical species may give rise to the observed peaks in the spectra; the results of these calculations are shown in Table 6.2. The VDEs of the lower two structures are very similar to one another and to that of Feature B. We thus attribute Feature B at $m/z = 72$ to a radical anion of this kind that has undergone at least one hydride shift, detaching to a neutral $\text{C}_4\text{H}_8\text{O}$ di-radical in its singlet state. The structure with the radical center on the carbon alpha to the oxygen atom cannot be treated accurately with DFT, as geometry optimizations of the anion lead to unphysical structures and a negative vertical detachment energy. As deuteration does not affect electronic states, the analogous species is also the likely source of Feature B in the THF-d8 spectra. The shift in Feature B toward higher VDE in the $n = 2-5$ PE spectra is then consistent with this ion being progressively solvated⁷³ until it is

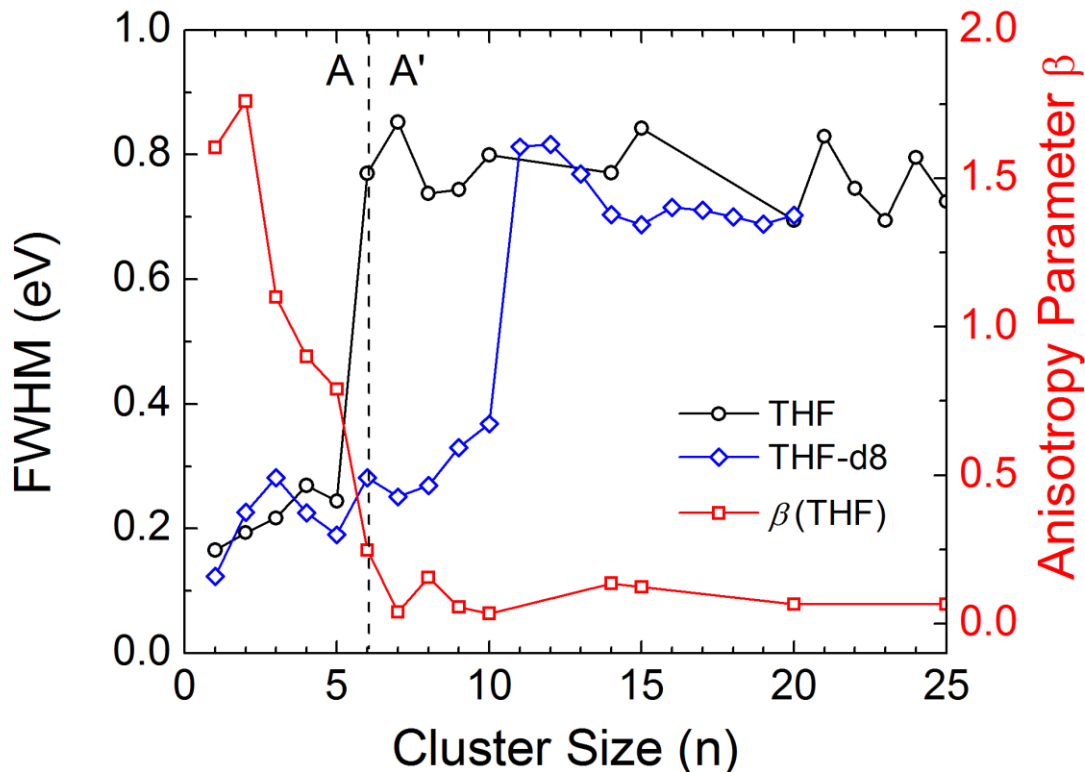


Figure 6.4. Full Width Half Maximum (FWHM) and photoelectron anisotropy parameter (β) as a function of cluster size for the $n \leq 25$. The change in the photoelectron angular distribution occurs at the same cluster size as the drastic change in the width of the spectrum from Feature A to Feature A' at $n = 6$. A dashed line is drawn through $n = 6$ to highlight the change.

bound by more than the photon energy (3.14 eV) by $n = 6$.

The origin of Feature A is more difficult to ascertain. Though the VDE is lower than that of Feature B, it is still too large to be from a dipole-bound state. Feature A could be from another open-shell anion structure that we were unable to locate by electronic structure calculations. However, this seems unlikely because as additional solvent molecules are added, its VDE evolves smoothly into that of Feature A' for the larger clusters. In fact, as shown in Fig. 6.5, the VDEs for Feature A over the entire size range $n = 1-5$ lie quite close to the straight line determined by the VDEs of the clusters with $n \geq 6$. Hence, although Feature A is quite distinct from Feature A' in terms of its width and photoelectron angular distribution (Fig. 6.4), it appears to arise from some type of anion structure that maps onto the solvated electron clusters with increasing size.

By varying the photon energy, the degree of localization of the excess electron can be qualitatively assessed. Since the photodetachment cross section is determined in large part by the transition dipole matrix element, and consequently by the degree of spatial overlap between the initial ion state and the outgoing free electron wavefunction, increasing the photon energy will lead to an enhanced overlap for a localized electron (conversely, a delocalized electron will show a decrease in detachment). The signal can be partitioned as:

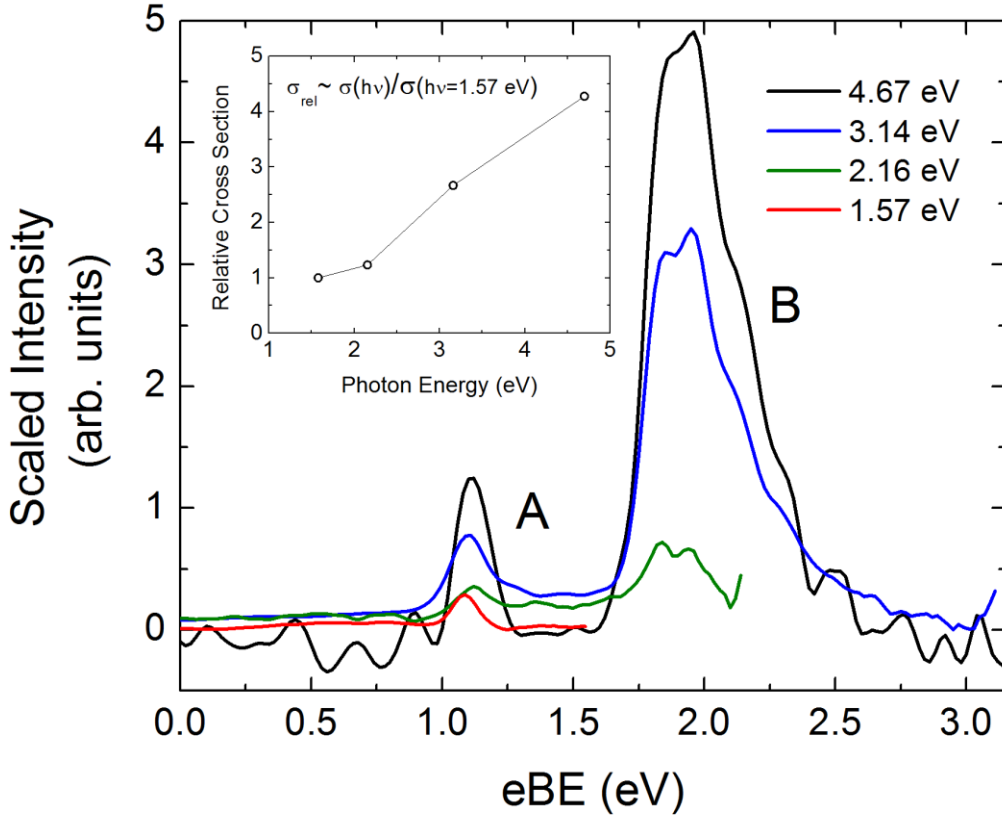


Figure 6.5. Scaled photoelectron spectra for $m/z = 72$ for four different photon energies. Inset: relative cross section values from the integrated areas of Feature A.

$$S \propto n_{\text{photon}} n_{\text{ion}} \sigma_{PD}(\omega) \eta \Delta t \quad (6.5)$$

where S is the integrated signal, n_{photon} is the number of incident photons, n_{ion} is the number of ions interrogated by the laser, $\sigma_{PD}(\omega)$ is the photodetachment cross section η is the overlap between the anion and laser beams, and Δt is the integration time. The number of photons can be derived from the average power of the incident laser by: $\langle P \rangle = n_{\text{photon}} \hbar \omega f = n_{\text{photon}} h c f / \lambda$, where f is the laser repetition rate, while the number of ions is proportional to the intensity as measured by the retractable ion detector (for constant gain). From this, changes in ion intensity and photon flux can be normalized out of the spectra. This is shown in Figure 6.5 for feature A at four different photon energies. Assuming a constant integration time and a similar overlap between the ion and laser beams at different frequencies, the relative photodetachment cross sections (Fig. 6.5 inset) can be approximated using:

$$\frac{\sigma_{PD}^{(2)}(\lambda_2)}{\sigma_{PS}^{(1)}(\lambda_1)} \propto \frac{S_2 \lambda_1 \langle P_1 \rangle n_{\text{ion}}^{(2)}}{S_1 \lambda_2 \langle P_2 \rangle n_{\text{ion}}^{(1)}} \quad (6.6)$$

As Fig 5.5 clearly shows, there is an increase in the photodetachment cross as the photon energy increases, suggesting that the state is fairly localized, as would be the case for a valence bound

anion. This is consistent with the relatively high binding energy; a dipole-bound electron for instance is expected to be delocalized and therefore would have an opposite trend with photon energy. It is also possible that Feature A arises from detachment from $(\text{C}_4\text{H}_8\text{O}-\text{OH}_8\text{C}_4)^{2-}$ dianion, the formation of which is energetically possible (if statistically improbable) within the electron-rich expansion. However, solvating this dianion by addition of THF molecules would result in intermediate peaks halfway between the primary cluster progression due to the second charge, and this is not seen in the mass spectra.

There is no evidence that an intact THF ring has a positive adiabatic electron affinity. It is possible, however, that a distorted ring can bind an electron, leading to a long-lived negative ion with a positive vertical detachment energy through stabilization of the lowest unoccupied molecular orbital (LUMO) in THF. Such a distorted structure could serve as the electron binding site in the anions with $n = 1-5$, resulting in Feature A upon photodetachment. The CO_2 and N_2O molecules are well known examples of this phenomenon. Neither molecule exhibits a positive adiabatic electron affinity⁷⁴, but in both cases, the LUMO is stabilized by bending to the extent that bent CO_2^- and N_2O^- anion have been observed in mass spectrometry and photoelectron spectroscopy experiments.⁷⁵⁻⁷⁷ These anions have positive VDEs (~ 1 eV) and live long enough for their photoelectron spectra to be measured. Moreover, the VDEs of the bare anions increase upon addition of additional solvent molecules, as is the case with Feature A. The HOMO-LUMO gap in THF is similar to that in CO_2 and N_2O (7.29 eV⁷⁸ and 6.52 eV⁷⁹, respectively, compared to 6.29 eV⁶² for THF), so a similar extent of stabilization induced by distortion is needed to bind an electron to THF. However, the PE spectra of bare and solvated CO_2^- and N_2O^- are about 0.7 eV wide, much broader than that of Feature A in the THF anion PE spectra, so it remains to be seen whether this analogy is plausible.

6.4.3 General remarks

THF is a widely used solvent for studying electron dynamics in the condensed phase. It is weakly polar, having a relatively low dielectric constant ($\epsilon_s = 7.33$ at room temperature), which makes it a versatile solvent. Additionally, its large spectral transmission window makes it very convenient for optical spectroscopy, particularly in the case of the solvated electron, which in THF absorbs intensely in the infrared. The electron is not known to interact strongly with one or


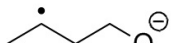
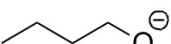
Hydride shifts	Anion structure	Neutral spin multiplicity	
		Singlet	Triplet
0		2.728	2.087
1		1.823	2.220
2		1.901	1.978

Table 6.2. Calculated vertical detachment energies for the butoxyl anion (eV).

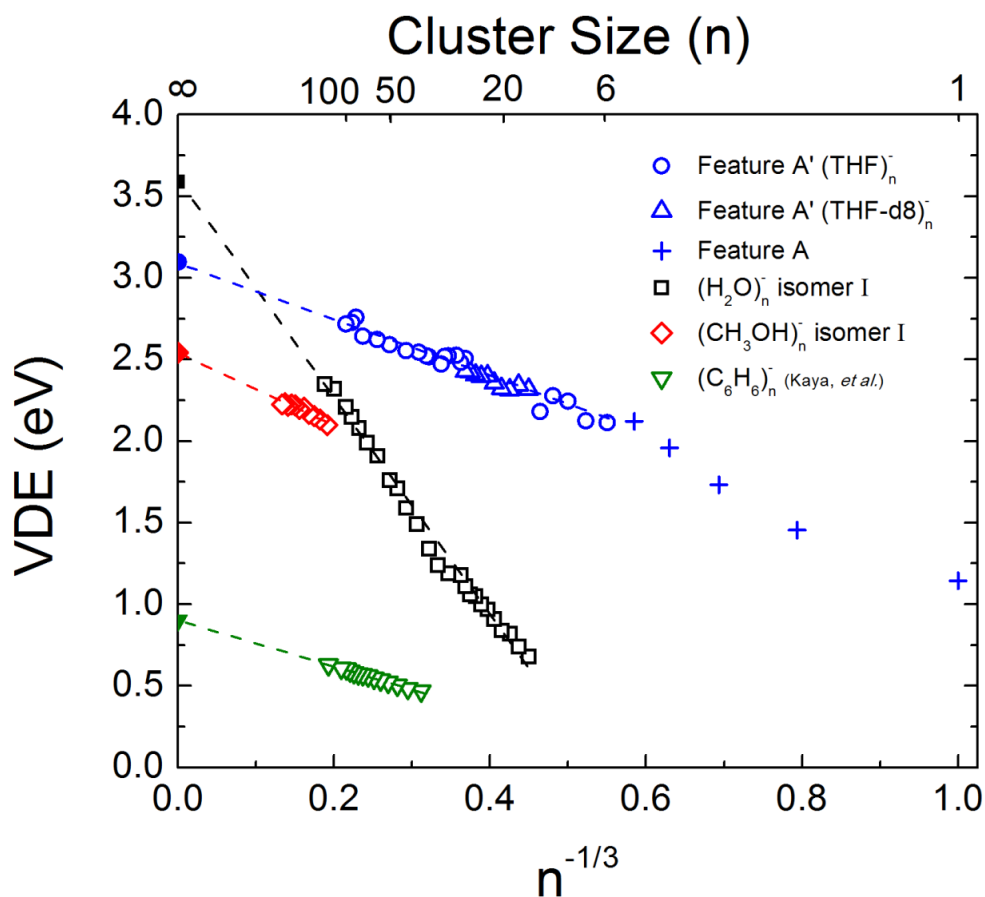


Figure 6.6. Vertical detachment energies (VDEs) of Feature A' $(\text{THF})_n^-$, $n \geq 6$ (open blue circles) and $(\text{THF-d8})_n^-$, $n \geq 11$ (open blue triangles) are shown, along with those of $(\text{C}_6\text{H}_6)_n^-$ (adapted from Mitsui, *et al.*¹⁷) and isomer I of $(\text{CH}_3\text{OH})_n^-$ (open red diamonds, adapted from Kammrath, *et al.*¹⁸) and $(\text{H}_2\text{O})_n^-$ (open black squares, adapted from Kammrath, *et al.*⁴⁸), vs. $n^{-1/3}$. Linear fits are superposed upon their respective data, projected out to $n = \infty$ (solid markers). VDEs for feature A for $(\text{THF})_n^-$, $n < 6$ (blue crosses) are also shown.

a small number of THF molecules directly, only associating with the collective dipole moments of those immediately surrounding it,³⁰ making it a true “solvated” electron. The formation of a stable or metastable THF^- anion would complicate this picture, particularly if this species can exist alongside the solvated electron. Prior to this study, it was not known if THF clusters could support an excess electron at all. However, the high value of the VDE of solvated electron state in THF at onset, higher than that of any comparably-sized solvent clusters studied thus far, suggests that the electron is highly stabilized, even for very small clusters.

As in the bulk, pre-existing electropositive voids within the clusters can act as natural traps for electron attachment, requiring little solvent reorganization to accommodate the excess charge. The relative agreement with the bulk values for even small clusters, which lie on the same line as those near $n = 100$, suggests that this feature of the bulk solvent structure might facilitate electron solvation in THF clusters. By contrast, neat liquid water does not exhibit these polarized cavities, and the injection of an electron requires the water network to reorder around it. Thus one would expect the binding energies in the anionic clusters to be smaller, and change more rapidly than those for clusters which naturally form these structures. Hydrogen-bonding interactions should be almost entirely absent in THF solution and clusters, so there is no strong

bonding network that must be disrupted in order to accommodate an excess electron internally. The liquid structure of THF is influenced by the formation of T-shaped pairings of the ether rings³⁶, evocative of the benzene dimer in the gas phase.⁸⁰

The absence of other isomers for the electron at these sizes for different source conditions differs from water and methanol cluster anions,^{18, 81} where colder conditions (higher backing pressures) were shown to produce anions with lower binding energies, attributed to surface-bound electron states. In THF, the presence of nascent voids could explain the lack of observation of a surface-bound state, as it would create a porous network with multiple, deep potential energy wells accessible to the electron, allowing for internal solvation. This suggests that the electrons are internally solvated within these clusters. It is interesting to note that the disk-like THF molecules could form a closed, hollow structure with as few as 6 molecules in a quasi-cubic arrangement. It would clearly be of interest to perform electron structure calculations on small THF anion clusters in order to gain a firmer understanding of the experimental trends observed here.

6.5 Conclusion

We have measured photoelectron spectra of size-selected tetrahydrofuran cluster anions up to $n = 100$ at $h\nu = 3.14$ eV. This study represents the first observation and characterization of $(\text{THF})_n^-$ clusters. The PE spectra of clusters with $n = 1-5$ exhibit two sharp peaks, Features A and B, that are attributed to an anion of the unopened THF ring and an open-chain butoxyl radical anion, respectively. PE spectra for clusters with $n \geq 6$ show a single broad peak, Feature A'. The size dependence of this feature exhibits characteristics of a cluster-solvated electron. With the THF cluster energetics established, we hope to investigate the time-resolved solvated electron dynamics analogous to our previous water¹³ and methanol¹⁹ work, as well as investigate the charge-transfer-to-solvent (CTTS) dynamics in the gas-phase to draw a direct comparison to the work done on the dynamics in the condensed phase⁸². Liquid jet measurements on the bulk solvated electron in THF will also be of use and will soon be underway in our laboratory.

6.6 References

- 1 J. Schnitker, and P. Rossky, *J. Chem. Phys.* **86** (6), 3471 (1987).
- 2 M. Boero *et al.*, *Phys. Rev. Lett.* **90** (22), 226403 (2003).
- 3 F. Arnold, *Nature* **294**, 732 (1981).
- 4 J. Simons, *Acc. Chem. Res.* **39**, 772 (2006).
- 5 H. F. Hameka, G. W. Robinson, and C. J. Marsden, *J. Phys. Chem.* **91** (12), 3150 (1987).
- 6 R. E. Larsen, W. J. Glover, and B. J. Schwartz, *Science* **329** (5987), 65 (2010).
- 7 E. J. Hart, and M. Anbar, *The Hydrated Electron* (Wiley-Interscience, New York, 1970).
- 8 W. Weyl, *Pogg. Ann.* **123**, 350 (1864).
- 9 G. R. Freeman, *J. Chem. Phys.* **77** (1), 7 (1973).
- 10 J.-P. Jay-Gerin, and C. Ferradin, *Radiat. Phys. Chem.* **36** (3), 317 (1989).
- 11 J. V. Coe *et al.*, *J. Chem. Phys.* **92** (6), 3980 (1990).
- 12 P. Ayotte, and M. A. Johnson, *J. Chem. Phys.* **106** (2), 811 (1997).
- 13 G. B. Griffin *et al.*, *J. Chem. Phys.* **131**, 194302 (2009).
- 14 L. Ma *et al.*, *J. Chem. Phys.* **131** (14), 144303 (2009).
- 15 M. Mitsui *et al.*, *Phys. Rev. Lett.* **91** (15), 153002 (2003).

- 16 R. M. Young *et al.*, Chem. Phys. Lett. **485**, 59 (2010).
17 M. Mitsui, A. Nakajimaa, and K. Kaya, J. Chem. Phys. **117** (21), 9740 (2002).
18 A. Kammrath *et al.*, J. Chem. Phys. **125**, 171102 (2006).
19 A. Kammrath *et al.*, J. Chem. Phys. **126**, 244306 (2007).
20 T. Maeyama *et al.*, Phys. Chem. Chem. Phys. **8**, 827 (2005).
21 J. V. Coe, Int. Rev. Phys. Chem. **20** (1), 33 (2001).
22 D. M. Neumark, Mol. Phys. **106** (16-18), 2183 (2008).
23 M. Allan, J. Phys. B: At. Mol. Opt. Phys. **40** (17), 3531 (2007).
24 C. S. Trevisan, A. E. Orel, and T. N. Rescigno, J. Phys. B: At. Mol. Opt. Phys. **39** (12), L255 (2006).
25 S. Tonzani, and C. H. Greene, J. Chem. Phys. **125** (9) (2006).
26 P. Sulzer *et al.*, J. Chem. Phys. **125** (2006).
27 B. C. Ibanescu, O. May, and M. Allan, Phys. Chem. Chem. Phys. **10** (11), 1507 (2008).
28 D. Duflot *et al.*, Chem. Phys. Lett. **495**, 27 (2010).
29 E. R. Barthel, I. B. Martini, and B. J. Schwartz, J. Chem. Phys. **112** (21), 9433 (2000).
30 M. J. Bedard-Hearn, R. E. Larsen, and B. J. Schwartz, J. Chem. Phys. **122**, 134506 (2005).
31 M. J. Bedard-Hearn, R. E. Larsen, and B. J. Schwartz, J. Chem. Phys. **125**, 194509 (2006).
32 M. C. Cavanagh, R. M. Young, and B. J. Schwartz, J. Chem. Phys. **129**, 134503 (2008).
33 A. E. Bragg, M. C. Cavanagh, and B. J. Schwartz, Science **321**, 1818 (2008).
34 O. Shoshana *et al.*, Phys. Chem. Chem. Phys. **8** (22), 2599 (2006).
35 X. Chen, and S. E. Bradforth, Annu. Rev. Phys. Chem. **59**, 203 (2007).
36 D. T. Bowron, J. L. Finney, and A. K. Soper, J. Am. Chem. Soc. **128**, 5119 (2006).
37 Y. S. Park *et al.*, J. Chem. Phys. **125** (7) (2006).
38 A. V. Davis *et al.*, J. Chem. Phys. **118** (3), 999 (2003).
39 U. Even *et al.*, J. Chem. Phys. **112** (18), 8068 (2000).
40 W. C. Wiley, and I. H. McLaren, Rev. Sci. Instrum. **26** (12), 1150 (1955).
41 A. T. J. B. Eppink, and D. H. Parker, Rev. Sci. Instrum. **68** (9), 3477 (1997).
42 V. Dribinski *et al.*, Rev. Sci. Instrum. **73** (7), 2634 (2002).
43 M. J. Travers, D. C. Cowles, and G. B. Ellison, Chem. Phys. Lett. **164** (5), 449 (1989).
44 K. L. Reid, Annu. Rev. Phys. Chem. **54**, 397 (2003).
45 J. Cooper, and R. N. Zare, J. Chem. Phys. **48**, 942 (1968).
46 M. J. Frisch *et al.*, (Gaussian, Inc., Wallingford, CT, 2004).
47 L. S. Alconcel, H.-J. r. Deyerl, and R. E. Continetti, J. Am. Chem. Soc. **123**, 12675 (2001).
48 A. Kammrath *et al.*, J. Chem. Phys. **125**, 076101 (2006).
49 J. V. Coe, S. M. Williams, and K. H. Bowen, Int. Rev. Phys. Chem. **27** (1), 27 (2008).
50 T. Kondow, T. Nagata, and K. Kuchitsu, Z. Phys. D **12** (1), 291 (1989).
51 K. R. Siefertmann *et al.*, Nature Chemistry **2** (4), 274 (2010).
52 Y. Tang *et al.*, Phys. Chem. Chem. Phys. **12** (15), 3653 (2010).
53 A. T. Shreve, T. A. Yen, and D. M. Neumark, Chem. Phys. Lett. **493**, 216 (2010).
54 R. N. Barnett, U. Landman, and C. L. Cleveland, Chem. Phys. Lett. **145** (5), 382 (1988).
55 X.-J. Wang *et al.*, J. Phys. Chem. B **114**, 2189 (2010).
56 F.-Y. Jou, and G. R. Freeman, Can. J. Chem. **54**, 3693 (1976).
57 W. Marbach, A. N. Asaad, and P. Krebs, J. Phys. Chem. A **103**, 28 (1999).

- 58 R. P. W. Scott, *J. Liq. Chromatog.* RT **23** (20), 3083 (2000).
- 59 G. Openhaim, and E. Grushka, *J. Chromatog. A* **942**, 63 (2002).
- 60 D. J. Metz, and A. Clines, *J. Phys. Chem.* **71** (4), 1158 (1967).
- 61 A. T. Shreve, M. H. Elkins, and D. M. Neumark.
- 62 L. W. Pickett, N. J. Hoeflich, and T.-C. Liue, *J. Am. Chem. Soc.* **73**, 4865 (1951).
- 63 P. Duffy, o. A. Sordo, and F. Wang, *J. Chem. Phys.* **128**, 125102 (2008).
- 64 D. D. Klug, and E. Whalle, *Can. J. Chem.* **51**, 4062 (1973).
- 65 D. R. Lide, in *CRC Handbook of Chemistry and Physics*, edited by D. R. Lide (CRC Press/Taylor and Francis, Boca Raton, FL, 2010), pp. 50.
- 66 J. A. D. Stockdale *et al.*, *Phys. Lett.* **25A** (7), 510 (1967).
- 67 S. Y. Han *et al.*, *J. Chem. Phys.* **109** (22), 9656 (1998).
- 68 K. R. Lykke, R. D. Mead, and W. C. Lineberger, *Phys. Rev. Lett.* **52** (25), 2221 (1984).
- 69 J. H. Hendricks *et al.*, *J. Chem. Phys.* **108** (1), 8 (1998).
- 70 N. I. Hammer *et al.*, *J. Chem. Phys.* **119** (7), 3650 (2003).
- 71 T. M. Ramond *et al.*, *J. Chem. Phys.* **112** (3), 1158 (2000).
- 72 P. S. Drzaic, J. Marks, and J. I. Brauman, in *Gas Phase Ion Chemistry*, edited by M. T. Bowers (Academic Press, Orlando, FL, 1984), p. 167.
- 73 A. W. Castleman, Jr., and K. H. Bowen, Jr., *J. Phys. Chem.* **100**, 12911 (1996).
- 74 S. T. Arnold *et al.*, in *Proceedings of the Enrico Fermi International School of Physics, CVII Course, Varenna*, edited by G. Scoles (North Holland, Amsterdam, 1989), pp. 467.
- 75 C. D. Cooper, and R. N. Compton, *Chem. Phys. Lett.* **14**, 29 (1972).
- 76 J. V. Coe, Ph. D. Thesis, The Johns Hopkins University, 1986.
- 77 J. V. Coe *et al.*, *Chem. Phys. Lett.* **124** (3), 274 (1986).
- 78 K. Yoshino *et al.*, *Journal of Quantitative Spectroscopy and Radiative Transfer* **55** (1), 53 (1996).
- 79 G. Selwyn, J. Podolske, and H. S. Johnston, *Geophys. Res. Lett.* **4** (10), 427 (1977).
- 80 K. C. Janda *et al.*, *J. Chem. Phys.* **63** (4), 1419 (1975).
- 81 J. R. R. Verlet *et al.*, *Science* **307**, 93 (2005).
- 82 A. E. Bragg, and B. J. Schwartz, *J. Phys. Chem. B* **112**, 483 (2008).

Chapter 7. Iodide Solvation in Tetrahydrofuran Clusters $\text{I}^-(\text{THF})_n$ ($1 \leq n \leq 30$)

The solvent structure and binding motif of iodide-doped tetrahydrofuran clusters, $\text{I}^-(\text{THF})_n$ ($1 \leq n \leq 30$) are investigated with anion photoelectron imaging. A dramatic decrease in the iodide differential stabilization energy and concomitant change in the mass spectrum at $n = 9$ suggest that the first solvation shell closes at $n = 9-10$ THF molecules. Analysis of the vertical detachment energy vs. inverse cluster radius suggests the solvent shell begins to close around $n = 19$. Evidence of a bound electronic excited state is also presented. The results are interpreted within the framework of the inefficient packing that occurs in bulk neat THF. The computational work in this chapter was done in collaboration with Julian Azar in the Head-Gordon group here at UC Berkeley.

7.1 Introduction

Ion solvation is a fundamental aspect of chemistry and biology, with broad implications for both natural systems and new materials. The mechanism of solvation and the degree of stabilization is strongly dependent on the structure and properties of both the solvent and solute. To better understand how the solvent structure affects ion solvation, it is advantageous to study a solute with no vibrational or rotational degrees of freedom, such as an atomic ion. Solvated atomic anions such as iodide also possess relatively low electron binding energies, making their energetics easily accessible in both gas-phase cluster experiments as well as in solution. As such they are excellent probes of the solvation process. Iodide itself has no bound electronic states in the gas phase; however solvation by only a few molecules is sufficient to stabilize an excited state in many solvents.^{1,2} This state is supported by the collective dipole moments of the solvent molecules and is stabilized by the long-range polarizability of the cluster.³ These states are precursors to the so-called charge-transfer-to-solvent (CTTS) states which are well characterized in the bulk.^{4,5} Excitation at energies near the vertical binding energy of the excess electron populates a diffuse excited state that has a large spatial extent.^{3,6,7} Subsequent fluctuations in the solvent molecules' motions lead to detachment from the iodine atom and localization onto the solvent cluster or, in solution, a solvent cavity, after which the electron relaxes as the solvent molecules adjust to the new charge distribution. Knowledge of the location of the iodide in the cluster and the nature of its interaction and perturbation of the solvent network is thus of critical importance to understanding the nature of these states and their associated dynamics. Here we use photoelectron imaging spectroscopy to examine the binding energy of iodide in THF clusters as a function of size to gain insight into where the iodide is located within the cluster and at what size the cluster can support a bound charge-transfer-to-solvent state.

Iodide solvation has been investigated in clusters of polar molecules such as water and acetonitrile (CH_3CN). In water, the presence of iodide leads to a large disruption of the hydrogen bond network due to the strong $-\text{OH}\cdots\text{I}^-$ attraction (450 meV).⁸ Anion photoelectron spectra⁸ show evidence for the closure of a solvent shell around $n = 6$, however this is not reproduced by molecular dynamics simulations or *ab initio* calculations. Rather, a surface-bound geometry is favored⁹ for clusters as large as $n \sim 55$ where the iodide is coordinated with a 3 or 4 water molecules; above this size internal solvation becomes favorable. Ultimately once the iodide is internally solvated it is highly stabilized, having a vertical binding energy of 7.7 ± 0.2

eV.¹⁰ This value matches the cluster extrapolation quite well (7.92 ± 0.05 eV).⁸ The situation is different, however, for acetonitrile, where photoelectron spectroscopy^{11, 12} and computational studies¹³ suggest the iodide is internally solvated even for clusters as small as $n = 2$. The photoelectron spectra suggest the ion is largely stabilized after $n = 12$, as the vertical detachment energies begin to level out, indicating the closure of the first solvation layer. Molecular dynamics simulations show the electropositive methyl groups are directed toward the halide while the CN groups point outward, allowing for weak hydrogen bonds to form with the second solvent layer. Extrapolation of the cluster photoelectron data¹² indicate that the vertical detachment energy of the excess electron on iodide is 8.0 ± 0.2 eV in bulk acetonitrile, a similar stabilization compared to water, despite the much larger dipole moment. As a point of contrast, iodide can also be solvated in a rare gas matrix such as a xenon cluster.^{2, 14} Here the geometry is governed by entropic effects, resulting in magic numbers in the mass spectrum appearing at sizes with closely-packed geometric structures (I^- is isoelectronic with and similar in size to Xe). Hence the excess charge on iodide is more likely to be internally solvated due to charge-induced dipole interactions. As one might expect, the (extrapolated) stabilization is much less significant in xenon, only about 1.4 eV.¹⁴ The ion only has to disrupt the weak van der Waals interactions between the xenon atoms in order to be inserted into the cluster.

A weakly polar solvent offers an intermediate case between a rare gas matrix and a cluster of strongly polar solvent molecules like water or acetonitrile. Tetrahydrofuran (THF, C_4H_8O) is weakly polar in that it has a sizeable dipole moment (1.63-1.75 D) but a relatively small static dielectric constant ($\epsilon_s \sim 7.5$). Neat THF has been shown to pack inefficiently, indicating a weaker solvent-solvent interaction. Mixed quantum/classical molecular dynamics simulations¹⁵ and neutron scattering experiments¹⁶ have shown that neat THF has large empty voids, ~ 2.5 -5 Å atom-to-atom, which are positively polarized. This has important implications for electron and ion solvation as these pockets may act as pre-existing traps for a negative ion or electron to become solvated in with little nuclear rearrangement. Transient absorption experiments show that after an excess electron is injected or excited using a femtosecond pulse it appears with its equilibrated absorption spectrum within the time-resolution of the experiment, consistent with injecting an electron into a pre-formed cavity.^{6, 17} This solvent structure would also be expected for neutral THF clusters of sufficient size, where the voids would act as favorable binding sites for excess electrons. Negatively charged THF clusters have recently been shown¹⁸ to bind an electron in clusters as small as $n = 6$ with a significant binding energy of about 2 eV. Extrapolation to infinite cluster size and photoelectron spectroscopy of liquid THF jets¹⁹ yield a bulk binding energy of about 3.1 eV, suggesting that the stabilization energy is not very large, just about 1 eV. This low stabilization energy and large initial binding energy together suggest that the solvent cluster readily accepts the excess electron even at small sizes. Given its effect on electron solvation, how this frustrated packing affects the location and degree of stabilization of iodide is an interesting question, specifically how the ion is stabilized as a function of cluster size.

Typically, cluster geometries are best studied with techniques that are highly sensitive to vibrational perturbations, such as infrared multiphoton dissociation/predissociation spectroscopy. Such studies have been carried out in a multitude of solvents, such as water,¹ methanol,²⁰⁻²³ and acetonitrile¹¹ doped with various halides. No analogous studies on THF have yet been done to determine the general location of the iodide. Here we study iodide solvation in THF clusters using anion photoelectron imaging which yields less detailed information about the ion position but gives insight into the strength of the halide binding interactions. We find that the I^- ion

likely resides inside the clusters with a first solvation shell composed of approximately 9 THF molecules. The solvation layer likely closes around $n = 19$. Using the dielectric continuum models as guides, the bulk binding energy of iodide in THF is hypothesized and with the aid of quantum chemical calculations its location within the cluster is discussed. We also present evidence for a bound electronic excited state beginning at $n = 4$.

7.2 Experimental

The photoelectron imaging apparatus has been described in detail previously.²⁴ Briefly, argon gas at 20-40 psig was flowed over reservoirs of THF and methyl iodide, co-expanded through a 100 Hz pulsed solenoid valve²⁵, and intersected with ~ 500 eV electrons from a ring anode. Secondary electron attachment led to dissociative electron attachment to CH_3I , forming free I^- which could either be captured by neutral THF clusters or act as a nucleation site for the formation of $\text{I}^-(\text{THF})_n$. These clusters were extracted perpendicularly into a Wiley-McLaren time-of-flight mass spectrometer²⁶ allowing for size-selection. Mass spectra were collected and integrated on a digital oscilloscope. To obtain photoelectron spectra, selected masses were interrogated by the appropriate laser pulse and ejected electrons were analyzed using velocity map imaging.²⁷ Collected images were transformed using the BASEX method,²⁸ reconstructing the molecular frame kinetic energy distribution. Electron kinetic energy (eKE) is transformed into electron binding energy (eBE) by conservation of energy: $eBE = h\nu - eKE$. The photoelectron spectrometer was calibrated against I^- detachment to ensure the proper electron affinity (3.059 eV) and spin-orbit splitting (0.943 eV) of iodine, and laser wavelength was measured using a fiber-optic spectrometer.

Laser pulses were generated using a commercial Ti:sapphire femtosecond oscillator and chirped-pulse multipass amplifier (KM Labs Griffin oscillator / Dragon amplifier) resulting in 35 fs FWHM pulses at 790 nm (1.57 eV). 1 mJ of this output was used to pump a continuum-seeded optical parametric amplifier (Light Conversion TOPAS-C). Ultraviolet detachment photons at 239 nm (5.19 eV) were generated by second harmonic generation of the sum-frequency signal OPA output in a β -barium borate (BBO) crystal at 56° , while the 290 nm - 320 nm (4.28 eV - 3.88 eV) excitation pulses were generated by doubling the sum-frequency idler output using a 40.5° BBO crystal.

7.3 Results and Analysis

7.3.1 Mass spectrum

Figure 7.1 shows a representative mass spectrum of iodide/THF. Iodide dominates the spectrum at $m/z = 127$ with clustering occurring every 72 mass units, indicative of $\text{I}^-(\text{THF})_n$ cluster formation. The shape of the mass spectrum is not constant or monotonic with cluster size: signal for clusters up to $n \sim 10$ are more intense than for $n > 10$, after which the distribution is more or less constant until single-cluster resolution is lost around $m/z \sim 4000$. While altering the source conditions always leads to changes in the mass spectrum, the relative enhancement of the first ten peaks to the larger sizes is always seen. The inset of Fig. 7.1 shows the first 15 clusters,

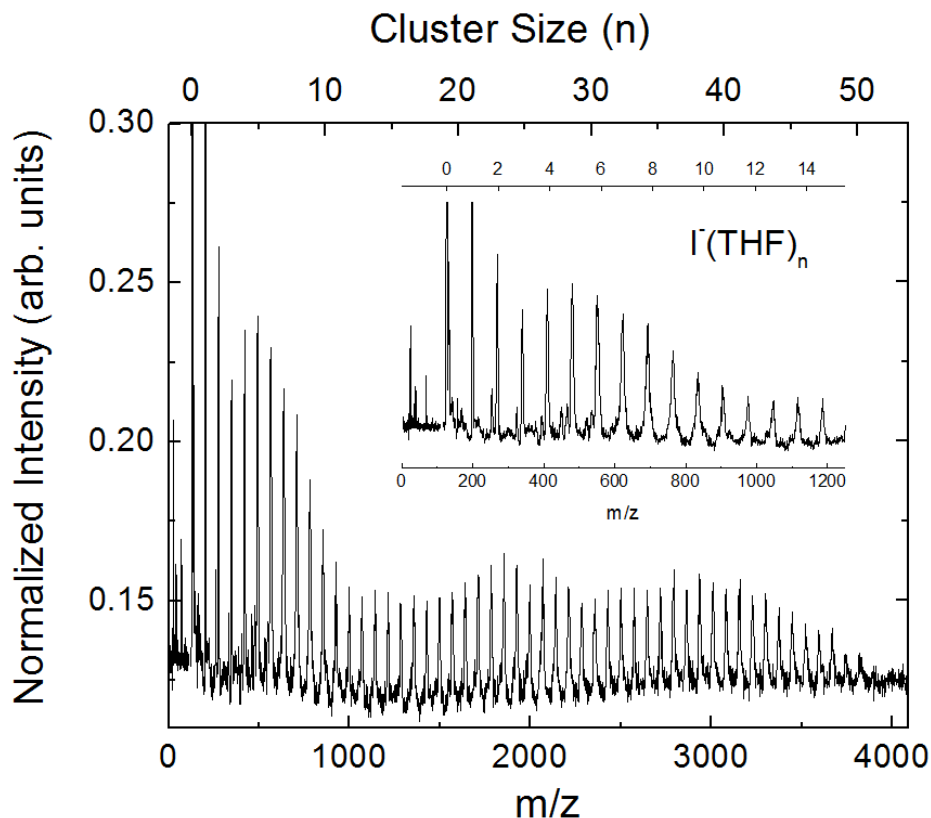


Figure 7.1. Time-of-Flight mass spectrum of $I^-(\text{THF})_n$ clusters showing cluster production out to about $n = 55$. Inset: zoom in on first 12 clusters, showing a change in intensity at $n = 9-10$.

highlighting this feature. Contamination from I_2^- is seen at small cluster sizes, but the mass resolution of the spectrometer is sufficient ($\Delta m/m \sim 1\%$) to isolate the desired clusters. Moreover, solvated I_2^- is spectroscopically distinct from atomic iodide and is not observed in any of the photoelectron spectra.

7.3.2 Photoelectron spectra

Photodetachment spectra are shown in Figure 7.2 for various sizes up to $n = 30$ using a photon energy of 5.19 eV. Detachment from solvated iodide shows the characteristic spin-orbit structure in the photoelectron spectrum of I^- , shifting to higher binding energies until $n = 6$ when detachment to the $^2P_{1/2}$ state of solvated neutral iodine is no longer energetically possible. After this size, the spectra show only detachment to the $^2P_{3/2}$ state. For all sizes studied here, the vertical detachment energy of the cluster is determined by subtracting the center a Gaussian fit of the eKE distribution of the $^2P_{3/2}$ peak [$E_0(n)$] from the photon energy: $VDE(n) = h\nu - E_0(n)$. The stabilization energy for a given cluster is computed as:

$$E_{stab}(n) = VDE(n) - EA[I^-(^2P_{3/2})]. \quad (7.1)$$

Varying the excitation energy has a marked effect on the shape of the photoelectron spectra for certain sizes. Figure 7.3 shows excitation of the $n = 4$ cluster with $h\nu = 4.05$ eV and $h\nu = 5.19$ eV [$VDE(n = 4) = 3.96$ eV]. Direct detachment (Feature A) is observed with both

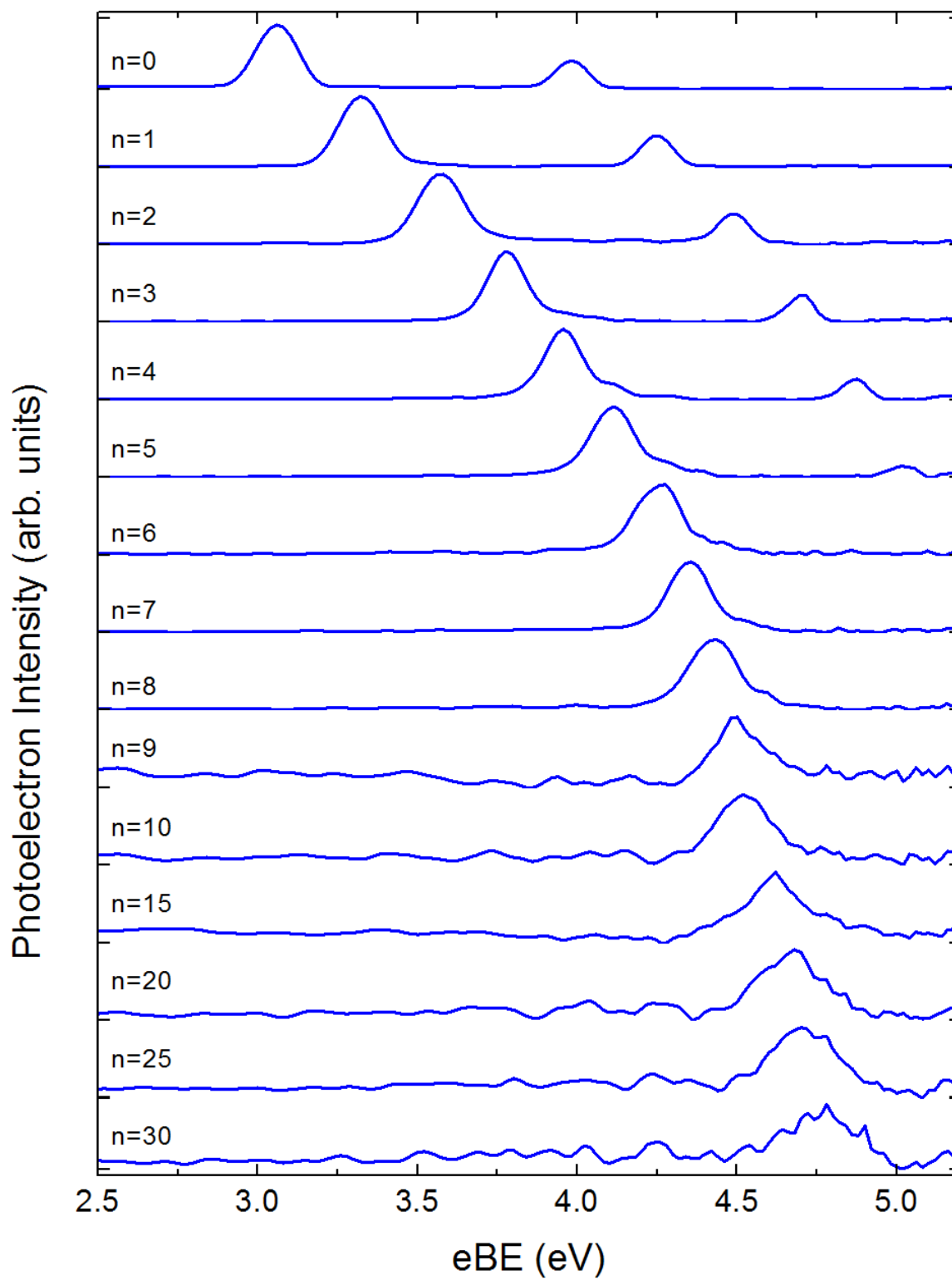


Figure 7.2. Photoelectron spectra of selected $\text{I}^-(\text{THF})_n$ ($0 \leq n \leq 30$) clusters at 5.19 eV photon energy.

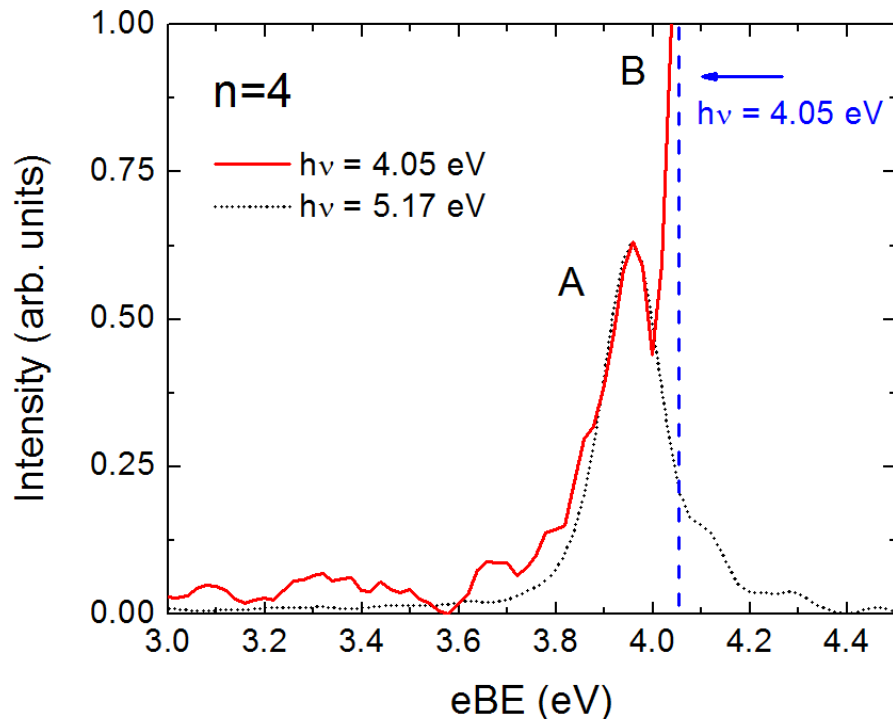


Figure 7.3. Photoelectron spectrum of $n = 4$ taken at 4.05 eV (red solid line) and 5.19 eV (dashed black line) photon energies, showing direct ground-state detachment (Feature A) as well as a narrow, intense feature at low kinetic energy, characteristic of excited state autodetachment (Feature B). The vertical blue dotted line marks the highest binding energy accessible by the 4.05 eV photons.

photon energies, while the sharp peak (Feature B) is only seen with 4.05 eV photons, just above the binding energy of cluster's ground state and where the excited state couples to the continuum. The shape of Feature B is characteristic of excited state autodetachment.²⁹⁻³¹ This feature is observed in the photoelectron spectra for $n = 4-7$, appearing to narrow with increasing cluster size when the photon energy is tuned to be on resonance (the autodetachment feature is most intense for a given cluster size and set of clustering/ionization conditions). By $n = 8$, no autodetachment feature was observed while pumping the cluster below and around the detachment threshold. Larger clusters ($n > 15$) were investigated with the third harmonic of the fundamental, closer to the expected absorption maximum. While weak two-photon detachment of the ground state was observed, no autodetachment was seen, despite being within 50-100 meV of the VDE.

7.4 Discussion

7.4.1 Photoelectron and mass spectra

While the location of the iodide cannot be definitively assigned from the photoelectron spectra alone, the spectra do give a great deal of insight into the nature of the stabilization and the infinite size limit. The evolution of the VDEs with cluster size is presented in Figure 7.4.

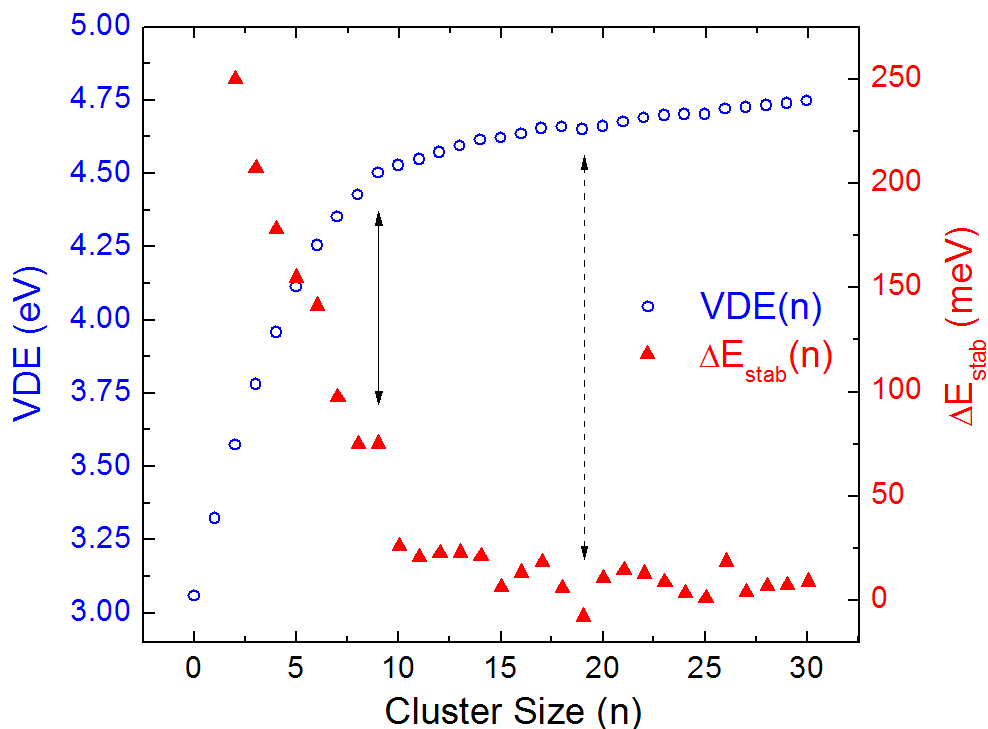


Figure 7.4. VDE vs. cluster size (n) for $\text{I}^-(\text{THF})_n$ ($0 \leq n \leq 30$), (blue circles) on the left axis, with differential stabilization energy, $\Delta E_{stab}(n) = E_{stab}(n) - E_{stab}(n-1)$ (red triangles), on the right axis. The left arrow marks the change at $n = 9$, while the right arrow marks the onset of the long-range interactions.

The left ordinate shows the VDE while the right shows the differential stabilization energy,

$$\Delta E_{stab} = VDE(n) - VDE(n-1). \quad (7.2)$$

The VDE's show a significant change in slope at $n = 9$, suggesting that some geometrical structure has been achieved such as a closed solvation shell or a maximization of the coordination number. The rate of change of the VDE, ΔE_{stab} is useful in determining the size range of relevant types of ion-solvent interactions. The solvated iodide interacts most strongly with the first 9 THF molecules; after this size the differential stabilization energy drops to only 10-25 meV/molecule. The solvent molecules beyond $n = 9$ only minimally stabilize the charge on the halide, suggesting coordination of the iodide to the solvent cluster is maximized (surface solvation), or possibly due to the closure of the first solvation shell (internal solvation).

The change in the relative interaction values of the solvent and ion at $n = 9$ coincides with an alteration in the shape of the mass spectrum at the same cluster size. The first 9 clusters in the mass spectrum are enhanced relative to the larger cluster sizes, which become about uniform in intensity around $n = 10$. The completion of this geometric structure results in a drop in the differential stabilization energy to only ~20 meV/molecule and generally decreasing with cluster size beyond that. Because the differential stabilization energy is equivalent to the cohesion energy of the cluster (which is related to the enthalpy of evaporation), it is intimately related to the mass spectrum where the larger sizes decay by evaporative loss. When the cluster cohesion

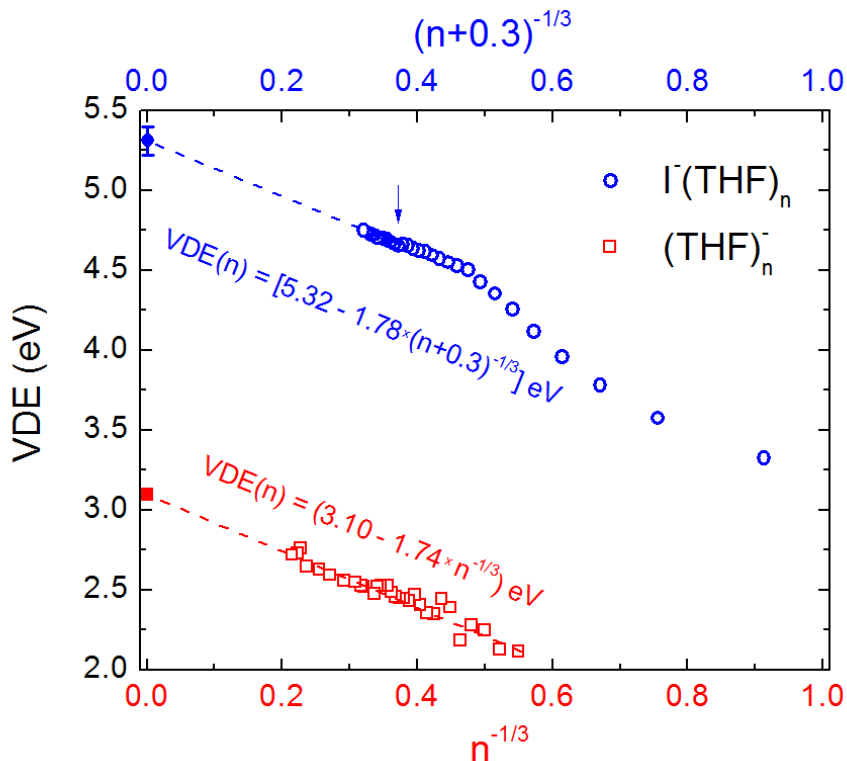


Figure 7.5. VDE vs. $(n+\xi)^{-1/3}$ for $\text{I}^{-}(\text{THF})_n$ (blue circles) and $(\text{THF})_n^{-}$ (red squares), adapted from Young, *et al.*¹⁸ For iodide, $\xi = 0.3$, while for $(\text{THF})_n^{-}$ $\xi = 0$. Linear fits are shown next to each data set. The similarity in the slopes indicates the same stabilizing interaction.

energy becomes small, evaporation becomes more probable, leading to the reduction in the measured ion population of those cluster sizes, as is seen in Fig. 7.1 after $n = 9$.

Motivated by dielectric continuum models where the ion is treated as a hard sphere within a uniform dielectric sphere,³²⁻³⁴ the VDEs are plotted in Figure 7.5 against the inverse cluster radius, $(n+\xi)^{-1/3}$, where ξ is the ratio of the ion volume to the molecular volume. The VDEs at corresponding cluster radii for bare THF cluster anions, $(\text{THF})_n^{-}$, are also shown in the figure. Using the hard-sphere ionic radius of iodide (216 pm) and the room-temperature density of THF to estimate its molar volume, ξ is approximately 0.3. Fitting the linear region of the $\text{I}^{-}(\text{THF})_n$ plot yields an estimate of the bulk VDE of I^{-} in THF (intercept) and the nature of the stabilization with increasing cluster size (slope). A close examination of Fig. 7.5 shows a second kink in the linear region, this time around $n = 19$, where the slope of the line increases. Fitting only this region ($19 \leq n \leq 30$) yields:

$$VDE(n) = [5.32 - 1.78(n + 0.3)^{-1/3}]eV \quad (7.3)$$

Fitting the entire linear range results in a lower slope (-1.47 ± 0.03 eV) but a similar intercept (5.2 ± 0.1 eV). At sufficiently large cluster sizes, the charge will still be stabilized by additional solvent molecules, however the ion's influence on the packing and structure will decrease, similarly to the case for a solvated electron.¹⁸ Comparing the slopes of the larger $\text{I}^{-}(\text{THF})_n$ VDEs (-1.78 ± 0.06 eV) to that of the $(\text{THF})_n^{-}$ (-1.74 ± 0.09 eV) shows that the nature of the stabilization is very similar, *i.e.* driven by long-range interactions. This similarity would

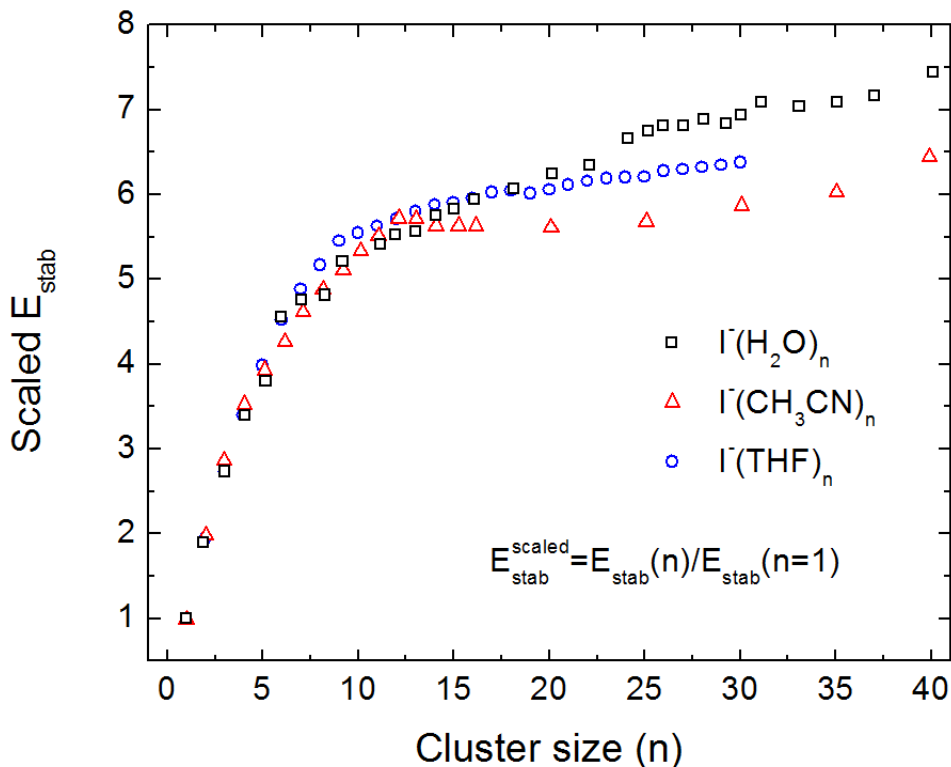


Figure 7.6. Scaled differential stabilization energy for iodide in water (black squares), acetonitrile (red circles), adapted from Markovitch, *et al.*,¹² and THF (blue circles).

indicate that around $n = 9$ the specific nature of the excess charge, such as its shape or general size is unimportant to how the clusters electrostatically stabilize the charge, with this effect becoming even less significant by $n = 19$. For instance, the solvated electron's radius of gyration in THF is $\sim 4 \text{ \AA}$,³⁵ while the ionic radius of iodide is about half that.

The linear extrapolation gives an approximation of the bulk binding energy of iodide in THF of about $5.3 \pm 0.1 \text{ eV}$, indicating a stabilization energy of 2.24 eV. The degree of stabilization is substantially different than that of iodide in water and acetonitrile where the ion is stabilized by about twice as much (4.6-4.8 eV),¹² but is similar to solvation in xenon clusters (1.4 eV).¹⁴ Like THF, xenon has no organized bonding network to disrupt, however the strong dipole of THF should lead to some enhanced stabilization not afforded by the Xe atoms.

7.4.2 Comparison to other solvents

Some insight can be gained by comparing these above inferences to systems where the location of iodide is generally known. In water, iodide is generally regarded to be at the cluster surface and the VDEs continue to rise until near $n \sim 60$. In contrast, in acetonitrile the closure of the first solvation shell in acetonitrile results in a loss of differential stabilization energy after $n = 12$; the VDE vs. cluster size curve is flat for larger sizes. Comparing the absolute stabilization energies for each solvent is difficult, because the nature of the interactions is differs vastly for each molecule (THF, for instance, is incapable of hydrogen bonding). Therefore, a common

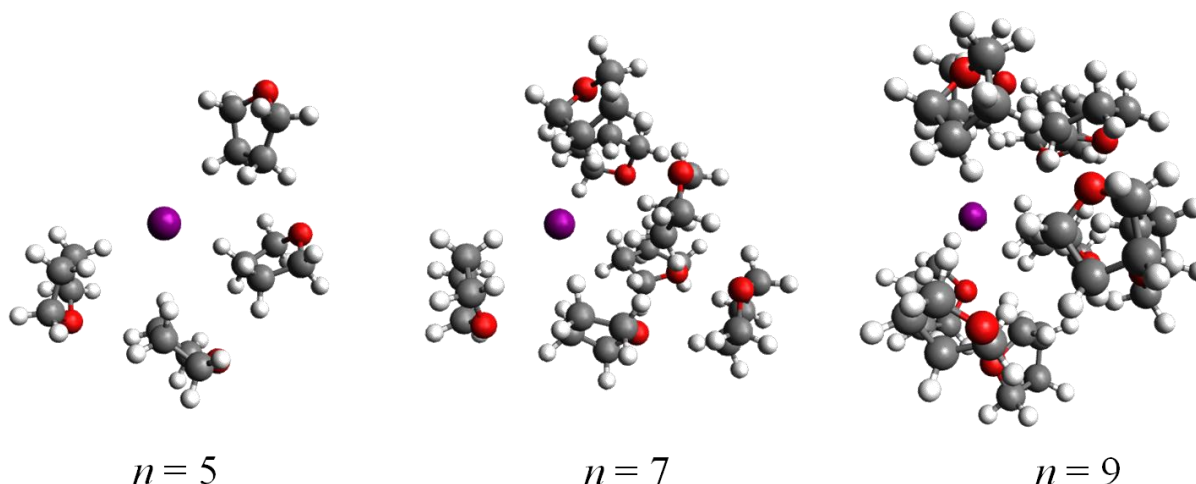


Figure 7.7. Computed structures of $I^-(\text{THF})_n$ for $n = 5, 7,$ and 9 from molecular dynamics simulations using a newly constructed AMOEBA force field.

energy scale must be established. This is done by scaling the stabilization energy of each solvent by the value of the iodide-solvent monomer interaction:¹²

$$\text{Scaled } E_{stab}^{(solvent)}(n) = E_{stab}^{(solvent)}(n) / E_{stab}^{(solvent)}(n=1) \quad (7.4)$$

This is shown in Figure 7.6 for iodide in THF, water and acetonitrile, with the latter two solvent values adapted from Markovitch, *et al.*¹² If water and acetonitrile act as the limiting cases of surface and internal solvation in this size range, respectively, then it can be seen from Fig. 7.6 that THF lies somewhat in between the two, suggesting that I^- is embedded within the cluster, perhaps toward the surface while still being highly coordinated.

7.4.3 Computational results

Quantum chemical calculations on the structures of the $I^-(\text{THF})_n$ clusters can help determine the nature of the ion's position in the cluster. VDEs of the clusters depend strongly on the nuclear geometry from which they are computed, so an equilibrated structure must first be found. Comparing these VDEs to those from experiment then becomes meaningful and inferences can be made.

Structures were first obtained by constructing a new AMOEBA force field - a pair-wise additive force field based off of the distributed multipoles of the THF molecule. The field is a hybrid of the -C-O-C- interaction from the existing diethyl ether field and the five-membered aliphatic carbon ring from a pyrrolidine force field. This approach is a legitimate first approximation since the multipole contributions are additive. Using this new field, iodide-doped THF cluster geometries were annealed in a classical molecular dynamics simulation at $T = 100$ K for ~55 picoseconds as they relaxed to their ergodic structures. The temperature was chosen to be close to that of the experiment as estimated from the evaporative ensemble.³⁶ The metric for equilibration was (one component of the) velocity autocorrelation function of the iodide atom; once it dropped sufficiently low such that changes in the structure were due solely to thermal

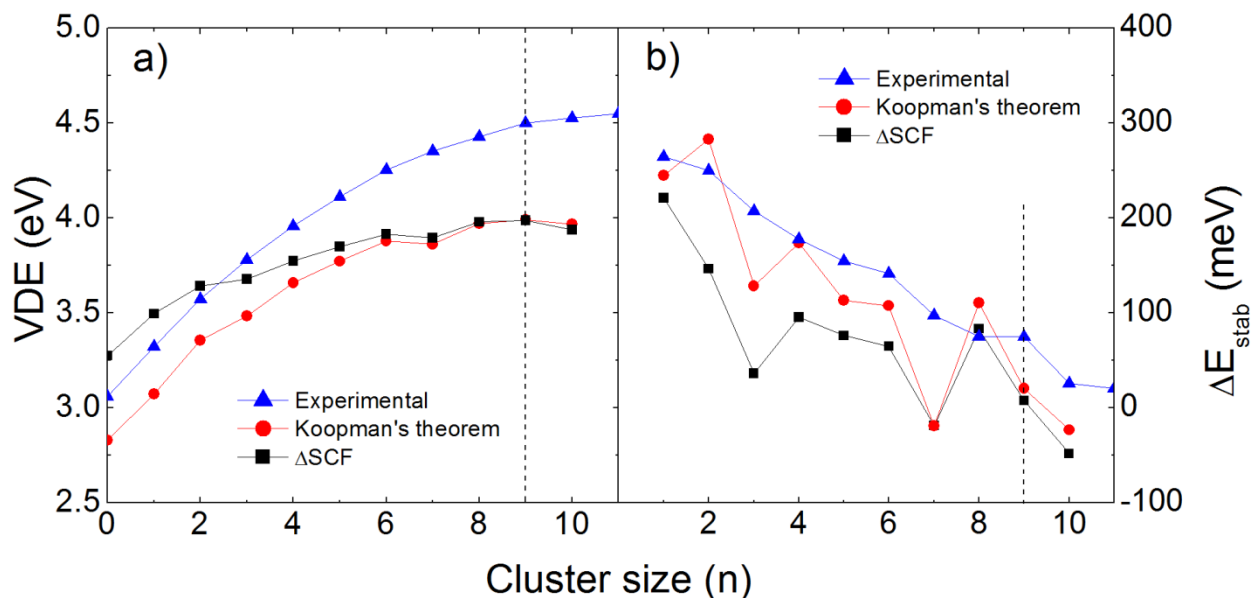


Figure 7.8a. Experimental and computed VDEs vs. cluster size n .

Figure 7.8b. Experimental and computer differential stabilization energies (slope of VDE) versus cluster size n . The dashed line in both figures marks the transition observed at $n = 9$.

fluctuations the structure was said to be relaxed. Several of these structures are shown in Figure 7.7. The energies of these clusters and their associated neutrals were calculated with density functional theory using the ω B97x-D functional with the 6-31+G* basis set and the LANL2DZ effective core potential for iodine. The difference between the neutral and anion energies at this fixed (anion) geometry is taken as the vertical detachment energy. These values can be computed by several different methods. Koopman's theorem provides a simple estimate of the energy by calculating the energy of the anion and then the neutral without letting the other electrons relax to the new electron distribution. Alternatively, the difference in the self-consistent field energies (Δ SCF) of the anion and the neutral at the fixed (anion) geometry can also be used. Both of these values are shown along with the experimental VDEs in Figure 7.8a. It can be seen that neither method exactly calculates the electron affinity of iodine, with Koopman's theorem underestimating it and the Δ SCF method overestimating. However, both values appear to converge by the larger clusters studied here ($n = 10$). Compared to the experiment, the quantitative agreement is poor, with both methods underestimating the experimentally determined VDE by ~ 600 meV for $n = 10$. Qualitatively the calculated values do show the same trend, however. The computed VDEs significantly slow their increase around $n = 7-9$. Figure 7.8b shows the slopes of the VDEs and it can be seen that by $n = 7-8$ the experimental and computation results are in reasonable agreement, suggesting that the iodide truly is partially exposed though still embedded to some degree in the solvent cluster.

7.4.4 Bound excited states

Excited state autodetachment is a strong indication of resonant excitation to a bound excited state (the precursors of the charge-transfer-to-solvent state) in smaller clusters, however

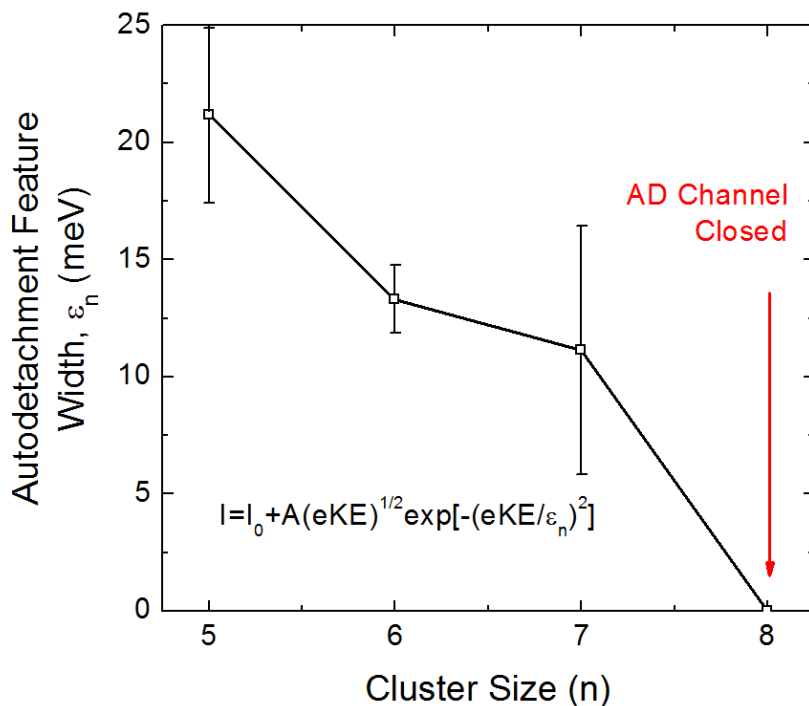


Figure 7.9. Spectral width (in meV) of the Autodetachment feature B at resonance vs. cluster size n . Widths are extracted from fits to Eq. 7.6. The width generally decreases with cluster size until $n = 8$ when Feature B is no longer observed ($\varepsilon = 0$).

this decay pathway is not open for all sizes. In $\text{I}^-(\text{H}_2\text{O})_n$, this channel is observed up to about $n = 15$, after which excited state dynamics are still observed but no low eKE electrons are seen.³⁷ The intensity of this band decreases as the clusters get larger and the channel closes. The lifetime of the autodetachment feature also increases, up to several nanoseconds or longer^{29, 37} in various solvents studied where the bare solvent cluster anion is observed to be adiabatically bound.³⁸⁻⁴⁰ This suggests the solvent cluster binds the electron strongly enough and has a sufficient number of vibrational states to support the excess energy after electron transfer. While strong autodetachment signals are seen for $n = 4-7$ in $\text{I}^-(\text{THF})_n$, the width of the feature when it is at its most intense (most resonant excitation) reduces with increasing cluster size, indicating that the autodetachment channel is closing. Indeed, scanning the excitation frequency over the range leading up to the vertical detachment energy of the cluster for $n = 8$ yielded no autodetachment electrons, suggesting full closure of the band at this size. The width of the autodetachment feature, ε , obtained by fitting to the expected profile for thermionic emission,

$$I(eKE; n) = I_0 + A(eKE)^{1/2} \exp\left\{-\left(\frac{eKE}{\varepsilon_n}\right)^2\right\}, \quad (7.5)$$

narrows considerably over the observed range; it must reach zero if the channel is to close by $n = 8$. This is shown in Figure 7.9.

Because bare $(\text{THF})_n^-$ clusters have been shown to bind an electron stably by $n = 6$ with significant binding energies (~ 2 eV), it is quite possible for clusters in this range to fully support the excess electron; the large number of modes associated with the relatively large solvent molecules (13 atoms/THF molecule) also provides a significant density of vibrational states to

support the excess energy deposited into the cluster after transfer. The notion that the solvated electron appears with its equilibrated absorption spectrum in transient absorption experiments was used to support the idea that the electron is injected into the pre-formed electropositive cavities and that the solvent structure of THF controls the electron's ultrafast dynamics.^{6, 17} A similar situation could exist in the clusters. Time-resolved cluster experiments are needed to fully investigate their excited state dynamics.

7.5 Conclusion

Using photoelectron imaging and density functional theory we have investigated the solvation of iodide in tetrahydrofuran clusters. In clusters larger than $n = 9$, The iodide ion appears coordinated to 7-9 THF molecules, embedded toward the surface of the cluster. The influence of the ion on the cluster geometry becomes negligible around $n = 19$ where the stabilization is due solely to long-range polarization interactions. A bound electronic excited state exists in clusters of as few as 4 THF molecules, with the excited state autodetachment channel closing by $n = 8$. This indicates the clusters can readily accept the electron and excess energy after electron transfer, as suggested by the nature of anionic THF clusters, $(\text{THF})_n^-$. More experimental work is needed to understand the dynamics of electron transfer in these clusters and is currently underway in our laboratory. Computational characterization of the excited state is also being studied in the Head-Gordon group. Additionally, infrared studies on both the iodide-doped and negative ions of THF clusters would be very useful in understanding the nature of charge/ion stabilization for this solvent. Moreover, these studies together with the ones presented here and in the last chapter lay the groundwork for the development of a detailed, molecular-level picture of the charge-transfer-to-solvent dynamics in THF clusters.

7.6 References

- 1 D. Serxner, C. E. H. Dessent, and M. A. Johnson, *J. Chem. Phys.* **105** (16), 7231 (1996).
- 2 B. J. Greenblatt, University of California, Berkeley, 1999.
- 3 S. E. Bradforth, and P. Jungwirth, *The Journal of Physical Chemistry A* **106** (7), 1286 (2002).
- 4 M. J. Blandamer, and M. F. Fox, *Chem. Rev.* **70** (59), 59 (1970).
- 5 X. Chen, and S. E. Bradforth, *Annu. Rev. Phys. Chem.* **59**, 203 (2007).
- 6 A. E. Bragg, and B. J. Schwartz, *J. Phys. Chem. B* **112**, 483 (2008).
- 7 A. E. Bragg, and B. J. Schwartz, *J. Phys. Chem. A* **112**, 3530 (2008).
- 8 G. Markovich *et al.*, *J. Chem. Phys.* **101** (11), 9344 (1994).
- 9 D. M. Koch, and G. H. Peslherbe, *Chem. Phys. Lett.* **359** (5-6), 381 (2002).
- 10 B. Winter *et al.*, *J. Am. Chem. Soc.* **127** (19), 7203 (2005).
- 11 C. E. H. Dessent, C. G. Bailey, and M. A. Johnson, *J. Chem. Phys.* **103** (6), 2006 (1995).
- 12 G. Markovich *et al.*, *J. Chem. Phys.* **105** (7), 2675 (1996).
- 13 T. Takayanagi, *J. Phys. Chem. A* **110** (22), 7011 (2006).
- 14 M. T. Zanni, University of California, Berkeley, 1999.
- 15 M. J. Bedard-Hearn, R. E. Larsen, and B. J. Schwartz, *J. Chem. Phys.* **122**, 134506 (2005).

- 16 D. T. Bowron, J. L. Finney, and A. K. Soper, *J. Am. Chem. Soc.* **128**, 5119 (2006).
17 I. B. Martini, E. R. Barthel, and B. J. Schwartz, *Science* **293** (5529), 462 (2001).
18 R. M. Young *et al.*, *J. Chem. Phys.* **133** (15), 154312 (2010).
19 A. T. Shreve, M. H. Elkins, and D. M. Neumark.
20 W. H. Robertson *et al.*, *J. Chem. Phys.* **116** (12), 4853 (2002).
21 J. P. Beck, and J. M. Lisy, *J. Phys. Chem. A* **114**, 10011 (2010).
22 O. M. Cabarcos *et al.*, *J. Chem. Phys.* **110** (19), 9516 (1999).
23 C. A. Corbett, T. J. Martinez, and J. M. Lisy, *J. Phys. Chem. A* **106** (42), 10015 (2002).
24 A. V. Davis *et al.*, *J. Chem. Phys.* **118** (3), 999 (2003).
25 U. Even *et al.*, *J. Chem. Phys.* **112** (18), 8068 (2000).
26 W. C. Wiley, and I. H. McLaren, *Rev. Sci. Instrum.* **26** (12), 1150 (1955).
27 A. T. J. B. Eppink, and D. H. Parker, *Rev. Sci. Instrum.* **68** (9), 3477 (1997).
28 V. Dribinski *et al.*, *Rev. Sci. Instrum.* **73** (7), 2634 (2002).
29 A. Kammrath *et al.*, *J. Phys. Chem. A* **109**, 11475 (2005).
30 O. T. Ehrler *et al.*, *J. Phys. Chem. B* **113**, 4031 (2009).
31 R. M. Young, M. A. Yandell, and D. M. Neumark, *J. Chem. Phys.* **134** (12), 124311 (2011).
32 R. N. Barnett, U. Landman, and C. L. Cleveland, *Chem. Phys. Lett.* **145** (5), 382 (1988).
33 G. Makov, and A. Nitzan, *J. Phys. Chem.* **98** (13), 3459 (1994).
34 R. D. Levine, *Molecular reaction dynamics* (Cambridge University Press, 2005).
35 W. Marbach, A. N. Asaad, and P. Krebs, *J. Phys. Chem. A* **103**, 28 (1999).
36 C. E. Klots, *Z. Phys. D* **20** (1), 105 (1991).
37 J. R. R. Verlet *et al.*, *J. Chem. Phys.* **123** (231102), 4 (2005).
38 J. V. Coe *et al.*, *J. Chem. Phys.* **92** (6), 3980 (1990).
39 J. R. R. Verlet *et al.*, *Science* **307**, 93 (2005).
40 A. Kammrath *et al.*, *J. Chem. Phys.* **125**, 076101 (2006).

Chapter 8. Thermal Effects on Energetics and Dynamics in Water Cluster Anions $(\text{H}_2\text{O})_n^-$ ($11 \leq n \leq 75$)

The electron binding energies and relaxation dynamics of water cluster anions $(\text{H}_2\text{O})_n^-$ ($11 \leq n \leq 75$) formed in co-expansions with neon were investigated using one-photon and time-resolved photoelectron imaging. Unlike previous experiments with argon, water cluster anions only exhibit one isomer class, the tightly-bound isomer I with approximately the same binding energy as clusters formed in argon. This result, along with a decrease in the internal conversion lifetime of excited $(\text{H}_2\text{O})_n^-$ ($25 \leq n \leq 40$), indicates that clusters are vibrationally warmer when formed in neon. A corroborates this. Over the ranges studied, the vertical detachment energies and lifetimes appear to converge to previously reported values.

8.1 Introduction

The hydrated electron, e_{aq}^- , has received much attention in recent years owing to its importance as a highly reactive chemical transient in many important processes ranging from atmospheric chemistry¹ to low-energy radiation damage to biological systems.² It is also of fundamental interest as the simplest quantum solute. While there is still some controversy as to the exact nature of how e_{aq}^- is solvated in water,³⁻⁹ the prevailing picture is that the electron resides within a $\sim 2\text{-}3$ Å radius cavity defined by ~ 6 water molecules in a quasi-octahedral arrangement.¹⁰ In the gas phase, water cluster anions $(\text{H}_2\text{O})_n^-$ offer another venue to understanding electron solvation, as they can be thought of as precursors to bulk hydrated electron.¹¹ However, there are concerns about the validity of inferring information on the energetics and dynamics of bulk hydrated electrons from extrapolations of cluster data, given the controversies surrounding the nature of electron binding to water clusters^{11, 12} and differences in temperature between cluster and bulk experiments.¹³ In this work, we examine how cluster formation conditions affect the binding energies and relaxation times in water cluster anions by preparing them in neon carrier gas and comparing the results to previous studies in Ar and in ion traps.

Much of our information on $(\text{H}_2\text{O})_n^-$ clusters derives from one-photon photoelectron spectroscopy,¹⁴⁻¹⁷ which yields size-dependent vertical detachment energies (VDEs), and infrared spectroscopy,¹⁸⁻²⁰ which yields a more direct structural probe of these species. The first photoelectron spectra, measured by Bowen and co-workers²¹ for clusters as large as $n = 69$, showed that the VDE of these clusters increased linearly as a function of the inverse cluster radius, $1/R = n^{-1/3}$, extrapolating to a value of 3.3 eV in the limit of $n \rightarrow \infty$. This implied value for the VDE of e_{aq}^- agrees with several recent direct measurements of this quantity via photoelectron spectroscopy of electrons in liquid water microjets,²²⁻²⁵ which yielded VDEs in the range of 3.3-3.6 eV.

However, this picture of a straightforward extrapolation of cluster to bulk properties is complicated by several factors. First, depending on the clustering conditions, water clusters can bind electrons in multiple ways.¹⁵ Clusters formed in argon at low backing pressures (typically associated with warmer expansions) around 30 psig had binding energies similar to those

previously reported, but at higher pressures (~ 70 psig) the spectra were dominated by a new, low-energy peak. The new, weakly-bound feature was labeled "isomer II" and attributed to a surface bound state, while the original, higher-binding energy feature was termed "isomer I" and was deemed the best candidate for an internally solvated electron. A third peak at very low binding energies (~ 0.2 eV) was also found and labeled "isomer III". Isomers II and III were attributed to metastable, higher energy structures formed by attaching electrons to very cold neutral clusters. VDEs for isomers II and III extrapolate to ~ 1.7 eV and ~ 0.6 eV, respectively, much lower than the estimate for the bulk hydrated electron. Recently, photoelectron spectroscopy of water cluster anions cooled to ~ 10 K in an ion trap²⁶ has shown that in these very cold clusters, the isomer I peak splits into multiple features beginning around $n = 25-30$. The higher binding energy feature (labeled "isomer Ib") extrapolates to about 4.0 eV, notably higher than the values from the near-room temperature liquid jet experiments. The effect of cluster temperature and other initial conditions on the electron binding energy and motif has been considered theoretically by Rossky,²⁷ Herbert,²⁸ and Jungwirth.^{13, 29}

Another set of experiments has focused on characterizing excited state dynamics in $(\text{H}_2\text{O})_n^-$ clusters. Here, time-resolved photoelectron spectroscopy experiments have been carried out³⁰⁻³² in which one excites the cluster analog³³ of the $s \rightarrow p$ transition of e_{aq}^- and follows the resulting relaxation dynamics. These yield internal conversion lifetimes for the p -state as a function of cluster size that can be compared to lifetimes inferred from transient absorption experiments in the bulk. The internal conversion lifetimes of isomer I clusters were shown to be between 300 fs for $n = 15$ and ~ 70 fs for $n = 200$. Extrapolating to infinite cluster sizes gave an estimate of the bulk internal conversion lifetime of 60 fs, very close to one of the timescales measured in transient absorption experiments.³⁴ This comparison helped solidify the idea that large isomer I clusters are precursors to the hydrated electron in the bulk and supported the "non-adiabatic" relaxation mechanism³⁵ for bulk hydrated electrons. Again, however, one must consider the validity of this type of extrapolation since the dependence of these dynamics on cluster temperature are not well understood.

The body of experimental and theoretical work on water cluster anions indicates that probing the effect of temperature on the energetics and dynamics of these species is of considerable interest. As indicated above, one approach has been to measure photoelectron and infrared spectra of clusters that are trapped and cooled to cryogenic temperatures.²⁶ Alternatively, in experiments based on free jet ion sources, the cluster temperature can be varied by adjusting the carrier gas backing pressure, as was demonstrated in our experiments with Ar,¹⁵ or by changing the carrier gas itself, as is described in this paper. Here, we generate clusters in a Ne expansion, which is generally expected to result in warmer clusters because Ne is a less efficient energy transfer medium than Ar.³⁶⁻³⁸ By carrying out one-photon and time-resolved photoelectron imaging, we test how this substitution affects the vertical detachment energies and the excited state internal conversion dynamics of the anion clusters.

Our key results are as follows. Unlike previous studies with argon as the carrier gas, only the strongly-bound isomer I is observed here, even at pressures much higher than previously used. We demonstrate that the vertical detachment energies of water cluster anions are relatively insensitive to the temperature of the cluster as determined by the source conditions. Conversely, the internal conversion lifetimes of excited water cluster anions are influenced by the cluster temperature, becoming shorter for nominally warmer clusters. However, both the binding energies and timescales appear to converge to previously reported values.

8.2 Experimental

A detailed description of the time-resolved photoelectron imaging apparatus has been published previously.³⁹ Briefly, the carrier gas of interest is flowed over a heated (50-75 °C) water reservoir, creating a mixture that is then expanded into a vacuum chamber through a solenoid valve pulsed at 600 Hz.⁴⁰ Clusters form from collisions with the carrier gas during the adiabatic expansion. They then pass through a ring-shaped hot filament cathode emitting electrons which are accelerated to ~200 eV and ionize the clusters via secondary electron attachment. These ions are then extracted perpendicularly into a mass spectrometer to achieve mass separation.⁴¹ Additional mass selection is accomplished with a pulsed electrostatic switch. The isolated ion packet of interest is then interrogated by the pump and probe laser pulses. Detached electrons are accelerated and analyzed using velocity map imaging⁴² which maps the emitted photoelectron velocity vectors onto a two-dimensional detector comprising a set of chevron-mounted microchannel plates and a phosphor screen. Images are captured using a CCD camera and inverted using the BASEX method after being 4-way symmetrized.⁴³ Inverted images are then converted to electron kinetic energy (eKE) distributions, which are transformed to binding energy distributions: $eBE = h\nu_{probe} - eKE$.

The femtosecond laser pulses are generated using a commercial Ti:sapphire oscillator/chirped-pulse multipass amplifier (KM Labs Griffin oscillator/ Dragon amplifier). Half (~1 mJ/pulse) of the 30 fs, 790 nm fundamental is then used to pump a continuum-seeded optical parametric amplifier (Light Conversion TOPAS-C) to create ~50 μ J/pulse of signal light between 1220 nm (0.98 eV) and 1260 nm (1.01 eV) for use as the pump pulse to excite the $p \leftarrow s$ transition for the smaller clusters.³³ The remainder of the amplifier output is attenuated and used as the probe (~100 μ J/pulse) for the time-resolved experiments. Temporal resolution is determined by measuring the cross-correlation time of the pump and probe pulses using a second nonlinear crystal for sum-frequency mixing; typical time resolution is 150 fs full-width at half-maximum (FWHM). For the one-photon experiments, the fundamental is frequency-doubled in a 29.1° BBO crystal yielding 395 nm (3.14 eV) light and attenuated to ~ 50 μ J/pulse. The resolution of the photoelectron spectrometer is limited by the bandwidth of the femtosecond laser and is about 45-50 meV FWHM for both the 1.57 eV and 3.14 eV detachment pulses.

8.3 Results and Analysis

Figure 8.1 shows a mass spectrum of $(\text{H}_2\text{O})_n^-$ formed in an expansion of 250 psig Ne. Clustering is seen out to $n \sim 45$. Mass spectra for cluster anions generated in Ar extend considerably further. Photoelectron spectra taken with $h\nu = 3.14$ eV for $(\text{H}_2\text{O})_{50}^-$ formed under various source conditions are shown in Figure 8.2. The spectra show the same broad, structureless shape seen in previous studies. In stark contrast to these earlier results, $(\text{H}_2\text{O})_n^-$ formed in neon exhibits only the high-binding energy isomer (isomer I) for all cluster sizes ($n = 11-75$) and pressures studied here (70-250 psig Ne). Intensities for ions formed in co-expansions with neon were lower than for ions made in argon; co-expansions with helium did not generate significant clustering in our source. No evidence for any other isomers with significantly lower (or higher) binding energies was found over this size range in either Ar or Ne.

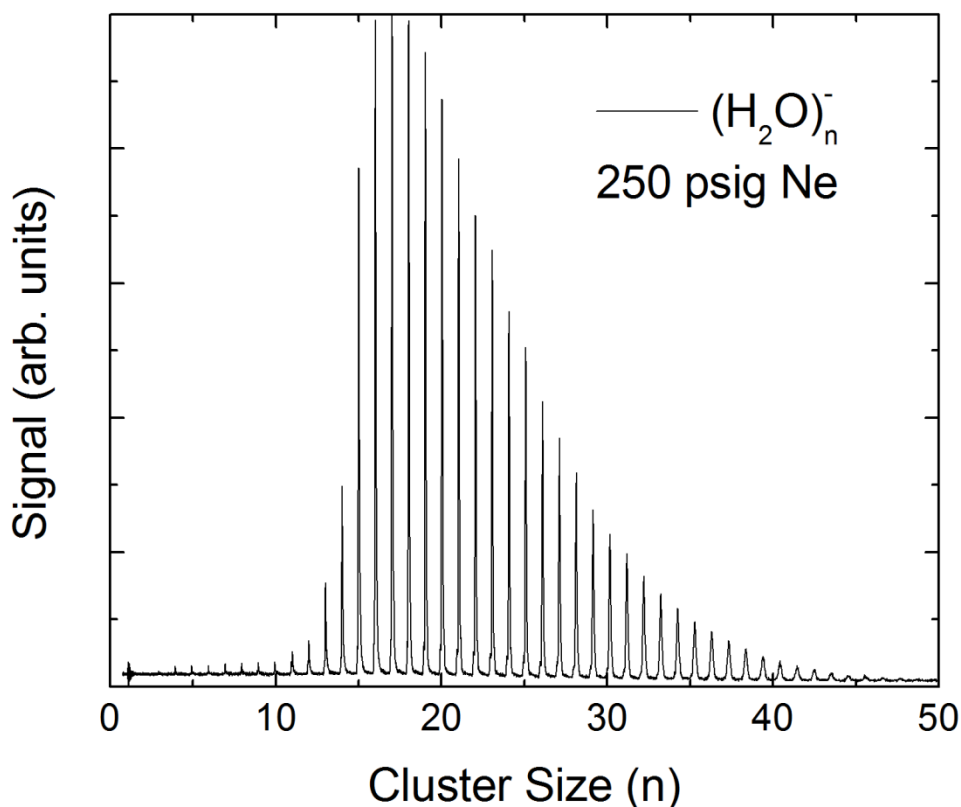


Figure 8.1. Time-of-flight mass spectrum for water cluster anions $(\text{H}_2\text{O})_n^-$ formed in Ne carrier gas.

Fitting the peak of the photoelectron binding energy distribution yields the vertical detachment energy (VDE) for each cluster. A Gaussian-Lorentzian (G-L) profile is assumed:^{26, 44, 45}

$$I(eBE; n) = \begin{cases} I_0 + A \exp\left[-(eBE - VDE_n)^2 / w_G^2\right] & eBE < VDE_n \\ I_0 + A \left[\frac{w_L^2}{(eBE - VDE_n)^2 + w_L^2} \right] & eBE \geq VDE_n \end{cases} \quad (8.1)$$

where I_0 is the baseline intensity, A is a scaling factor, VDE_n is the VDE of the cluster of size n , and w_G and w_L are the half-widths of the Gaussian and Lorentzian sides, respectively. VDEs for selected clusters $n = 11-75$ formed in 100 psig and 250 psig neon are plotted in Figure 8.3 against $n^{-1/3}$ along with previously reported values.¹⁷ Over the size range reported here, the VDEs range from 0.78 eV to 2.21 eV and are generally in good agreement with the previous isomer I VDE's (red squares). Time-resolved photoelectron spectra were taken from $n = 25-40$. A representative TRPE spectrum is shown in Figure 8.4 for $(\text{H}_2\text{O})_{30}^-$. Four main features are seen: excited-state autodetachment at very low eKE (Feature A), direct probe detachment from the ground state (B) around 0.25 eV, resonant two-photon detachment (R2PD) from the pump (Feature C) around 0.6 eV, and transient excited-state signal (pump-probe, Feature D) appearing between 1.00 and 1.50 eV kinetic energy.

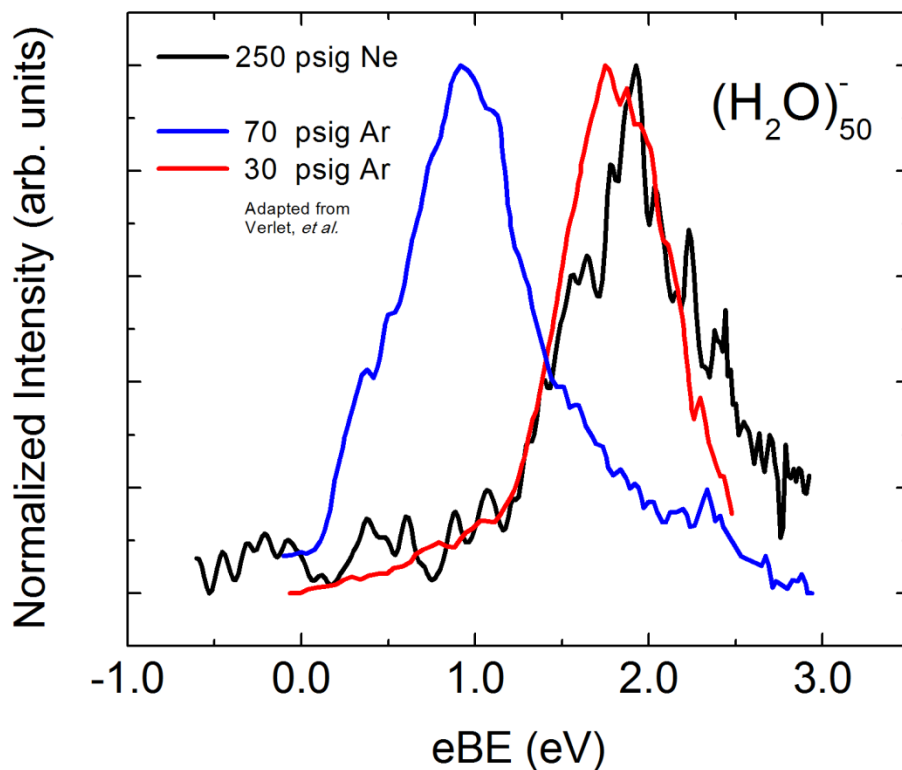


Figure 8.2. Photoelectron spectra of $(\text{H}_2\text{O})_{50}^-$ with $h\nu = 3.14$ eV for different source gasses and pressures: 250 psig neon (black); 70 psig argon (blue); 30 psig argon (red). Spectra taken in argon are adapted from Verlet, *et al.*

Integrated intensities of these features yield their associated population dynamics. The intensities of Features B and D are shown in the inset of Figure 8.4. Feature B is depleted and D is created at the zero of pump-probe delay (t_0) before recovering and decaying on the same timescale, respectively. Feature B does not recover to its initial population owing to R2PD from the pump depleting the ground state population at positive pump-probe delays. Because of the excited state lifetime and temporal resolution of the laser are comparable, the integrated intensities are fit to the convolution of a single exponential decay with a timescale τ_{IC} and the instrumental response function (a Gaussian with width σ , where $\text{FWHM} = 2\sigma\sqrt{2\ln 2}$):

$$I_p(t) = e^{-t^2/\sigma^2} * \begin{cases} I_0 & t < t_0 \\ I_0 + A \exp[-(t-t_0)/\tau_{IC}] & t \geq t_0 \end{cases} \quad (8.2)$$

The σ parameter is taken as the cross-correlation time of the laser pulses taken either in situ from cross-correlation limited above-threshold signals or from a measurement outside the vacuum chamber. Based on the complementary behavior of the ground- and excited-state dynamics, the lifetime of the excited state Feature D is taken as the internal conversion time. Figure 8.5 shows an overlay of the integrated intensity of Feature D for $(\text{H}_2\text{O})_{35}^-$ clusters formed in 100 psig neon (red circles) and 40 psig argon (black squares). Both traces have the same functional form, and the rise times are very similar (within 10 fs), however the decay time is shorter in the neon-born

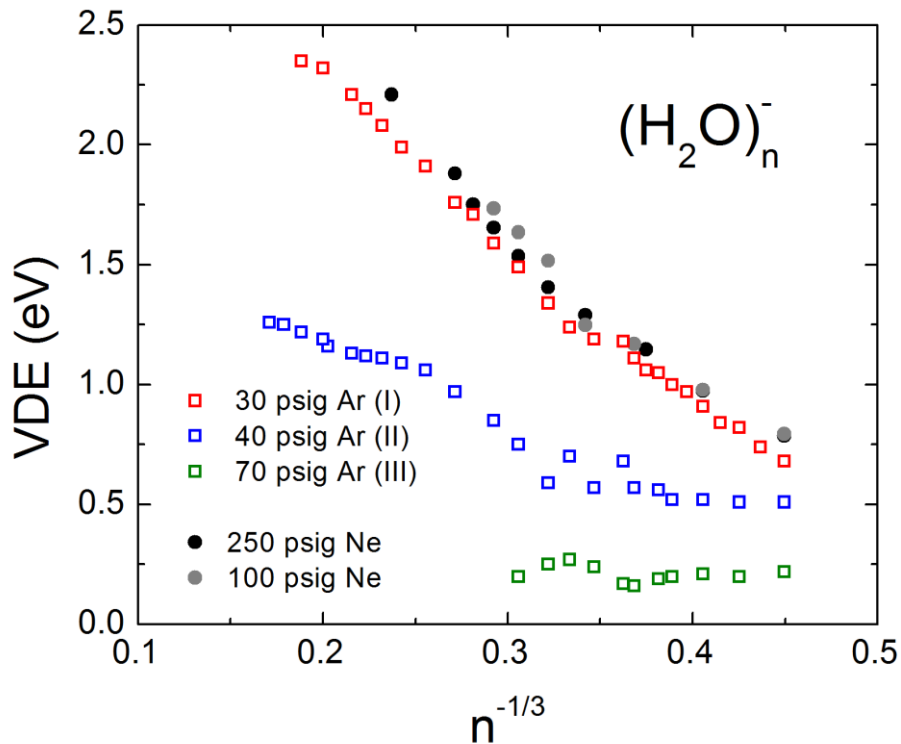


Figure 8.3. Vertical detachment energies (VDEs) of $(\text{H}_2\text{O})_n^-$ under various source conditions: 250 psig neon (black circles); 100 psig neon (grey filled circles); 30 psig argon (red squares); 70 psig argon (isomer II: blue squares; isomer III: green squares).

clusters: 111 vs 154 fs. Following previous arguments,^{30, 32, 46, 47} internal conversion lifetimes were plotted against the inverse cluster size, $1/n$. Internal conversion times are shown in Figure 8.6 for $n = 25-40$ vs. $1/n$ with error bars estimated as the standard error from the fit. While the data follow the same qualitative trend, it can be seen that the lifetimes for clusters born in neon are systematically shorter than for those in argon; time constants for clusters in one gas do not fall within the error bars of the other.

8.4 Discussion

The results in the Section IV indicate that in our ion source, the mass spectrum of $(\text{H}_2\text{O})_n^-$ clusters using Ne as a carrier gas cuts off at smaller cluster sizes than when Ar is used. The largest observable size with sufficient intensity to take a photoelectron spectrum was $n = 75$ for clusters formed in neon, compared to $n = 200$ for those formed in argon.^{17, 32} These effects are reminiscent of those seen in the size distribution of Na_n clusters formed in free jet expansions with various seed gases.⁴⁸ In addition, our photoelectron spectra show that only isomer I clusters are formed in the adiabatic expansion with neon even at backing pressures as high as 250 psig; under similar conditions in Ar, isomer III was found to dominate the photoelectron spectrum. Neon has previously been observed to be less effective than argon at deactivating vibrationally excited organic molecules like toluene^{49, 50} and azulene.^{51, 52} It is therefore reasonable to expect

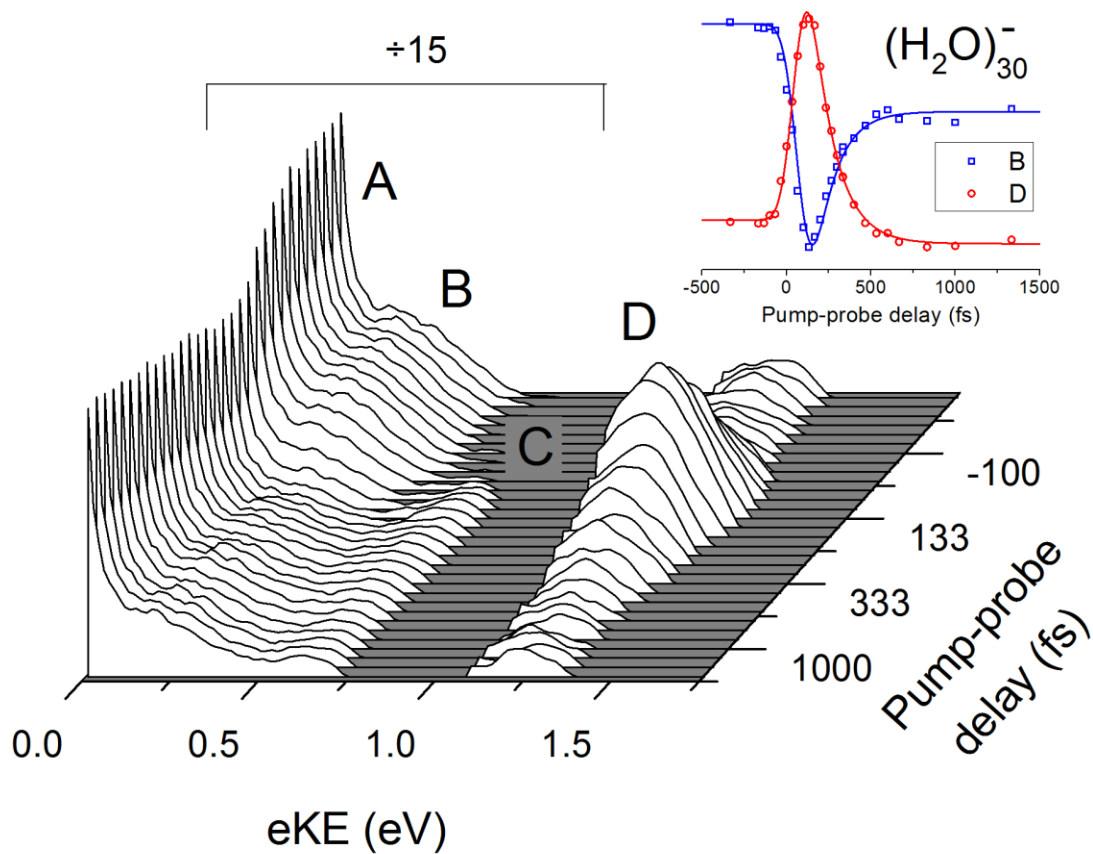


Figure 8.4. Time-resolved photoelectron spectrum of $(\text{H}_2\text{O})_{30}^-$. The $p \leftarrow s$ transition is excited with $h\nu_{\text{pump}} = 1.00$ eV ($\lambda_{\text{pump}} = 1250$ nm); electrons are detached with $h\nu_{\text{probe}} = 1.57$ eV. TRPES of these clusters strongly resembles the spectra of isomer I water cluster anions reported previously.^{31,32} The spectrum below 1.0 eV is scaled by a factor of 15.

less efficient cooling of water cluster anions using Ne as the carrier gas, and we can understand our results in this context.

Although the detailed mechanism for water cluster anion formation is not fully understood, it most likely proceeds from attachment of a low energy electron to a neutral water cluster. The resulting anion cluster can grow via collisions with other water molecules in the free jet. Both electron attachment and additional aggregation add to the internal energy of the cluster, whereas it can lose energy by collisions with the carrier gas in the higher pressure region of the expansion and by evaporation of water molecules. When Ne rather than Ar is used as a carrier gas, one expects the distribution of neutral water clusters prior to electron attachment to be shifted toward smaller sizes, and for cooling collisions subsequent to electron attachment to be less efficient. These effects combine to yield smaller anion clusters compared to experiments in Ar, as is observed here.

In the “evaporative ensemble” model of cluster formation, the cluster sheds waters by evaporative cooling until its internal energy is roughly comparable to the binding energy of a water molecule to the cluster.⁵³ Under these circumstances, once one is in a size regime where the binding energy of a water is relatively independent of cluster size, then a mass spectrum that cuts off at smaller sizes indicates a warmer cluster distribution. We estimate the temperature of our clusters to be ~ 180 K.^{53,54} In fact, not only the mass spectrum but also the isomer

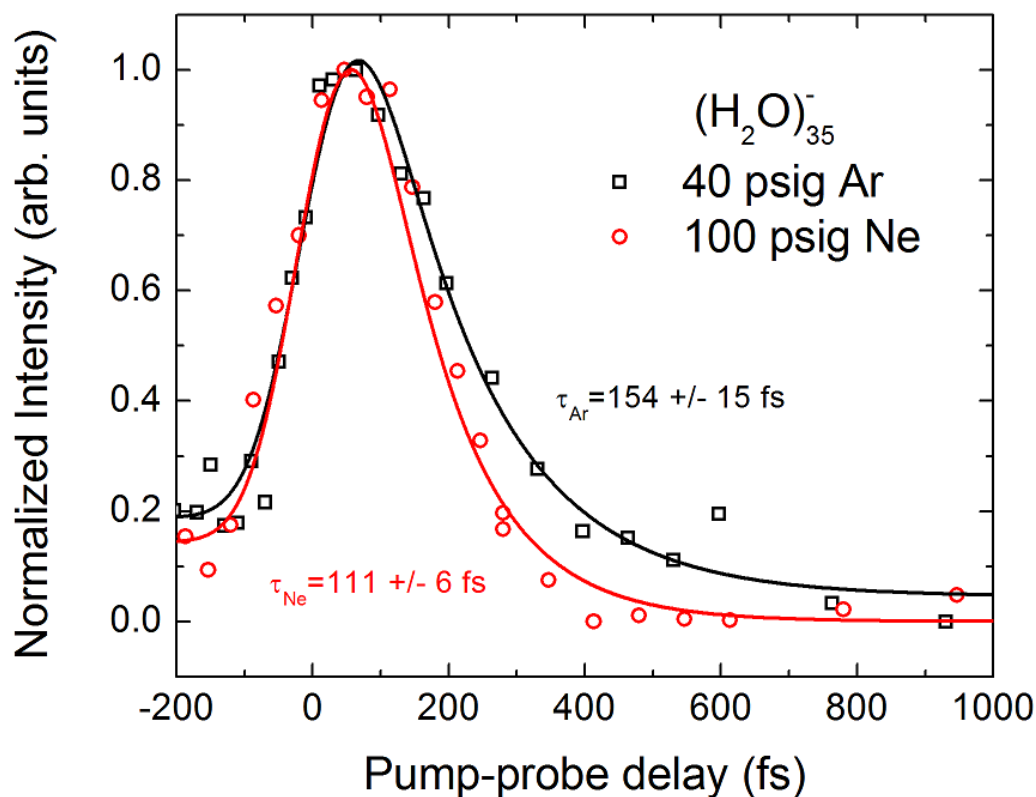


Figure 8.5. Integrated intensities of Feature D for $(\text{H}_2\text{O})_{35}^-$ clusters formed in a seeded expansion of 40 psig argon (black squares) and 100 psig neon (red circles). Relaxation is $\sim 30\%$ faster in the clusters from the neon expansion at this size.

distribution suggest that the clusters formed in Ne are warmer. The formation of isomers II and III under “cold”, *i.e.* high pressure, expansion conditions in Ar has been attributed by us and others to the trapping of water cluster anions in a metastable state,^{13, 15, 28} as indicated in Figure 8.7. This trapping could occur if the neutral clusters were very cold and arranged in a geometry similar to that of one of the local minima in Figure 8.7. Such a scenario is not unreasonable, because the lowest energy structures in neutral water clusters are generally quite different from those in water cluster anions.⁵⁵ Once electron attachment occurs, rapid energy removal by the Ar carrier gas then traps the anion in the isomer II (or III) well. In a Ne expansion, we expect the neutral clusters to be warmer prior to attachment, and energy removal from the anion by the Ne to be less efficient. Both effects lessen the probability of trapping in a local minimum as opposed to the global minimum in Figure 8.7 corresponding to isomer I. While we can rationalize the differing isomer distributions in the two carrier gases, it is nonetheless remarkable that there is no evidence for anything other than isomer I clusters when Ne is used.

As it appears that the water cluster anions formed in Ne are warmer than in our previous work in Ar, we now examine the one-photon and time-resolved PE spectra in more detail. Figure 8.3 shows that the VDEs from the one photon PE spectra are in agreement with those of isomer I previously reported by our group,¹⁵ although they are systematically higher by ~ 50 - 100 meV. The photoelectron spectra also appear slightly narrower (e.g. 0.85 eV FWHM in Ne, compared to 0.92 eV in Ar for $n = 75$). The VDE's in Figure 8.3 lie between those found by von Issendorff and co-workers²⁶ for isomers 1a and 1b in their investigation of cold (~ 10 K)

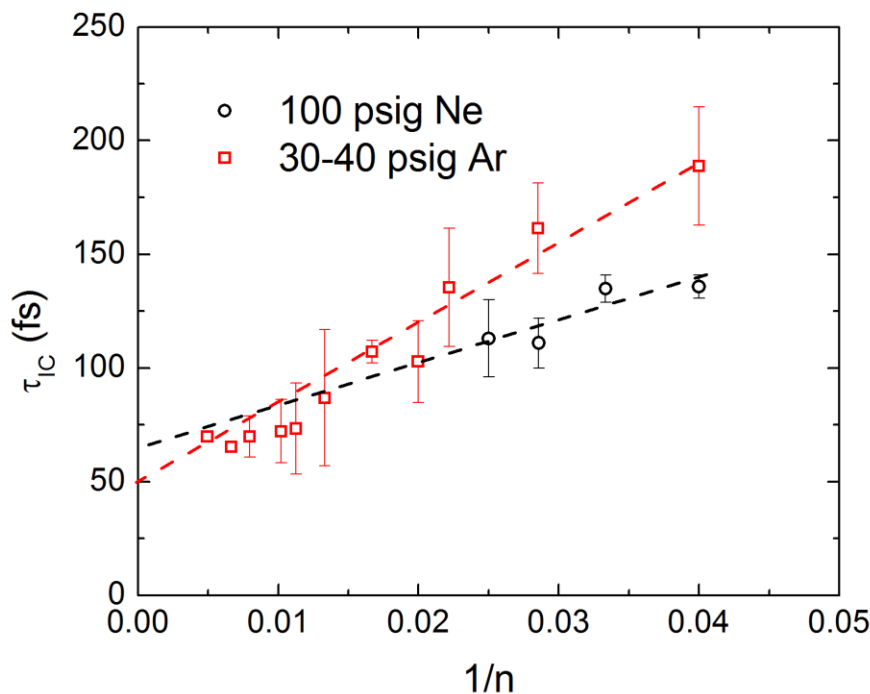


Figure 8.6. Timescales for internal conversion following resonant excitation ($p \leftarrow s$) for $(\text{H}_2\text{O})_n^-$ isomer I clusters from different source conditions: 100 psig neon (black squares); 40 psig argon (red circles, adapted from Griffin, *et al.*³²). The values and slopes are different while appearing to converge to the same bulk limit (50-60 fs).

water clusters; as discussed by Herbert,²⁸ isomers 1a and 1b may be “partially-embedded” surface states and cavity states of the excess electron, respectively. Our spectra were well fit to a single G-L profile, as compared to a sum of multiple G-L functions needed to fit their spectra. These differences may reflect not only the temperature but also the rather different means of ion formation in their study,²⁶ in which relatively warm ions formed in a gas aggregation source were then cooled in an ion trap prior to spectroscopic interrogation. In any case, there is mounting evidence that “isomer I” comprises multiple close-lying structures rather than a single geometry for a given cluster size.^{26, 28, 44} One can therefore envision that the cluster anions at 10 K are trapped in multiple minima separated by small barriers, while the warmer cluster anions in our experiment represent a more averaged structure and thus result in a single-peaked photoelectron spectrum.

The time-resolved spectra show more pronounced differences between clusters formed in Ne and Ar; the results in Figures 8.5 and 8.6 clearly show faster internal conversion using Ne as the carrier gas. This result is consistent with increased vibrational energy in the cluster, which can promote faster internal conversion through a variety of mechanisms that have been proposed for p -state relaxation in water cluster anions. For example, consider the “energy gap” law for internal conversion, in which the rate is essentially limited by Franck-Condon (FC) factors.⁵⁶ The FC overlap is highly sensitive to the energy gap between electronic levels: small energy differences between the two electronic states generally leads to better FC overlap than for larger ones. The overlap tends to fall off exponentially with increasing energy gap. The less efficient cooling of the water clusters in neon leaves them with higher-peaked vibrational energy distributions, leading to more Franck-Condon overlap with higher-lying vibrational states, and

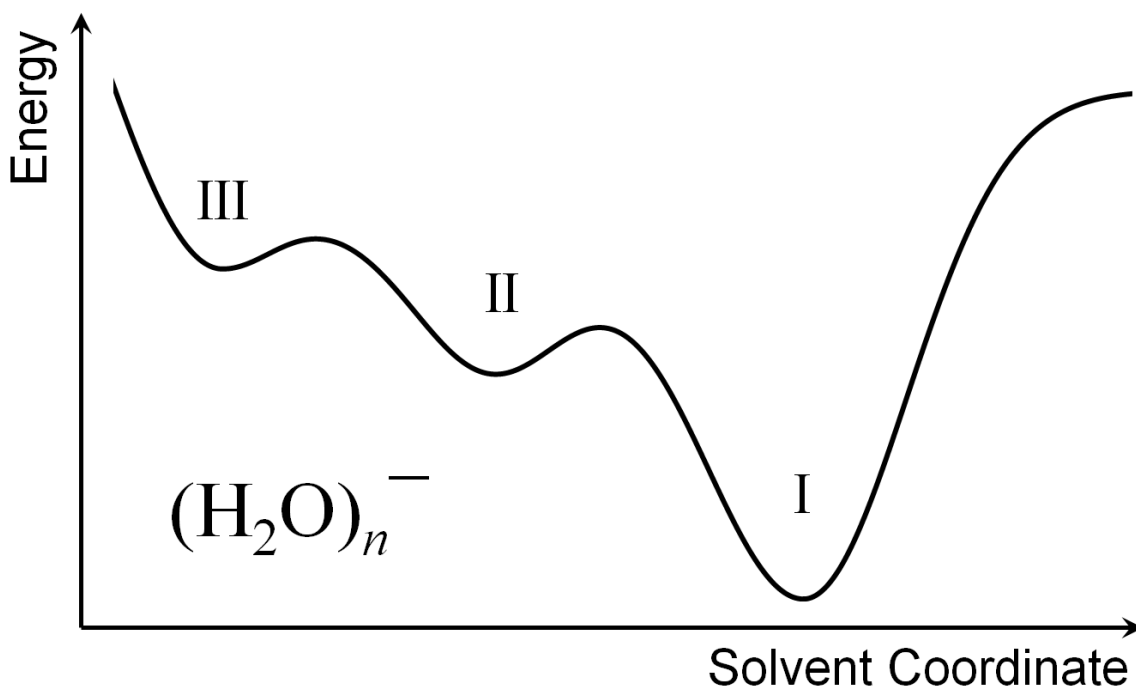


Figure 8.7. Schematic potential energy surface for isomers I-III in water cluster anions $(\text{H}_2\text{O})_n^-$ with relative well depths scaled to reported values for $n = 20$.^{15, 17}

therefore higher internal conversion rates (lower lifetimes). The temperature sensitivity is also implied by the non-adiabatic coupling model proposed by Fischer and Dietz to explain the $1/n$ dependence in clusters.⁴⁶ In this model, internal conversion is induced by coupling of the OH stretch transition dipole to the electronic transition dipole, giving the rate an overall $1/R^3$ ($=1/n$) dependence. The coupling is weighted by the FC factors for the $s \leftarrow p$ transition which are dominated by the molecules in the first solvation shell, so the same temperature argument applies. Alternatively, the dynamics of internal conversion for bulk hydrated electrons have been shown to be driven by solvent fluctuations.^{57, 58} The electronic energy level gap is structurally sensitive and will fluctuate with the solvent configuration. Some of these variations will bring the energy gap to near zero, inducing an electronic transition back to the ground state. These effects will be more pronounced at higher temperatures as the amplitude of the fluctuations increases. Generally speaking, the increased thermal energy will typically increase the rate of transition, regardless of the details of the dynamical model.

Figure 8.6 suggests that internal conversion timescales for clusters born in neon and argon converge at larger sizes. More data points are necessary to make a definitive statement to this as well as the extrapolation to bulk. Moreover, although there is some temperature dependence, the timescales still yield a rapid, <100 fs internal conversion time in the bulk limit, supporting the validity of previous extrapolations of cluster dynamics.^{30, 32}

It would be of great interest to explore the effects seen here in other solvent cluster anions. The ability to bind excess electrons in multiple ways is not unique to water: methanol cluster anions have been shown in both photoelectron experiments^{59, 60} and simulations⁶¹ to have at least two binding motifs. Time-resolved measurements similar to those performed on water have been carried out⁴⁷ so the effect could be readily observed. This may help resolve some of the discrepancy between the bulk electron binding energies extrapolated from the clusters and

measured in liquid jets.⁶² Additionally, ammonia cluster anion $(\text{NH}_3)_n^-$ have been formed and analyzed out to $n = 1100$,⁶³ but dielectric continuum analysis suggests that the clusters are more likely to be solid. Forming the clusters in neon could prove a way to generate *liquid* ammonia cluster anions and help better understand the nature and validity of the $n^{-1/3}$ extrapolation for the VDEs.

8.5 Conclusions

One-photon and time-resolved photoelectron imaging were used to investigate the effects of the carrier gas on electron binding and dynamics in water cluster anions. Only isomer I clusters using neon at backing pressures as high as 250 psig, whereas for clusters formed in argon the photoelectron spectra are dominated by weakly bound isomers at pressures as low as 70 psig. These results are consistent with the formation of warmer water cluster anions in Ne. VDEs were determined to be relatively insensitive to the carrier gas, while the internal conversion lifetimes subsequent to $p \leftarrow s$ excitation were shorter in Ne. Extending this study to larger cluster sizes in order to explore the tentative lifetime extrapolation presented here as well as the validity of the $1/n$ extrapolation in general would be very useful. Studies in other solvent clusters such as methanol would also shed light on how cluster formation conditions affect the nature of electron binding and solvent dynamics in aggregate systems.

8.6 References

- 1 F. Arnold, *Nature* **294**, 732 (1981).
- 2 J. Simons, *Acc. Chem. Res.* **39**, 772 (2006).
- 3 H. F. Hameka, G. W. Robinson, and C. J. Marsden, *The Journal of Physical Chemistry* **91** (12), 3150 (1987).
- 4 R. E. Larsen, W. J. Glover, and B. J. Schwartz, *Science* **329** (5987), 65 (2010).
- 5 L. D. Jacobson, and J. M. Herbert, *Science* **331** (6023), 1387 (2011).
- 6 L. Turi, and Á. Madarász, *Science* **331** (6023), 1387 (2011).
- 7 R. E. Larsen, W. J. Glover, and B. J. Schwartz, *Science* **331** (6023), 1387 (2011).
- 8 J. M. Herbert, and L. D. Jacobson, *The Journal of Physical Chemistry A* (2011).
- 9 B. Abel *et al.*, *Phys. Chem. Chem. Phys.* **14** (1), 22 (2012).
- 10 L. Kevan, *Acc. Chem. Res.* **14**, 138 (1980).
- 11 D. M. Neumark, *Mol. Phys.* **106** (16-18), 2183 (2008).
- 12 L. Turi, W.-S. Sheu, and P. J. Rossky, *Science* **309** (5736), 914 (2005).
- 13 O. Marsalek *et al.*, *Phys. Rev. Lett.* **105** (4), 043002 (2010).
- 14 J. V. Coe, S. M. Williams, and K. H. Bowen, *Int. Rev. Phys. Chem.* **27** (1), 27 (2008).
- 15 J. R. R. Verlet *et al.*, *Science* **307**, 93 (2005).
- 16 J. V. Coe *et al.*, *J. Chem. Phys.* **92** (6), 3980 (1990).
- 17 A. Kammrath *et al.*, *J. Chem. Phys.* **125**, 076101 (2006).
- 18 N. I. Hammer *et al.*, *Science* **306**, 675 (2004).
- 19 J. R. Roscioli, N. I. Hammer, and M. A. Johnson, *The Journal of Physical Chemistry A* **110** (24), 7517 (2006).
- 20 K. R. Asmis *et al.*, *J. Chem. Phys.* **126** (19), 191105 (2007).

21 J. V. Coe *et al.*, J. Chem. Phys. **92** (6), 3980 (1990).
22 K. R. Siefertmann *et al.*, Nat Chem **2** (4), 274 (2010).
23 Y. Tang *et al.*, Phys. Chem. Chem. Phys. **12** (15), 3653 (2010).
24 A. T. Shreve, T. A. Yen, and D. M. Neumark, Chem. Phys. Lett. **493** (4-6), 216 (2010).
25 A. Lubcke *et al.*, Phys. Chem. Chem. Phys. **12** (43), 14629 (2010).
26 L. Ma *et al.*, J. Chem. Phys. **131** (14), 144303 (2009).
27 Á. Madarász, P. J. Rossky, and L. Turi, J. Chem. Phys. **130**, 124319 (2009).
28 L. D. Jacobson, and J. M. Herbert, J. Am. Chem. Soc. (2011).
29 T. Frigato *et al.*, J. Phys. Chem. A **112**, 6125 (2008).
30 A. E. Bragg *et al.*, Science **306**, 669 (2004).
31 A. E. Bragg *et al.*, J. Am. Chem. Soc. **127**, 15283 (2005).
32 G. B. Griffin *et al.*, J. Chem. Phys. **131**, 194302 (2009).
33 P. Ayotte, and M. A. Johnson, J. Chem. Phys. **106** (2), 811 (1997).
34 Y. Kimura *et al.*, The Journal of Physical Chemistry **98** (13), 3450 (1994).
35 K. Yokoyama *et al.*, J. Phys. Chem. A **102** (35), 6957 (1998).
36 J. R. Barker, and B. M. Toselli, Int. Rev. Phys. Chem. **12** (2), 305 (1993).
37 R. G. Gilbert, Aust. J. Chem. **48** (11), 1787 (1995).
38 J. Westergren, S. Nordholm, and A. Rosen, Eur. Phys. J. D **22** (1), 81 (2003).
39 A. V. Davis *et al.*, J. Chem. Phys. **118** (3), 999 (2003).
40 U. Even *et al.*, J. Chem. Phys. **112** (18), 8068 (2000).
41 W. C. Wiley, and I. H. McLaren, Rev. Sci. Instrum. **26** (12), 1150 (1955).
42 A. T. J. B. Eppink, and D. H. Parker, Rev. Sci. Instrum. **68** (9), 3477 (1997).
43 V. Dribinski *et al.*, Rev. Sci. Instrum. **73** (7), 2634 (2002).
44 J. V. Coe *et al.*, J. Chem. Phys. **125** (1), 014315 (2006).
45 R. M. Young *et al.*, J. Chem. Phys. **133** (15), 154312 (2010).
46 S. F. Fischer, and W. Dietz, Z. Phys. Chem **221**, 585 (2007).
47 A. Kammrath *et al.*, J. Chem. Phys. **126**, 244306 (2007).
48 M. M. Kappes, R. W. Kunz, and E. Schumacher, Chem. Phys. Lett. **91** (6), 413 (1982).
49 H. Hippler, J. Troe, and H. J. Wendelken, J. Chem. Phys. **78** (11), 6709 (1983).
50 B. M. Toselli *et al.*, J. Chem. Phys. **95** (1), 176 (1991).
51 H. Hippler, L. Lindemann, and J. Troe, J. Chem. Phys. **83** (8), 3906 (1985).
52 J. Shi, and J. R. Barker, J. Chem. Phys. **88** (10), 6219 (1988).
53 C. E. Klots, Z. Phys. D **20** (1), 105 (1991).
54 S. T. Arnold *et al.*, J. Phys. Chem. **100** (8), 2900 (1996).
55 J. M. Herbert, and M. Head-Gordon, The Journal of Physical Chemistry A **109** (23), 5217 (2005).
56 R. Englman, and J. Jortner, Mol. Phys. **18** (2), 145 (1970).
57 B. J. Schwartz, and P. J. Rossky, J. Chem. Phys. **101** (8), 6917 (1994).
58 B. J. Schwartz, and P. J. Rossky, J. Chem. Phys. **101** (8), 6902 (1994).
59 A. Kammrath *et al.*, J. Chem. Phys. **125**, 171102 (2006).
60 A. E. Kammrath, University of California, Berkeley, 2007.
61 L. Mones, P. J. Rossky, and L. Turi, **135** (8), 084501 (2011).
62 H. Shen *et al.*, Chem. Lett. **39** (7), 668 (2010).
63 H. W. Sarkas *et al.*, J. Chem. Phys. **116** (13), 5731 (2002).

Appendix 1. Revised Triggering Scheme

Over the course of the TRPEI apparatus lifetime, various adjustments have been made to the way the devices are triggered by each other. Upgrades and changes of equipment, such as the laser and the pulsed valve have caused the triggering scheme to be revised several times. The triggering scheme in its present form is summarized in this appendix.

One particularly subtle feature of the triggering setup deserves attention. As is typical of gas-phase studies with pulsed lasers, the laser and ion pulses generated from the same trigger pulse do not interact with each other; the same pulse which actuates the Pockels cell and the pump laser in the amplifier also controls when the valve opens. However, the ions move far slower than the laser pulse, such that by the time the original laser pulse has passed through the interaction region, the ions are still being formed (only ~80-200 μs after the valve is fired); the ions actually interact with the *next* laser pulse generated in the sequence. Because everything is matched one-to-one (same repetition rate) this does not cause a problem, unless there is some instability in the triggering itself.

A fundamental concept with ultrafast lasers is that the laser pulse generation cannot be accomplished electronically; rather it must be achieved optically through the modelocking technique (see Chapter 2). This means that for all ultrafast systems, everything which must sync to a laser pulse must be triggered off of the original oscillator pulse train. This signal is the "master" trigger; it is obtained from a photodiode inside the oscillator which monitors the 83 MHz pulse train (pulse-to-pulse separation is 12 ns, determined by round-trip time of the light in the cavity: $\Delta t = 2L/c$). The fast photodiode is positioned near the Ti:sapphire crystal face in order to monitor the 800 nm reflection, which is pulsed under mode-locking conditions. Unfortunately, due to the intrinsic design of the multipass amplifier system and the lack of any feedback suppression, such as by a Faraday rotator, poor alignment of the amplifier ring can allow for significant counter-propagation of amplified spontaneous emission (ASE) into the oscillator, which in its most severe form can be powerful enough to actually disrupt the lasing process in the oscillator itself, leading to an immediate cease in operation and opening of the interlock circuits. More commonly, however, the ASE intensity is not enough to interfere with lasing but can be high enough to override the signal on the photodiode from the unamplified MHz pulse train and disrupt the triggering process. This instability will cause a drop in signal level (as fewer laser pulses are interacting with the ions, on average) and larger signal fluctuations (both in magnitude and frequency).

This effect can be monitored in real time during the photoelectron experiment by observing the rising edge of the signal from the fast photodiode on the laser table. If the rising edge appears to jitter in time, then the trigger is close to being overridden by ASE. Adjustments in the pump laser timing and oscillator prisms can compensate for this, but doing so will change the conditions of the experiment (amplifier spectrum, power, laser delay) and should be avoided. The same monitoring can be done during the amplifier alignment process by monitoring the Reference Trigger on the oscilloscope and looking for similar jitter in the rising edge (the scope must be externally triggered, however, for this to work). Note that the falling edge of the photodiode is typically an unreliable metric for this effect due to saturation effects (even when off). If the back reflection off the crystal face gives an insufficient signal and cannot be raised by optimizing the oscillator power, the diode can be relocated to another reflection spot, such as off of one of the prisms, however the crystal face provides the most stable reflection since it is

not adjusted during routine alignments or day-to-day adjustments. Thus, when optimizing the alignment of the oscillator for power and spectrum, the direct output of the photodiode should also be monitored on an oscilloscope and optimized by carefully adjusting the diode position. A signal of ≥ 40 mV Ω will provide a robust and sufficient trigger to avoid being swamped by ASE. The new Nd:YAG pump laser (Lee laser) delivers a shorter pulse of 532 nm light, which should reduce the amount of ASE and render this problem less severe.

The oscillator trigger sequence is given to a pulse delay generator inside the KM Labs Dragon control rack which converts the 83 MHz pulse train to a Pulse Repetition Frequency (PRF) entered into the DragonMaster control software. This value can range from 520 Hz to 3 kHz. The PRF entered into the software is divided by a factor determined by the precise repetition frequency of the original femtosecond pulse train in order to ensure that the derived pulse rate is an exact integer divisor of the 83 MHz master signal. **In our system, this value is 1.039.** For example, to run at 1 kHz, the input should be $1.000/1.039 = 0.9625$.

The generated signal drives the entire rest of the system. Specifically, the KM rack outputs 3 different signals all of the same duration, but with their own individually set delays: 1) Pump laser, controlled by "Pump 1"; 2) Pockels Cell, controlled by "PC 1"; Reference trigger, controlled by "Free 1". The reference trigger drives the ion system, including the imaging detector. Because the pulsed valve is typically the rate-limiting piece of equipment in the apparatus, it is possible that this 520+ Hz is too high of a repetition rate, in which case the trigger can be routed through a second pulse delay generator (DEI PDG 2510) to bring the pulse down as low as the single cycle-per-second range. From here, this trigger sequence is supplied to the other pulse delay generators which preserve the PRF but allow for other channels to be pulsed with controlled delays. These boxes pulse the mass spectrometer plates, the valve and ionizer, along with the VMI repeller plate (mass gate), the oscilloscope and, importantly, the optical chopper. Recently, the triggering scheme has been reworked in order to control the length of the transistor-transistor-logic (TTL) pulse driving the Even-Lavie valve in order to deliver a short trigger pulse (~ 10 μ s).

It is important to note that, currently, the front MCP of the imaging detector is pulsed at the PRF directly out of the KM rack, such that the optical chopper may be necessary to reduce laser noise from laser pulses which do not have an accompanying ion pulse to interact with. This can, in principle be avoided by pulsing the MCP detector at the same trigger sequence as the valve. The current arrangement appears to be one of convenience.

Currently, the CCD camera shutter is triggered internally, making it technically out of phase with the apparatus. We can get away with this because of the combination of the relaxation time of the phosphor screen and the repetition rate of the experiment. Because the electrons are impinging on the MCPs at 100-1000 Hz and the phosphor has a natural relaxation time of 16 ms (~ 60 Hz), the image on the phosphor screen is being refreshed much more rapidly than it can decay, such that the camera rarely misses the most intense light from the phosphor screen.

The trigger scheme is detailed graphically in the following diagram, including channel labels and typical delay times.

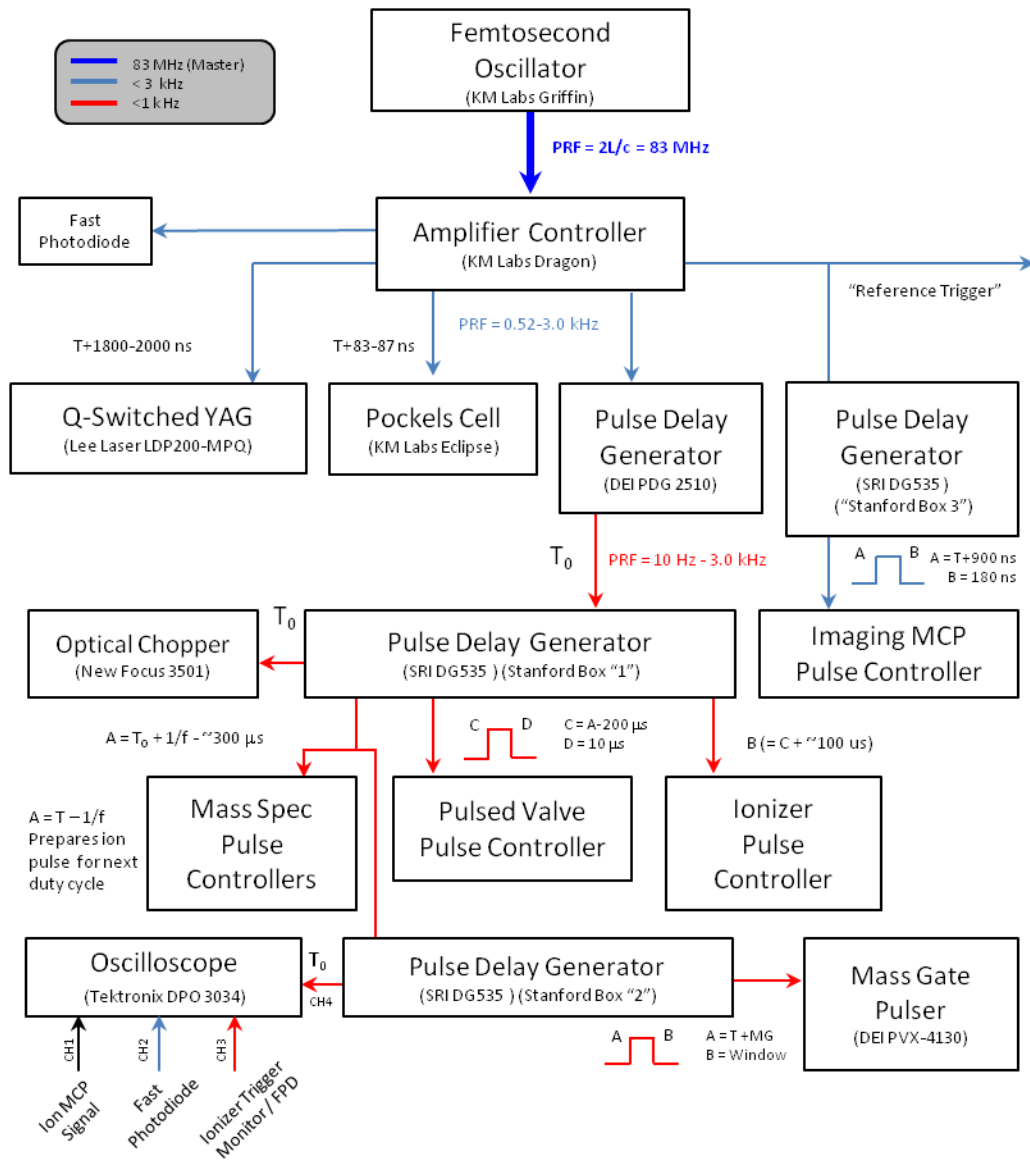


Figure A1.1. Trigger diagram for TRPEI apparatus.

Appendix 2. Isotope effect on free rotation period of methanol

It was shown in Chapter 5 that the dynamics of electron solvation in small methanol clusters following charge-transfer from iodide is controlled by the rotation of one or possibly more methanol molecules as it flips end-over-end to bring the hydroxyl group in toward the cluster center and establish a stronger hydrogen bond network. This rotation was observed to occur over a 5-30 ps ($1/e$) timescale for clusters of 4-11 methanol molecules, consistent with the 20.7 ps rotation period (~ 10.4 ps end-over-end half period) of the $J = 1$ rotational state of methanol. As the solvation process hinges on the restructuring of the solvent network, bonds must be broken and reformed, so the overall dynamics should be slower than the free-rotation period, and should slow further as the solvent network increases in complexity. However, certain aspects of the free rotation should still come into play in the dynamics which can be useful for corroborating this mode in the electron solvation process. Specifically, there should be a kinetic isotope effect for the (free) rotation, so having some quantitative predictions for the effect of single- (CH_3OD) and per-deuteration (CD_3OD) would be quite useful.

To estimate the kinetic isotope effect on the free rotation the moments of inertia must be calculated. Due to the lack of symmetry and the three-dimensional geometry of methanol, simply estimating the moment by $I \sim mr^2$ will be insufficient. However the calculation of the moments is well established in the physics of rigid body motion.^{1,2} An extended body possesses three moments of inertia corresponding to rotation about three mutually perpendicular axes. After first establishing the proper coordinate system for the given molecule, the inertia tensor is constructed and then diagonalized, with the eigenvalues being the principle moments. These moments can then be used to estimate the rotational (or half-rotational) period for the molecule given a single quantum of angular momentum ($J = 1$). By changing the mass of the various hydrogen atoms and comparing the eigenvalues/rotational periods, an estimate for the isotope effects can be obtained.

A2.1 Inertia tensor calculation

First we establish a coordinate system. For simplicity, the origin is centered on the C atom with the C-O bond directed along the x -axis. One of the methyl hydrogen atoms (H1) is placed at $z = 0$; this defines the x - y plane. Bond lengths and angles are taken from zero-point structures obtained from microwave spectroscopy and electron diffraction experiments.³ The coordinate system is depicted in Figure A2.1. In this frame, the atomic positions are:

$$\vec{r}_C = \begin{pmatrix} 0 \\ 0 \\ 0 \end{pmatrix}; \quad \vec{r}_O = \begin{pmatrix} l_{CO} \\ 0 \\ 0 \end{pmatrix}; \quad \vec{r}_{H4} = \begin{pmatrix} l_{CO} - l_{OH} \cos \psi \\ l_{OH} \sin \psi \cos \alpha \\ l_{OH} \sin \psi \sin \alpha \end{pmatrix} \quad (\text{A2.1})$$

$$\vec{r}_{H1} = \begin{pmatrix} l_{CH} \cos \theta \\ -l_{CH} \sin \theta \\ 0 \end{pmatrix}; \quad \vec{r}_{H2} = \begin{pmatrix} l_{CH} \cos \theta \\ l_{CH} \sin \theta \cos \chi \\ l_{CH} \sin \theta \sin \chi \end{pmatrix}; \quad \vec{r}_{H3} = \begin{pmatrix} l_{CH} \cos \theta \\ l_{CH} \sin \theta \cos \chi \\ -l_{CH} \sin \theta \sin \chi \end{pmatrix} \quad (\text{A2.2})$$

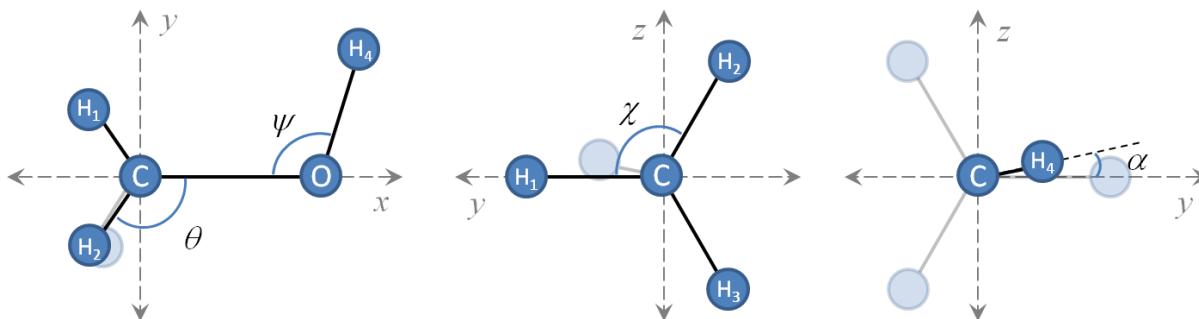


Figure A2.1. Coordinate system for methanol projected along various planes.

The bond lengths are: $l_{CO} = 1.429 \text{ \AA}$, $l_{CH} = 1.098 \text{ \AA}$, $l_{OH} = 0.975 \text{ \AA}$; the bond angles are (as defined in Fig. A2.1): $\theta = 109.1^\circ$, $\psi = 287.6^\circ$, $\chi = 120^\circ$, $\alpha = 3.40^\circ$.

The moments of inertia can be computed in this frame, however, they would represent rotation (or revolution) about the origin. Proper moments about the molecular center of mass can be computed using the Steiner parallel axis theorem² or, more simply, by switching to the center-of-mass frame:

$$\vec{r}_{CM} = \frac{1}{M} \sum_i m_i \vec{r}_i \quad (\text{A2.3})$$

$$\vec{R}_i = \vec{r}_i - \vec{r}_{CM} \quad (\text{A2.4})$$

Using these coordinates, the products of inertia can be computed within the molecular frame:

$$I_{ij} = \sum_k (\delta_{ij} r^2 - x_i x_j)_k \quad (\text{A2.5})$$

These products form the elements of the 3x3 inertia tensor, and from Eq. A2.5 it can be seen that this tensor is symmetric. While some care was taken to ensure that rotation was constrained about the center-of-mass, that coordinate system is not guaranteed to lie along the natural axes of rotation for the molecule. The natural axes (and the moments about them) can be determined by diagonalizing the inertia tensor by solving the eigenvalue equation:

$$\underline{\underline{I}} \cdot \vec{\omega} = I \vec{\omega} \quad (\text{A2.6})$$

$$\det(\underline{\underline{I}} - \lambda \underline{\underline{1}}) = 0 \rightarrow \{I_A, I_B, I_C\} \quad (\text{A2.7})$$

The eigenvalues calculated here are labeled I_A , I_B , and I_C in order of decreasing value. For the fully hydrogenated system with the bond lengths and angles given above (and in the given exact geometry above), the principle moments of inertia for methanol are: $I_A = 20.38 \text{ amu \AA}^2$; $I_B = 19.55 \text{ amu \AA}^2$; $I_C = 4.06 \text{ amu \AA}^2$. I_A corresponds to rotation about the z -axis, while I_B is for rotation about the y -axis, both of which can be thought of as the "end-over-end" rotation (indeed, both moments are very similar in magnitude). Rotation about the x -axis (the long-axis) of the methanol molecule will have the smallest moment, I_C . Determining the lowest energy (longest)

rotational period is simply done by equating the classical expression for angular momentum with one quantum of angular momentum:

$$\hbar = I\omega = 2\pi\nu I \quad (\text{A2.8})$$

yielding:

$$\tau = \frac{2\pi I}{\hbar} \quad (\text{A2.9})$$

From this the full-period rotation times associated with the $J = 1$ rotation are $\tau_A = 20.16$ ps, $\tau_B = 19.35$ ps, and $\tau_C = 4.01$ ps, respectively. The first two times are in excellent agreement with the 20.67 ps rotation time observed from microwave spectroscopy.⁴ Some of the disagreement can be due to the specific structure used; hindered rotation of the OH group about the x -axis can lead to small changes in the moments (changing angle α). The *half-periods* for the end-over-end rotations are 10.08 ps and 9.673 ps, which agree well with the changes in the VDE and spectral width of the excited state feature in the iodide-doped methanol cluster data from Chapter 5.

From here we can actually compute the effects of specific deuteration on the rotation times by changing the values of the mass for the various hydrogen atoms. The values of the moments of inertia and their respective rotation periods are summarized in Table A2.1, with their ratios for different degrees of deuteration listed in Table A2.2. Deuteration has a small effect on the end-over-end rotation, leading to at best a 30% increase in the rotational period, which is comparable to the uncertainties in the extracted time constants of the non-deuterated clusters. Therefore studying the deuterated species does not definitively pin down the end-over-end rotation as the dominant mode of the relaxation process in these systems, though it is not ruled out (for example, if the isotope effect were too large). It should also be emphasized that this calculation is for a free rotation; the disruption of the hydrogen bond network will hinder this process, possibly obscuring isotope effects.

	I_A (amu \AA^2)	I_B (amu \AA^2)	I_C (amu \AA^2)	τ_A (ps)	τ_B (ps)	τ_C (ps)
d_0	20.38	19.55	4.06	20.16	19.35	4.01
d_1	21.37	19.76	4.84	21.14	19.55	4.79
d_4	26.45	24.84	8.07	26.17	24.58	7.98

Table A2.1. Moments of inertia of methanol and associated periods of free rotation for $J = 1$ excitation.

	Isotope effect: $\tau_{dx}/\tau_{d0} = I_{dx}/I_{d0}$		
	A	B	C
d_1	1.05	1.01	1.19
d_4	1.30	1.27	1.99

Table A2.2. Effect of deuteration on rotation timescales/moments: $\tau_{dx}/\tau_{d0} = I_{dx}/I_{d0}$, where $x = 1,4$

A2.2 References

- 1 H. Goldstein, *Classical mechanics* (Addison-Wesley Pub. Co., 1980).
- 2 S. T. Thornton, and J. B. Marion, *Classical dynamics of particles and systems* (Brooks/Cole, 2004).
- 3 T. Iijima, *Journal of Molecular Structure* **212**, 137 (1989).
- 4 R. M. Lees *et al.*, *Journal of Physical and Chemical Reference Data* **2** (2), 205 (1973).

Appendix 3. Fitting Mass Spectra

This appendix describes a method for assigning the cluster size distribution from the time-of-flight (TOF) mass spectrum based solely on the cluster spacing. Due to the nonlinear relationship between mass and TOF the spacing between adjacent cluster peaks is a function of the ion's mass, thus the spacing can be used to back-out the cluster sizes through nonlinear least-squares analysis.

As discussed in Chapter 2, our apparatus employs a Wiley-McLaren-type mass spectrometer which is based off a three-plate design (Repeller/Extractor/Ground). Having the extraction plate at a tunable voltage allows for control over the ions' acceleration as they leave the extraction region, making it possible to control the longitudinal (temporal) focal point of the ion beam. The applied voltage to the plates is pulsed, such that the ion packet created by the source can enter the extraction region unperturbed (minimizing the spread in the ion velocities) before the voltages are applied. The voltage pulse timing is optimized to extract the majority of the ion packet and can be controlled relative to the pulsing time of the valve/ionizer assembly. Ions are accelerated perpendicularly into a shielded, field-free flight tube with a typical repeller voltage of -2 kV, while the extraction voltage is tuned from about -1.3 kV to -1.8 kV depending on the desired ion mass.

The material in this section is highly simplified, but captures the salient features of our mass spectrometer system. The full classical electrostatic calculations are carried out in their entirety in the original paper by Wiley & McLaren.¹ However, the approximations and simplifications herein are made in order for this appendix to act as a primer how to assign mass distributions for a cluster progression.

A3.1 Time-of-Flight Mass Spectrometry

To first approximation, each ion is given the same kinetic energy upon application of voltage to the mass spectrometer plates. Motion along other axes is ignored, as the (roughly) thermal velocities of the ions during the expansion are but a few percent of their velocity after acceleration ($k_bT \ll q_e V_{\text{extraction}}$). Ions with masses m_1 and m_2 will have velocities v_1 and v_2 (along the flight tube axis) according to:

$$\frac{1}{2} m_1 v_1^2 = \frac{1}{2} m_2 v_2^2 \quad (\text{A3.1})$$

Assuming the size of the ion packet is initially very small, the distance of each ion to the detector is equivalent, allowing the above equation to be simplified (neglecting turn-around time):

$$t_2 = t_1 \sqrt{\frac{m_2}{m_1}} \quad (\text{A3.2})$$

For a homogeneous cluster distribution, each cluster is composed of n units (atoms or molecules) of mass m_0 . If the monomer ion is observed, then the flight times scale simply as the square root of n :

$$t_n = t_1 \sqrt{n} \quad (\text{A3.3})$$

However, in many cases, such as water cluster anions for example, the monomer anion is not observed so a more general form must be used. In the case that cluster n is observed, then the flight time for cluster $n+1$ will be

$$t_{n+1} = t_n \sqrt{1 + \frac{1}{n}} \quad (\text{A3.4})$$

This equation will form the basis of the fitting routine presented in the next section. The concepts can be readily extended to heterogeneous clusters composed of two different species. For instance, as is the case for iodide-doped clusters where a single iodide atom with mass m_I is complexed with a cluster of n solvent molecules of mass m_0 , the calculated flight time is:

$$t_n = t_I \sqrt{1 + \frac{nm_0}{m_I}} \quad (\text{A3.5})$$

Eqn. A3.4 also defines the separation between the clusters (the same operations can be used for A3.5). In the case of large n the cluster separation becomes more closely spaced as n increases. In this case, $1/n$ is small, and the expression can be approximated using the binomial expansion:

$$t_{n+1} = t_n \left(1 + \frac{1}{n}\right)^{\frac{1}{2}} \approx t_n \left(1 + \frac{1}{2n}\right) \quad (\text{A3.6})$$

Thus we can define the separation between adjacent peaks Δt_n in terms of the cluster number and the flight time of cluster n :

$$\Delta t_n = t_{n+1} - t_n \approx \frac{t_n}{2n} \quad (\text{A3.7})$$

When this number becomes smaller than the width of the ion peak in the mass spectrum single-cluster resolution has been lost. Of course, this spacing will depend on many parameters, such as the acceleration potential, the flight tube, and the monomer mass, which is all embedded in the flight time t_n . If the ion (with mass $m_n = nm_0$) experiences the effective voltage from the two plates V_{eff} instantaneously (ignoring acceleration effects) then the energy imparted to the ion is:

$$\frac{1}{2} m_n v_n^2 = q_e V_{eff} \quad (\text{A3.8})$$

For the given flight tube length L , this yields the flight time:

$$t_n = L \sqrt{\frac{nm_0}{2qV_{eff}}} + t_0 \quad (\text{A3.9})$$

Finally, this equation combines with Eqn. A2.7 to give a cluster separation in terms of the cluster monomer mass:

$$\Delta t_n = \frac{L}{2} \sqrt{\frac{m_0}{2nqV}} \quad (\text{A3.10})$$

A3.2 Fitting Cluster Distributions

Ideally, the cluster distribution generated by the ionization conditions is clean and well-resolved. This requires the expansion to be free of any easily ionized contaminants due to leaks in the manifold or impurities in the sample. It is also desirable that the cluster monomer itself not fragment or electrolyze upon bombardment with high energy electrons from the ionization process, as these daughter products could appear in the mass spectrum on their own, or possibly worse, solvate with the clusters formed from aggregation of the intact molecules, obfuscating the desired mass spectrum. On the other hand, if these conditions can be achieved and a pristine cluster distribution is generated, often there are no well-known peaks on which to calibrate. If the system is well-studied, the earliest stable cluster or other "magic numbers" may be known and the cluster progression can be assigned readily (these, however, can often be obscured by the system timings or ion optic settings). Without any peaks on which to calibrate directly, we must appeal to equations A2.5-6 and assign the cluster distribution indirectly via the relative spacing. Thus, assigning the cluster distribution is equivalent to finding the smallest stable/measurable cluster. This can be accomplished readily with nonlinear least squares analysis.

Because the cluster units are by definition integer values, this parameter must be restricted to that set of numbers. The following description is for how to implement this algorithm into a spreadsheet program like Microsoft Excel. Taking the first apparent peak as the "seed" and guessing (educated, hopefully) at its cluster number based on either magic numbers or the photoelectron spectrum,

$$t_{n_{seed}+\delta} = t_{seed} \sqrt{1 + \frac{\delta}{n_{seed}}}, \quad (\text{A3.11})$$

where δ is an integer. From Eq. A2.11, a predicted TOF can be generated for each cluster size after n_{seed} ($n_{seed} + 1, n_{seed} + 2 \dots n_{seed} + \delta$), and when compared to the experimentally observed peak positions (flight times) can be used to generate the value of n_{seed} which minimizes the sum of the squares of the differences between the measured and predicted values. This method has been used successfully to identify the smallest $(\text{CH}_3\text{CN})_n^-$ cluster observed on our apparatus as $n = 13$, as well as to show that the THF monomer anion is stable (or at least metastable) in the $(\text{THF})_n^-$ experiments. Both of these situations were carefully analyzed and independently

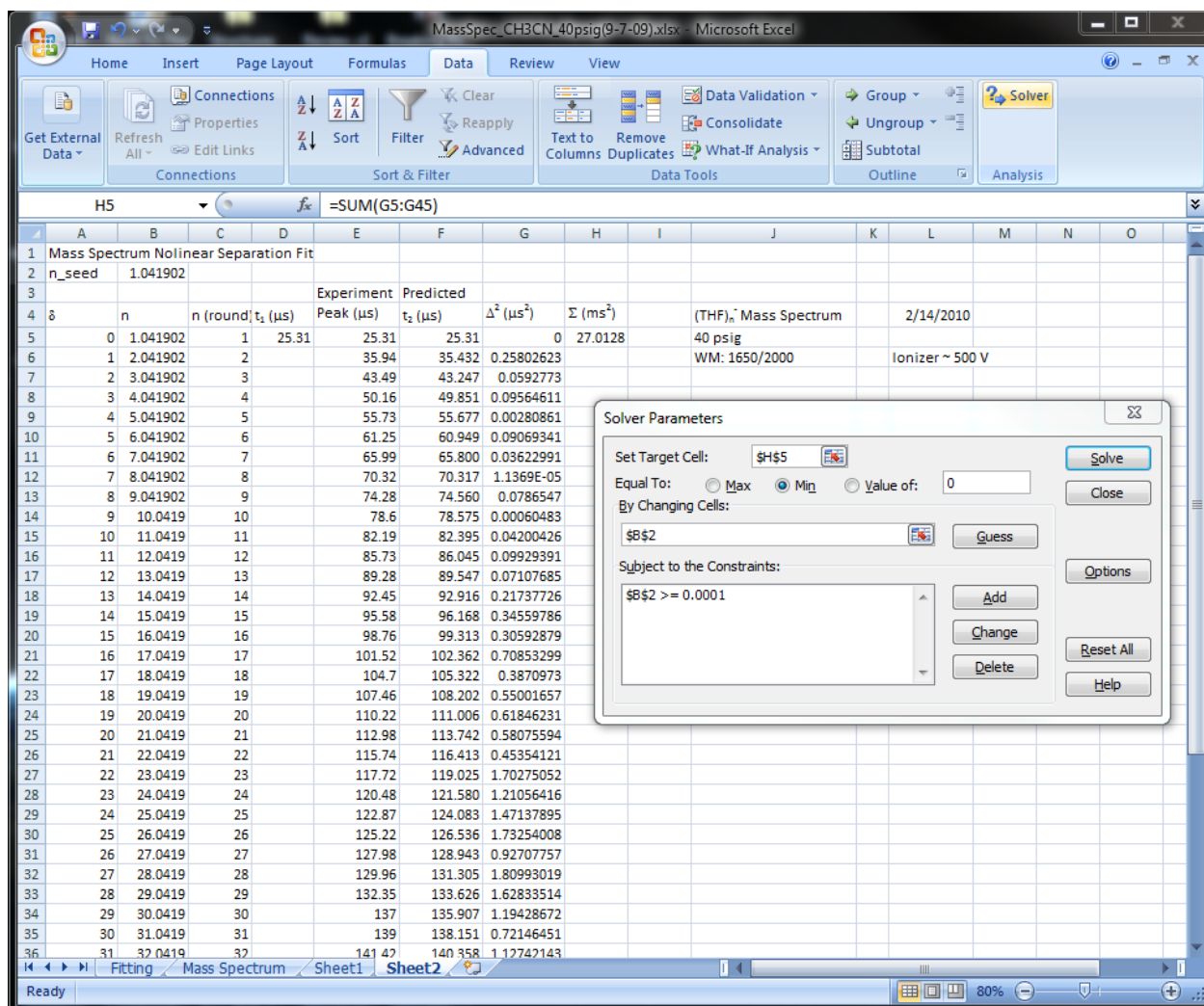


Figure A3.1. Screenshot of the fitting routine implemented in Microsoft Excel 2007 for (THF) $_n^-$ clusters.

verified with other calibrants still available in the mass spectrometer (such as I^- or CN^-) as well as with photoelectron spectroscopy. The method can also be easily extended to heterogeneous clusters, such as the $\text{I}^-(\text{solvent})_n$ clusters, with the reasonable assumption that the dopant is the same for all clusters, as was done for $\text{I}^-(\text{THF})_n^-$.

A screenshot of the method is shown below as implemented in Microsoft Excel 2007 for tetrahydrofuran cluster anions.

A3.3 References

- 1 W. C. Wiley, and I. H. McLaren, Rev. Sci. Instrum. **26** (12), 1150 (1955).

Appendix 4. Image DAQ 2.0

This appendix presents an overview of the features and basic principles behind the ImageDAQ 2.0 software program used for acquiring single color and time-resolved photoelectron images. Historically, the motivation for updating the program came from the antiquated nature of the data acquisition computer used to run ImageDAQ 1.0 written by Roland Wester. The way the images were (and currently still are) saved takes up a fair amount of space, approximately 1 MB/image since each image is a 512×512 pixel² 12-bit array (bitmap) along with some header information. After many scans of averaging and many pump-probe delays the total disk space required for a day's experiment could be very large, up to hundreds of megabytes. Even after compression, these files were too large to be stored on removable media, and with the obsolescence of the Zip drive and the lack of USB support in Windows NT4, the only way to access the data on a different computer would be to upload the content to the servers or burn the data on rewriteable CD. Unfortunately, in 2009 UC Berkeley's IT department stopped supporting Windows NT4 and halted network access on those computers. Moving the camera interface and acquisition program to a different computer proved impossible, since the frame grabber (the high-speed interface between the CCD camera and the computer) was incompatible with newer operating systems and the manufacturer was not making new drivers. Worse still, the CCD camera was not compatible with newer frame grabbers, so we were stuck.

So instead of being forced to record each day's data onto rewritable CD (which added up to an hour of rather of waiting time at the end of the day) we opted to design a new data acquisition program with new features we had determined to be useful, using a new frame grabber, a new CCD camera (taken from the old anion photoelectron spectroscopy/imaging experiment after it had been decommissioned to make room for the liquid jet experiment), and most importantly a new, modern computer. The lab was very fortunate to have an extremely gifted diploma student named Markus Niemeyer studying with us at the time who helped iron out the details of the computer's requirements and took to the task of learning LabView very quickly. The program described below was coded entirely by Markus Niemeyer with the input of the graduate students present at the time. The code is not included in this overview; this appendix serves to describe the features and the interface of the program and detail the possible next steps and improvements for subsequent versions.

A4.1 Program Structure

This version of the ImageDAQ program works similarly to the old program, especially in the way it saves its data. The details of that program are outlined in the thesis of Alison Davis. In summary, the CCD camera acquires the 1024×1024 pixel² image in 12-bit depth at 30 frames/sec, which is then converted by the frame grabber to a format readable by the computer. Each frame of this image is then binned in the firmware to 512×512 pixel². The user specifies the number of frames to be integrated together before saving ("Frames" in the form generator). Before integration, each binned frame is analyzed by LabView. First, the program removes "dead" or "hot" pixels (spots on the CCD camera which always give signal) by setting the values of each of those pre-determined pixels to the average of the eight pixels surrounding it. Then, an intensity "threshold" is applied by only counting the intensity of those pixels which register

above that number. This number is set by the user to throw out signal from ambient light hitting the CCD camera and any background signal off the phosphor screen not due to photoelectrons, effectively discriminating the data. Then the intensity of each pixel above that threshold is then integrated to a single number for each frame and passed to the RAM. This number can be monitored in real time or averaged over a certain number of frames for smoother monitoring in order to gauge the stability of the data. This readout replaces the numeric "Intenisty" and "ClusterN" metrics in the last program with a plot of intensity of pixels above threshold (IoPAT) in updated in real time. Each frame's IoPAT is integrated when the image is saved to the disk such that the intensity of that saved image can be monitored; this value is then added to the IoPAT of the next image saved *at that delay* in order to gauge the overall stability of the experiment.

Several checks are done at the end of each save to ensure that nothing has gone wrong during the acquisition of that image, a new and very useful feature. A minimum IoPAT for a given image can be specified and enforced during the run of the experiment, such that an image can be rejected for save if the signal level has dropped sufficiently. Also, if the optical chopper has fallen out of phase, either the IoPAT limit will be triggered or the chopper communication check will fail and the image will be rejected. If communication is lost with the translation stages, the next image will be not be saved because there is no guarantee the stage has actually moved; this prevents polluting of the images with data from the wrong delay. Once the image is accepted by the program, the translation stages are moved and the program creates a new image file for the next set of frames, repeating the same process.

After an image at each stage delay has been acquired once and all the files have been created, the program loops back to continue collection of the same delays for better averaging. The same process happens as before, but instead of combining this new set of integrated frames to the previously saved set, a new image is appended to the old, preserving both scans (and increasing the file size). This is done intentionally not only to prevent overwriting, but also so that a scan that was determined to be unacceptable by the user (for instance, due to intensity fluctuations) can be thrown out and not contaminate the "good" data during analysis. Appending the images also has the added benefit of allowing the program to be resumed if something should cause the program to be interrupted without losing previously acquired data.

Lastly, a maximum number of scans can be specified. The program will terminate acquisition and return to standby mode. Other functions have also been integrated into this program, such as external status monitoring, and automated file compression and uploading. The final outputs of this program are the collected image files (individual *.dat file format), text files with user-generated notes and the settings for the given experiment (positions of each translation stage, number of frames, number of scans, and the total intensity above threshold for all the images at a given delay). All of these files are compressed in one archive and uploaded to a specified ftp address.

The program is outline schematically in Figure A4.1.

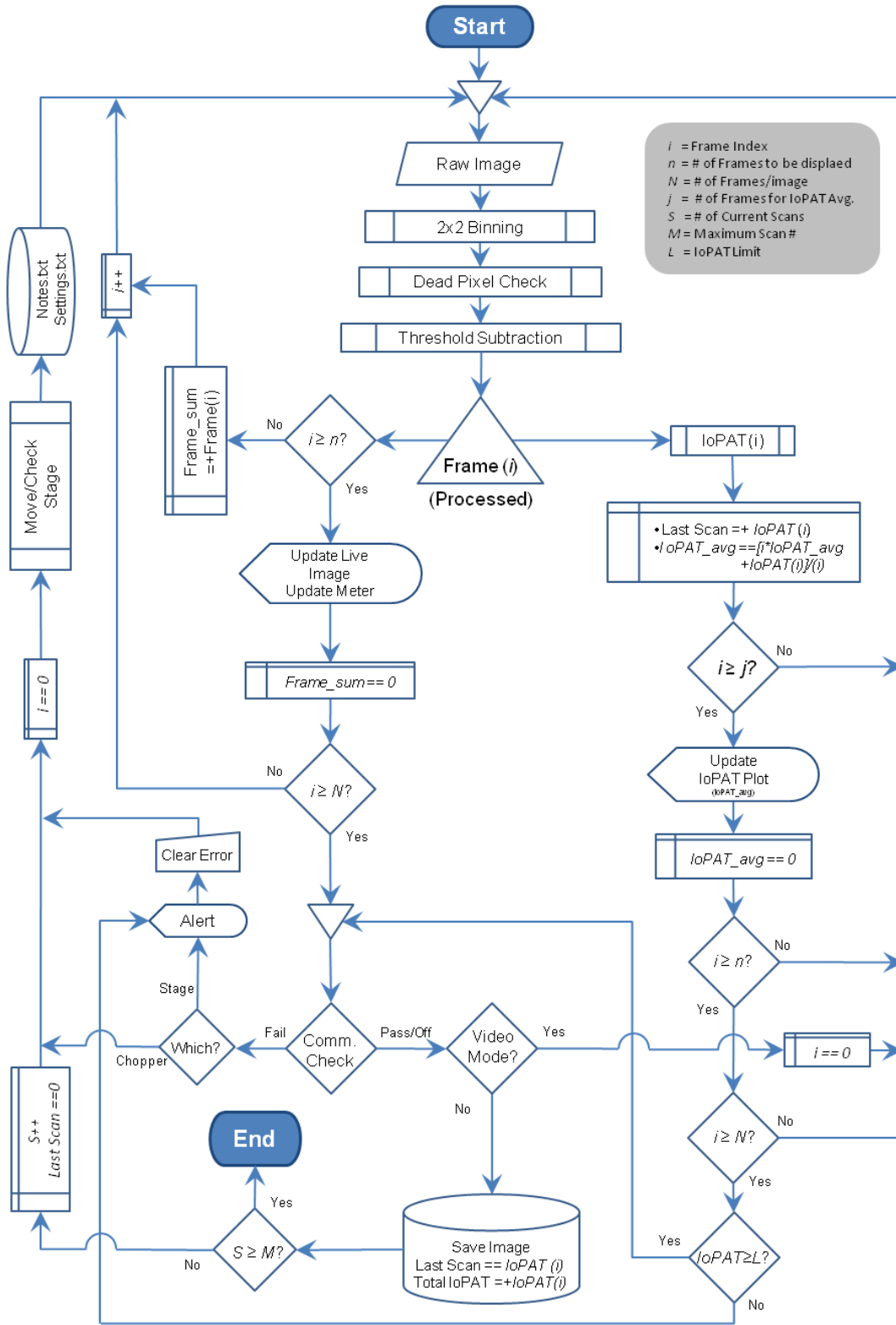


Figure A4.1. Flowchart of the ImageDAQ in acquisition and video modes.

A4.2. ImageDAQ 2.0 Interface

The *MainCaller.vi* LabView routine opens a menu wherein the user can choose either the DAQ or Analysis module. Selecting *DAQ* will give the user the option of loading an old form, the set of delays and parameters for the experiment or creating a new one. A folder on the hard drive is created from the name of the material being studied, and a subdirectory is created for that days date, preventing the overwriting of data which pervaded the old program. In the case that the same material with the same delays is run multiple times on the same date, an "ID" code is generated starting at zero to differentiate the data sets and prevent overwriting. Each (integer) stage delay specified in the form is used to code the file name, along with the delay index (ranging from zero to the 1 minus the number of delays created). For example: if an image is to be acquired at Stage1 position X1 and Stage2 position Y1, and a second at Stage1 position X2 and Stage2 position Y2, then the file names will be automatically generated as "*0_X1_Y1.dat*" and "*1_X2_Y2.dat*", etc, all within that days directory. The indexing allows for the data to be imported into Origin in order. Most experiments only move one stage so typically one of these numbers is always zero. The number of frames per image ("*N*", frames integrated together before being written to the disk) must be inputted, typically 400, requiring approximately 13 s/image. Other values can be chosen depending on the stability of the ion source. The background wavelengths can also be specified for organizational completeness. The form can be set to "One Color" mode, where the stage is not moved but more than one image can still be saved, allowing other parameters, such as cluster size to be varied without having to rewrite the form. This is achieved by giving each image a name beginning with a letter instead of a number, as the program will always advance to the next image in the list beginning with a number. Thus the background (one color spectra, ion noise, and laser noise) do not get updated at the end of each scan, and a one color photoelectron image can be acquired and saved as long as necessary. File names can be changed when the program is in standby mode by double-clicking the "#" field and typing in the desired name.

Once the form is specified, the program opens the main acquisition window, the layout of which is shown in Figure A4.2. The setup for the particular experiment is displayed at left while the raw or processed image is on the right. The options to load a new form (start a new experiment) or load an old form (resume an interrupted experiment - the images are always appended at each save so nothing is overwritten) are in the upper left. Below that are the operating options, including external device interface controls. These buttons control communication between the translation stages and the optical chopper, as well as the ability to transpose the image (more on that later) as well as to ensure that the same number of images is saved for each delay ("Same Scan Number"). The ability to exclude dead pixels from the saved images and to specify exact pixels is also managed through this box. An output of all communications and errors to a Twitter feed is also included for when someone may want to monitor the status of the experiment remotely, though this is seldom used. A list of all generated error messages for the day is displayed under this control as well.

Dominating the left side is the grid showing the settings for that day's experiment. At top is the "Information" field, showing what material is being studied, the date and the "ID". A "notes" field is included which can be updated at any time during the experiment to include specific information about the day, such as which scans should be thrown out, laser powers, VMI settings or anything else deemed important for that experiment. (Note: the notes field is not saved until one loop of the program is completed, either at the end of a scan or after Video Mode

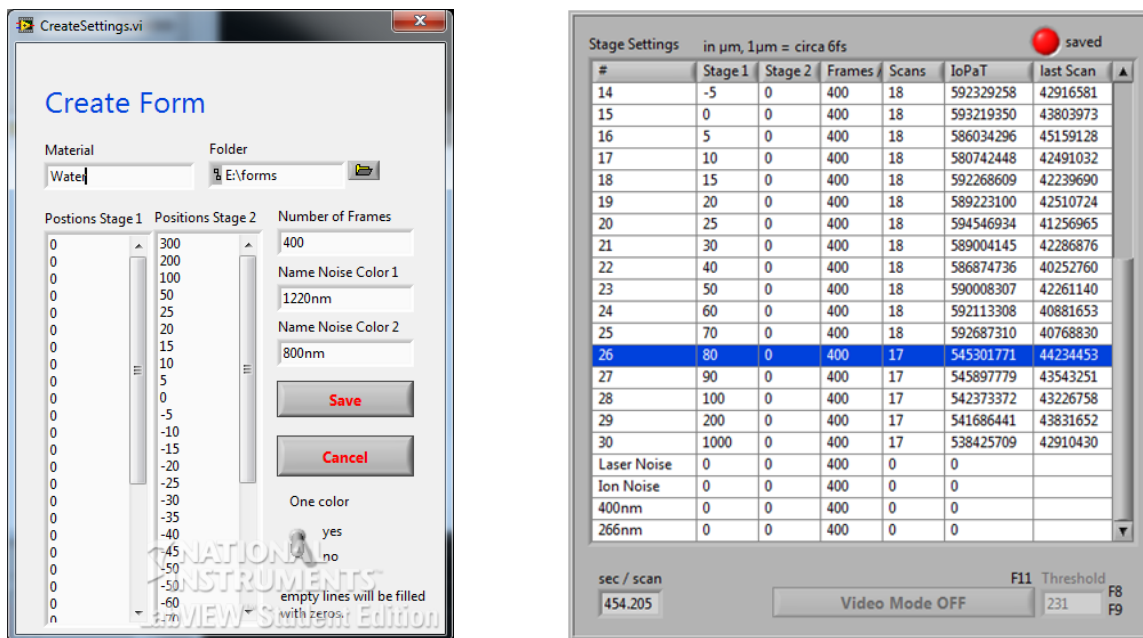


Figure A4.2. Form creator (left) and collection status grid (right).

has been activated and deactivated - doing this will force a save and is needed especially at the end of the experiment when the saving loops are complete).

The largest field on the left is the grid displaying the information from the form, including the delay index ("#"), the stage delays in μm ("Stage X"), the number of frames per image saved ("Frames"), the number of acquired scans ("Scans", "S"), the total number of pixels above the specified threshold over the all images acquired at that delay ("IoPaT"), and the number of pixels above threshold in the last image saved at that delay ("Last Scan"). This field is saved to a text file and updated at the end of every save loop. At the bottom of this field is a timer giving the time elapsed during that scan (or from when the Start button was clicked until the end of a scan); it is reset after every complete scan.

At the bottom left is the status readout and main control. The current status of the program is output at the very bottom ("Grabbing frames" or "Moving stage" or "Saving"), along with a button that will query the stage controller for any current errors. Above this is a readout of the current scan number, current stage positions in μm , and current chopper status. The control box allows the user to begin or stop data acquisition or to enter "Video Mode" where all functions except saving and moving the translation stages are performed. The maximum number of scans can be specified in the "Max Scan" ("M") field (Note that if this number equals the "Actual Scan No" then "Video Mode" will only run for one scan - this is fixed by changing the "Max Scan" number to any higher value). A "Max Scan" value of zero will make the program run indefinitely. The user can "Stop After Scan" if they wish the current scan to be the last. A timer calculating minutes to the end of acquisition will yield a value only if a maximum scan number is given and will only work in "One Color" mode.

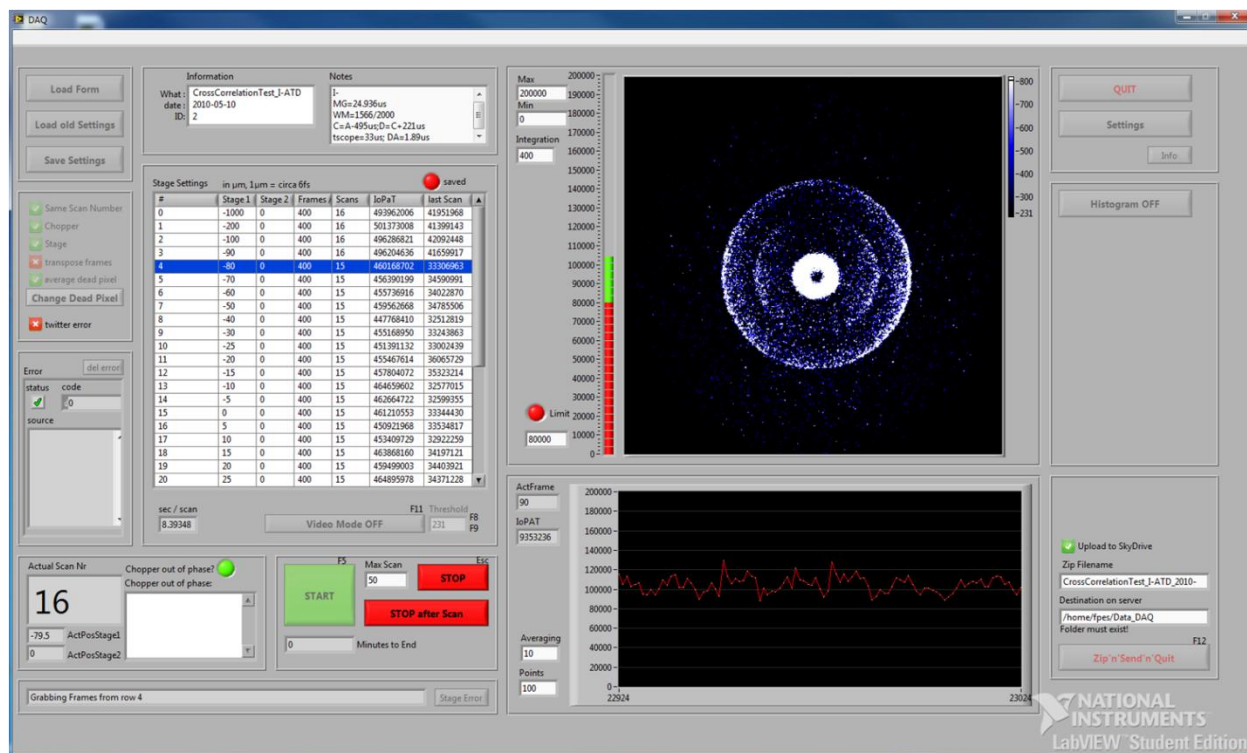


Figure A4.3. Interface of the ImageDAQ 2.0 during acquisition mode.

Importantly, next to the "Video Mode" box is the field controlling the image "Threshold". This value is typically determined by looking at the images at a fairly fast refresh rate (see below) and increasing the threshold until the intensity from the ambient light (typically around the sides of the camera enclosure) is eliminated. The threshold can also be set with the help of the "Histogram" at the middle-right part of the screen, which shows a histogram of the number of pixels with a given intensity.

On the right side is the processed image display, showing the binned 512×512 pixel² image false-color mapped to the scale on the upper right of the image box. The scale will map from black to blue in increasing intensity from two specified values. Most instructive is when the lower value is the "Threshold" value and the upper value is the threshold+1, yielding a monochrome, 1 bit-depth image. The upper value can be raised to whatever level is most instructive depending on the image intensity (above threshold). This scale is referred to as the "Image Scale". To the left of the image is the control for the refresh rate of this screen, called the "Integration" ("n"). This field can take values from 1 to the values specified in "Frames", since after that number has been acquired images are passed from the RAM and saved to the disk and cannot be processed by this routine any longer. This value typically requires one save cycle to update. Next to this is a green "tank" or an intensity meter showing the intensity above threshold summed over the number of frames being integrated/displayed at each update. The minimum and maximum of this tank can be controlled by the appropriate fields in the upper left of the image box. At the bottom left of this box is the "Limit" ("L") field, where the minimum acceptable IoPAT is set and a button to activate this level of discrimination.

Below the image box is a graphical representation of the IoPAT shown as a function of

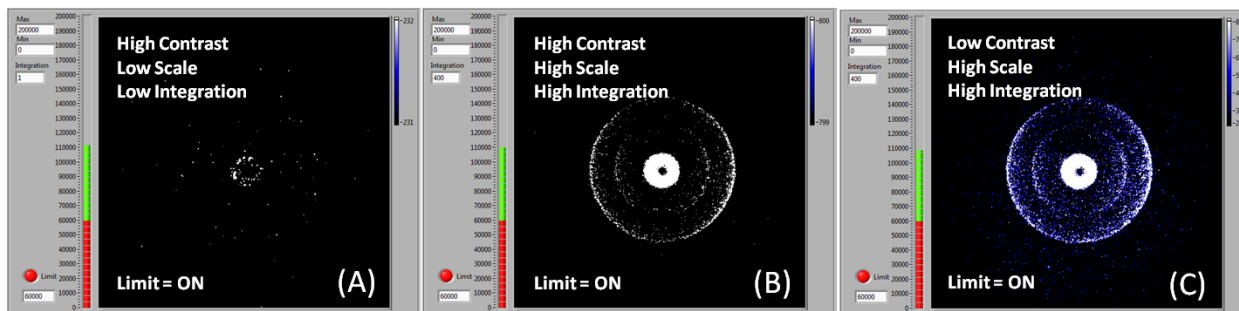


Figure A4.4. Processed images from simultaneous detachment of I^- with 263 nm and 395 nm. (A) shows the single frame (low integration) with high contrast and a low scale. A single frame corresponds to PRF/30 fps, in this case 20 laser pulses per frame at 600 Hz (though the ion source was at 100 Hz, so photoelectron signal is about 3.3 pulses/frame). (B) Shows the effect integration, while (C) shows the effect of contrast on the image.

time. The plot will display a specified number of IoPAT values ("Points" field to the lower left) averaged over the specified number of frames ("j", Averaging" field above "Points"). The x-axis is in units of frames. This plot is perhaps the most useful in the suite as it allows for real-time monitoring of signal stability as well a method for finding the appropriate laser/ mass spectrometer time delay (SRS box 1, channel "A").

At the very right are the controls to quit and modify the settings. If the data are wished to be archived and uploaded to a server, the name of the archive file and the address on the server are inputted in the fields in the lower right. The folder on the server must exist prior to upload otherwise the upload will fail (there is always a default folder on the server, but if this directory is changed in the field the upload will fail). Archiving and uploading are achieved with the "Zip 'n' Save 'n' Quit" button, which also terminates the program, bringing the user back to the "Main Caller" menu.

A4.3 Modifying Parameters and Setting Dead Pixels

Many of the parameters used by ImageDAQ 2.0 are stable and do not need to be changed during normal operation, such as network connectivity settings and the location of dead pixels. However, these values are easily changeable in the event the server address or the camera conditions change. Figure A4.4 shows the Settings menu on the left and the Dead Pixel locator on the right. Adjustable parameters in the settings menu include the default directory for data storage and the general purpose interface bus (GPIB) addresses of the translation stage controller and the optical chopper, as well as the camera threshold. The file containing the locations of the dead pixels is also specified in this menu. The remaining settings control contact with the server, specifically the FTP address, port and hostkey, along with the user account and password. Remote status monitoring is controlled via a batch file specified at the very bottom. New values to be saved are displayed on the left while the current values set to be discarded are displayed on the right for reference.

Selection of dead pixels is straight forward: once the location of a dead pixel has been determined, simply enter that pixel's location (x,y) in the open field of the "Change Dead Pixel" menu and save to file. Determining the location of the pixel in question can be done by recording an image with the detector completely off and the threshold at normal conditions and then analyzing the image in any bitmap viewing program that reads off a pixel's coordinate, such

$$\begin{array}{c|c|c}
 1 & 2 & 0 \\
 \hline
 1 & 10^{12} & 1 \\
 \hline
 1 & 2 & 0
 \end{array}
 \longrightarrow
 \begin{array}{c|c|c}
 1 & 2 & 0 \\
 \hline
 1 & 1 & 1 \\
 \hline
 1 & 2 & 0
 \end{array}$$

Figure A4.5. Dead pixel averaging

as Windows Paint. These locations are then saved to the text file read by the ImageDAQ 2.0 setting routine and can be archived for later inspection.

Dead pixels are not simply set to zero; indeed this could have deleterious effects on the quality of the data. Rather, the value of the dead pixel in the image matrix is replaced by the average of the eight pixels surrounding it. The averaging operation is done after the binning process though it would be entirely equivalent as far as the quality of the data; the images are smaller after binning requiring less processor time per image, thus speeding up the acquisition/pre-analysis process. Note that the top and bottom rows (0 and 511) have been deleted (set to zero) and are not controlled by this routine.

A4.4 Error Codes, Known Issues, and Future Improvements

Error handling is a key feature of this version of the program. The following section details most of the errors encountered during normal operation of ImageDAQ 2.0. Certain error codes are designed to only occur if the program rejects images based on user-entered constraints, such as de-phasing of the chopper or unacceptable image intensity.

- Chopper out of phase
- Intensity Dropped Below Limit

The program rejects the image for save in each of these cases and goes into standby mode, allowing the user to either address the signal in video mode or wait for the chopper to re-phase. The stage error must be cleared, however the chopper communication error will result in an audible "beep" and an automatic re-acquisition of that image.

The other main errors result from disruptions in communications with either the translation stage controller (Newport MM3000) or the optical chopper (New Focus 3501), both of which are daisy-chained to the same GPIB interface card. The daisy-chaining frequently causes these errors to be coupled, however it is a minor inconvenience and not worth the cost of another GPIB card.

- Wrong Chopper
- Chopper Off
- "I can't feel my arms" - Cannot Communicate with Stage Controller
- VISA write-in/write out error.

The chopper errors tend to clear on their own after restarting the program (either Video Mode or Acquisition Mode), unless of course the chopper was left off unintentionally. Alternatively, if laser-induced electron noise is not a concern, communication with the chopper can be

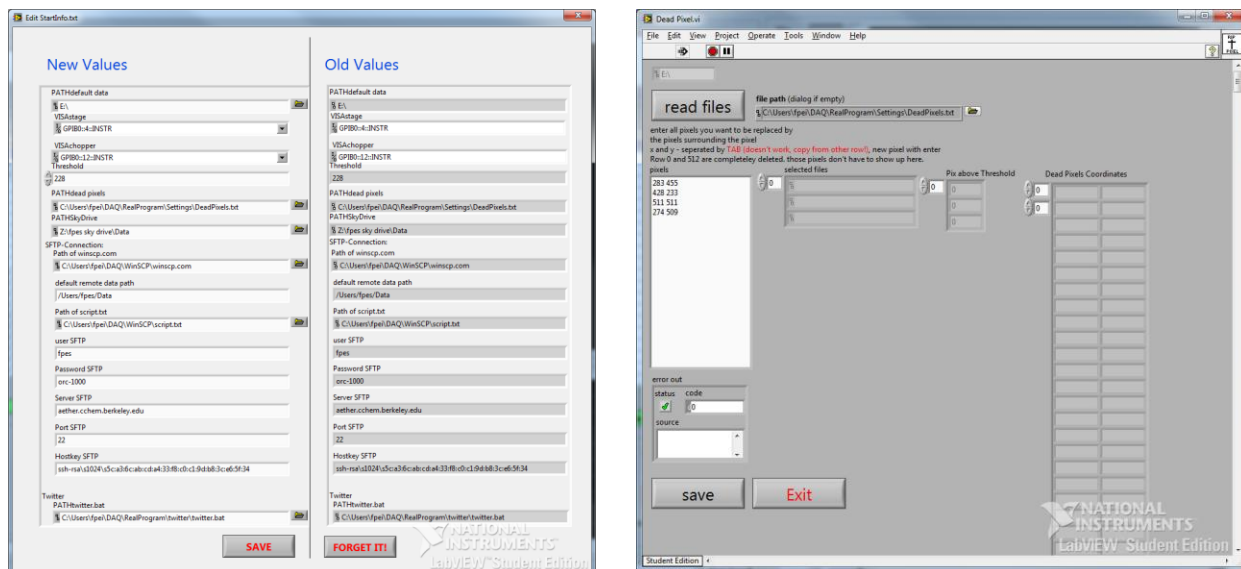


Figure A4.6. Settings (left) and Dead Pixel (right) control panels.

disengaged by clicking the "Chopper" button in the communications control box (see above). When communication with the stage has been lost the error code must be cleared and the MM3000 must be reset manually (with the "Reset" button on the front panel of the controller). *This does not change t_0* - the MM3000 has internal memory that is not cleared by the reset control. Unfortunately, it frequently takes more than one attempt to clear this error, but it has always worked, if not always the first time. For one-color experiments, this can be avoided altogether by disengaging communication with the stage. Other errors are possible, such as a "write error" when the computer's hard disk is full, but this is readily fixed by deleting old data.

ImageDAQ 2.0 does have some known bugs, but they are small in number and easily worked around. Most prominently is the location of the saved data when a form is edited more than once in the same session. Typically, a form is opened/edited and the time-resolved data set is ready to be acquired. However, sometimes the location of t_0 needs to be changed from the initial guess or the number/values of the delays must be changed. If the user selects "Load Form" and reloads or edits the existing form, then the program will again create a directory in the same place as before, but with a new ID tag (as it should to avoid overwriting). However, if the program was not "Quit" first, the location of the saved images is not updated and will still be saved in the original folder (from the first time the form was loaded in that session). Typically this is harmless as it is usually done before any data are saved, such that overwriting is a non-issue. Changes in the delay settings also typically change the combination of delay index and stage positions enough to avoid (many) overlapping delays. However, in general this should not happen at all, and as such is a "bug". It can be addressed by selecting "Quit" before adjustment of the form.

The original intent of the form creation was to have "Material" create a folder for a given material being studied, and then the filename would be whatever cluster size or varied parameter was being studied in that data set. Once the set of experiments on that material were done, a new material folder could be created, automatically organizing the data. This ended up being implemented as a redundant filename system where the folder and the filename did not lead to any natural organization system. Again, this is a minor (but known) issue and can be addressed

in the next version. There also exists a "transpose image" button which must always be activated in order to collect the correct image orientation. The intent of this was actually to be able to simply rotate the image by 90° to correct for possible issues with the frame grabber. Removal or switching the default option of this tool should be accomplished in the next version.

Aside from addressing these "bugs", in the future it would be useful to have all the programs we utilize for data acquisition and analysis to be merged together. ImageDAQ 2.0 is meant to be interfaced directly with the data analysis software suite originally developed for BASEX by Dr. Oli Ehrler in 2008 and can be readily made to work with the newer version meant to employ BASEX,¹ pBASEX² and the Polar Onion Peeling algorithm³ currently under development by Sarah King. The image input format, however for each of these algorithms is different and must first be unified. Since a unified image format would require recoding of the three different analysis packages, a converter has been created to address this. Merging this converter with the data analysis suite (once it is completed) would simplify the process. (However, having a stand-alone converter/analysis program in addition to the unified suite is still preferable as it allows for remote image reconstruction on multiple, personal computers). Considering the large size and numbers of the images, changing the default image file structure from a bitmap to an ASCII text-based image (in conjunction with the converter) would be beneficial as ASCII files are only KBs in size. Unifying the ImageDAQ/analysis suite with the stand-alone stage control software used for finding t_0 and the module used to process the reconstructed spectra into an Origin file written by Dr. Ehrler would also be useful.

Other more stringent tests of the data as they are being acquired could also be useful. Specifically, the IoPAT Limit check only provides a lower limit on the intensity of an image acceptable for saving. While this is very useful, it can be easily defeated by choosing too low of a limiting value such that oscillations much higher than the limit are ignored. Thus an upper limit would also be useful. Moreover, the stability of the signal in a time-resolved experiment is of paramount importance. If the signal level drops rapidly and does not recover before the next delay then the image will be rejected on account of its low IoPAT value. However, if the intensity recovers quickly enough the total intensity could still be sufficient. The fluctuations during the recording of this image could render it unreliable. Installing another check based on the derivative of the (probably averaged) IoPAT such that it cannot fluctuate too rapidly would be extremely useful toward ensuring the best data quality. The check would have to be done at each update of the (averaged) IoPAT readout, which could slow data collection, or it could be done before saving at the end of the frame accumulation. Depending on the nature of the fluctuation, such as from the detector arcing causing a large intensity spike or from loss/interruption of the trigger, it would likely be better for the check to be done in real time, allowing the warning screen and sound to be activated immediately.

A4.5 References

- 1 V. Dribinski *et al.*, Rev. Sci. Instrum. **73** (7), 2634 (2002).
- 2 G. A. Garcia, L. Nahon, and I. Powis, Rev. Sci. Instrum. **75** (11), 4989 (2004).
- 3 G. M. Roberts *et al.*, Rev. Sci. Instrum. **80** (5), 053104 (2009).

Appendix 5. Publications from Graduate Work

1. R. M. Young, D. M. Neumark, "Solvated Electron Dynamics in Clusters", *Chemical Reviews*, In preparation.
2. R. M. Young, M. A. Yandell, S. B. King, D. M. Neumark, "Thermal Effects on Energetics and Dynamics in Water Cluster Anions $(\text{H}_2\text{O})_n^-$ ", In preparation.
3. R. M. Young, J. Azar, M. A. Yandell, S. B. King, M. Head-Gordon, D. M. Neumark, "Iodide solvation in tetrahydrofuran clusters $\text{I}^-(\text{THF})_n$ clusters ($1 \leq n \leq 30$)", In preparation.
4. M. A. Yandell, R. M. Young, S. B. King, D. M. Neumark, "Effects of Excitation Energy on the Autodetachment Lifetimes of Small Iodide-Doped ROH Clusters ($\text{R}=\text{H}, \text{CH}_3, \text{CH}_2\text{CH}_3$)", *J. Phys. Chem. A.*, In press.
5. R. M. Young, M. A. Yandell, D. M. Neumark, "Dynamics of electron solvation in $\text{I}^-(\text{CH}_3\text{OH})_n$ clusters ($4 \leq n \leq 11$)", *J. Chem. Phys.* **134**, 124311 (2011)
6. R. M. Young, M. A. Yandell, M. Niemeyer, D. M. Neumark, Photoelectron imaging of tetrahydrofuran cluster anions $(\text{THF})_n^-$, *J. Chem. Phys.* **133**, 154312 (2010)
7. R. M. Young, G. B. Griffin, A. Kammrath, O. T. Ehrler, and D. M. Neumark, Time-resolved dynamics in acetonitrile clusters anions $(\text{CH}_3\text{CN})_n^-$, *Chem. Phys. Lett.* 485, 59 (2010)
8. G. B. Griffin, R. M. Young, O. T. Ehrler, and D. M. Neumark, Electronic relaxation dynamics in large anionic water clusters: $(\text{H}_2\text{O})_n^-$ and $(\text{D}_2\text{O})_n^-$ ($n = 25-200$), *J. Chem. Phys.* **131**, 194302 (2009).
9. R. M. Young, G. B. Griffin, O. T. Ehrler, A. Kammarath, A. E. Bragg, J. R. R. Verlet, O. Cheshnovsky and D. M. Neumark, Charge carrier dynamics in semiconducting mercury cluster anions, *Phys. Scr.* **80**, 048102 (2009)
10. G. B. Griffin, O. T. Ehrler, A. Kammarath, R. M. Young, O. Cheshnovsky and D. M. Neumark, "Auger recombination and excited state relaxation dynamics in Hg_n^- ($n = 9 - 20$) anion clusters" *J. Chem. Phys.* **130**, 231103 (2009)
11. O. T. Ehrler, G. B. Griffin, R. M. Young, and D. M. Neumark, "Photoinduced electron transfer and solvation in iodide-doped acetonitrile clusters" *J. Phys. Chem. B* **113**, 4031 (2009).

12. G. B. Griffin, A. Kammarath, O. T. Ehrler, R. M. Young, O. Cheshnovsky and D. M. Neumark, "Auger recombination dynamics in Hg_{13}^- clusters", *Chem. Phys.* **350**, 69 (2008).
13. A. Kammarath, G. B. Griffin, J. R. R. Verlet, R. M. Young and D. M. Neumark, "Time-resolved photoelectron imaging of large anionic methanol clusters: $(\text{Methanol})_n^-$ ($n \sim 145 - 535$)" *J. Chem. Phys.* **126**, 244306 (2007).